Simulation of Strong Ground Motions in Mashiki Town, Kumamoto, Based on the Seismic Response Analysis of Soils and the Dynamic Rupture Modeling of Sources

SUN JIKAI

Abstract

The sequence of 2016 Kumamoto earthquake caused a devastating disaster in downtown Mashiki, Kumamoto Prefecture, Japan. Considerable number of buildings were damaged during the mainshock. Among different structural types, the damages to wooden houses were especially severe, approximately 28% of them were heavily damaged. According to the survey results of the Architectural Institute of Japan (AIJ), it generated a damage belt spread mainly in the east-west direction in the area between the Prefecture road No. 28 and the Akitsu river in Mashiki. Also, some liquefaction sites were found in areas near the river. It is indispensable to validate a unified approach for earthquake damage prediction in order to make quantitative assessment of future seismic hazard and risk. The damage distribution in Mashiki has raised the following three important questions to answer: a) What was the contribution of local site amplifications to create the damage belt? b) What was the seismic performance of local buildings during the mainshock? c) What was the contribution of the source process to the strong ground motions during the mainshock?

The aim of this study is to answer to these questions and validate the approach for earthquake damage predictions. To find the answers, first, the site effects of Mashiki were investigated by performing the linear analysis (LA), equivalent linear analysis (ELA), and nonlinear analysis (NA). Then, the dynamic rupture analysis for the mainshock of the 2016 Kumamoto earthquake was carried out, to study the source effects, in order to understand the contribution of the source rupture process. Before the site response study, subsurface soil structures of Mashiki was required, so the inversion of earthquake horizontal-to-vertical spectral ratio (EHVR) or pseudo-EHVR (pEHVR) would be applied in the research. Because the pEHVR was obtained from the microtremor horizontal-to-vertical spectral ratio (MHVR), microtremor observations in Mashiki were conducted in 2016 and 2018. Furthermore, construction periods of wooden houses are necessary to evaluate the damage probability of Mashiki wooden houses. More than 50 years have passed since Mashiki started from a small center and developed into the current large downtown, so the analysis model of building damage probability in this study needs to consider the construction age. Ten chapters of this study explains these results.

Chapter 1 is the introduction of research background and purposes of the study. This chapter describes the detail information about the 2016 Kumamoto earthquake, the damage caused by the earthquake and related research results. The problems to be solved in this study, the specific research steps and methods, the expected research results, and related discussions are also described. Then, the structure of this thesis is presented.

Chapter 2 illustrates the microtremor observations in downtown Mashiki and results of analyses of MHVRs. A map of the fundamental frequencies at 86 microtremor observation sites is shown. It was found that the fundamental frequencies obtained from MHVRs show higher values in the northeastern side (up to 4.6 Hz) and lower values in the southwestern side (<1.0 Hz) of Mashiki.

Chapter 3 presents the analysis of EHVR and pEHVR, which is the transformed EHVR from MHVR. This chapter includes the introduction of the method to transform MHVR to EHVR (the EMR method). The pEHVRs, MHVRs, and EHVRs are compared at and around the strong motion sites in Mashiki, and pEHVRs are found to be the good choice to be used for the identification of subsurface velocity structures in a wide area of Mashiki.

Chapter 4 explains about the identified subsurface velocity structures in Mashiki. Inversion of the pEHVRs and EHVRs in Mashiki were carried out by using the hybrid heuristic search method. The resultant structures can reproduce observed EHVRs or estimated pEHVRs quite well. The depth distribution of the engineering bedrock is derived from the inversion results and the distribution of time-averaged share wave velocity of top 30m (Vs30) of Mashiki is generated. The results show that the stack of soft layers is thicker in the southwestern part, especially for the area close to the Akitsu River.

Chapter 5 explains the methodology and result of the estimation of strong ground motions in Mashiki by using the linear ground response analysis (LA) and equivalent-linear ground response analysis (ELA). The properties of shallow subsurface layers and observed ground motions during the mainshock at the KiK-net Mashiki station, KMMH16, is briefly introduced, the method to estimate

the seismological bedrock motions based on the diffuse field concept is explained, and comparisons of the estimated and observed ground motions at KMMH16 are discussed. Finally, the distribution of the peak ground acceleration (PGA) and the peak ground velocity (PGV) in Mashiki is obtained. It is found that the PGVs in the southwestern area are larger than other areas, which is consistent with the distribution of the building damage.

Chapter 6 illustrates the estimation of strong ground motions in Mashiki by using the nonlinear analysis (NA) with liquefaction. This chapter introduces the two models to consider the nonlinear soil response, namely the Ramberg−Osgood model for representing the soil nonlinear property and the bowl model (owan model) for considering the effects of the excess pore water pressure. The distribution map of water table depth in Mashiki is obtained, the nonlinear properties of shallow subsurface layers at four borehole drilling sites are analyzed, the sand properties for Mashiki sites are classified into four categories, the strong ground motions in Mashiki are estimated by NA, and the distribution map of soil liquefaction sites in Mashiki is shown. The estimated PGV distribution show similar characteristics to the ELA results in Chapter 5. Most of the liquefaction sites are next to the river, which is similar to the observed results.

Chapter 7 reports the determination of construction periods of existing buildings in Mashiki. The buildings of Mashiki are classified into four categories based on their construction periods: before 1950, 1951−1970, 1971−1980, and after 1981. The results show that the percentage of old buildings in the central part of Mashiki is larger than other areas in Mashiki. This means that the age distribution should also contribute the creation of the observed damage belt.

Chapter 8 shows the analyses results of building damage probabilities (DP) in Mashiki, based on the estimated strong ground motions by ELA and NA. The DPs are calculated based on the estimated strong ground motions by ELA and NA. The estimated DP by ELA and NA are similar to the AIJ field survey results, especially the estimated DP by NA showed closer distribution to the AIJ results. This means that a higher DP zone appears at the southwestern area of Mashiki. The site-specific strong ground motions and building construction periods are found to be two influential factors of the building damage distributions during the Kumamoto earthquake.

Chapter 9 explains the strong ground motions simulated by the dynamic rupture analysis for the mainshock. A set of parametric studies were performed based on the finite difference calculations with a slip-weakening dynamic fault rupture model to find the relationships of the assumed stress drop and the resultant slip amount. It was found that the forward directivity effect has a significant influence to produce the large PGA and PGV along the direction of rupture propagation, the peak slip velocity increases greatly inside the asperity as rupture propagates and the high PGV on the surface is created by the high slip-velocity areas, but not by the large slip areas. These findings, together with the inverted slip distribution on the fault segment beneath Mashiki, suggested that the observed high PGV at Mashiki wascaused by the strong rupture directivity from the asperity immediately beneath Mashiki. Peak values of estimated ground motions by the rupture dynamics analysis at KMMH16 were similar to the observed ones. The estimated seismological bedrock motions at KMMH16 and KMMP58 were almost identical. Thus, the same seismological bedrock motions could be used in Mashiki when doing the site response analysis. Moreover, PGV and PGD distributions showed obvious effects of rupture directivity during the mainshock. It also resulted in a significant amplitude in the east-west component of the ground motions in Mashiki. These results provide encouraging evidence for future delineation of the dynamic properties of the seismogenic fault during the 2016 Kumamoto earthquake.

Chapter 10 provides the discussions and conclusions of this thesis.

In summary, this thesis investigates the surface soil structures of Mashiki from observed earthquakes and microtremors, evaluates the contribution of nonlinear amplification characteristics in the strong ground motions, reproduces the building damage based on the estimated age distribution, and evaluate possible contribution of the dynamic rupture propagation on the fault to the observed high peak ground velocity at Mashiki during the mainshock. The approach proposed here can be used for any earthquake disaster investigations in the future and the information derived here can be used for the sophisticated earthquake risk evaluation.

Contents

Chapter 1: Introduction

1.1 Research background 1-1

1.1.1. 2016 Kumamoto earthquake 1-1

1.1.2. Building damage survey and soil liquefaction survey at Mashiki 1-2

1.2 Research purposes 1-6

1.3 Research contents 1-7

References (Chapter 1)

Chapter 2: Microtremor observation and microtremor horizontal-to-vertical spectral ratio analyses in Mashiki

2.1 Introduction 2-1

2.2 Microtremor observation in 2016 and 2018 2-1

2.3 Analyses of microtremor horizontal-to-vertical spectral ratio 2-3

2.4 Fundamental peak frequency of Mashiki 2-4

2.5. Conclusion 2-6

Reference (Chapter 2)

Chapter 3: Pseudo earthquake horizontal-to-vertical spectral ratio analyses in Mashiki

3.1 Introduction 3-1

3.2 Earthquake horizontal-to-vertical spectral ratios at Mashiki 3-2

3.3 Discussion and conclusion 3-5

Reference (Chapter 3)

Chapter 4: Identification of subsurface velocity structures in Mashiki

4.1 Introduction 4-1

4.2. Inversion of EHVRs and pEHVRs 4-1

4.3 Distributions of engineering bedrock depth and V_s30 4-7

4.4. Conclusion 4-9

Reference (Chapter 4)

Appendix 4.1

Chapter 5: Linear and equivalent linear analyses of subsurface velocity structures in Mashiki

5.1 Introduction 5-1

5.2. Nonlinear soil property at KMMH16 5-2
5.3. Horizontal seismological bedrock motions at KMMH16 5-6
5.4 Linear analysis and equivalent linear analysis of subsurface velocity structures at KMMH16 and KMMP58 5-10
5.5. Linear analysis and equivalent linear analysis in Mashiki 5-16
5.5.1. Results of 57 sites 5-16
5.5.2. Results of 592 sites. 5-16
5.5.3. Discussion 5-17
5.6. Conclusion 5-23
Reference (Chapter 5)

Chapter 6: Nonlinear analyses of subsurface velocity structures in Mashiki

6.1. Introduction 6-1
6.2. Theory of the Fukutake model 6-3
6.2.1. Hyperbolic model and its parameters 6-3
6.2.2. Bowl model and its parameters 6-5
6.3. Nonlinear response analysis of 592 sites in Mashiki 6-10
6.3.1. Water table depth of Mashiki 6-11
6.3.2. Estimated seismic motions at engineering bedrock 6-13
6.3.3. Nonlinear analysis of soil column at KMMH16 6-15
6.3.4. Nonlinear analysis of soil column at KMMP58 6-23
6.3.5. Nonlinear analysis of soil column at MSA32 6-32
6.3.6. Nonlinear analysis of soil column at MS9-6 6-41
6.3.7. PGA and PGV distribution of Mashiki based on the NA 6-50
6.4. Conclusion 6-53
Reference (Chapter 6)

Chapter 7: Investigation of building construction period in Mashiki

7.1 Introduction 7-1
7.2. Definition of building construction period in Mashiki 7-1
7.3. Conclusion 7-8
References (Chapter 7)

Chapter 8: Damage probability estimations of Mashiki wooden houses using estimated ground motions of linear, equivalent linear, and nonlinear analyses

8.1 Introduction 8-1
8.2. Nonlinear response models of wooden building 8-4

8.3. Building damage probability estimation of KMMH16 8-5
8.3.1. Using the ELA ground motions 8-5
8.3.2. Using the NA ground motions 8-8
8.4. Damage probability estimation of Mashiki 8-11
8.4.1. Damage probability estimation results of ELA 8-11
8.4.2. Damage probability estimation results of NA 8-15
8.5. Conclusion 8-18
References (Chapter 8)

Chapter 9: Simulation of strong ground motions in Mashiki during the mainshock of 2016 Kumamoto earthquake using rupture dynamics model
9.1. Introduction 9-1
9.2. Parameter study of the rupture dynamic simulation model for a M6.7 earthquake 9-1
9.2.1. Numerical modeling and parameterization 9-2
9.2.2. Simulation result of no-basin structure 9-6
9.2.3. Simulation result of basin structure 9-13
9.2.4. Slip velocity function of dynamic rupture simulations 9-18
9.3. Simulation of mainshock of 2016 Kumamoto earthquake 9-20
9.3.1. Fault property distributions of the mainshock 9-21
9.3.2. Comparisons between estimated and observed ground motions in Mashiki 9-25
9.3.3. Distributions of PGV and PGD 9-43
9.4. Conclusion 9-46
Reference (Chapter 9)

Chapter 10: Conclusion
10.1. Conclusion 10-1

Data and Resources

Acknowledgement

Publication

Chapter 1

Introduction

1.1. Research background

1.1.1. 2016 Kumamoto earthquake

1.1.2 Building damage survey and soil liquefaction survey at Mashiki

1.2. Research purposes

1.3. Research contents

References (Chapter 1)

1.1. Research background

1.1.1 *2016 Kumamoto earthquake*

The 2016 Kumamoto earthquake sequence included two major earthquakes, both seismic faults were located in Kumamoto, Japan. According to the Japan Meteorological Agency (JMA), the first large earthquake occurred at 21:26 Japan standard time (JST) on April 14 (12:26 coordinated universal time, UTC) and had a magnitude of 6.5 on the JMA magnitude scale (M_{JMA}), which converts to a moment magnitude (M_W) of 6.2. Its focal depth was 11 km, and the highest JMA seismic intensity of VII was recorded in downtown Mashiki. The second large earthquake occurred at 01:25 JST on April 16, 2016 (16:25 UTC on April 15, 2016). The reported M_{JMA} was 7.3 (M_W = 7.0) and the focal depth was 12 km. The highest JMA seismic intensity of VII was also recorded in Mashiki [1–8]. Hereafter, we refer to the M_{JMA} 6.5 earthquake on April 14, 2016 as the foreshock and the M_{JMA} 7.3 earthquake on April 16, 2016 as the mainshock. This was the first time the Japan Meteorological Agency (JMA) had recorded seismic intensity of VII twice within two days [9].

There were over 4,000 earthquakes with seismic intensities of one or more within six months of the first tremor, exceeding even the figure for the active 2004 Mid-Niigata Prefecture Earthquake period [9]. Aftershock activity from the Kumamoto Earthquake continues, although a trend of decay is observed. The focal mechanism of the foreshock exhibited strike-slip faulting with a north-south tension axis. The focal mechanism of the mainshock exhibited strike-slip faulting with a northwest (NW) to southeast (SE) tension axis [9,10]. The Headquarters for Earthquake Research Promotion judged that the foreshock occurred along the Hinagu fault zone (Takano-Shirahata section), while the mainshock occurred mainly along the Futagawa fault zone (Futagawa section) [9,11].

These two events caused enormous damage to structures most of which were wooden houses. They caused 251 direct and indirect fatalities, 2,792 injuries and 205,897 records of residential damage, including 8,677 total collapses, in Kumamoto Prefecture and the prefectures of Yamaguchi, Fukuoka, Saga, Nagasaki, Oita and Miyazaki and elsewhere. Evacuee numbers were as high as 183,883 in Kumamoto Prefecture and a total of 190 sediment-related incidents were also reported [9].

Downtown Mashiki is located near the junction of the western end of the Futagawa fault zone and the northeastern end of the Hinagu fault zone in the east of Kumamoto city. It was heavily damaged by the mainshock. The locations of epicenters of the two earthquakes and downtown Mashiki are shown in Fig. 1.1

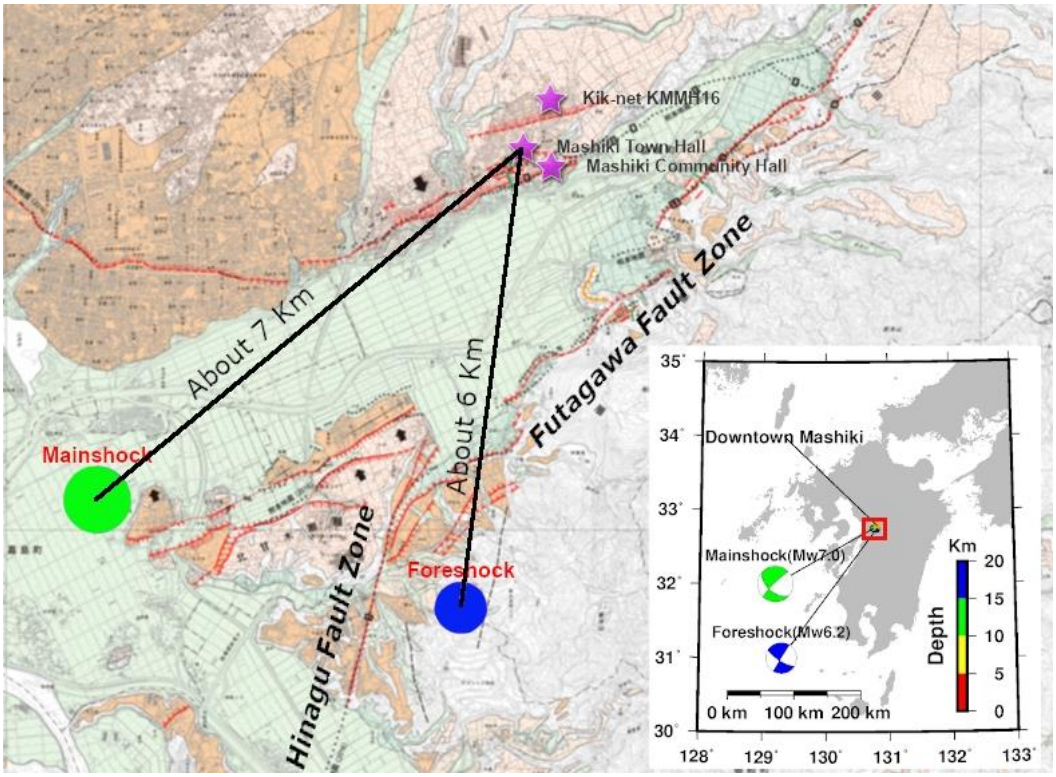

Fig. 1.1 Locations of downtown Mashiki and epicenters of two large earthquakes [8]. The three stars marks the locations of the strong motion stations in Mashiki. The centers of the circles are the epicenters of the two large earthquakes. The dotted lines are the fault zones in this region. The inserted map at the bottom right of the figure shows the location of Mashiki and the focal mechanisms for the foreshock and mainshock. The earthquake information can be accessed at the National Research Institute for Earth Science and Disaster Resilience F-net website [10]. The background map is the fault zone maps obtained from the Geospatial Information Authority of Japan [12].

1.1.2 *Building damage survey and soil liquefaction survey at Mashiki*

After the mainshock, the Architectural Institute of Japan (AIJ) performed a field survey to evaluate the building damage, as shown in Fig. 1.2 [13]. The damage ratio of each cell in Fig. 1.2 is the ratio between the total number of buildings with ≥D4 damage and the total number of buildings in a cell (approximate 57 * 57 m). Obviously, most of the heavily damaged buildings appeared at the area between the local road No. 28 and the Akitsu River [4,8]. However, Fig. 1.2 does not depict the building damage in the northwestern area of the town because they were not included. Yamada et al. [3] estimated the building damage distribution in Mashiki by the aerial photo analysis departed before, after, and during the interval of the foreshock and mainshock. Moya et al. [14] discussed the building damage in the south part of Mashiki using the empirical fragility functions. Yamazaki studied the

relationship between the building damage ratio and building construction period in Mashiki [6]. Although the AIJ reported the building damage distributions in the central area of Mashiki, the reasons for causing the great damage to wooden houses were not clear. As most of the older buildings were found in the heavy damaged area, the construction period of buildings may be one of the reasons to have caused the heavy damages at central Mashiki. Furthermore, in the northwestern part of Mashiki, AIJ report does not indicate any building damage distribution. Because some older buildings also located in this area, heavy damage may have happened during the mainshock.

After the mainshock, researchers conducted observation of soil liquefactions at Mashiki. Most of the liquefied sites were close to the Akitsu River (Figs. 1.3 and 1.4), where the building damage was not strong compared with the adjacent area in the north. Moreover, the observed strong ground motions at KiK-net Mashiki (KMMH16) [National Research Institute for Earth Science and Disaster Resilience (NIED), 2019] and Mashiki Town Hall (KMMP58) had significant difference, although the distance of two sites were about few hundred meters. Maybe the soil liquefaction had strong effect on the ground motions during the mainshock. Further, these ground motions may have generated the different damage levels for areas near the river and other areas in the northern part. In addition, the source effects may be one of the reasons to cause the large difference between these observed strong ground motions in Mashiki.

Upon studying the 1995 Hyogo-ken Nanbu (Kobe) earthquake, Kawase [15] concluded that the region with both a high PGA and a high PGV corresponded to the observed damage belt in Kobe city. Montalva et al. [16] studied the 2010 M_w 8.8 Chilean earthquake and found a strong correlation between the building damage distribution in Concepcion, Chile, and the estimated PGV. After the mainshock of the 2016 Kumamoto earthquake, Kawase et al. [4] proposed the idea that the heavy damage distribution in Mashiki may be caused by the high peak ground acceleration (PGA) and peak ground velocity (PGV). Yamada et al. [3] also mentioned that the building damage in Mashiki may be related to the local site effect and building construction period.

There are two permanent stations for strong-motion observation in Mashiki, as shown in Figs. 1.1 and Fig. 1.2. One station is the KMMH16 and the other is KMMP58, the Kumamoto Prefecture's Instrumental Intensity Seismometer, which was set up on the first floor of the Mashiki Town Hall [17]. In this paper, we will call the Mashiki Town Hall station as "KMMP58" for convenience. After the mainshock, they moved the station at the town hall to the *Bunkakaikan* (also called the Mashiki Community Hall) temporarily.

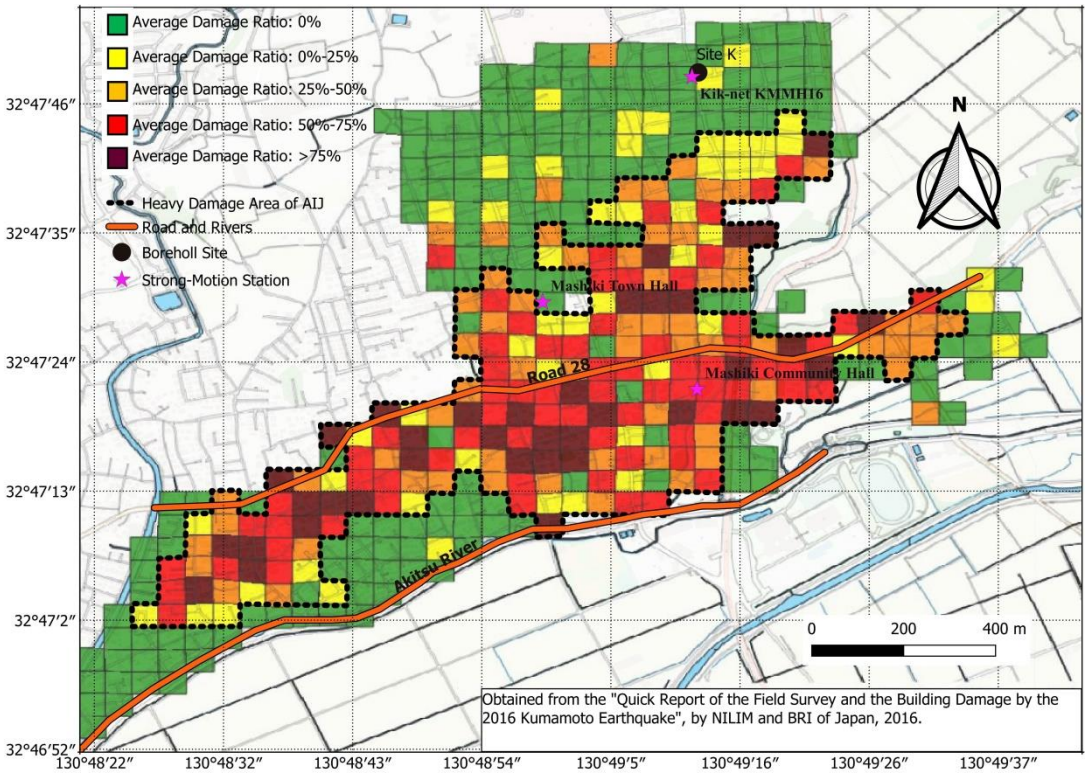

Fig. 1.2. Building damage survey results of AIJ [13]. The heavy damage percentage of each grid is the ratio of the number of heavily damaged buildings in the grid to the total number of buildings in the grid. Five colors represent the average value of the damage ratios in each grid. The dotted line is a rough outline of the heavily damaged area. The large stars marks the strong-motion stations in Mashiki. Site K, which is marked by a black dot, is a borehole-drilling site and is obtained from the studies by Arai [18] and Nakagawa et al. [19].

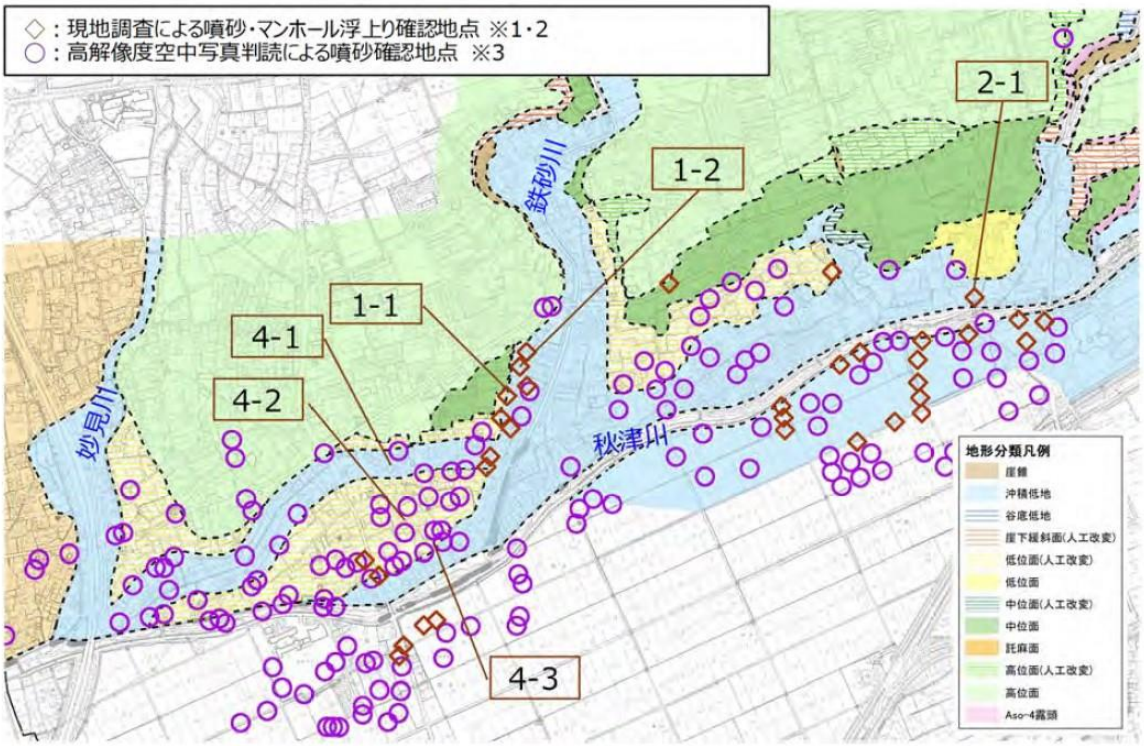

Fig. 1.3. Soil liquefaction site distribution in Mashiki [20]**, obtained from the Ministry of Land, Infrastructure, Transport and Tourism (MLIT).**

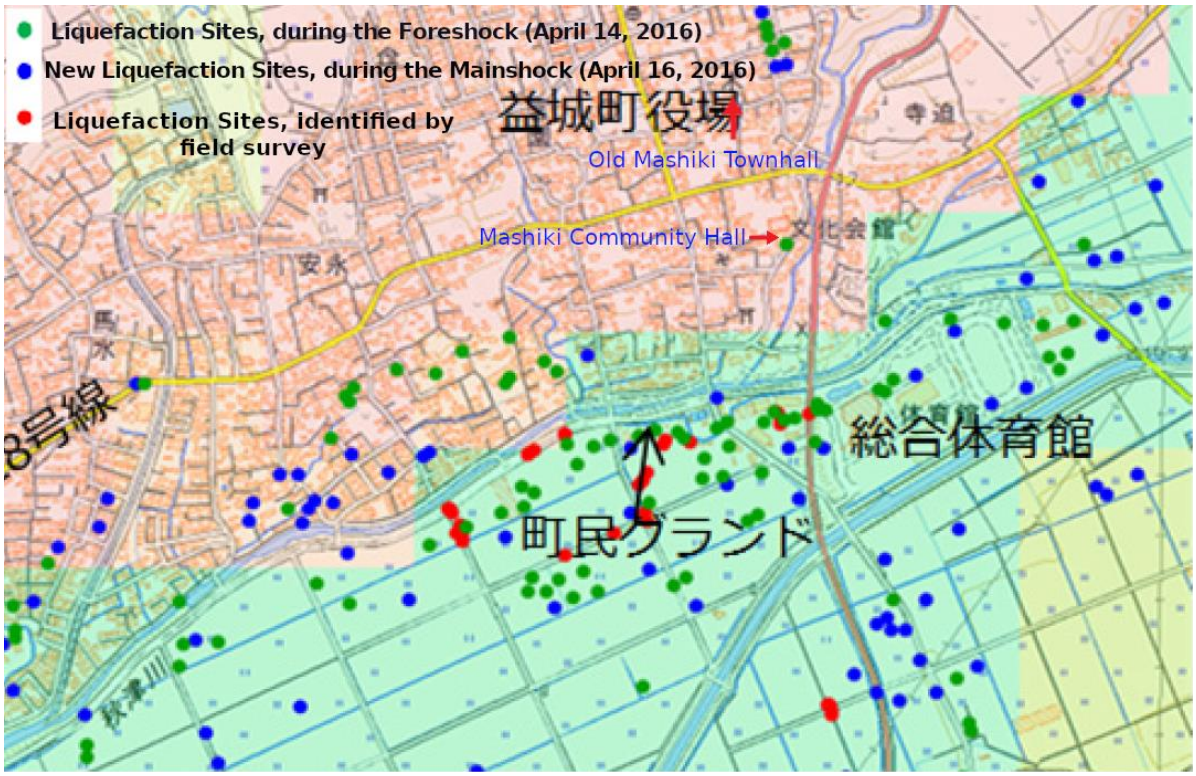

Fig. 1.4. Soil liquefaction sites at Mashiki, obtained from previous study[21].

1.2. Research purposes

In this study, the following questions would be understood: (i) How much degree did the site effects contribute to the heavy damage in downtown Mashiki? (ii) Did the soil nonlinearity have strong influence on the ground motions? (iii) Did the construction period have an important influence to the wooden house damage? (iv) Did the soil liquefaction affect the observed ground motions and damage of wooden house at Mashiki? (v) Did the heavy damage of wooden building appear in the northwestern part of Mashiki? (vi) Did source effects have strong influence on the observed ground motions at Mashiki?

To estimate the damage probability distribution of wooden houses in Mashiki, Yoshida model [22,23] was used. Yoshida model is a nonlinear response analysis model of structures, which was developed based on Nagato-Kawase model [24,25]. Yoshida model considers the construction period as an important parameter to estimate the building damage probability. Also, the spatial distribution of strong ground motions during the mainshock are required for the nonlinear response of structures.

To evaluate the spatial distribution of local strong ground motions in Mashiki, there are two methods. The first one is to estimate the input ground motions at the seismological bedrock and then analyze the ground response of subsurface velocity structure at each site. The seismological bedrock is the layer where the shear wave velocity is equal to or larger than 3 km/s; at this layer, we need not consider site amplifications [26]. The theoretical evaluation of local site effects requires information of velocity structures, especially those of the sedimentary layers above the bedrock [27–30]. Because accurate information of the subsurface velocity structures in Mashiki were not available except for the borehole logging data up to a depth of 252 m at KMMH16 [31] and two borehole drilling sites by other researchers [18,19], single-station measurements of microtremors in and around the damage-concentrated area in Mashiki were performed to delineate the subsurface velocity structures.

The second method is to estimate the input ground motions by the dynamic rupture analysis [32,33]. For this method, the source parameters are necessary. The subsurface velocity structures along the Futagawa and Hinagu fault zones are important to obtain before the analysis.

The aim of this study is to answer to the three questions raised from the damage distribution in Mashiki: a) What was the contribution of local site amplifications to create the damage belt? b) What was the seismic performance of local buildings during the mainshock? c) What was the contribution of the source process to the strong ground motions during the mainshock? Ten chapters of this study are focused on solving these problems. To find the answers, first, the site effects of Mashiki were investigated by performing linear analysis (LA), equivalent linear analysis (ELA), and nonlinear analysis (NA). Then, the dynamic rupture analysis for the mainshock of the 2016 Kumamoto earthquake was carried out to study the source effects, in order to understand the contribution of the source rupture process. Before the site response study, subsurface soil structures of Mashiki was required, so the inversion of pseudo horizontal-to-vertical spectral ratio (pEHVR) would

be applied in the research. EHVRs are obtained from the microtremor horizontal-to-vertical spectral ratio (MHVR), so microtremor observation in Mashiki were conducted in 2016 and 2018. Furthermore, construction periods of wooden houses are necessary to evaluate the damage probability of Mashiki wooden houses. More than 50 years have passed since Mashiki started from a small center and develop into the current large downtown, so the analysis model of building damage probability in this study needs to consider the construction age.

1.3. Research contents

Chapter 1, introduction of research background and purposes.
Chapter 2, microtremor observation and the analysis of MHVR in Mashiki.
Chapter 3, analysis of EHVR and pEHVR in Mashiki.
Chapter 4, identification of subsurface velocity structures in Mashiki.
Chapter 5, estimations of strong ground motions in Mashiki, by LA and ELA.
Chapter 6, estimations of strong ground motions in Mashiki, by NA.
Chapter 7, construction period definitions of buildings in Mashiki.
Chapter 8, analyses of building damage probabilities in Mashiki, based on the estimated strong ground motions of LA, ELA and NA.
Chapter 9, estimations of strong ground motions by the dynamic rupture analysis for the mainshock.
Chapter 10, discussions and conclusions.

References (Chapter 1)

[1] Asano K, Iwata T. Source rupture processes of the foreshock and mainshock in the 2016 Kumamoto earthquake sequence estimated from the kinematic waveform inversion of strong motion data. Earth, Planets and Space 2016;68:147. https://doi.org/10.1186/s40623-016-0519-9.

[2] Sugino M, Yamamuro R, Kobayashi S, Murase S, Ohmura S, Hayashi Y. Analyses of Building Damages in Mashiki Town in the 2016 Kumamoto Earthquake. Journal of Japan Association for Earthquake Engineering 2016;16:10_69-10_83. https://doi.org/10.5610/jaee.16.10_69.

[3] Yamada M, Ohmura J, Goto H. Wooden building damage analysis in Mashiki town for the 2016 Kumamoto earthquakes on April 14 and 16. Earthquake Spectra 2017;33:1555–72. https://doi.org/10.1193/090816EQS144M.

[4] Kawase H, Matsushima S, Nagashima F, Baoyintu, Nakano K. The cause of heavy damage concentration in downtown Mashiki inferred from observed data and field survey of the 2016 Kumamoto earthquake. Earth, Planets and Space 2017;69:3. https://doi.org/10.1186/s40623-016-0591-1.

[5] Yamanaka H, Chimoto K, Miyake H, Tsuno S, Yamada N. Observation of earthquake ground motion due to aftershocks of the 2016 Kumamoto earthquake in damaged areas. Earth, Planets and Space 2016;68:197. https://doi.org/10.1186/s40623-016-0574-2.

[6] Yamazaki F, Suto T, Matsuoka M, Horie K, Inoguchi M, Liu W. Statistical analysis of building damage in Japan based on the 2016 Kumamoto earthquake. 17th US-Japan-New Zealand Workshop on the Improvement of Structural Engineering and Resilience 2018.

[7] Nagao T, Lohani TN, Fukushima Y, Ito Y, Hokugo A, Oshige J. A study on the correlation between ground vibration characteristic and damage level of structures at Mashiki town by the 2016 Kumamoto earthquake. Journal of Japan Society of Civil Engineers, Ser A1 (Structural Engineering & Earthquake Engineering (SE/EE)) 2017;73:I_294-I_309. https://doi.org/10.2208/jscejseee.73.I_294.

[8] Sun J, Nagashima F, Kawase H, Matsushima S. Site effects analysis of shallow subsurface structures at Mashiki town, Kumamoto, based on microtremor horizontal-to-vertical spectral ratios. Bulletin of the Seismological Society of America 2020. https://doi.org/10.1785/0120190318.

[9] Japan Meteorological Agency. Report on the 2016 Kumamoto Earthquake. Japan Meteorological Agency; 2018.

[10] NIED. NIED F-net. NIED Earthquake Mechanism Search 2020. http://www.fnet.bosai.go.jp/event/search.php?LANG=en (accessed March 5, 2020).

[11] Headquarters for Earthquake Research Promotion. Information about the 2016 Kumamoto earthquake. the Headquarters for Earthquake Research Promotion 2016. https://www.jishin.go.jp/main/oshirase/2016kumamoto.html.

[12] Geospatial Information Authority of Japan. Geospatial Information Authority of Japan. Geospatial Information Authority of Japan 2020. https://www.gsi.go.jp/ENGLISH/.

[13] NILIM, BRI. Quick report of the field survey and the building damage by the 2016 Kumamoto earthquake. National Institute for Land and Infrastructure Management; 2016.

[14] Moya L, Mas E, Koshimura S, Yamazaki F. Synthetic building damage scenarios using empirical fragility functions: A case study of the 2016 Kumamoto earthquake. International Journal of Disaster Risk Reduction 2018;31:76–84. https://doi.org/10.1016/j.ijdrr.2018.04.016.

[15] Kawase H. The cause of the damage belt in kobe: "the Basin-Edge effect," constructive interference of the direct s-wave with the basin-induced diffracted/rayleigh waves. Seismological Research Letters 1996;67:25–34. https://doi.org/10.1785/gssrl.67.5.25.

[16] Montalva GA, Chávez-Garcia FJ, Tassara A, Jara Weisser DM. Site Effects and Building Damage Characterization in Concepción after the Mw 8.8 Maule Earthquake. Earthquake Spectra 2016;32:1469–88. https://doi.org/10.1193/101514EQS158M.

[17] Kawase H, Matsushima S, Nagashima F, Baoyintu, Nakano K. The cause of heavy damage concentration in downtown Mashiki inferred from observed data and field survey of the 2016 Kumamoto earthquake 2016 Kumamoto earthquake sequence and its impact on earthquake. Earth, Planets and Space 2017. https://doi.org/10.1186/s40623-016-0591-1.

[18] Arai H. Influence of ground characteristics in the center of Mashiki-cho on strong ground motion in the 2016 Kumamoto earthquake. BRI-H29 lecture; 2017.

[19] Nakazawa T, Sakata K, Sato Y, Hoshizumi H, Urabe A, Yoshimi M. Stratigraphy and distribution patttern of volcanogenic sediments beneath downtown Mashiki, Kumamoto, SW Japan, seriously damaged by the 2016 Kumamoto Earthquake. Jour Geol Soc Japan 2018;124:347–59. https://doi.org/10.5575/geosoc.2017.0077.

[20] Ministry of Land, Infrastructure, Transport and Tourism. Report on safety measures for the reconstruction of Mashiki Town for the 2016 Kumamoto Earthquake (final report). Ministry of Land, Infrastructure, Transport and Tourism; 2017.

[21] WAKAMATSU K, SENNA S, OZAWA K. Liquefaction and its Characteristics during the 2016 Kumamoto Earthquake. Journal of Japan Association for Earthquake Engineering 2017;17:4_81-4_100. https://doi.org/10.5610/jaee.17.4_81.

[22] Yoshida K, Hisada Y, Kawase H. Construction of damage prediction model for wooden buildings considering construction age, Hokkaido: 2004.

[23] Yoshida K, Hisada Y, Kawase H, Fushimi M. Study of damage rate function and destructive force index of wooden buildings based on seismic response analysis, Kinki: Abstracts of the 2005 Architectural Institute of Japan Conference; 2005, p. 161–2.

[24] Nagato K, Kawase H. Damage evaluation models of reinforced concrete buildings based on the damage statistics and simulated strong motions during the 1995 Hyogo-ken Nanbu earthquake.

Earthquake Engineering & Structural Dynamics 2004;33:755–74. https://doi.org/10.1002/eqe.376.

[25] Nagato K, Kawase H. A SET OF DYNAMIC MODELS OF STEEL BUILDINGS FOR DAMAGE EVALUATION. Journal of Structural and Construction Engineering (Transactions of AIJ) 2002;67:101–6. https://doi.org/10.3130/aijs.67.101_7.

[26] Kawase H, Sanchez-Sesma FJ, Matsushima S. The optimal use of horizontal-to-vertical spectral ratios of earthquake motions for velocity inversions based on diffuse-field theory for plane waves. Bulletin of the Seismological Society of America 2011;101:2001–14. https://doi.org/10.1785/0120100263.

[27] Bard P-Y, Bouchon M. The two-dimensional resonance of sediment-filled valleys. Bulletin of the Seismological Society of America 1985;75:519–41.

[28] Satoh T, Kawase H, Iwata T, Higashi S, Sato T, Irikura K, et al. S-Wave Velocity Structure of the Taichung Basin, Taiwan, Estimated from Array and Single-Station Records of Microtremors. Bulletin of the Seismological Society of America 2001;91:1267–82. https://doi.org/10.1785/0120000706.

[29] Pilz M, Parolai S, Picozzi M, Wang R, Leyton F, Campos J, et al. Shear wave velocity model of the Santiago de Chile basin derived from ambient noise measurements: a comparison of proxies for seismic site conditions and amplification: Velocity model of the Santiago de Chile basin. Geophysical Journal International 2010:no-no. https://doi.org/10.1111/j.1365-246X.2010.04613.x.

[30] Kawase H, Matsushima S, Satoh T, Sánchez-Sesma FJ. Applicability of Theoretical Horizontal-to-Vertical Ratio of Microtremors Based on the Diffuse Field Concept to Previously Observed Data. Bulletin of the Seismological Society of America 2015;105:3092–103. https://doi.org/10.1785/0120150134.

[31] NIED. KMMH16-J.pdf. 2019.

[32] Pitarka A, Irikura K, Iwata T, Sekiguchi H. Three-Dimensional Simulation of the Near-Fault Ground Motion for the 1995 Hyogo-ken Nanbu (Kobe), Japan, Earthquake. Bulletin of the Seismological Society of America 1998;88:428–40.

[33] Pitarka A. 3D Elastic Finite-Difference Modeling of Seismic Motion Using Staggered Grids with Nonuniform Spacing. Bulletin of the Seismological Society of America 1999;89:54–68.

Chapter 2

Microtremor observation and microtremor horizontal-to-vertical spectral ratio analyses in Mashiki

2.1. Introduction
2.2. Microtremor observation in 2016 and 2018
2.3. Analyses of microtremor horizontal-to-vertical spectral ratio
2.4. Fundamental peak frequency of Mashiki
2.5. Conclusion
Reference (Chapter 2)

2.1. Introduction

The use of microtremors in site response analysis has been studied long ago in Japan, while it has been long been very controversial in other parts of the world, especially the “western world”. The microtremor study method is a low cost, convenient technique and attracted many new users [1]. Microtremors have been used basically in four different ways related with site conditions: absolute spectra, spectral ratios with respect to a reference site, H/V spectral ratio and velocity structure inversion through array recordings [1,2].

Single-station three-component microtrmor observations are highly mobile and inexpensive. The microtremor horizontal-to-vertical spectral ratio (MHVR) is obviously more stable than the power spectra [3]. Moreover, MHVR is useful to find the fundamental frequency of a local site and useful for site characterization and microzonation [1,4,5]. Recently, a few studies have found that the MHVR corresponded to the square root of the ratio of the sum of the imaginary parts of horizontal displacements for horizontal unit harmonic loads and the imaginary parts of the vertical displacement for a vertical unit harmonic load, based on the diffuse field concept (DFC) [6,7]. The DFC theory has been validated by many previous studies [8–11]. According to these results, the root mean square (RMS) value of the east–west (EW) and north–south (NS) components of MHVRs were obtained for Mashiki after checking the directional dependence.

2.2. Microtremor observation in 2016 and 2018

Twice microtremor observations were performed in Mashiki. During the first observation, 61 microtremors were recorded from April 29th to May 1st, 2016 [12,13], which was two weeks after the mainshock. Then, 35 more microtremors in Mashiki were obtained in 2018. For the measurement in 2016, ten sets of microtremor observation systems were prepared. The SMAR-6A3P model instrument from the Mitsutoyo Corporation (previously Akashi Corporation) were used, along with a data logger LS-8800 from the Hakusan Corporation. This model is capable of detecting acceleration in the frequency range of 0.1–80 Hz [14]. In the observation plan, ten measurement lines (Line 01−Line 10) were planned from north to south. Each line was offset by approximately 100−150m and had six or seven observation sites. The observation at each site, which lasted a little longer than 15 min, recorded with a sampling frequency of 100 Hz and a 500-times analog amplifier. Several roads were rendered inaccessible by the damaged houses or retaining walls, causing us to cancel out plans to visit some sites. That is why some of the observation lines appear a little winded, especially in the southern part, where most collapsed buildings were located. Fig. 2.1 illustrates the locations of the 2016 microtremor observation sites marked by rectangles. The 2016 observation sites are marked as “MSn-m”, where “MS” means that the observation sites are in Mashiki Town, “n” is the number of observation line from 1 to 10, and “m” indicates the observation order along each line from 1 to 7.

As seen in Fig. 2.1, the observation grids between Line 03 and Line 04 are separated by a wide area. Additionally, the grid density in the southwestern part was not enough, especially in the area abutting the Akitsu River. Therefore, microtremors in those areas were measured again, after the locals had removed the damaged houses and retaining walls, to remedy the sparsely populated areas on the map of the observation sites. Moreover, the measurements were taken again at the sites with noisy microtremors that were probably caused by debris removal activities during the first observation. From June 3rd to June 4th, 2018, microtremor records for 15 to 20 min at 35 sites were obtained in Mashiki [15]. Fig. 2.1 also illustrates the locations of the 2018 microtremor observation sites are marked as triangles. The 2018 observation sites were named as "MSAii," in which "MSA" indicates the added microtremor observation sites in Mashiki and "ii" is the number of observation sequences in the observation.

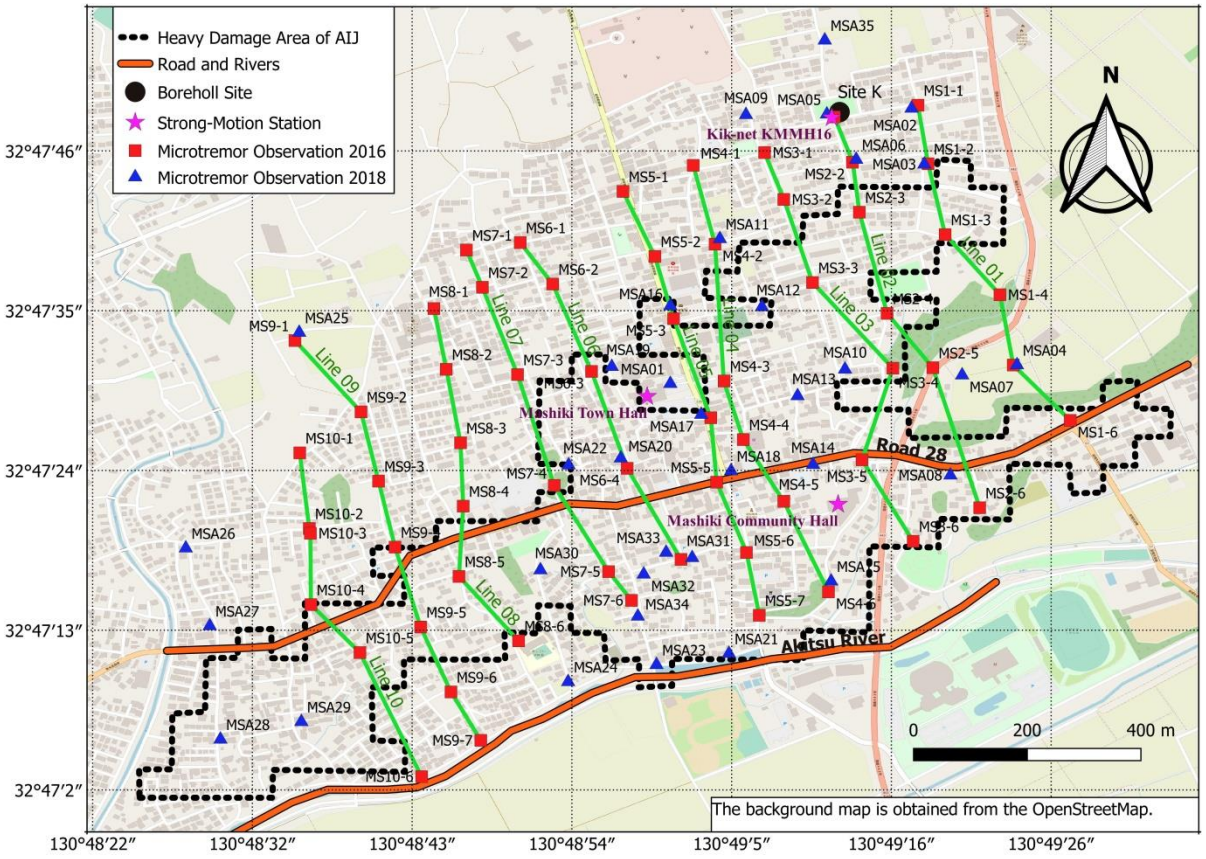

Fig. 2.1. 2016 and 2018 microtremor observation sites. The rectangles represent the site locations of the 2016 microtremor observations at 61 sites. The triangles represent the site locations of the 2018 microtremor observations at 35 sites. The large stars are the locations of the three strong-motion stations, which were managed by the NIED and Kumamoto Prefecture. The solid lines are the ten observation routes during the 2016 microtremor observation.

2.3. Analyses of microtremor horizontal-to-vertical spectral ratio

Once obtaining these microtremors for Mashiki, analysis of microtremors were carried out according to the following steps:

1) Divide the microtremor signals into 40.96s segments with 50% overlap,

2) Obtain the Fourier spectrum by the fast Fourier transform method (FFT) with a 0.1 Hz wide Parzen window smoothing,

3) Discard the spectra of noisy sections whose characteristics are visibly different from the microtremor spectra of the quiet sections,

4) Calculate the spectral ratio of the horizontal component with respect to the vertical one. Both the independent ratios of EW/UD (UD denotes up-down) and NS/UD and their RMS values are obtained by Eq. (2-1),

5) Calculate the average values of the MHVRs.

$$MHVRs(RMS) = \sqrt{\frac{[MHVRs(\frac{NS}{UD})]^2+[MHVRs(\frac{EW}{UD})]^2}{2}}. \quad (2\text{-}1)$$

The fundamental peak frequency of the MHVR is the frequency that corresponds to the lowermost peak frequency with the highest MHVR amplitude that first appears on the spectrum. As mentioned earlier by several researchers, the fundamental frequency of the horizontal site amplification factor equals that of the MHVR [1,16,17]. In this research, for the sites observed in 2016, 48 MHVRs out of 61 observed sites can be used with a relatively clear fundamental peak. Because the microtremor data at several sites would be contaminated by heavy traffic noise or noise from the debris removal activities, the fundamental peaks of their MHVRs in an ordinary frequency range (namely, between 0.3 Hz and 10.0 Hz) were not evident. Out of the MHVRs of the 2018 observation sites, 35 MHVRs were used for the present analysis. Fig. 2.2 shows eight MHVRs for Mashiki as representative values. For some MHVRs, the highest peaks seem to have appeared at a frequency less than 0.1 Hz, which can be attributed to the noise from the observation equipment. Therefore, the peaks appearing at frequencies lower than 0.5 Hz were not considered as fundamental peak frequencies.

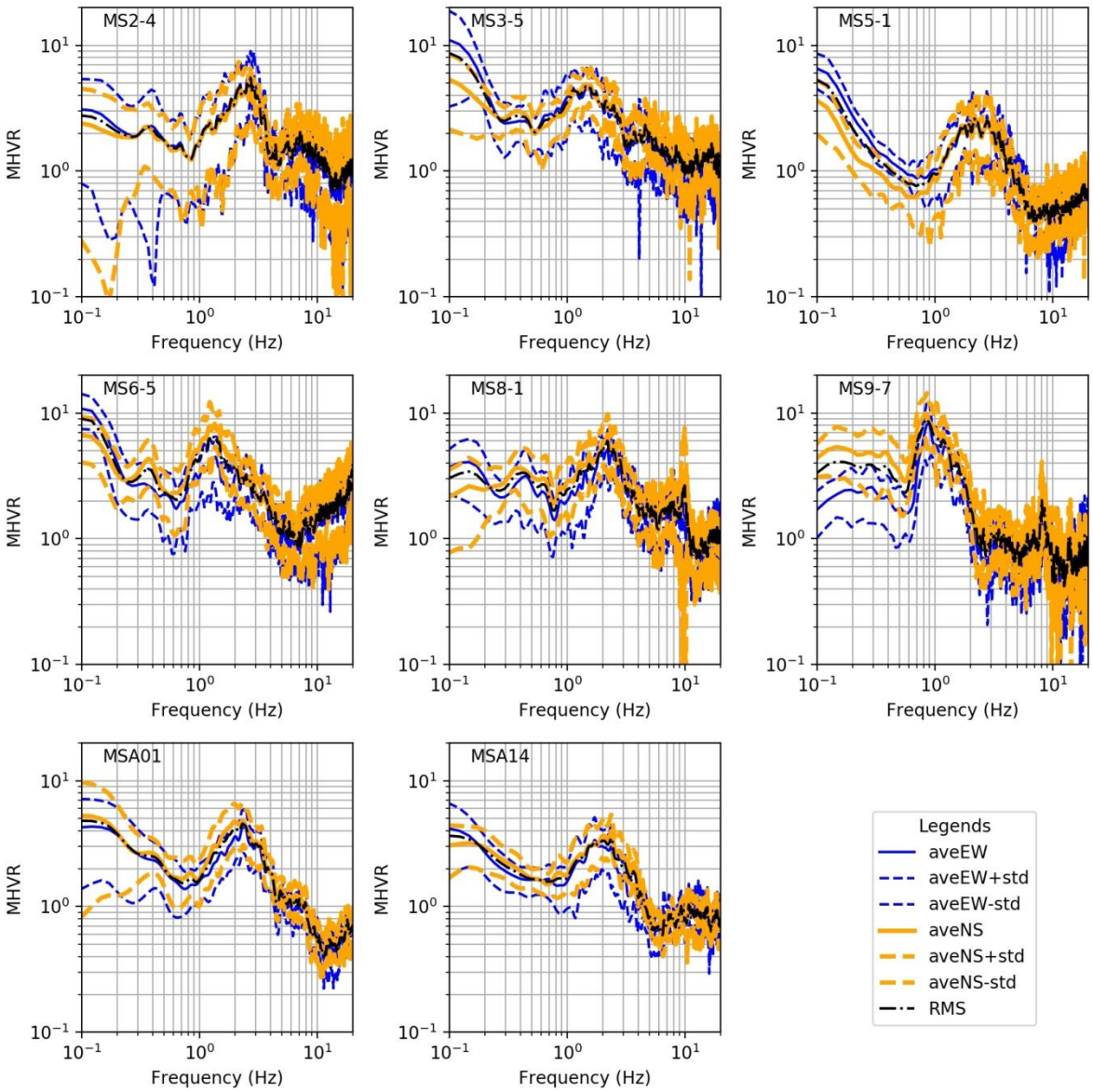

Fig. 2.2. MHVRs of eight microtremor observation sites. Six sites were observed in 2016, and two sites were observed in 2018. The thin solid line in each panel represents the MHVR of the EW component. The thin dashed lines represent the average plus/minus standard deviation of the EW component. The heavy solid and heavy dashed lines in each panel denote those of the NS component. The dash-dotted lines represent the RMS values of the averaged EW and NS components.

2.4. Fundamental peak frequency of Mashiki

The fundamental peak frequencies of the efficient microtremor observation sites were obtained from the peak frequency of the MHVR. Thus, 83 meaningful fundamental peak frequencies

of the measured sites were derived in Mashiki. Fig. 2.3 shows a distribution map of the fundamental peak frequencies of the microtremor observation sites in Mashiki. In this research area, the frequencies in the northeastern part are higher than other parts, while those in the southwestern part are lower than others. Several sites at the southeastern boundary of the observation area have frequencies higher than 3.0 Hz. This suggests that at the same depth, the shallow subsurface layer in the southwestern part may be softer than that in the northeastern part, or the soft subsurface layers in the southwestern part may be thicker than those in the northeastern part. The fundamental peak frequency distribution has a relationship with the topography of Mashiki. The northeastern part is situated at a higher elevation than the southwestern part. The highest peak frequency of 4.93 Hz is found on a hill in the southeastern side, while the lowest peak frequency of a little less than 1.0 Hz is obtained at the southwestern side close to the Akitsu River.

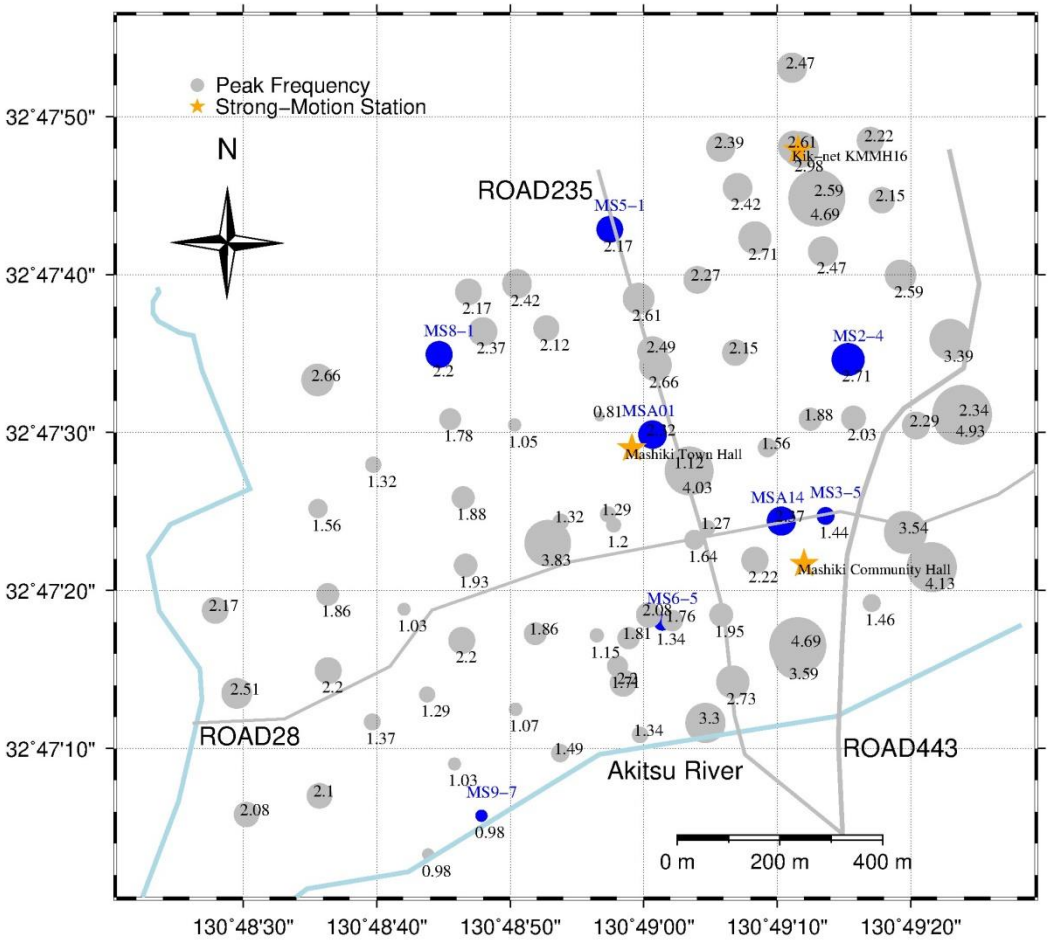

Fig. 2.3. Fundamental frequency distribution map of microtremor observation sites. A larger gray circle indicates that the fundamental frequency of this site is higher. Specifically labeled circles are the microtremor sites showed in Figure 4, while star symbols represent the strong motion stations.

2.5. Conclusion

61 and 35 microtremors were observed in Mashiki in 2016 and 2018, respectively. Analysis procedures of MHVRs were detailed explained in this Chapter. The predominant frequencies of most microtremor sites were really obvious on the MHVR curves. Fundamental frequency of each microtremor site was determined and its distribution map was generated. The fundamental frequencies were higher in northeast while they were lower in southwest of Mashiki, especially they were less than 1 Hz in the near river areas. Moreover, the highest fundamental frequency equals to 4.93 Hz was found in the southeast, where is at the top of a hill. The other two 4.69 high frequency sites were found in the northeast and southeast. Fundamental frequencies of different areas were quite different, which implied that the shallow subsurface velocity structures of different areas were not similar in Mashiki.

Reference (Chapter 2)

[1] Bard P-Y. Microtremor measurements: A tool for site effect estimation? vol. 3. 1999.

[2] Lermo J, Chávez-García FJ. Are microtremors useful in site response evaluation? Bulletin of the Seismological Society of America 1994;84:1350–64.

[3] Uebayashi H, Kawabe H, Kamae K. Reproduction of microseism H/V spectral features using a three-dimensional complex topographical model of the sediment-bedrock interface in the Osaka sedimentary basin. Geophysical Journal International 2012;189:1060–74. https://doi.org/10.1111/j.1365-246X.2012.05408.x.

[4] Matsushima S, Hirokawa T, De Martin F, Kawase H, Sanchez-Sesma FJ. The Effect of Lateral Heterogeneity on Horizontal-to-Vertical Spectral Ratio of Microtremors Inferred from Observation and Synthetics. Bulletin of the Seismological Society of America 2014;104:381–393. https://doi.org/10.1785/0120120321.

[5] Nakamura Y. A method for dynamic characteristic estimation of subsurface using microtremor on the ground surface. Japan: 1989.

[6] Weaver RL, Sánchez-Sesma FJ, Rodríguez-Castellanos A, Perton M, Campillo M. Two perspectives on equipartition in diffuse elastic fields in three dimensions. The Journal of the Acoustical Society of America 2009;126:1125–30. https://doi.org/10.1121/1.3177262.

[7] Sánchez-Sesma FJ, Rodríguez M, Iturrarán-Viveros U, Luzón F, Campillo M, Margerin L, et al. A theory for microtremor H/V spectral ratio: Application for a layered medium. Geophysical Journal International 2011;186:221–5. https://doi.org/10.1111/j.1365-246X.2011.05064.x.

[8] García-Jerez A, Luzón F, Sánchez-Sesma FJ, Lunedei E, Albarello D, Santoyo MA, et al. Diffuse elastic wavefield within a simple crustal model. Some consequences for low and high frequencies: DIFFUSE FIELD IN A SIMPLE CRUSTAL MODEL. Journal of Geophysical Research: Solid Earth 2013;118:5577–95. https://doi.org/10.1002/2013JB010107.

[9] Kawase H, Matsushima S, Satoh T, Sánchez-Sesma FJ. Applicability of theoretical horizontal-to-vertical ratio of microtremors based on the diffuse field concept to previously observed data. Bulletin of the Seismological Society of America 2015;105:3092–103. https://doi.org/10.1785/0120150134.

[10] Lontsi AM, Sánchez-Sesma FJ, Molina-Villegas JC, Ohrnberger M, Krüger F. Full microtremor H/V(z, f) inversion for shallow subsurface characterization. Geophysical Journal International 2015;202:298–312. https://doi.org/10.1093/gji/ggv132.

[11] Lunedei E, Malischewsky P. A Review and Some New Issues on the Theory of the H/V Technique for Ambient Vibrations. In: Ansal A, editor. Perspectives on European Earthquake Engineering and Seismology: Volume 2, Cham: Springer International Publishing; 2015, p. 371–394. https://doi.org/10.1007/978-3-319-16964-4_15.

[12] Kawase H, Matsushima S, Nagashima F, Baoyintu, Nakano K. The cause of heavy damage concentration in downtown Mashiki inferred from observed data and field survey of the 2016 Kumamoto earthquake. Earth, Planets and Space 2017;69:3. https://doi.org/10.1186/s40623-016-0591-1.

[13] Sun J, Kawase H, Nagashima F. Estimation of The Strong Motions at Mashiki Town, Kumamoto, During The 2016 Kumamoto Earthquake, Based on Microtremor Horizontal-to-Vertical Spectral Ratios. Disaster Prevention Research Institude Annuals 2018;61:238–246.

[14] Kudo K, Takahashi M, Sakaue M, Kanno T, Kakuma H, Tsuboi D. A highly over-damped moving coil type accelerometer for mobile strong motion observation and its performance tests. 1998.

[15] Sun J, Nagashima F, Kawase H, Matsushima S. Site effects analysis of shallow subsurface structures at Mashiki town, Kumamoto, based on microtremor horizontal-to-vertical spectral ratios. Bulletin of the Seismological Society of America 2020. https://doi.org/10.1785/0120190318.

[16] Konno K, Ohmachi T. Ground-Motion Characteristics Estimated from Spectral Ratio between Horizontal and Vertical Components of Microtremor. Bulletin of the Seismological Society of America 1998;88:228–241.

[17] Satoh T, Kawase H, Iwata T, Higashi S, Sato T, Irikura K, et al. S-Wave Velocity Structure of the Taichung Basin, Taiwan, Estimated from Array and Single-Station Records of Microtremors. Bulletin of the Seismological Society of America 2001;91:1267–1282. https://doi.org/10.1785/0120000706.

Chapter 3

Pseudo earthquake horizontal-to-vertical spectral ratio analyses in Mashiki

3.1. Introduction

3.2. Earthquake horizontal-to-vertical spectral ratios at Mashiki

3.3. Discussion and conclusion

Reference (Chapter 3)

3.1. Introduction

A couple of researchers successfully used the Diffuse Field Concept (DFC) for MHVR proposed by Sánchez-Sesma et al. [1] to explain the observed MHVRs [2,3]. Then, Garcia-Jerez et al. [4] presented a new calculation scheme that uses the residue integrals to increase the efficiency of Green's functions computation. Although the method developed by these researchers [4] is better than the ordinary wave number integration scheme of the MHVR, its inversion process is still time consuming, because of the unavoidable summation that is required to account for the multiple contributions of poles in the wavenumber domain. Kawase et al. [5] demonstrated that the inversion required for EHVR is much more efficient than that for the MHVR, because one needs to consider the body wave contributions in one wavenumber only. Moreover, the inverted S-wave velocity structure from the EHVR can be readily applied to obtain the S-wave amplification factor for the site from the seismological bedrock to the ground surface. For these reasons, I prefer EHVR over MHVR for the velocity structure inversion in this study.

However, MHVR is easier to obtain in most cases. Since the occurrence of seismic events would not be controlled by humans, the recordings of the seismic-wave signals would not be arbitrarily obtained at any moment and so plentiful continuous earthquake observations were required to derive the average EHVR at one site. Besides, using the earthquake observation to cover an area with a grid length of 100–300 m would be much more expensive than using the microtremor observation. Earthquake signal observations with a grid length of 100–300 m require simultaneous records at multiple sites, while single−site microtremor observation does not. Studies have shown that the MHVR and EHVR at one site are similar until the fundamental peak frequency has been reached, and thereafter in the range higher than the peak frequency of MHVR they diverge significantly. Considering these facts, Kawase et al. [5] proposed the EMR method to connect the MHVR with the EHVR of one site. Each EMR is simply the ratio between the EHVR and the MHVR as shown in Eq. 3.1. The EHVR and MHVR for the equation are calculated based on the observational data of one site. They calculated the EHVR and MHVR at 100 strong motion stations in Japan and obtained 100 EMRs. Then, they classified the 100 EMRs into five categories, based on the fundamental peak frequency of the MHVR, and calculated the average EMR of every category. Finally, they obtained five averaged EMRs, which will be referred as the Japan average EMR database. By referencing to this database, the pseudo-EHVRs of the microtremor observation sites could be calculated by Eq. 3.2. The resulting EHVRs were named as pseudo-EHVRs (pEHVR) to distinguish them from the observed EHVRs.

$$EMR = EHVR / MHVR \tag{3.1}$$

$$pEHVR = MHVR \times EMR \tag{3.2}$$

Explained below is the method to use the Japanese average EMR database to calculate the pEHVR by Eq. (3.2). For example, the EMR represented by the heavy solid curve in Fig. 3.1 will be applied when the fundamental peak frequency of the MHVR is between 0.2 and 1.0 Hz. Then, the interpolation of the EMR at each frequency corresponding to the MHVR frequency range was calculated. After that, equation (3) would be used to obtain the pEHVR of the site. Similarly, the EMRs of 1.0–2.0 Hz, 2.0–5.0 Hz, 5.0–10.0 Hz, and 10.0–20.0 Hz were applied when the peak frequency of the MHVR is included in these frequency ranges, respectively. With the EMR method, the pEHVR of each microtremor observation site would be obtained.

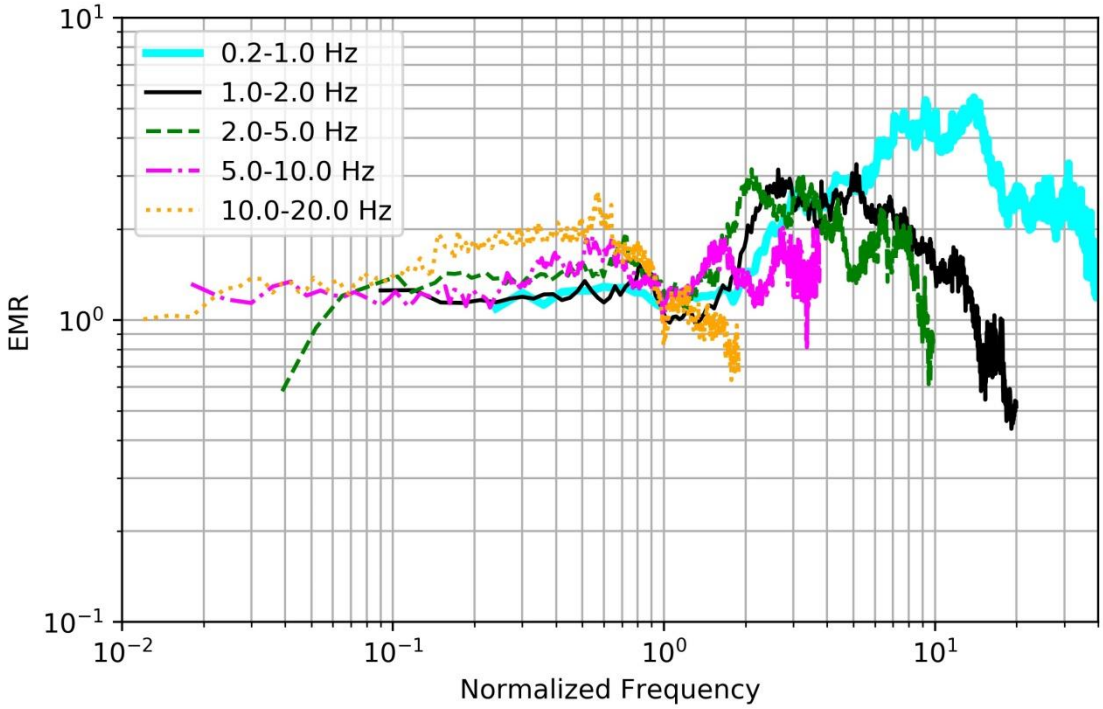

Fig. 3.1. Five categories of EMRs [5]**. The heavy solid line represents the EMR whose peak frequency is between 0.2 and 1.0 Hz. The thin solid line denotes the EMR whose peak frequency is between 1.0 and 2.0 Hz. Similarly, the dashed line, dash-dotted line, and dotted line represent the EMRs whose peak frequencies are in the ranges of 2.0–5.0 Hz, 5.0–10.0 Hz and 10.0–20.0 Hz, respectively.**

3.2. Earthquake horizontal-to-vertical spectral ratios at Mashiki

As mentioned in Chapter 1, there are three strong-motion stations in Mashiki, the KMMH16 site by NIED, the KMMP58 site by Kumamoto Prefecture, and the Bunkakaikan (Mashiki

Community Hall) by the JMA after the mainshock. To calculate the EHVRs of these sites, the earthquake ground motions at the KMMH16 sites recorded three months after the mainshock event (i.e., only the records after July 16, 2016 until December 5, 2016) were obtained. However, 5 and 25 earthquake recordings at KMMP58 and Bunkakaikan were recorded after July 16, 2016, which are not sufficient for the stable analysis. Thus, using all the earthquake recordings recorded at these two sites was a suitable method (except for the foreshock and the mainshock at KMMP58). Earthquake waves whose PGA was between 1 and 50 cm/s^2 were selected, because the S-wave may not be discernible for a record with PGA less than 1.0 cm/s^2 and the underground structure may exhibit nonlinear behavior for a record with PGA exceeding 50.0 cm/s^2 [6]. Finally, 88, 70, and 167 strong ground motions were collected at KMMH16, KMMP58, and Bunkakaikan, respectively. Listed below are the steps taken to analyze the three EHVRs:

Select the eligible small earthquake ground motions with three components (EW, NS, and UD) by the method detailed above.

Calculate the Fourier spectra of the EW, NS, and UD components using the FFT algorithm.

Calculate the spectral ratios of EW/UD and NS/UD, followed by the RMS of the two components.

Upon obtaining the RMS–EHVR of each strong ground motion, calculate the average EHVR. This is the EHVR of one site.

With this method, the average EHVRs of three strong-motion stations were obtained. the EHVRs at the three stations were compared with the pEHVRs and MHVRs, which are located in the vicinity of the strong-motion stations (Fig. 3.1). In Fig. 3.1−(g), the left columns are the residual between the EHVR and the nearby pEHVR, whereas the right columns are the residual between the EHVR and nearby MHVR. The residual in the frequency range of 0.5–10.0 Hz (f_{max} and f_{min} in Eq. (3.3)) were calculated. The points to calculate the difference were interpolated in the logarithmic scale on the frequency axis.

$$Residual = \sum_{f_{min}}^{f_{max}} (Nearby\_HVR(f) - EHVR(f))^2 \qquad (3.3)$$

where, Nearby_HVR(f) is either the MHVR or pEHVR of a microtremor site around a strong-motion station, and EHVR(f) denotes the EHVR of that station.

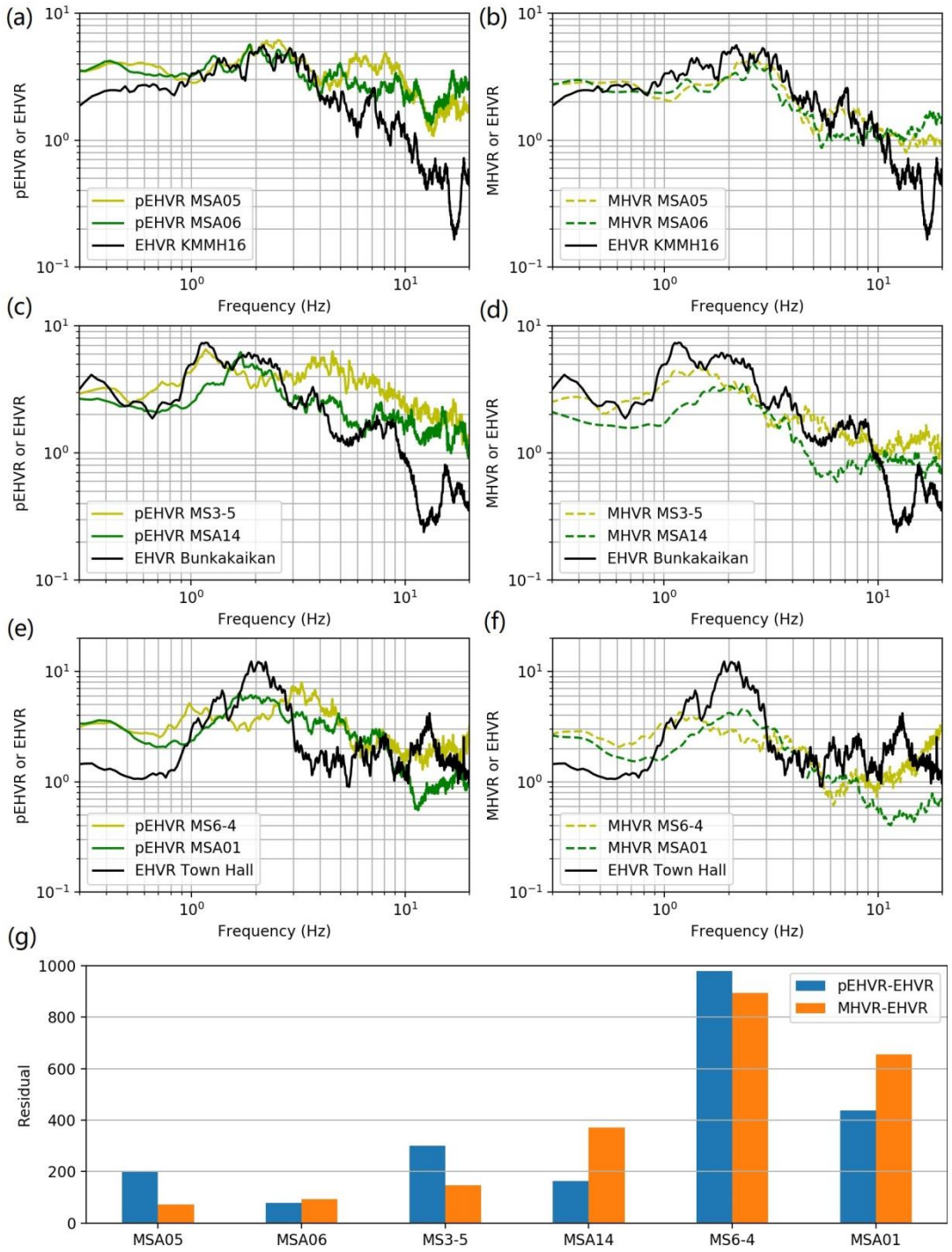

Fig. 3.2. Comparisons of EHVR with MHVRs and pEHVRs. (a) Comparison of EHVR of KMMH16 and pEHVRs of surrounding microtremor observation sites, (b) comparison of EHVR of KMMH16 and MHVRs of its surrounding microtremor observation sites. (c) and (d) EHVR of *Bunkakaikan* in comparison with pEHVRs and MHVRs of its surrounding microtremor observation sites, respectively. (e) and (f) EHVR of KMMP58 in comparison with pEHVRs and MHVRs of its surrounding microtremor observation sites, respectively. (g) Residual between MHVR or pEHVR and nearby EHVR.

3.3. Discussion and conclusion

The EMR method and EHVR analysis method were explained in this Chapter. Five kinds of EMRs and the applying method were detailed showed. Moreover, pEHVRs of sites with sufficient MHVRs in Mashiki were obtained. According to the comparison of the residuals at the KMMH16 and *Bunkakaikan*, they revealed that the MHVR residual was smaller at one nearby site, while the pEHVR is smaller at the other nearby site. At the KMMP58, the pEHVR residual at MSA01 was the smallest among the four comparisons. It was admitted that these comparisons are not decisively supporting the use of pEHVRs at these three sites. This comes primarily from the fact that the necessary EMR at these sites may be smaller than the EMR used for the correction here, which is the empirical one averaged over 15 to 20 sites in Japan in each category [5,7]. We may need further studies for a better EMR specific for Mashiki. By considering the physical difference between the MHVR and EHVR as suggested by the DFC, we used the pEHVR to identify the subsurface velocity structure. Since the EMR correction makes the amplitude of the pEHVR equal to or higher than that of the EHVR in the most important frequency range from 1 to 10 Hz, the estimated S-wave amplification derived from the pEHVR is expected to be equal to or higher than the actual amplification in this frequency range.

Reference (Chapter 3)

[1] Sanchez-Sesma FJ, Weaver RL, Kawase H, Matsushima S, Luzon F, Campillo M. Energy Partitions among Elastic Waves for Dynamic Surface Loads in a Semi-Infinite Solid. Bulletin of the Seismological Society of America 2011;101:1704–1709. https://doi.org/10.1785/0120100196.

[2] Salinas V, Luzon F, Garcia-Jerez A, Sanchez-Sesma FJ, Kawase H, Matsushima S, et al. Using Diffuse Field Theory to Interpret the H/V Spectral Ratio from Earthquake Records in Cibeles Seismic Station, Mexico City. Bulletin of the Seismological Society of America 2014;104:995–1001. https://doi.org/10.1785/0120130202.

[3] Kawase H, Matsushima S, Satoh T, Sánchez-Sesma FJ. Applicability of theoretical horizontal-to-vertical ratio of microtremors based on the diffuse field concept to previously observed data. Bulletin of the Seismological Society of America 2015;105:3092–103. https://doi.org/10.1785/0120150134.

[4] García-Jerez A, Piña-Flores J, Sánchez-Sesma FJ, Luzón F, Perton M. A computer code for forward calculation and inversion of the H/V spectral ratio under the diffuse field assumption. Computers & Geosciences 2016;97:67–78. https://doi.org/10.1016/j.cageo.2016.06.016.

[5] Kawase H, Mori Y, Nagashima F. Difference of horizontal-to-vertical spectral ratios of observed earthquakes and microtremors and its application to S-wave velocity inversion based on the diffuse field concept. Earth, Planets and Space 2018;70:1. https://doi.org/10.1186/s40623-017-0766-4.

[6] Kawase H, Sanchez-Sesma FJ, Matsushima S. The optimal use of horizontal-to-vertical spectral ratios of earthquake motions for velocity inversions based on diffuse-field theory for plane waves. Bulletin of the Seismological Society of America 2011;101:2001–2014. https://doi.org/10.1785/0120100263.

[7] Kawase H, Nagashima F, Nakano K, Mori Y. Direct evaluation of S-wave amplification factors from microtremor H/V ratios: Double empirical corrections to “Nakamura” method. Soil Dynamics and Earthquake Engineering 2018. https://doi.org/10.1016/j.soildyn.2018.01.049.

Chapter 4

Identification of subsurface velocity structures in Mashiki

4.1. Introduction

4.2. Inversion of EHVRs and pEHVRs

4.3. Distributions of engineering bedrock depth and V_s30

4.4. Conclusion

Reference (Chapter 4)

Appendix 4.1

4.1. Introduction

Kawase et al. [1] proposed the DFC for earthquakes by assuming plane body waves, from which they derived the theoretical formula for the EHVR as follows.

$$\frac{H(0,\omega)}{V(0,\omega)} = \sqrt{\frac{\alpha_H}{\beta_H}} \frac{|TF_{Horizontal}(0,\omega)|}{|TF_{Vertical}(0,\omega)|} \tag{4.1}$$

Here, *H(0, ω)* and *V(0, ω)* are the horizontal and vertical Fourier spectra at the ground surface; α_H and β_H denote the P- and S-wave velocities of the half-space, i.e., the seismological bedrock; $|TF_{Horizontal}(0,\omega)|$ and $|TF_{Vertical}(0,\omega)|$ are the absolute values of the transfer function for the horizontal and vertical motions, respectively. It should be emphasized that the absolute value of the transfer function is an amplification factor of the surface motion with respect to the motion of the seismological bedrock, and not the surface-to-borehole spectral ratio. Another important point to note is that we must consider the entire velocity structure down to the seismological bedrock in the EHVR. As the factor $(\frac{\alpha_H}{\beta_H})$ suggests, EHVR depends on the equipartitioned energy ratios at the seismological bedrock and the transfer functions of the P- and S-waves from the seismic bedrock to the ground surface, as shown in Eq. (5.1). The EHVR is a function of not only the shallow sediments above the engineering bedrock, but also the deep basin structure, even in the high-frequency range. Therefore, once the S-wave velocity structure has been successfully inverted, an S-wave site amplification factor from the seismological bedrock can be obtained.

Nagashima et al. [2] proposed an EHVR inversion scheme. They studied the velocity structures at MYG004 (K-NET) and the surrounding areas by using a temporary deployment of the aftershock observation after the 2011 Tohoku earthquake. They used the hybrid heuristic search (HHS) method, which was originally proposed by Yamanaka (2007), to invert the S-wave velocity structures. The method does not need an initial model, but it would be better to have a reference model to constrain the range of important parameters to be identified.

4.2. Inversion of EHVRs and pEHVRs

Because the borehole information down to 252 m at KMMH16 (NIED, see Data and Resources) were collected, and the approximated S- and P-wave velocities (V_s and V_p) down to the seismic bedrock from the J-SHIS model for the shallow crustal structure (< 10 km) (J-SHIS Map, see Data and Resources) were also obtained. In the inversion of pEHVR and EHVR, the P-wave velocities were not the target. Instead, they were translated from the inverted S-waves based on the empirical formula of Ludwig et al. [4]. Here, it was assumed that the damping ratio equals to 1.1% for all the layers, which does not contribute much to modifying the EHVR amplitude. Misfit between the

target EHVR (observed EHVR or pEHVR) and the theoretical EHVR was calculated by Eq. (4.2). This is the scale of inversion to select the best-fit velocity model at one site.

$$Misfit = \sum_{f_{min}}^{f_{max}} [\log(HVR_{OBS}(f)) - \log(HVR_{THE}(f))]^2 \quad (4.2)$$

where, HVR_{OBS} represents the target pEHVR or EHVR, HVR_{THE} denotes the theoretical EHVR calculated based on DFC for earthquakes. f_{min} and f_{max} are the minimum and maximum frequencies used in the EHVR inversion; they will be determined according to the frequency range of interest.

The HHS method is a combination of the genetic algorithm (GA) and the simulated annealing algorithm. The details of the method can be found in Nagashima et al. [2]. The relationship between the density of each layer $\rho_i$and its V_s follows Eq. (4.3) [5], in which the unit of density is g/cm^3, and that of V_s is km/s. Nagashima identified the subsurface velocity structure based on the EHVR of KMMH16, as shown in Table 4.1. This model was referred as the initial one when invert the subsurface velocity structures at other sites.

Upon the stable determination of the velocity structure, only the thickness could be changed for the velocity structure identification. The searching ranges of thickness of the 1st – 8th layers from 100 to 400% were adopted, and the thicknesses of the 9th – 15th were kept the same as in the reference model. Moreover, the V_s and V_p of all the layers were set to be the same as in the reference model. From Cases 1 to 4, the searching ranges of thickness of the 1st – 8th layers were individually set to ±100%, ±200%, ±300%, and ±400%. In Case 5, the searching range of thickness of the 1st – 4th layers was set to ±200%, and that of the 5th – 8th layers was set to ±100%. Similarly, from Cases 6 to 9, the searching ranges of thickness of the 1st – 4th and 5th – 8th layers were "±300% & ±100%," "±400% & ±100%," "±300% & ±200%," and "±400% & ±200%."

For the velocity model identification, the residual of the theoretical HVR (HVR_{THE}) and target HVR (HVR_{OBS}) was calculated using Eq. (4.2). After the EHVR or pEHVR inversion of 86 sites for these nine cases, the theoretical HVR was found to be close to the target HVR when the residual is less than 50, as shown in Fig. 4.1. The residual of a single site will become slightly smaller if the searching range of thickness are larger (Fig. 4.2), however, the deviation from site to site is much larger than the deviation from the different searching ranges. The residuals of more than 66% of the sites in Case 1 to 5 are less than 50 (Fig. 4.3). Therefore, those sites with residuals less than 50 were determined as the effective sites, for the next step. Among the nine cases, the case with the smallest searching range of thickness yielded the smallest angle of inclination of the subsurface layers among the microtremor observation sites, but with the largest differences between the theoretical and the target HVRs as a tradeoff.

Table 4.1

Reference model of subsurface velocity structure identifications in Mashiki town (Nagashima and Kawase, 2018)

Layer Number	Thickness (m)	Depth (m)	V_p (m/s)	V_s (m/s)	Density (g/cm^3)
1	3.00	3.00	296.56	154.87	1.66
2	12.00	15.00	760.00	249.36	1.73
3	5.29	20.29	1841.61	337.07	1.79
4	2.10	22.39	1918.07	483.09	1.87
5	15.80	38.19	1995.00	598.03	1.92
6	12.50	50.69	1995.09	733.19	1.97
7	25.30	75.99	2529.23	790.10	2.00
8	16.13	92.12	2558.47	827.70	2.01
9	44.92	137.04	2768.98	990.51	2.07
10	29.23	166.27	4078.39	1172.19	2.13
11	64.60	230.87	4796.23	1468.35	2.21
12	15.52	246.39	4813.21	1790.20	2.30
13	905.78	1152.17	5776.98	1871.20	2.32
14	3100.31	4252.48	5786.36	3264.74	2.61
15	0.00	4252.48	6000.00	3400.00	2.64

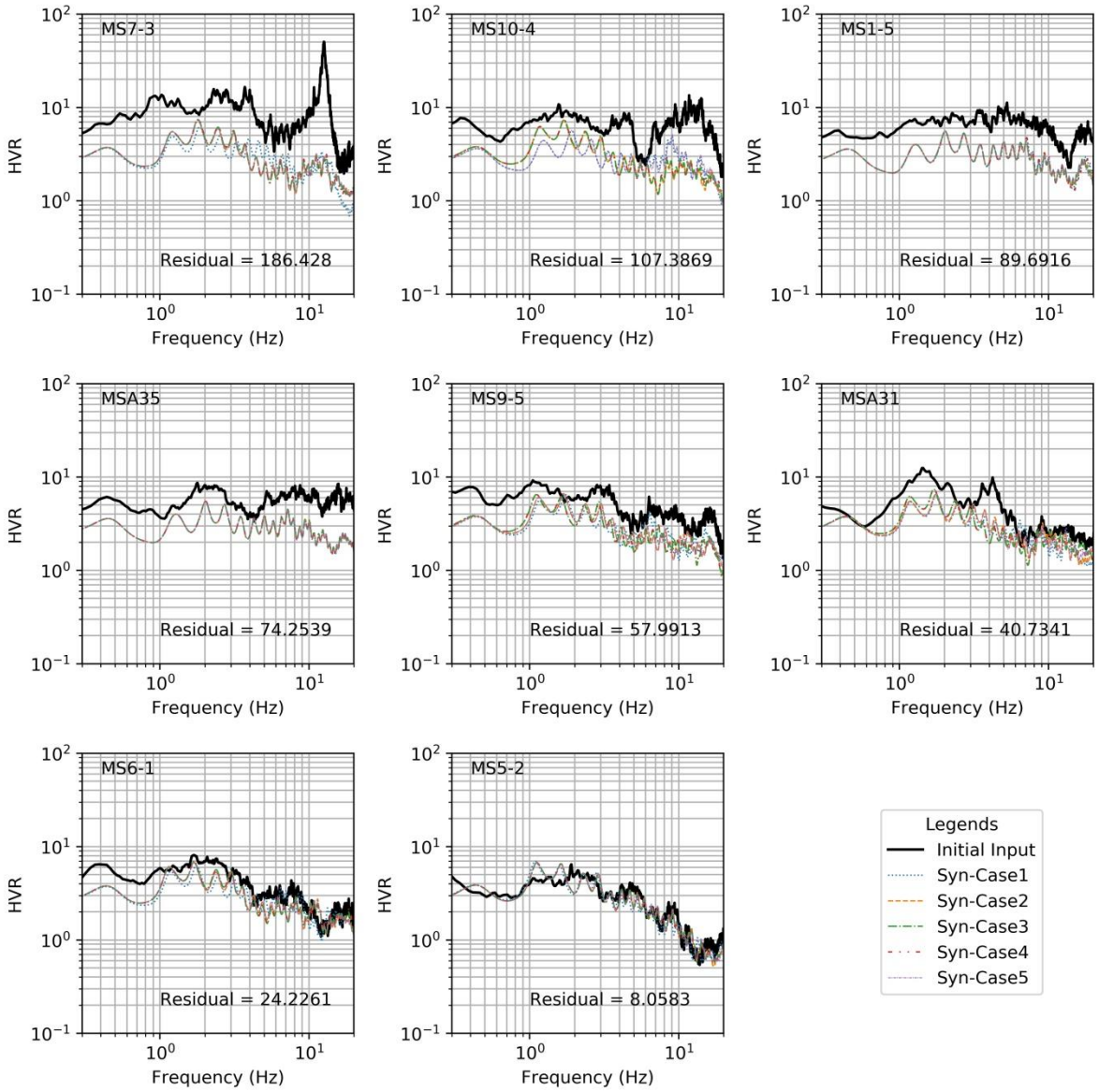

Fig. 4.1. Comparisons of theoretical and target HVRs of eight sites. The heavy solid lines denote the target pEHVRs. Other lines are the synthetic HVRs of Cases 1−5. Residuals shown in each panel are the analysis results from 0.3 to 20 Hz in Case 4.

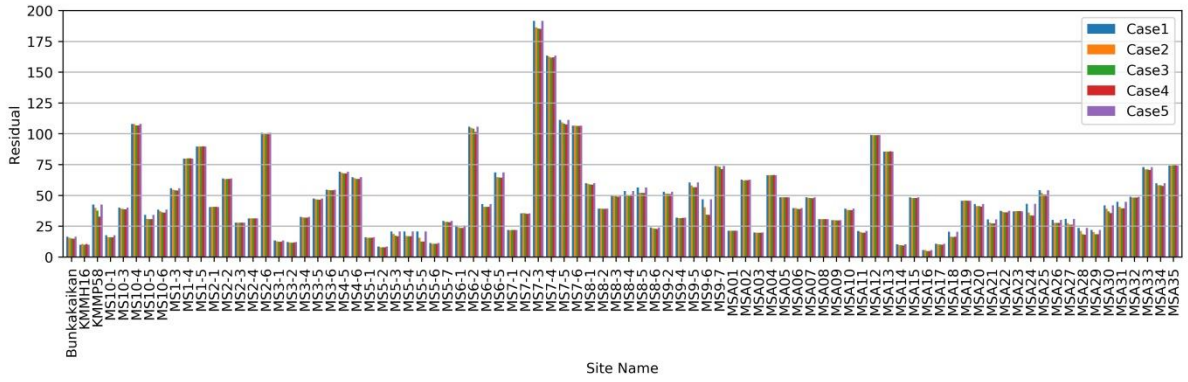

Fig. 4.2. Residuals between theoretical and target EHVRs of 86 sites in five cases (Cases1−5). The five bars for each site from left to right represent the analytical residuals in Cases 1−5.

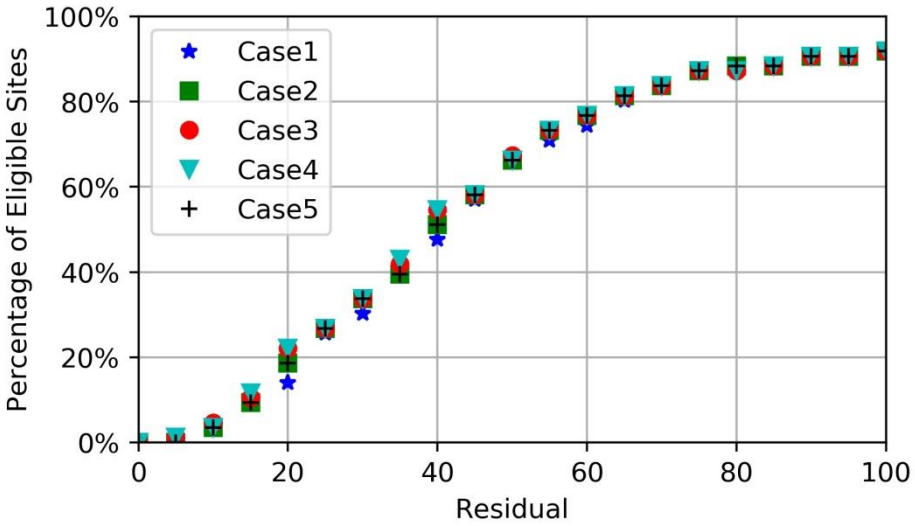

Fig. 4.3. Percentage of sites whose theoretical and target EHVR residuals are less than filter condition. The star, square, circle, inverted triangle, and plus markers represent the results for Cases 1−5, respectively.

Among all these cases, Case 5 was chosen as the best result for this research as it satisfied the key points mentioned above. In Fig. 4.4, three identification results are shown for Case 5. These results include the "comparison of HVR_{OBS} and HVR_{THE} of ten trials," "comparison of residuals of ten trials," and "comparison of reference velocity model and ten estimated models". As mentioned earlier, ten trials were analyzed for every site. The ten theoretical EHVRs or pEHVRs of one site are quite similar. The best-fit V_s and V_p models were selected with the smallest residual of the 10 trials. Finally, 57 velocity models were obtained for the Mashiki town as the effective sites. Additionally, the depths of upper 8 layers of three identified velocity models are exhibited in Table 4.2.

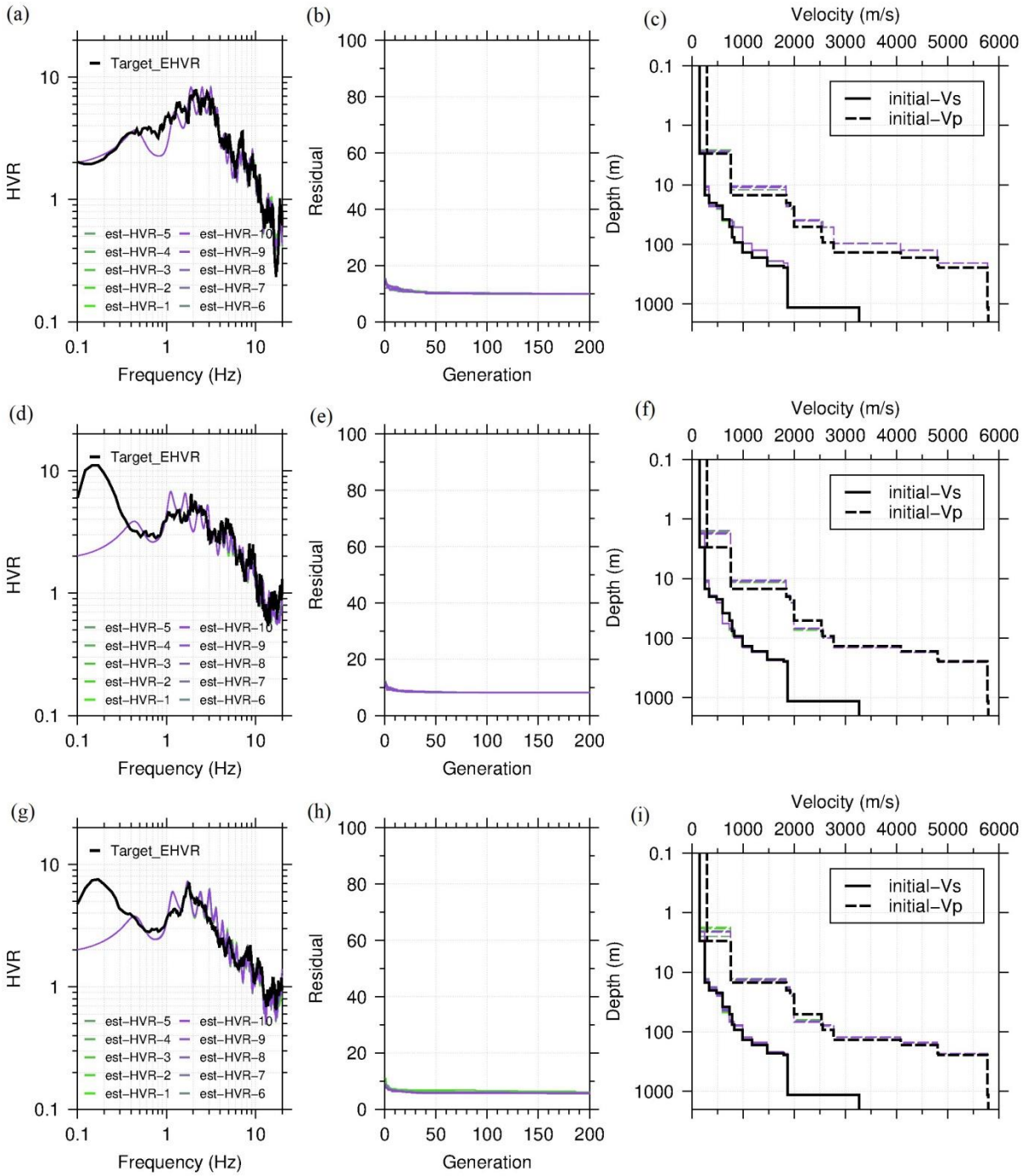

Fig. 4.4. Velocity structure identification results of three sites. (a) Comparison of synthetic EHVR and target EHVR of KMMH16. The heavy solid line represents EHVR for KMMH16. (b) Residual convergence between synthetic EHVR and target EHVR of KMMH16 from 0.3 to 20 Hz for ten trials. (c) Comparison of reference velocity model (Table 4.1) with ten identified V_s and V_p velocity structures of KMMH16. The heavy solid line represents the reference V_s model, and the heavy dash line represents the reference V_p model. Similarly, (d), (e), and (f) show the results for MS5-2, and (g), (h), and (i) show the results for MSA16.

Table 4.2

Velocity structures of upper eight layers of KMMH16, KMMP58, and MSA16, identified by using EHVRs at KMMH16 and KMMP58 and pEHVR at MSA16.

Layer	V_s (m/s)	V_p (m/s)	Density (g/cm^3)	KMMH16 Depth (m)	KMMP58 Depth (m)	MSA16 Depth (m)
1	154.87	296.56	1.66	2.77	2.12	2.08
2	249.36	760	1.73	10.93	3.02	13.12
3	337.07	1841.61	1.79	23.16	18.81	17.68
4	483.09	1918.07	1.87	24.5	25.08	23.77
5	598.03	1995	1.92	38.65	47.93	45.04
6	733.19	1995.09	1.97	38.83	60.67	68.63
7	790.1	2529.23	2.00	48.34	60.93	68.94
8	827.7	2558.47	2.01	51.52	61.09	76.38

4.3. Distributions of engineering bedrock depth and V_s30

Since the thickness of the upper 8 layers can change among the pre-supposed searching range, the depth of the bottom of the 8th layer is important. All the identified subsurface velocity structures were listed at Mashiki in Appendix 4.1 section, which included the upper eight layers of every site. Here, Fig. 4.5−(a) illustrates the contour map of that in Case 5. Fig. 4.5−(b) and (c) show the cross-sections of the east-west (AA' cross-section) and the south-north (BB' cross-section) directions. It is easy to see that the southwestern part of Mashiki, which is near the Akitsu River, the depth of the 8th layer was larger than the other areas with the same V_s and V_p. Moreover, the 8th subsurface layer in the south of Road 28 was deeper than the northern area. Associating to the field survey of wooden house damage distribution in Fig. 1.2, in the damage concentrated area between the Road 28 and Akitsu River, the depth of the 8th layers was larger than other parts. This suggests that the depth of the soft layers may be one of the reasons for causing heavy building damage during the mainshock.

Although the method of site amplification evaluation based on the time-averaged S-wave velocity of the top 30 m (V_s30) was not used in this study, the V_s30 of each site was also calculated for readers to reference as it was popular used in the site effect studies [6–10]. Figure 13 demonstrates the distribution of V_s30 for the target area. The distribution of V_s30 reflects the deviations of the

fundamental frequency in Figure 5 and so the V_s30 of the southwestern area was smaller than that of the surrounding area.

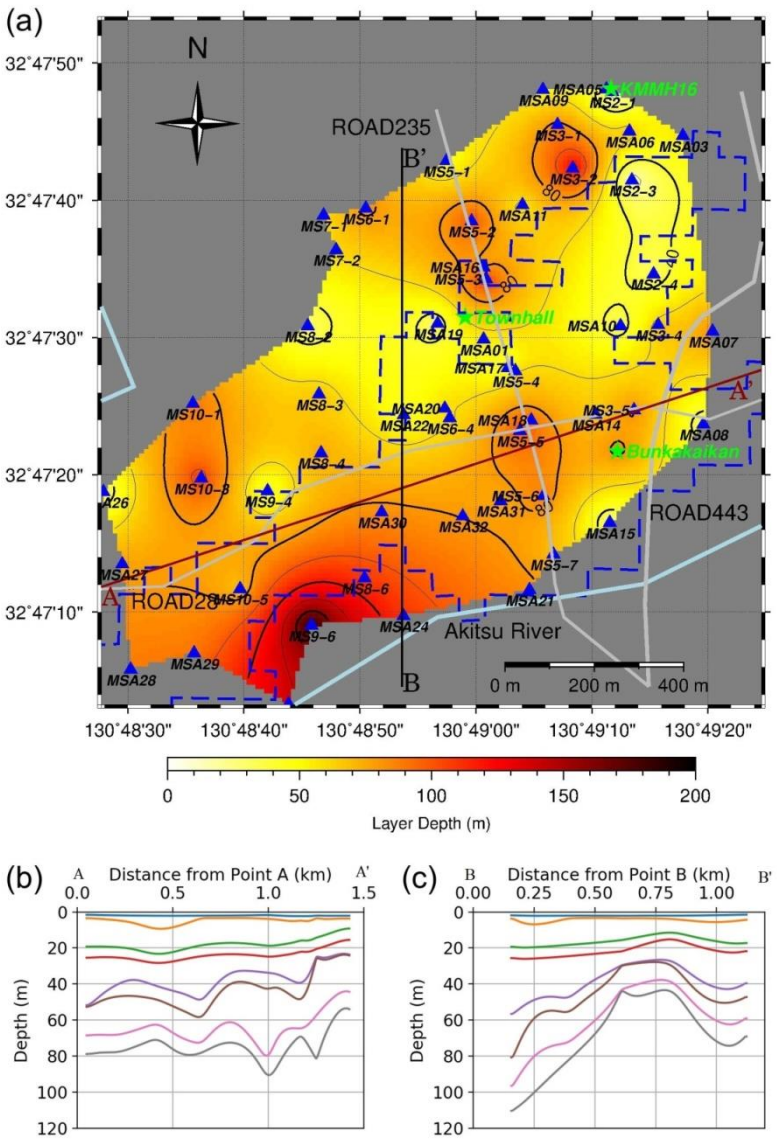

Fig. 4.5 Depth contour of 8th layer and cross sections of subsurface layers in Case5. (a) Contour map of 8th layer. The triangles represent the microtremor observation sites and strong-motion stations in Mashiki, and the stars represent the strong-motion stations. The Akitsu River passes through the southern part of Mashiki from east to west. There are three main roads, namely Road 28, Road 443, and Road 235, passing through Mashiki. (b) Cross section of AA' (west to east along Road 28) and (c) cross section of BB' (south to north) of the upper eight layers. The locations of the AA' and BB' lines are shown in (a). In (b) and (c), the x-axis is the distance between points A and B, and the y-axis is the depth from the ground surface to the bottom boundary. Each colored line represents the bottom of one layer; e.g., the top most line represents the bottom of the 1st layer where V_s = 154.87 m/s and V_p = 296.56 m/s (Table 4.1).

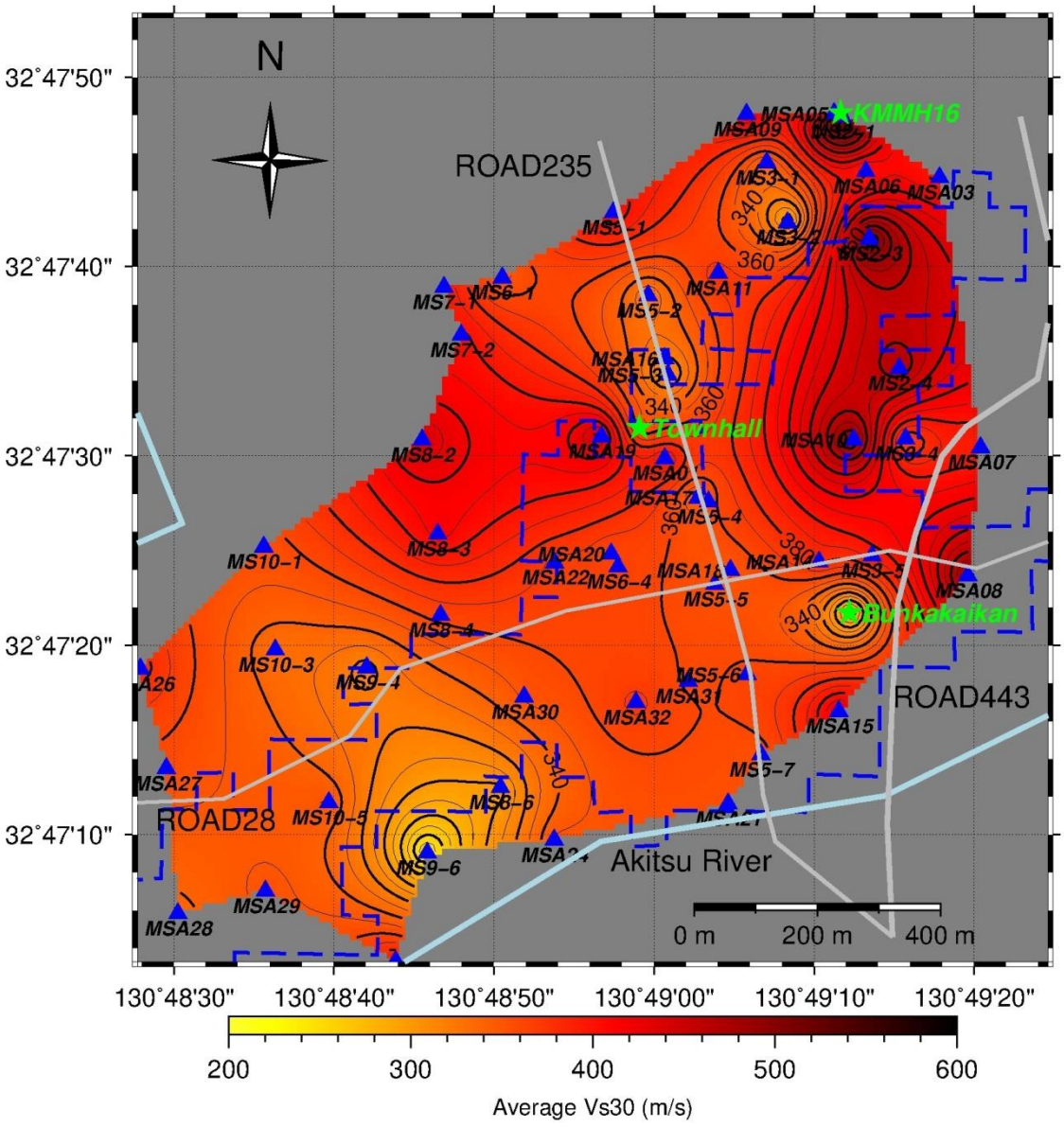

Fig. 4.6. *V_s30* distribution. The dark areas are regions with a higher *V_s30* value. The stars represent the locations of the strong-motion stations, and the triangles represent the locations of the microtremor sites.

4.4. Conclusion

The procedure of identifying subsurface velocity structure of pEHVR or EHVR was introduced in detail. Nine cases of pEHVR and EHVR inversion were performed. Then, the most suitable velocity models of Mashiki were determined. The synthetic EHVRs were close to the original pEHVRs or EHVRs for more than 68% sites. Furthermore, the synthetic EHVRs of nine cases for every site were quite similar, which indicates the searching range of shallow layer thickness does not

affect so much for the identified results. Considering obtaining the best identified velocity structures, results of Case 5 were found to be the best. According to the depth distribution of the engineering bedrock, shallow subsurface layers were thicker in the area between Road No.28 and the Akitsu River. In the northeastern region, shallow subsurface layers were also slightly deeper at MS5-3 and MS3-2, which were closely similar to the V_s30 distribution in Mashiki. Although the V_s30 distribution were not totally in consistent with the distribution of engineering bedrock depth surrounding some sites, V_s30 also reflects the local shallow geological conditions in Mashiki.

Reference (Chapter 4)

[1] Kawase H, Sanchez-Sesma FJ, Matsushima S. The Optimal Use of Horizontal-to-Vertical Spectral Ratios of Earthquake Motions for Velocity Inversions Based on Diffuse-Field Theory for Plane Waves. Bulletin of the Seismological Society of America 2011;101:2001–14. https://doi.org/10.1785/0120100263.

[2] Nagashima F, Matsushima S, Kawase H, Sanchez-Sesma FJ, Hayakawa T, Satoh T, et al. Application of Horizontal-to-Vertical Spectral Ratios of Earthquake Ground Motions to Identify Subsurface Structures at and around the K-NET Site in Tohoku, Japan. Bulletin of the Seismological Society of America 2014;104:2288–302. https://doi.org/10.1785/0120130219.

[3] Yamanaka H, Aldea A, Fukumoto S. Results From Single-Station and Array Microtremor Measurements in Bucharest , Romania 2007.

[4] Ludwig WJ, Nafe JE, Drake CL. Seismic Refraction. The Sea 1970;4:53–84.

[5] Kobayashi K, Abe Y, Uetake T, Mashimo M, Kobayashi H. Inversion of spectrum ratio of horizontal to vertical component of preliminary tremors. Summaries of Technical Papers of Annual Meeting Architectural Institute of Japan 1995;B-2:308–9.

[6] Borcherdt RD. Estimates of Site-Dependent Response Spectra for Design (Methodology and Justification). Earthquake Spectra 1994;10:617–53. https://doi.org/10.1193/1.1585791.

[7] Abrahamson N, Atkinson G, Boore D, Bozorgnia Y, Campbell K, Chiou B, et al. Comparisons of the NGA ground-motion relations. Earthquake Spectra 2008;24:45–66. https://doi.org/10.1193/1.2924363.

[8] Zhao J, Xu H. A Comparison of VS30 and Site Period as Site-Effect Parameters in Response Spectral Ground-Motion Prediction Equations. Bulletin of the Seismological Society of America 2013;103:1–18.

[9] Gregor N, Abrahamson NA, Atkinson GM, Boore DM, Bozorgnia Y, Campbell KW, et al. Comparison of NGA-West2 GMPEs. Earthquake Spectra 2014;30:1179–97. https://doi.org/10.1193/070113EQS186M.

[10] Kamai R, Abrahamson NA, Silva WJ. VS30 in the NGA GMPEs: Regional Differences and Suggested Practice. Earthquake Spectra 2016;32:2083–108. https://doi.org/10.1193/072615EQS121M.

Appendix 4.1

The upper 8 layers of identified subsurface velocity structures at Mashiki.

NO.	Latitude	Longitude	Lay1	Lay2	Lay3	Lay4	Lay5	Lay6	Lay7	Lay8
Bunkakaikan	32.78937	130.8201	3.83	15.36	27.32	33.53	64.98	78.75	81.75	83.16
KMMH16	32.7967	130.8199	2.77	10.93	23.16	24.5	38.65	38.83	48.34	51.52
Townhall	32.79208	130.8164	2.12	3.02	18.81	25.08	47.93	60.67	60.93	61.09
MS10-1	32.79033	130.8099	1.86	4.34	18.22	23.54	34.91	35.03	85.38	90.42
MS10-3	32.78882	130.8101	2.03	7.17	19.91	26.18	33.78	39.11	89.45	107.03
MS10-5	32.78658	130.811	2.09	3.2	18.99	25.25	32.51	51.13	62.9	69.91
MS10-6	32.78425	130.8122	2.19	3.58	10.5	16.77	37.69	56.41	106.76	138.85
MS2-1	32.79664	130.8199	2.23	3.02	9.61	9.65	9.8	9.93	10.18	10.34
MS2-3	32.79485	130.8204	2.05	3.21	6.98	12.82	12.97	13.1	13.35	13.51
MS2-4	32.79295	130.8209	1.82	3.81	10.32	10.42	10.58	10.71	25.36	31.27
MS3-1	32.79597	130.8186	1.69	6.98	19.65	25.92	48.69	49.16	66.26	84.25
MS3-2	32.79509	130.819	2.3	14.44	23.5	29.77	61.21	82.31	117.23	126.2
MS3-4	32.79192	130.821	1.95	3.8	15.99	22.26	41.61	41.74	64.76	65.57
MS3-5	32.7902	130.8205	1.99	3.13	13.82	20.09	23.36	23.65	56.37	81.79
MS5-1	32.79524	130.816	0.89	1.45	14.74	16.36	27.16	43.69	44.12	44.28
MS5-2	32.79402	130.8166	1.8	11.37	19.15	25.42	56.86	70.74	72.34	99.23
MS5-3	32.79285	130.8169	1.87	9.77	25.56	31.83	56.35	81.17	86.51	111.26
MS5-4	32.79099	130.8176	2.04	2.77	18.56	24.83	32.54	43.26	43.51	57.39
MS5-5	32.78978	130.8177	1.39	3.79	19.58	25.84	33.31	43.05	92.29	101.13
MS5-6	32.78846	130.8183	2.04	3.18	17.26	22.03	32.87	50.68	71.27	86.59
MS5-7	32.78728	130.8185	1.98	3	18.72	24.74	47.85	48.15	69	69.77
MS6-1	32.79428	130.814	1.76	4.26	20.05	26.32	47.13	47.29	72.18	85.35
MS6-4	32.79004	130.816	2.03	2.73	16.59	22.86	33.79	44.54	48.65	57.89
MS7-1	32.79414	130.813	1.9	2.8	13.51	18.77	25.68	26.03	42.08	60.2
MS7-2	32.79344	130.8133	1.99	2.97	10.67	16.94	38.48	47.74	54.77	62.26
MS8-2	32.7919	130.8126	1.94	3.13	10.98	11.23	20.7	20.82	25.56	26.45
MS8-3	32.79052	130.8129	1.98	2.88	11.43	17.39	23	23.12	39.71	66.63
MS8-4	32.78933	130.813	2.1	2.83	17.12	22.09	32.48	51.22	69.5	74.51
MS8-6	32.7868	130.814	2.55	13.87	21.35	27.62	48.16	48.28	76.68	108.78
MS9-4	32.78856	130.8117	2.07	8.79	22.66	26.3	35.16	35.59	36.06	36.45
MS9-6	32.78584	130.8127	2.29	38.11	53.9	60.17	86.34	105.51	155.86	187.96
MSA01	32.79163	130.8169	1.09	2.9	14.22	15.13	40.07	40.21	43.88	55.46
MSA03	32.79575	130.8216	1.66	2.98	13.7	19.97	25.37	25.9	51.26	56.19
MSA05	32.79669	130.8198	1.87	3.77	10.58	10.96	11.39	11.51	29.43	30.19

MSA06	32.79584	130.8203	1.97	2.91	11.66	17.93	35.78	52.01	55.46	64.29
MSA07	32.79179	130.8223	2.16	4.93	10.86	16.97	37.39	37.78	60.8	81.67
MSA08	32.78991	130.8221	2.18	2.98	5.96	12.23	12.38	12.52	28.62	29.21
MSA09	32.79668	130.8183	2.09	3.03	10.8	17.07	21.18	21.3	36.59	50.98
MSA10	32.7919	130.8201	2.02	2.72	5.9	12.17	12.59	12.84	21.14	32.27
MSA11	32.79435	130.8178	2.16	3.39	14.08	20.34	36.77	37.5	52.89	55.86
MSA14	32.79011	130.8195	2.07	2.97	13.55	19.82	35.54	44.16	61.25	64.39
MSA15	32.78792	130.8199	1.89	2.58	12.51	18.78	18.93	19.06	26	26.16
MSA16	32.79309	130.8169	2.08	13.12	17.68	23.77	45.04	68.63	68.94	76.38
MSA17	32.79105	130.8174	2.35	10.53	15.39	21.66	29.29	39.52	39.77	39.93
MSA18	32.78999	130.818	2.03	3.41	19.2	25.47	31.15	31.27	59.24	91.34
MSA19	32.79195	130.8158	2.22	3.5	8.43	10.96	21.08	21.21	29.89	30.19
MSA20	32.79023	130.8159	2.1	3.32	16.9	23.17	29.6	29.81	40.53	59.43
MSA21	32.78656	130.818	1.99	2.89	18.68	24.95	48.37	50.93	64.96	83.37
MSA22	32.7901	130.8149	2.16	3.62	15.65	21.92	29.44	29.57	42.68	43.03
MSA24	32.78603	130.8149	1.89	3.27	19.06	25.33	56.77	81.65	96.64	109.92
MSA26	32.78854	130.8078	1.88	2.06	17.53	17.62	26.82	26.95	27.22	27.42
MSA27	32.78708	130.8082	1.46	3.23	19.02	25.29	52.52	52.65	65.77	77.02
MSA28	32.78495	130.8084	2.07	4.72	20.51	26.78	58.23	58.78	82.25	89.17
MSA29	32.78528	130.8099	2.22	3.3	18.04	24.29	45.65	46.65	82.05	89.8
MSA30	32.78813	130.8144	2.05	3.07	18.86	25.13	56.57	66.57	79.13	83.27
MSA31	32.78836	130.8173	2.09	2.9	17.75	24.02	32.89	33.01	74.68	74.85
MSA32	32.78805	130.8164	2.05	3.91	16.44	22.71	23.17	23.3	52.63	79.6

Chapter 5

Linear and equivalent linear analyses of subsurface velocity structures in Mashiki

5.1. Introduction

5.2. Nonlinear soil property at KMMH16

5.3. Horizontal seismological bedrock motions at KMMH16

5.4. Linear analysis and equivalent linear analysis of subsurface velocity structures at KMMH16 and KMMP58

5.5. Linear analysis and equivalent linear analysis of soil columns in Mashiki

- 5.5.1. Results of 57 sites
- 5.5.2. Results of 592 sites.
- 5.5.3. Discussion

5.6. Conclusion

Reference (Chapter 5)

5.1. Introduction

Estimation of ground motions by using the dynamic response of soil structures is a good choice. Different analysis method with nonlinear characteristics of soil material could be chose to use in different cases. Several methods for evaluating the effect of local soil conditions on ground response during earthquake are presently available. Most of these methods are based on the assumption that the main responses in a soil deposit are caused by the upward propagation of shear waves from the underlying rock formation. Analytical procedures based on this concept incorporating nonlinear soil behavior, have been shown to give results in good agreement with field observations in a number of cases. As shown in Fig. 5.1, the linear analysis (LA) would be appled when the soil material is rock, the analysis of gravel, sand, and clay would be choose to use the equivalent linear analysis (ELA) or the nonlinear analysis method (NA), based on the results of the laboratory tests. The ELA is usually effective when the effective shear strain is less than 1% or a little larger than that [1–3].

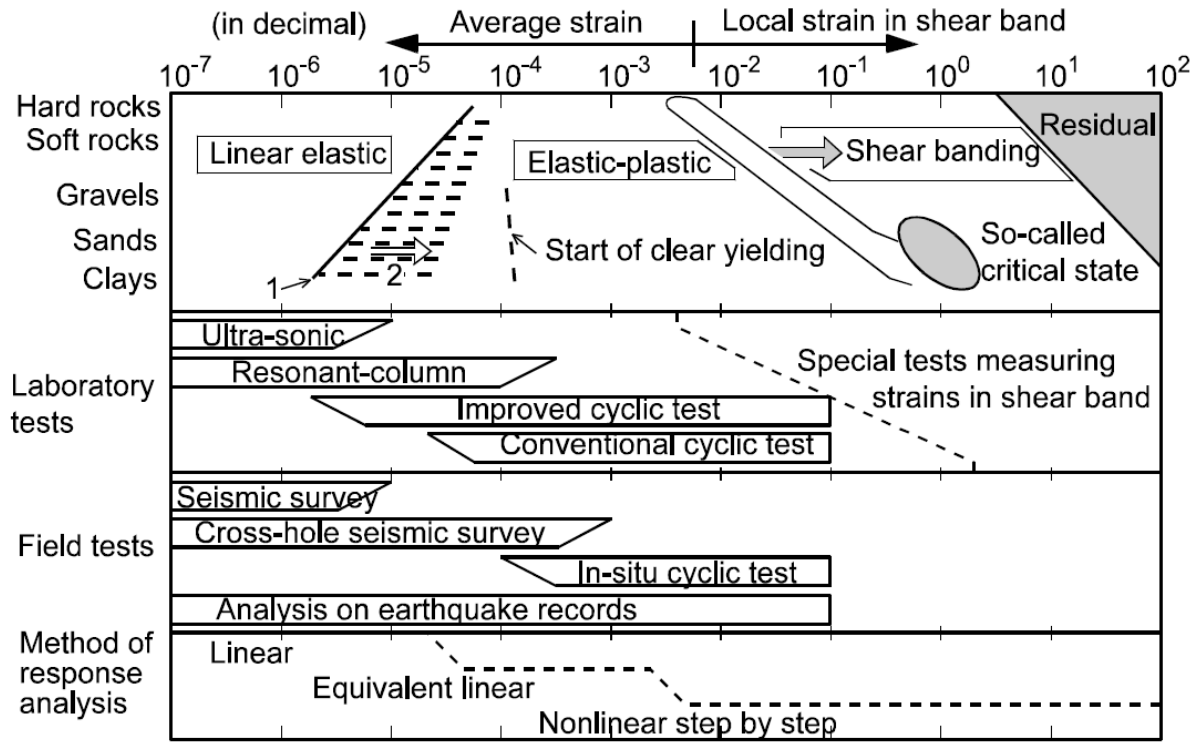

Fig. 5.1. Nonlinear characteristics of soil, test and analysis method [2].

A one-dimensional (1D) site response of soil deposit can be used if the soil structure is essentially horizontal [1]. Based on the ELA method and multiple reflection theory, 'DYNEQ' was developed by Dr. Yoshida and his colleagues [2,3]. They developed this program by employing some

new ideas in addition to the concept of SHAKE, which is a famous computer code developed by Schnabel et al. [1]. Although nonlinear analysis based on the step-by-step time integration method tracing the nonlinear behavior of material is better, the multiple reflection theory is an exact solution of the wave propagation equation. The results by using the ELA and the reflection theory would be presented in this chapter. Then, the results by using the step-by-step time integration method (NA) would be shown in Chapter 6. New concepts were considered in DYNEQ, such as regarding frequency-dependent characteristics like damping due to scattering. Additionally, the overestimation of the peak acceleration under a strong ground motion and the underestimated amplification at high frequencies were considered. The DYNEQ was designed based on a dynamic memory allocation system, which means that it has no memory limitation, just considering as long as the computer allows [2].

Nonlinear characteristics of the soil are usually called dynamic deformation characteristics. Here, the term dynamic does not indicate rapid loading but repeated loading. In the dynamic deformation test, tri-axial test apparatus, torsional shear test, etc. are used, in which shear modulus G and damping ratio h are computed from the hysteresis loops, as shown in Fig. 5.1. They are summarized into the so-called $G-\gamma$ and $h-\gamma$ (γ denote the shear strain). Although this expression is not perfect in expressing the nonlinear characteristics, it is frequently used because it is easy to handle and has large amount of accumulated result in the past [2]. The nonlinear soil properties of the subsurface layers are important. Moreover, The $G-\gamma$ and $h-\gamma$ of shallow subsurface layers were ontained in Mashiki.

5.2. Nonlinear soil property at KMMH16

According to the experimental results of borehole drilling at the site near KMMH16 in Mashiki [4–6], the relationships of $G-\gamma$ and $h-\gamma$ for three kinds of soils (Soil 1, 2, and 3) were obtained at site K as shown in Fig. 5.2. To get the special pairs of parameters for the three soils, which will be used later in the ELA by DYNEQ, two sets of equations were applied to calculate interpolations of the relationships $G-\gamma$ and $h-\gamma$, based on the experimental results.

The experimental data of Site K, O, M, and A were shown in Figs. 5.3 and 5.4. They did the tri-axis experiments of three kinds of soil at Site K. However, the value sets of experimental results were not as the wanted ones in the ELA, it was needed to get the interpolated data sets of $G-\gamma$ and $h-\gamma$ as precise as we can. Thus, a function proposed by Fredlund and Xing [7] were referred to and some variables were set to replace the constants in their equations. Eq. (5.1) and Eq. (5.2) were obtained to interpolate the relationship $G-\gamma$.

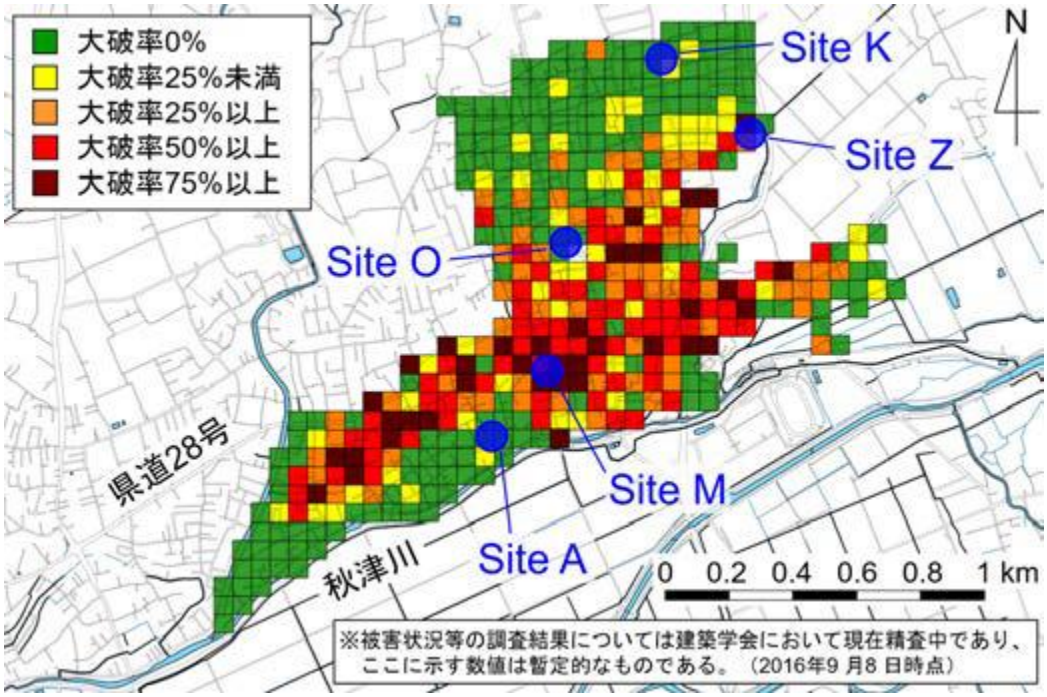

Fig. 5.2. Sites of borehole drilling for the tri-axial experiments in Mashiki. Site K was located close to the KMM16 [4].

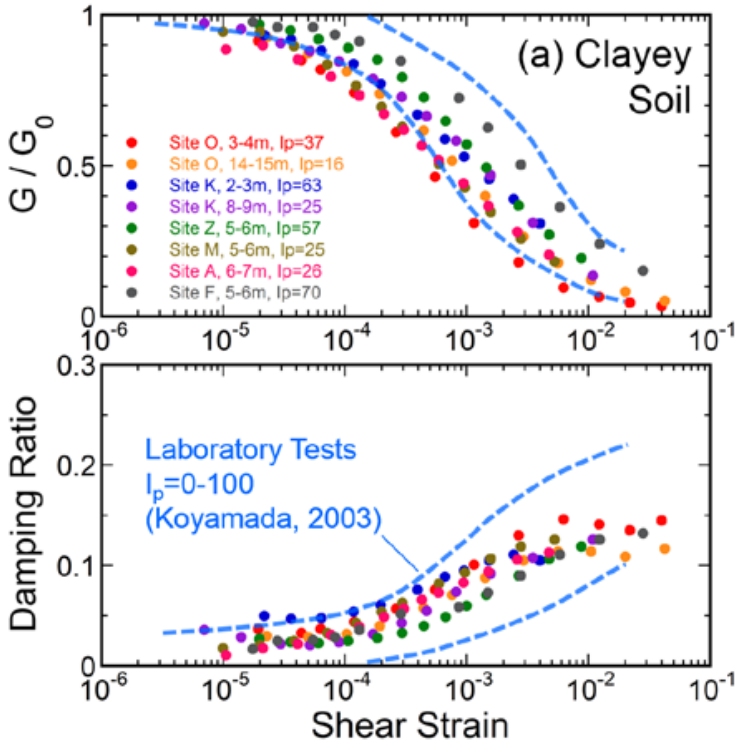

Fig. 5.3. *G*–*γ* and *h*–*γ* of the first and/or second layer at Site K, O, M, A, and Z, by using the tri-axis experiments [4].

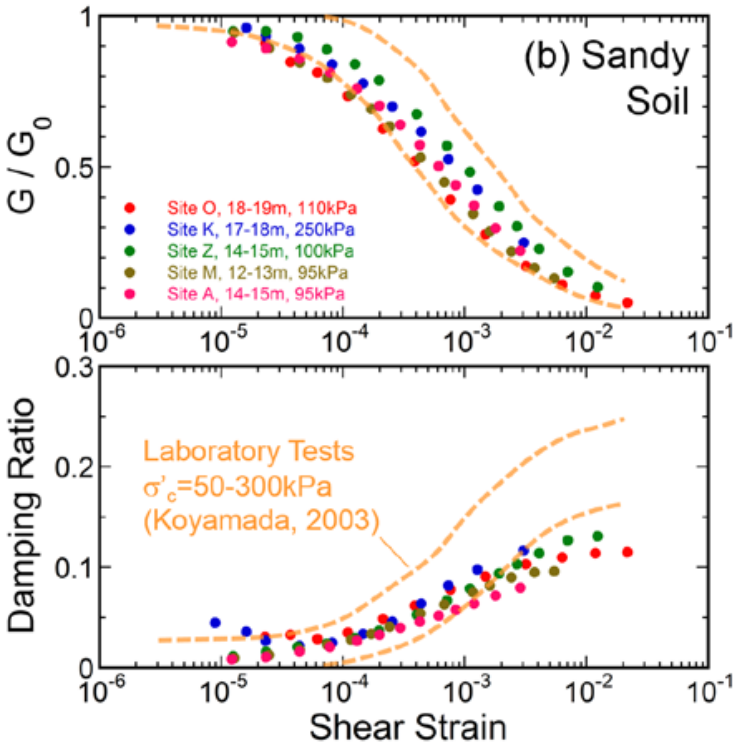

Fig. 5.4. *G*−*γ* and *h*−*γ* of the deeper layer at Site K, O, M, A, and Z, by using the tri-axis experiments [4].

$$\frac{G}{G_{max}} = f(\gamma) \times \frac{1}{(ln(e+(\frac{\gamma}{b})^n)^m}, \tag{5.1}$$

$$f(\gamma) = 1 - \frac{ln(1+\frac{\gamma}{b})}{ln(1+\frac{1000000}{b})}, \tag{5.2}$$

where, e is the Euler's number, b, m, and n are real variables to be determined.

Then, the equation that explains the relationship between the damping ratio and shear strain (h−γ) were obtained by referring to previous research results [8] (Senetakiset al., 2013; Hardin and Drnevich, 1972). Similar to the steps described above, we used six variables to replace the constants of their equation. The modified equation is shown in Eq. (5.3).

$$h = x + y \times (z + i \times \gamma^j)^q, \tag{5.3}$$

where, x, y, z, i, j, and q are variables to be determined, h denotes the damping ratio, and γ denotes the shear strain

After that, the experimental data sets for Clay 1, Sand 1, and Sand 2 at site K were installed into Eqs. (5.1), (5.2), and (5.3), to calculate the nine variables in these equations for three kinds of soil. By using the Python3 Scipy package referred to the Levenberg–Marquardt algorithm [9,10], a model based on the above three equations was established. Then, the experimental data was inputted into the model to perform the calculation of supervised learning. After 10,000 loops of computation, the best-fit equation to interpolate the experimental data would be achived. By this method, three sets of variables of these equations for three nonlinear soils could be derived, as listed in Table 5.1. Finally, eight special pairs of data were obtained, whose shear strain values were 5.00×10^{-6}, 1.00×10^{-5}, 5.00×10^{-5}, 1.00×10^{-4}, 5.00×10^{-4}, 1.00×10^{-3}, 5.00×10^{-3} and 1.00×10^{-2}, using Eqs. (5.1), (5.2), and (5.3) for each nonlinear soil. The interpolated results were shown in Fig. 5.5 (a), (b) and (c) of site K for three types of soil materials. In this research, the nonlinear property of gravel material is also needed. The research results of gravel material by Imazu and Fukutake [11] were also used in this study, as shown in Figure 5.5 (d).

Table 5.1. Variables in equation (5.1), (5.2) and (5.3) used to represent nonlinear soil properties of Soil 1, 2, and 3

Variable	Soil 1	Soil 1	Soil 2
b	0.000542	0.020638	0.001642
n	0.708890	0.560170	0.671570
m	1.611900	9.585700	3.543500
x	0.047665	0.021717	0.020568
y	3.924900	8.956300	42.578000
z	84.514000	1.016900	4.114800
i	0.000092	0.000024	0.001160
j	-1.785100	-0.695390	-0.888110
q	-0.933580	-257.760000	-4.165600

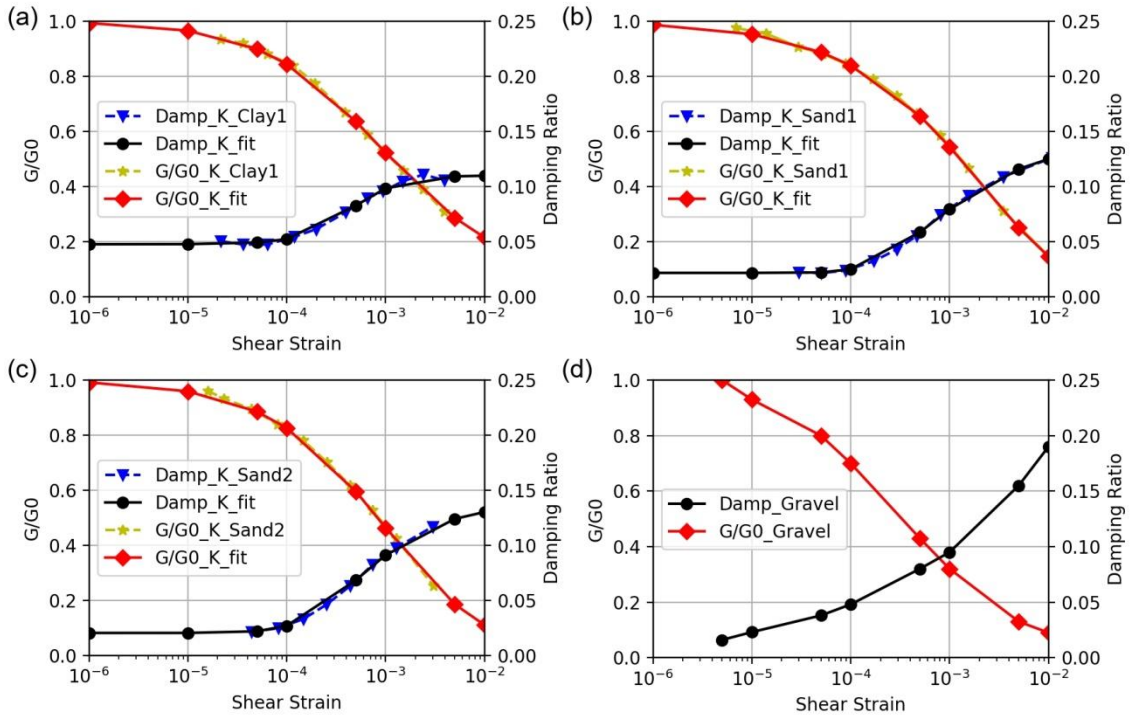

Fig. 5.5. Four types of nonlinear soil properties. (a), (b), (c) are the interpolated soil nonlinear properties at 'site K', referred from the experimental data [4–6]. (a) Soil property of 'Soil 1', (b) soil property of 'Soil 2', (c) soil property of 'Soil 3', and (d) soil property of gravel which was referred to Imazu and Fukutake (1986) are shown. In (a), (b), and (c), the dash lines with stars are experimental data of "G/G_{max}−Shear Strain" and the lines are linearly interpolated. The dash lines with inverted triangles are the experimental data of "Damping Ratio−Shear Strain," whose lines are linearly interpolated. The solid lines with diamonds are the curve fitting and interpolated results of "G/Gmax − Shear Strain" obtained through equations (7) and (8). The solid lines with circles are the curve fittings and interpolated results of the "Damping Ratio − Shear Strain" using equations (9). In (d), the solid lines with diamonds and circles are "G/G_{max}−Shear Strain" and "Damping Ratio−Shear Strain", respectively.

5.3. Horizontal seismological bedrock motions at KMMH16

Before carrying out the linear and equivalent linear analysis at Mashiki, it is needed to get the input seismic waves at the seismological bedrock (with V_s = 3.4 km/s) during the mainshock. The theoretical transfer functions can be used to obtain the S-wave amplification factor of strong ground motions, if the nonlinear characteristics of the soft soil sediments are known. However, it is not easy to precisely reproduce nonlinear characteristics of soil, and therefore it would be faced a large uncertainty on the estimated input motion during strong shaking. Nagashima et al. [12] and Nagashima and Kawase [13] attempted to estimate the horizontal seismological bedrock motions from

the observed vertical strong ground motions based on the DFC for earthquakes. If we assume that the vertical transfer function of the S-wave portion does not change between weak and strong motions, the horizontal seismological bedrock motion of S-wave portion is equal to the ratio of the vertical ground motion on the surface divided by the linear transfer function of the vertical component, along with the amplitude correction factor between the horizontal and vertical components at the seismological bedrock, as Eq. (5.4) shows. The transfer function used here is only the absolute value.

$$Spectra_{horizontal}^{bedrock} = \frac{Spectra_{horizontal}}{|TF_{horizontal}|} = \sqrt{\frac{\alpha}{\beta}}\frac{Spectra_{vertical}}{|TF_{vertical}|} \tag{5.4}$$

where, $\mathrm{Spectra}_{\mathrm{horizontal}}^{\mathrm{bedrock}}$ and $\mathrm{Spectra}_{\mathrm{horizontal}}$ are the Fourier spectra of the horizontal component at the seismic bedrock and on the ground surface; $|\mathrm{TF}_{\mathrm{horizontal}}|$ is the absolute value of the horizontal transfer function; $\mathrm{Spectra}_{\mathrm{vertical}}$ is the Fourier spectra of the vertical component on the ground surface; $|\mathrm{TF}_{\mathrm{vertical}}|$ is the absolute value of the vertical transfer function; β is the Vs of the seismological bedrock; α is the Vp of the seismological bedrock.

As the vertical transfer function can be considered unaffected by the input level of strong motion, the transfer function of the vertical component calculated from the identified model for weak seismic motions can be applied to Eq. (5.4). In the actual calculation of the bedrock motions at KMMH16, Nagashima and Kawase [13] first applied Eq. (5.5) to the early coda immediately after the main part of the S-wave to calculate nonlinear horizontal transfer function $|TF_{horizontal}^{Nonlinear}|$. They used the early coda part of the horizontal component to calculate the nonlinear transfer function because it is not strongly affected by the directivity and the radiation pattern, whereas it is affected by the soil nonlinearity to the same degree as the main part.

$$|TF_{horizontal}^{Nonlinear}| = Spectra_{horizontal}^{Early\ coda} \times (\sqrt{\frac{\alpha}{\beta}} \times \frac{Spectra_{vertical}}{|TF_{vertical}|})^{-1} \tag{5.5}$$

By assuming that the nonlinear transfer function of the early coda retains its shape during the strong shaking, the seismological bedrock wave can be calculated from Eq. (5.6).

$$Spectra_{horizontal}^{Bedrock} = \frac{Spectra_{horizontal}^{Main}}{|TF_{horizontal}^{Nonlinear}|} \tag{5.6}$$

where, $Spectra_{horizontal}^{Main}$ denotes the Fourier spectra of the horizontal component at the ground surface during the mainshock (for the whole duration); $|TF_{horizontal}^{Nonlinear}|$ is the absolute value of the transfer function of the horizontal component derived from Eq. (5.5).

These spectral calculations are performed for both north−south (NS) and east−west (EW) components separately. Once obtaining the Fourier spectra at the seismological bedrock, the synthetic waveforms will be calculated by using the inverse fast Fourier transform (FFT) with the phase information of the observed borehole waveforms at KMMH16. Fig. (5.6) shows the seismological bedrock motions estimated by Eq. (5.6).

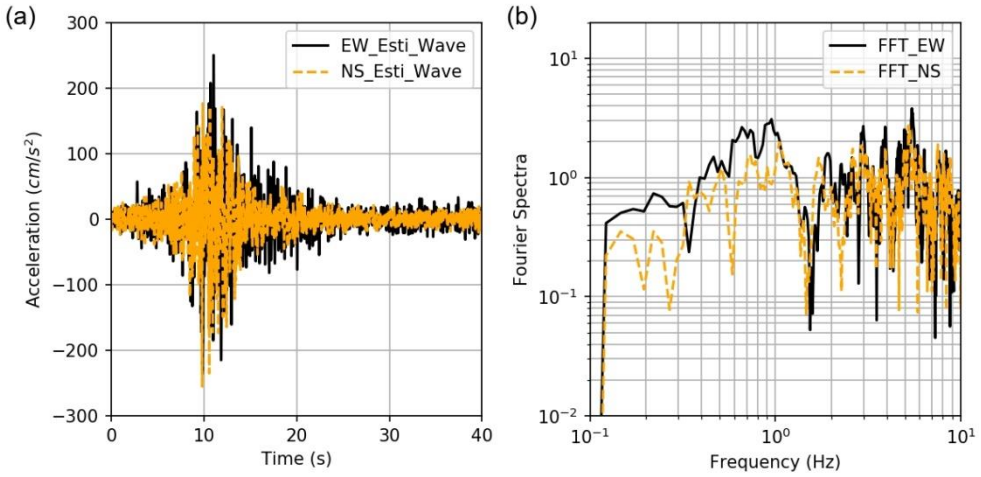

Fig. 5.6. Time and frequency domains of the estimated horizontal seismological bedrock motions referred to the previous study [13]. (a) Solid and dash lines denote the estimated acceleration of the EW and NS components, respectively. (b) Solid and dash lines are the EW and NS components of the Fourier spectra of the estimated bedrock motions, respectively.

Here, it is necessary to explain the reason why the same seismological bedrock motions can be used to estimate the ground motions during the mainshock in Mashiki. On the one hand, as the epicenter located in the southwest of the target area (Fig. 1.1), the epicentral distances at the southwestern and northeastern corners (hereafter, SW and NE points, as shown in Fig. 5.7) are the shortest and longest in the target area, which are 5.6 and 7.3 km, respectively. Referring to the velocity structure of KMMH16 (surface to 4.2 km below) and J-SHIS model (from 4.2 km to 12 km), the propagation distances from the source to the SW and NE points were calculated to be 13.26 and 14.07 km, based on the Snell's Law of plane S-wave propagation in the stack of homogeneous layers (Orfnidis, 2016). The difference between these propagation distances is 6.15%. The amplitude error over the target area was considered as small enough to ignore. On the other hand, if we consider the vertical incidence from the strong-motion generation area immediately below the region, as delineated

in the source rupture process inverted by Yoshida et al. [14], the amplitude difference due to the source distance should be negligibly small. Thus, the ground motions can be estimated by using the same seismological bedrock motions.

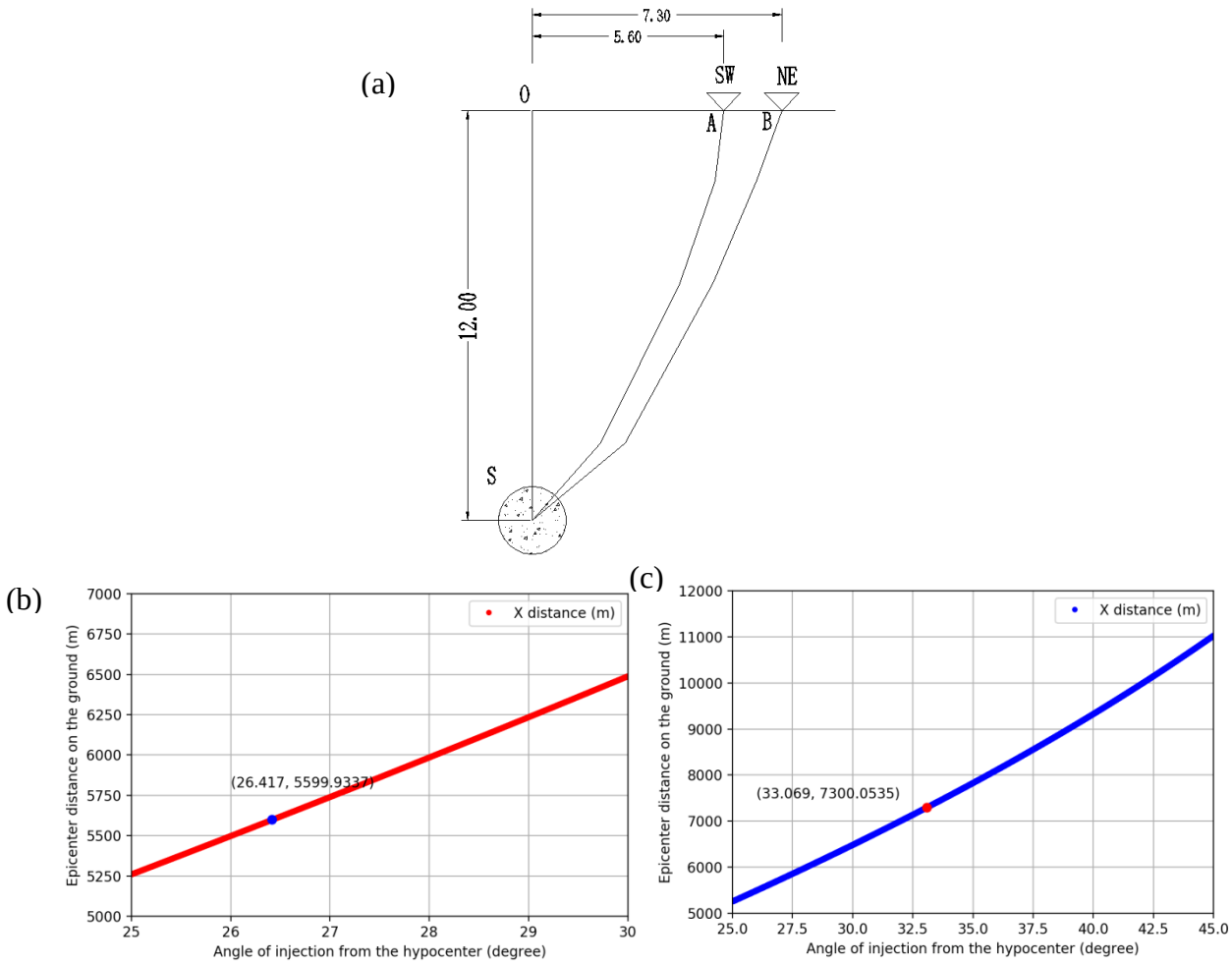

Fig. 5.7. Ray-tracing for the hypocentral distance calculation. (a) A schematic diagram of ray-tracing in a one-dimensional medium from the hypocenter to the ground sites. The point O denotes the epicenter of the mainshock, the point S the hypocenter, the point A the south-west point which is closest to the epicenter O, and the point B the north-east point which is furthest from the epicenter O. (b) and (c) are the figures to find the angle of injection from the hypocenter to each site. In (b), the x-axis is the wave injection angle from the hypocenter, while the y-axis is the epicentral distance from the point O to the point A. The correct wave injection angle to the point A is found to be 26.417 degree as shown by a blue dot. Similarly, the wave injection angle to the point B is 33.069 degree as shown by a red dot in (c).

5.4. Linear analysis and equivalent linear analysis of subsurface velocity structures at KMMH16 and KMMP58

KMMH16 has records of borehole logging data down to 252 m which included information of the V_s, V_p, layer depth, and soil type. Combining with the experimental results of Arai or Nakagawa et al. [4,6], the nonlinear soil property based on the Vs and Vp were calculated, as shown in Table 5.2. 'Soil 1', 'Soil 2', 'Soil 3', and 'Gravel' layers were applied to the soil properties as shown in Figure 14a, b, c, and d. For the linear soil property of the 8th – 15th layers ('Linear' layers in Table 5.2), the damping ratios were set to be 1.1%, as according to previous studies [12,15]. In both LA and ELA, the 1D S-wave amplification analysis software "DYNEQ" was applied in this study.

Table 5.2. The velocity, density, and the choice of soil property used in the ground response analyses. The thickness and depth are those of the inverted velocity model at KMMH16, the shaded part of which will be replaced by the values inverted at each site.

Layer Number	V_s (m/s)	V_p (m/s)	Thickness (m)	Depth (m)	Density (g/cm^3)	Soil Property
1	154.87	296.56	2.77	2.77	1.66	Soil 1
2	249.36	760.00	8.16	10.93	1.73	Soil 2
3	337.07	1841.61	12.23	23.16	1.79	Soil 3
4	483.09	1918.07	1.34	24.5	1.87	Soil 3
5	598.03	1995.00	14.14	38.65	1.92	Gravel
6	733.19	1995.09	0.18	38.83	1.97	Gravel
7	790.10	2529.23	9.51	48.34	2.00	Gravel
8	827.70	2558.47	3.18	51.52	2.01	Linear
9	990.51	2768.98	44.92	96.44	2.07	Linear
10	1172.19	4078.39	29.23	125.67	2.13	Linear
11	1468.35	4796.23	64.6	190.27	2.21	Linear
12	1790.20	4813.21	15.52	205.79	2.30	Linear
13	1871.20	5776.98	905.78	1111.57	2.32	Linear
14	3264.74	5786.36	3100.31	4211.88	2.61	Linear
15	3400.00	6000.00	0	4211.88	2.64	-

Upon obtaining the soil properties, seismological bedrock motions, and soil material characteristics, first the linear and equivalent linear analyses were performed at KMMH16. The dynamic response results of EW and NS components were shown in Figs. 5.8 and 5.9, separately. For the EW component, the acceleration reproduced by the LA was stronger than that by the ELA as well as the observed acceleration, while the PGA reproduced by the ELA was close to the observed one at KMMH16. The acceleration Fourier spectra of the ELA also matched the observed acceleration

Fourier spectra better than the LA result. The observed amplification factor is calculated as a ratio between the observed horizontal spectrum on the surface and estimated bedrock spectrum, both of that are the Fourier spectrum of the incident signal, although the bedrock spectrum is not purely the observed one. It was also close to the estimated amplification factor of the ELA. Then, it is found that the maximum strain used in the ELA was less than 1.0%, which means that the ELA is suitable for the dynamic analysis of the subsurface structure at KMMH16 during the mainshock. The estimation results of LA and ELA at KMMP58 were shown in Figs. 5.10 and 5.11. The estimated results of ELA were also close to the observational data at KMMP58.

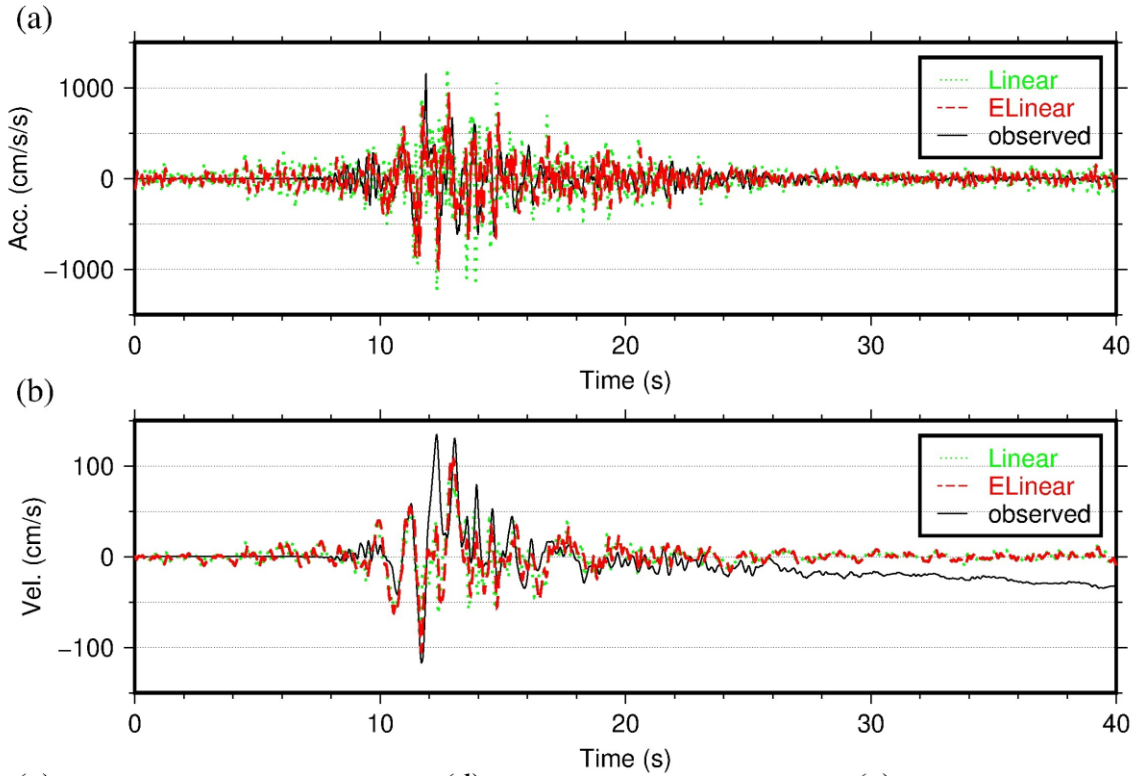

Fig. 5.8. Linear and equivalent linear analysis results of EW component at KMMH16. (a) The estimated ground acceleration of LA (dotted line) and ELA (dash line), compared with the observed strong ground motion of the EW component at KMMH16 (solid line) during the main shock. (b) The estimated ground velocity of LA (dotted line) and ELA (dash line), compared with the observed ground motion of the EW component at KMMH16 (solid line) during the mainshock.

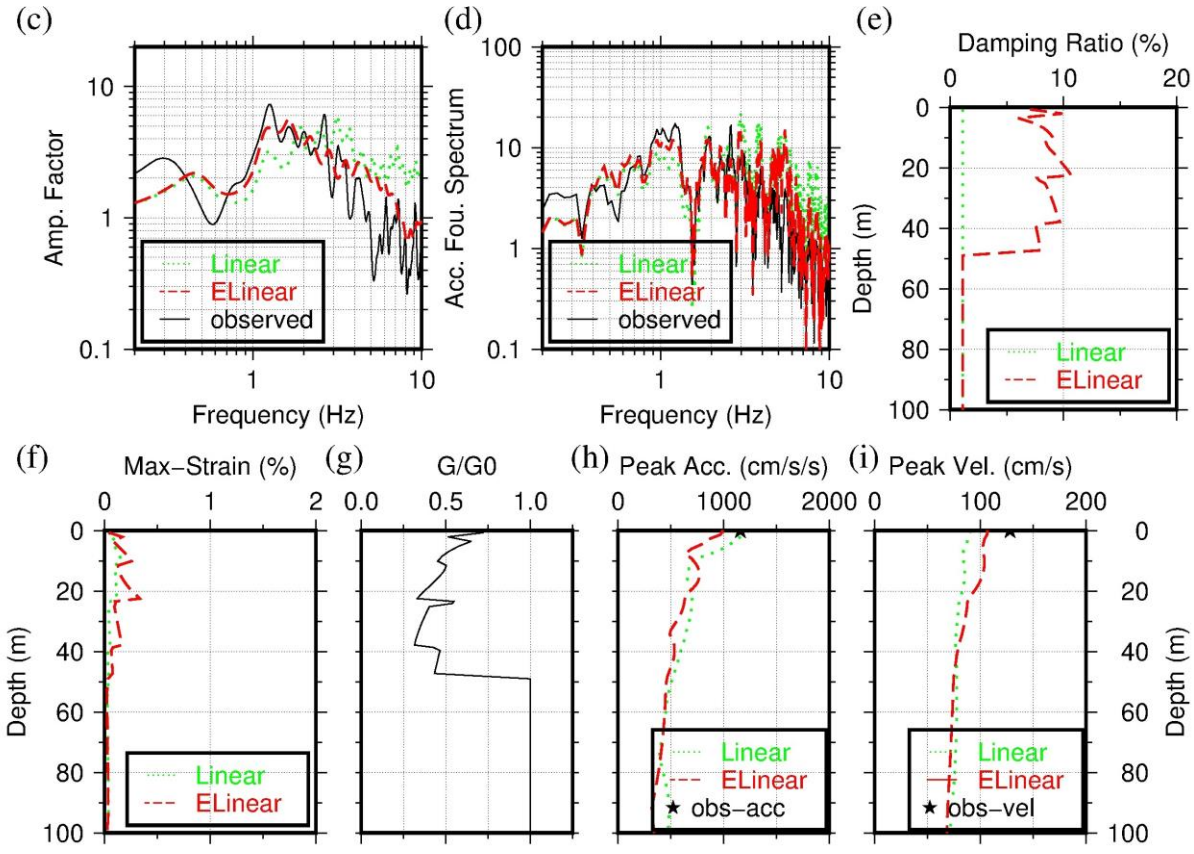

Continue Fig. 5.8. (c) Amplification factors of the LA (dotted line) and ELA (dash line) from the ground surface to the seismological bedrock, compared with the ratio of the observed spectrum on the ground surface to the estimated one at the bedrock (solid line). (d) Acceleration Fourier spectra at the ground surface of the LA (dotted line) and ELA (dash line), compared with the observed EW component (solid line) during the mainshock. (e) Damping ratio of each subsurface layer of the LA (dotted line) and ELA (dash line). (f) Maximum shear strain of each subsurface layer of the LA (dotted line) and ELA (dash line), in "%". (g) Shear modulus ratio (G/Gmax) of the ELA. (h) PGA of each subsurface layer of the LA (dotted line) and ELA (dash line), the star is the observed PGA at KMMH16 during the mainshock. (i) PGV of each subsurface layer of the LA (dotted line) and ELA (dash line), the star is the observed PGV at KMMH16 during the mainshock.

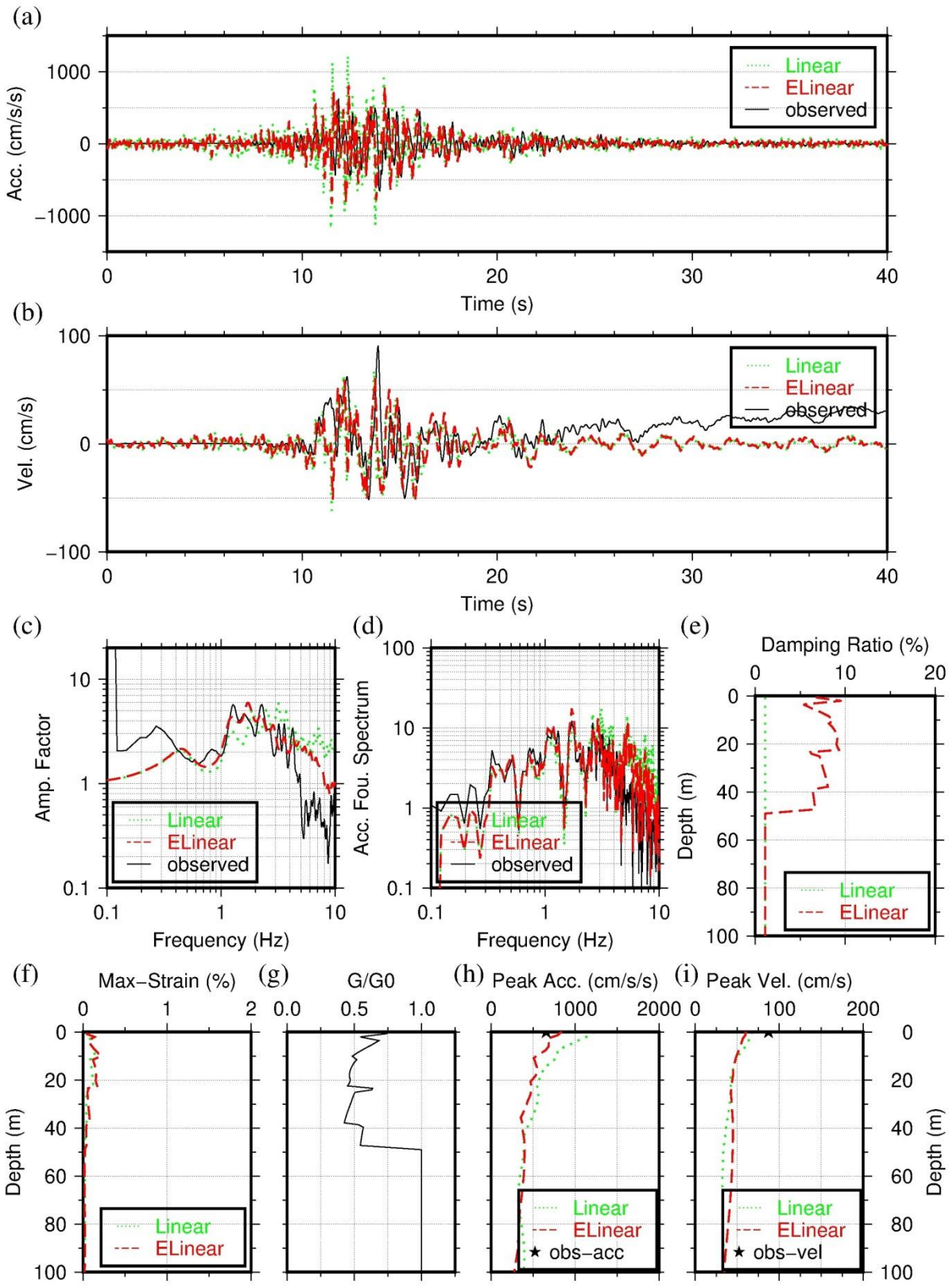

Fig. 5.9. Linear and equivalent linear analysis results of the NS component at KMMH16. The meaning of the line is the same as in Figure 14, but for the NS direction (both observed and estimated data).

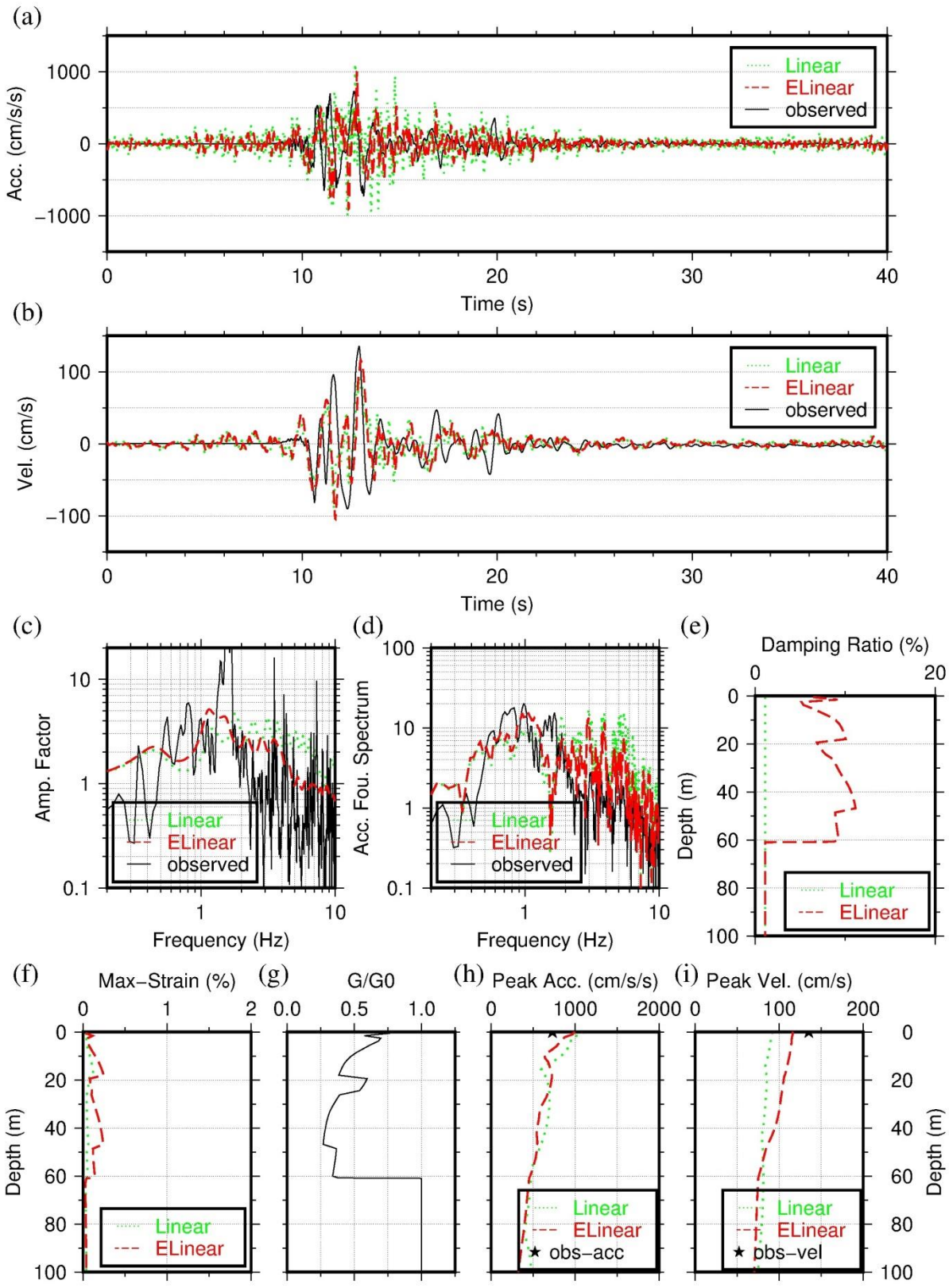

Fig. 5.10. Linear and equivalent linear analysis results of the EW component at KMMP58. The meaning of the line is the same as in Figure 14, but for data at KMMP58 in the EW direction (both observed and estimated data).

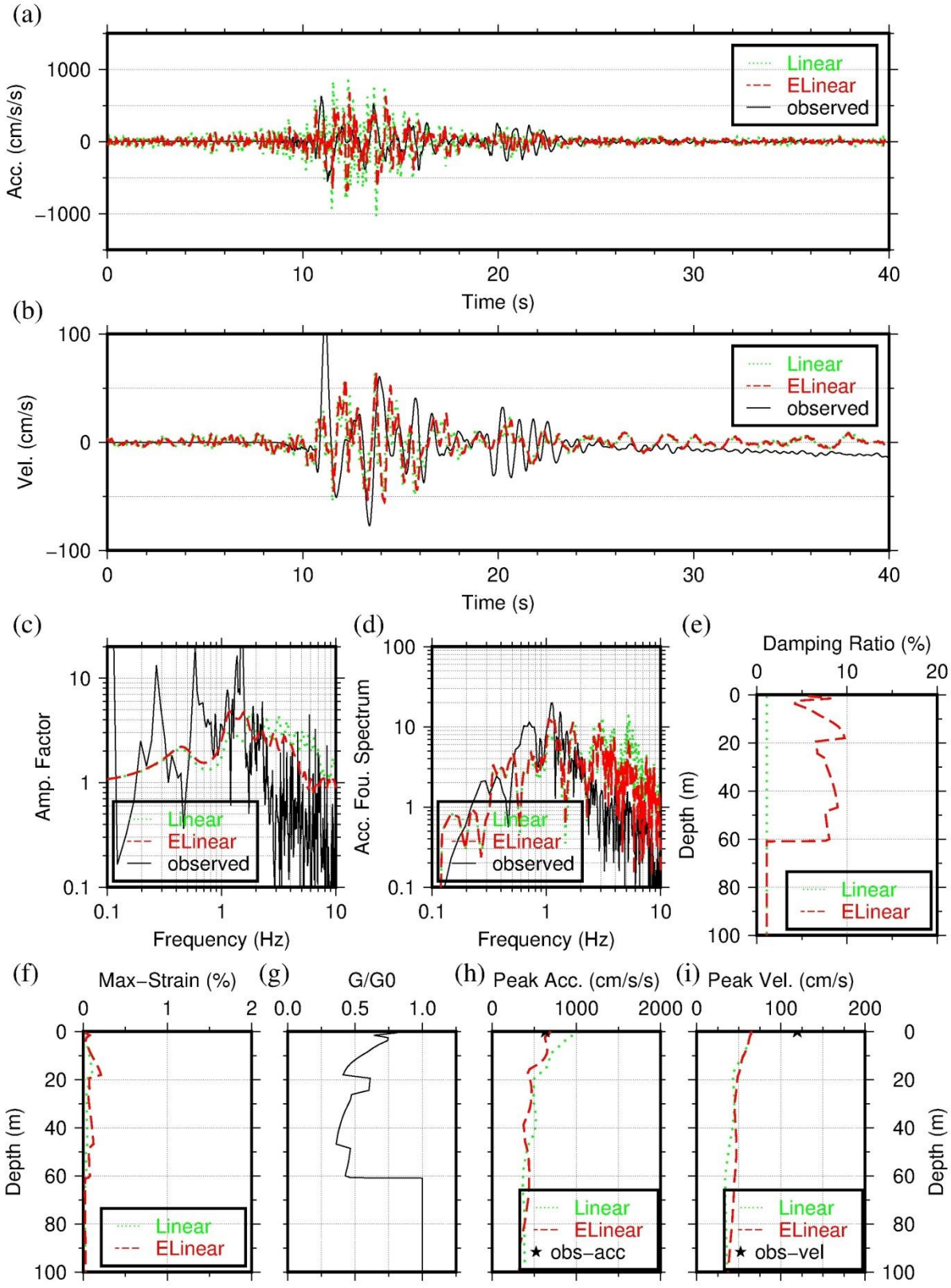

Fig. 5.11. Linear and equivalent linear analysis results of the NS component at KMMP58. The meaning of the line is the same as in Figure 14, but for data at KMMP58 in the NS direction (both observed and estimated data).

5.5. Linear analysis and equivalent linear analysis of soil columns in Mashiki

5.5.1. Results of 57 sites

Since both acceleration and velocity waveforms were successfully reproduced at KMMH16 and KMMP58, the 1D simulation analyses were expanded to all 57 sites in Mashiki using the delineated velocity structures at those sites. For these research results, the maximum strain of each site for both LA and ELA simulations were obtained and the ELA maximum strains were always larger than the LA. There were three sites with the ELA maximum strains greater 1% in the EW component, namely MS5-3, MS9-6, and Bunkakaikan. However, the maximum strains of ELA in the NS component were smaller than 1% for all 57 sites. The estimated ground motions for ELA were close to the observed seismic waves on the ground surface at KMMH16 and KMMP58, as mentioned above. Therefore, the nonlinear properties of soil materials and ELA method could be used to analyze the dynamic response of soil layers in Mashiki.

After the site response analysis of 57 sites by the LA and ELA, the peak ground acceleration (PGA) and peak ground velocity (PGV) of every site were obtained. The PGA and PGV distribution maps were shown in Figs. 5.12 and 5.13. In Fig. 5.12, the PGAs in the northern part of the town tend to be larger than those in the southern part. Especially at MS2-3 and MSA19, both EW-PGA and NS-PGA were larger than those of the other areas in the ELA case. In Fig. 5.13, the EW component of the LA results for PGV, the high PGVs were concentrated in the southwestern part and along the Municipal Road No.28. Furthermore, some PGVs in the northern part were a little larger than those in the surrounding areas. In the EW component of the ELA results, the region of large PGV is located along the Road No.28. According to the LA results, there is a small region of PGV concentration area in the northern part as well. The PGV distribution of the NS component of the ELA has a similar distribution as the EW component. However, the absolute values of PGVs in the NS component are much smaller than those in the EW component. The main reason for this difference is that the amplitude of the EW component of the seismological bedrock motion was larger than that of the NS component mainly in the low frequency range. This corresponds to the fact that the EW component of the mainshock was responsible mainly for the heavy building damages at Mashiki, as discussed in the previous study [16]. The estimated PGV of ELA were similar as the previouse results of Sugino et al. [17], while their calculated PGVs were a little larger than my estimations in the building damage belt area, especially in the area near MS5-6 and MSA32.

5.5.2. Results of 592 sites.

Based on the 57 1D subsurface velocity structures, a 30×30 grid along the horizontal plane of each subsurface layer were generated for the target area (each grid representing an area of approximately

47 m × 47 m) by using linear interpolation method for a 3D space [18,19]. Finally, 535 velocity structures of Mashiki were obtained. The upper 8 layers (from ground to the engineering bedrock) were shown in Fig. 5.14.

Then, the site responses of 592 sites by the LA and ELA were analyzed, including the microtremor observation sites and interpolated grid sites. Fig. 5.15 depicts the distribution maps of the estimated PGAs and PGVs according to ELA. Fig. 5.15 has a more detailed spatial resolution of the PGA and PGV distribution in Mashiki, especially for the sites which were not analyzed as shown in Figs. 5.12 and 5.13, Fig. 5.15 showed more accurate results. PGV distribution of the ELA showed close relationship with the building damage distribution from the AIJ survey. Moreover, it provided us with power conditions to calculate the damage probability of every building in Mashiki when the site-specific estimated ground motions during the mainshock were obtained.

5.5.3. Discussion

Comparing these estimated PGA and PGV maps with the distribution of building damage at Mashiki after the mainshock from the literatures, the PGA maps did not correspond so much to the damage distribution, while the PGV maps were quite consistent with the damage distribution of the heavily damaged area. It was also found a few high PGV spots outside the heavily damaged area, for example, in the northeastern area. It might because most houses in this area were newly built ones [20], so most of them were not heavily damaged during the mainshock as there was a large code modification in 1981 that lead to a significant improvement of seismic performance [21]. Thus, these simulated waveforms can be used to explain quantitatively the damage pattern observed at Mashiki during the 2016 Kumamoto earthquake, through a nonlinear dynamic response analysis of structures, which will be calculated in Chapter 8.

It is not surprising to obtain a better correlation of building damage with the PGV, rather than the PGA. In the empirical approach, several reports have compared the correlations of building damages with the observed or inferred PGAs and PGVs in the past earthquakes that occurred in Japan [22,23]. Theoretically, the reason why we need both high PGA and PGV to make buildings collapsed or heavily damaged could be explained by using a concept of ductility and energy demand of a seismically well-designed structure. The high (~0.8 g) PGA was required to make a low or mid-rise building nonlinear since the generated shear-force is proportional to the acceleration multiplied by the weight of the building. If the building is brittle, which means, if it cannot sustain a large deformation, it will be collapsed by the ground motion with high PGA. However, if the building is ductile, which means, if it can deform a large amount in the horizontal direction keeping the restoring shear-force after the maximum level (i.e., the yield level), the plastic flow of deformation starts. The building will survive until the deformation reaches the critical deformation level (approximately 1/10 for a wooden house and 1/30 for steel and reinforced concrete buildings). The maximum response of deformation is

proportional to the energy demand of input, and the energy that the building has to absorb, which is proportional to the PGV (strictly speaking, PGV^2). The high PGV (~100 cm/s) is needed to make buildings collapsed or heavily damaged for well-designed buildings, however, the threshold PGV level will be lower if the regulations are soft or the construction quality is poor. Note that ground motions with high PGV but low PGA would not create heavy damage to low to mid-rise buildings, but may create heavy damage to long-period structures such as high-rise buildings.

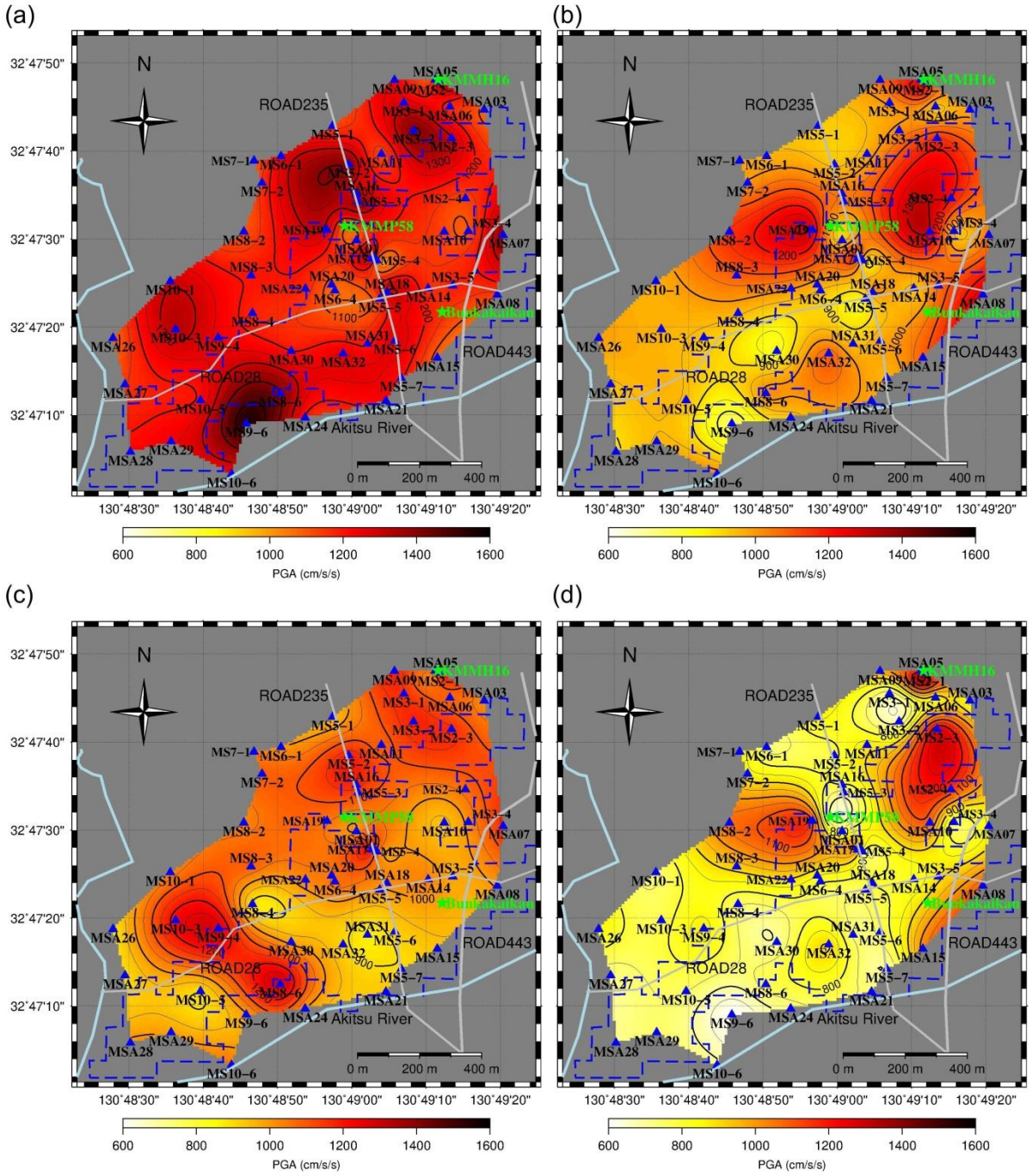

Fig. 5.12. Estimated PGA distribution maps of Mashiki. (a) and (c) are the estimated PGAs of the LA for the EW and NS components, respectively. (b) and (d) are the estimated PGAs of the ELA for the EW and NS component, respectively. In each figure, the triangles denote the microtremor sites, stars denote the strong motion stations. The Akitsu River passes through Mashiki from east to west. There are three main roads (Roads 28, 235, and 443) passing through Mashiki. In these four figures, the unit of PGA is cm/s^2. The dashed lines denote the outlines of the building damage concentration area as shown in Fig. 1.2. The GMT interpolation function is used.

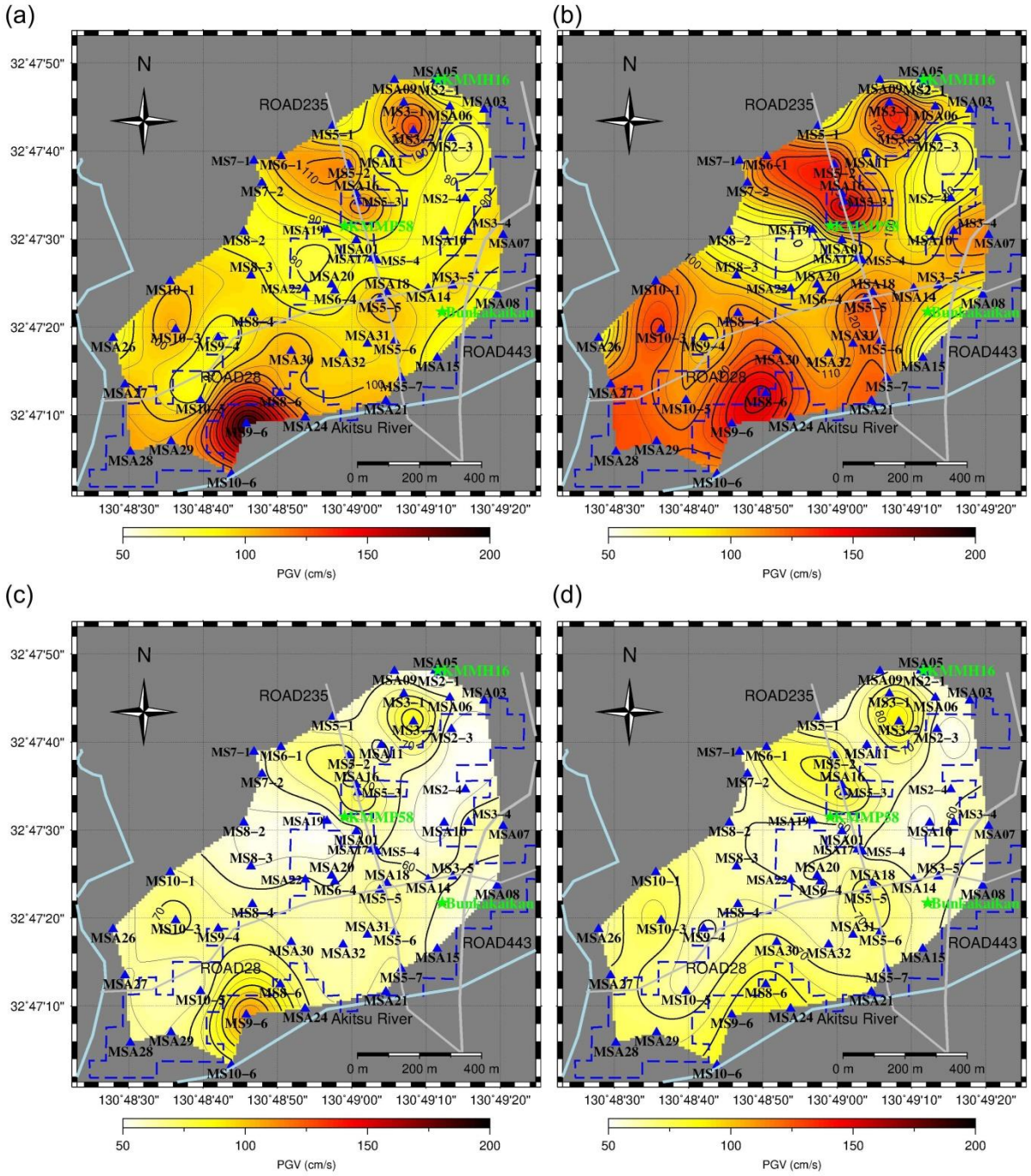

Fig. 5. 13. Estimated PGV distribution maps of Mashiki. (a) and (c) are the estimated PGVs of the LA for the EW and NS components, respectively. (b) and (d) are the estimated PGVs of the ELA of the EW and NS components, respectively. In each figure, triangles denote the microtremor sites, stars denote strong motions stations. In all the figures, the unit of PGV is cm/s. The dashed lines denote the outlines of the building damage concentration area as shown in Fig. 1.2. The GMT interpolation function is used.

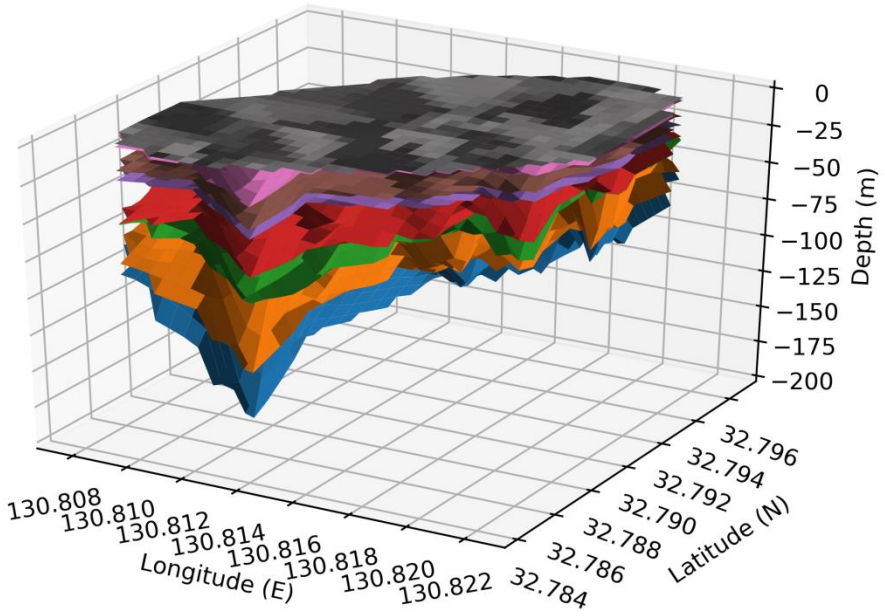

Fig. 5.14. Grid model of the identified velocity structures in the target area. Each colored surface represents the boundary between two subsurface layers. The shading indicates the difference in layer depth (darker means deeper). Each grid has a size of approximately 47 m × 47 m from the top view.

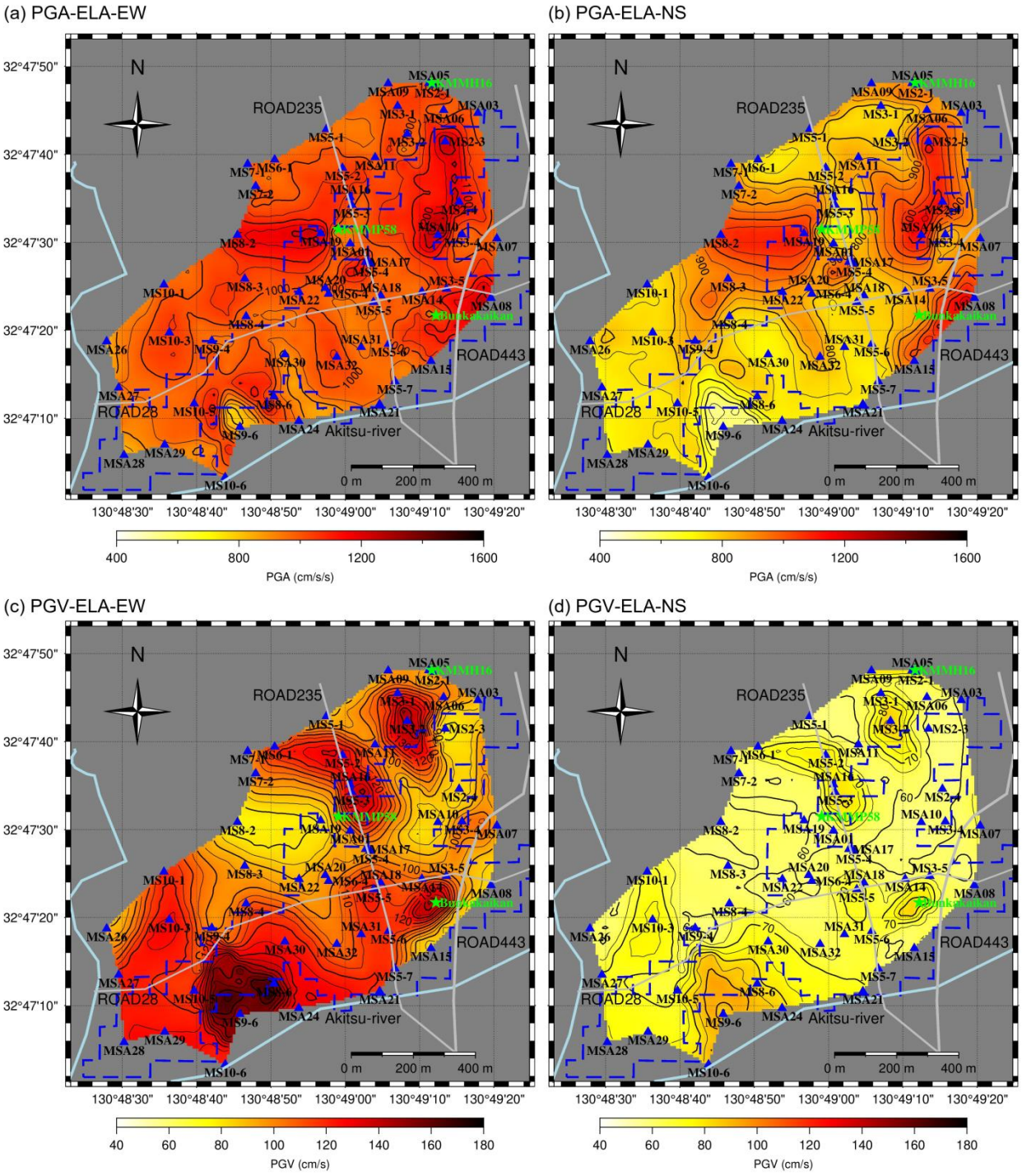

Fig. 5.15. Estimated PGA and PGV distribution maps. PGA distributions for the (a) EW and (b) NS components with the ELA. PGV distributions for the (c) EW and (d) NS components with the ELA. The triangles mark the 57 microtremor observation sites. The stars mark the three strong motion stations. The blue dashed line denotes the boundary of the heavily damaged area shown in Fig. 1.2. GMT5 interpolation function was used.

5.6. Conclusion

LA and ELA method were introduced in this Chapter. Nonlinear soil properties of Site K were explained and new equations to interpolate the necessary soil parameters in ELA were proposed. Moreover, the method to estimate the seismological bedrock motions during the mainshock based of DFT for earthquakes was explained at great length. In addition, 3D interpolated velocity models were obtained based on the 1D identified velocity structures. According to the estimation results of KMMH16, estimated ground motions were similar as the observed ground motions during the mainshock. Also, estimated Fourier spectra and amplification factor were close to the observed ones. Maximum shear strain of the ELA results at most sites were less than 1%, which means the ELA method was suitable for site response in most areas of Mashiki. PGV distributions of both EW and NS by both LA and ELA were related to the AIJ building damage distributions, especially the PGV-EW-ELA results showed close relation with the AIJ field survey results. The estimated PGV-EW-ELA results were also similar to the results of Sugino et al. [17], although their estimated PGVs were a little larger at several sites. Besides, the PGA distributions did not show close correlation to the AIJ building damage distribution. Thus, the PGV is an important factor to evaluate the building damage in Mashiki.

Reference (Chapter 5)

[1] Schnabel PB, Lysmer J, Seed B. A COMPUTER PROGRAM FOR EARTHQUAKE RESPONSE ANALYSIS OF HORIZONTALLY LAYERED SITES. 1972.

[2] Yoshida N. DYNEQ - A computer program for Dynamic response analysis of level ground by Equivalent Linear Method. 2014.

[3] Yoshida N. Dynamic soil properties and modeling, Istanbul, Turkey: 2001.

[4] Arai H. Influence of ground characteristics in the center of Mashiki-cho on strong ground motion in the 2016 Kumamoto earthquake. BRI-H29 lecture; 2017.

[5] Shingaki Y, Yoshimi M, Goto H, Kurata T, Sato K, Hosoya T, et al. Physical and dynamic properties of the volcanic ash soil in the heavily damaged site of the 2016 Kumamoto earthquake, Mashiki town. Journal of Japan Society of Civil Engineers, Ser A1 (Structural Engineering & Earthquake Engineering (SE/EE)) 2017;73:552–559. https://doi.org/10.2208/jscejseee.73.552.

[6] Nakazawa T, Sakata K, Sato Y, Hoshizumi H, Urabe A, Yoshimi M. Stratigraphy and distribution patttern of volcanogenic sediments beneath downtown Mashiki, Kumamoto, SW Japan, seriously damaged by the 2016 Kumamoto Earthquake. Jour Geol Soc Japan 2018;124:347–359. https://doi.org/10.5575/geosoc.2017.0077.

[7] Fredlund DG, Xing A. Equations for the soil-water characteristic curve. Canadian Geotechnical Journal 1994;31:521–532. https://doi.org/10.1139/t94-061.

[8] Senetakis K, Anastasiadis A, Pitilakis K. Normalized shear modulus reduction and damping ratio curves of quartz sand and rhyolitic crushed rock. Soils and Foundations 2013;53:879–893. https://doi.org/10.1016/j.sandf.2013.10.007.

[9] Levenberg K. A method for the solution of certain non-linear problems in least squares. Quarterly of Applied Mathematics 1944:164–168. https://doi.org/10.1090/qam/10666.

[10] Marquardt DW. An Algorithm for Least-Squares Estimation of Nonlinear Parameters. Journal of the Society for Industrial and Applied Mathematics 1963;11:431–441. https://doi.org/10.1137/0111030.

[11] Imazu M, Fukutake K. A Study on Data Processing of Dynamic Deformation Properties. The 21st Geotechnical Engineering Conference of Japan 1986:603–604.

[12] Nagashima F, Kawase H, Matsushima S. Estimation of horizontal seismic bedrock motion from vertical surface motion based on Horizontal-to-Certical Spectral ratios of earthquake motions, Santiago Chile: 2017.

[13] Nagashima F, Kawase H. Estimation of the incident spectrum at the seismic bedrock by using the observed vertical motion at the ground surface based on diffuse field theory, Proceedings of the 15th Japan Earthquake Engineering Symposium; 2018.

[14] Yoshida K, Miyakoshi K, Somei K, Irikura K. Source process of the 2016 Kumamoto earthquake (Mj7.3) inferred from kinematic inversion of strong-motion records. Earth, Planets and Space 2017;69. https://doi.org/10.1186/s40623-017-0649-8.

[15] Nagashima F, Matsushima S, Kawase H, Sanchez-Sesma FJ, Hayakawa T, Satoh T, et al. Application of Horizontal-to-Vertical Spectral Ratios of Earthquake Ground Motions to Identify Subsurface Structures at and around the K-NET Site in Tohoku, Japan. Bulletin of the Seismological Society of America 2014;104:2288–2302. https://doi.org/10.1785/0120130219.

[16] Kawase H, Matsushima S, Nagashima F, Baoyintu, Nakano K. The cause of heavy damage concentration in downtown Mashiki inferred from observed data and field survey of the 2016 Kumamoto earthquake. Earth, Planets and Space 2017;69:3. https://doi.org/10.1186/s40623-016-0591-1.

[17] Sugino M, Yamamuro R, Kobayashi S, Murase S, Ohmura S, Hayashi Y. Analyses of Building Damages in Mashiki Town in the 2016 Kumamoto Earthquake. Journal of Japan Association for Earthquake Engineering 2016;16:10_69-10_83. https://doi.org/10.5610/jaee.16.10_69.

[18] Virtanen P, Gommers R, Oliphant TE, Haberland M, Reddy T, Cournapeau D, et al. SciPy 1.0: fundamental algorithms for scientific computing in Python. Nature Methods 2020;17:261–72. https://doi.org/10.1038/s41592-019-0686-2.

[19] Barber CB, Dobkin DP, Huhdanpaa H. The quickhull algorithm for convex hulls. ACM Trans Math Softw 1996;22:469–483. https://doi.org/10.1145/235815.235821.

[20] Yamada M, Ohmura J, Goto H. Wooden building damage analysis in Mashiki town for the 2016 Kumamoto earthquakes on April 14 and 16. Earthquake Spectra 2017;33:1555–1572. https://doi.org/10.1193/090816EQS144M.

[21] Nagato K, Kawase H. Damage evaluation models of reinforced concrete buildings based on the damage statistics and simulated strong motions during the 1995 Hyogo-ken Nanbu earthquake. Earthquake Engineering & Structural Dynamics 2004;33:755–774. https://doi.org/10.1002/eqe.376.

[22] Yamaguchi N, Yamazaki F. Estimation of strong motion distribution in the 1995 Kobe earthquake based on building damage data. Earthquake Engineering & Structural Dynamics 2001;30:787–801. https://doi.org/10.1002/eqe.33.

[23] Wu H, Masaki K, Irikura K, Kurahashi S. Empirical Fragility Curves of Buildings in Northern Miyagi Prefecture During the 2011 off the Pacific Coast of Tohoku Earthquake. Journal of Disaster Research 2016;11:1253–70. https://doi.org/10.20965/jdr.2016.p1253.

Chapter 6

Nonlinear analyses of subsurface velocity structures in Mashiki

6.1. Introduction

6.2. Theory of the Fukutake model

6.2.1. Hyperbolic model and its parameters

6.2.2. Bowl model and its parameters

6.3. Nonlinear response analysis of 592 sites in Mashiki

6.3.1. Water table depth of Mashiki

6.3.2. Estimated seismic motions at engineering bedrock

6.3.3. Nonlinear analysis of soil column at KMMH16

6.3.4. Nonlinear analysis of soil column at KMMP58

6.3.5. Nonlinear analysis of soil column at MSA32

6.3.6. Nonlinear analysis of soil column at MS9-6

6.3.7. PGA and PGV distribution of Mashiki based on the NA

6.4. Conclusion

Reference (Chapter 6)

6.1. Introduction

After the mainshock, Kurita [1] did the nonlinear analysis at the KiK-net KMMH16 based on the borehole data. Nakano et al. [2] studied the soil-structure interaction response at Mashiki Townhall during the mainshock. Kagami et al. [3] and Yasuhara et al. [4] discussed the shallow subsurface soil properties in Mashiki. Some researchers [5,6] studied the soil liquefaction sites caused by the mainshock. However, they did not study the effects of soil liquefaction to the ground motions in Mashiki during the mainshock. In this section, the author would like to introduce the site response of soil deposit derived from nonlinear analysis (NA) by inputting three-component waveforms, and considering the effects of soil liquefactions. The soil liquefaction sites in Mashiki would be simulated in the process.

There are various constitutive modeling equations used for dynamic analysis. Some researchers have performed different kinds of dynamic analysis to simulate the experimental simulations by using different constitutive equations of soil [7–9]. The constitutive equations are more effective than the basic equations and equations of numerical analysis method. The stress−strain relationship is reflected as the restoring force characteristic in the Newtonian equation of motion. Thus, the constitutive equations to explain the complex behavior of soil are quite important to analyze the soil accurately, while the constitutive equations are formulated based on some approximations [10].

Fig. 6.1 shows the classification of constitutive equations used for the nonlinear dynamic analysis in various approaches. Among them, (1) cannot be applied to the effective stress analysis; (8) is not a macroscopic equation, but it is a method of expressing the soil particles with rigid bodies, springs, dashpots, and sliders, etc. There were some examples of application to liquefaction analysis [11]; (2) expresses the relationship of stress−strain using linear springs and slip elements, which is also called the Iwan model. Some problems are known for using this model for the nonlinear analysis, such as correspondence with ground physical properties, and some studies on dynamic effective stress analysis of the soil deposit were also analyzed by this method [12]. (3) is a model focusing on the hysteresis function of shear strain and shear stress. It was widely used for nonlinear seismic response analysis of the subsurface stratified layers. This model is a relatively simple one-dimensional (1D) constitutive equation consisting of the bone curve and hysteresis curve using the Massing law. It also can accurately express the nonlinearity of soil to some extent. For example, the Ramberg−Osgood model (RO model) formulated by exponential function [13–15], and the hyperbolic model formulated by hyperbolic function (the Hardin−Drnevich model) [16]. This kind of models are simple and easy to use, especially the RO model has good simulation results of seismic observation records [17,18]. In Chapter 5, the ELA by using the RO model was introduced. The soil nonlinear property of each layer was obtained by the tri-axis experiment. However, this model does not consider the soil dilatancy. Therefore, if we want to evaluate the dilatancy and pore water pressure, another model would be

applied together with this model. Effective stress analysis also could be used by applying the function of effective stress [10].

(2) and (3) models generally defines the relationship between shear stress and shear strain, while the dilatancy (excess pore water pressure) is not considered. Thus, it was necessary to add a new model to analyze the dilatancy, such as model (4), to evaluate the dilatancy of soil. Because the dilatancy is converted to excess pore water pressure under the non-drainage conditions, it is also called the excess pore water pressure model. In this model, the dilatancy is calculated, and the effective stress and excess pore water pressure are calculated under the non-drainage conditions. The effective stress and excess pore water pressure can be directly obtained. Therefore, the soil nonlinear behavior can be exactly calculated by combining the dilatancy model and the hysteresis model. Many models of this type are based on empirical formulas and empirical formulas. Although formulas vary depending on different models, they are relatively easy to use. Such as the stress path model proposed by Kenji and Ikuo [19], strain space multishear mechanism model [20,21], and Martin-Finn-Seed model [22]. (5) is the model of elastoplastic theory. A wide variety of theoretical developments have been made on the concepts developed for metallic materials such as the yield function, plastic potential, hardening function, etc., this kind of model is somewhat complicated. Model (6) is based on the Endocbronic theory. This theory was originally based on metallic materials and thermodynamics. It has been modified when applied to the soil materials. It is a method to determine the relationship between strain and stress by the physical quantity accumulated inside, without specifying the yield function. The typical models are Tanaka model [23] and Densification model [24]. (7) is the granular theory model. The origin of soil is made of an aggregate of particles that obeying the friction law. Then, granule theory was used to derive the constitutive equation [25,26]. In the theory, the relationship between stress and particle structure and the relationship between strain and particle structure are obtained, and in many cases, the method was used to derive the stress－strain－dilatancy relationship based on the particle structure. Then, the physical mechanism is clear. The theory of Matsuoka and Nakai [25] was a typical theory of it. This theory considered not only the shear behavior but also the anisotropic consolidation behavior, and uniformly explains the deformation characteristics of soil under arbitrary stress paths, including the rotation of the principal stress [27]. Furthermore, the repeated shear behavior was explained by Matsuoka by focusing on the deviation of the particle contact angle distribution [28]. They also constructed the Compounded Mobilized Plane (CMP) theory and the 3D Space Mobilized Plane (SMP) theory to extend the two-dimensional constitutive equation to three-dimensional conditions [29,30]. Fukutake modified their model and applied to two-dimensional and three-dimensional liquefaction analysis [10,31].

In this chapter, the results on the nonlinear analysis by using the soil model of Fukutake will be presented, the Bowl model (“Owan model” in Japanese) together with the hysteresis model. In the theory of Fukutake model, the Bowl model is used to analyze the dilatancy, and work together with the hysteresis model to conduct the nonlinear analysis.

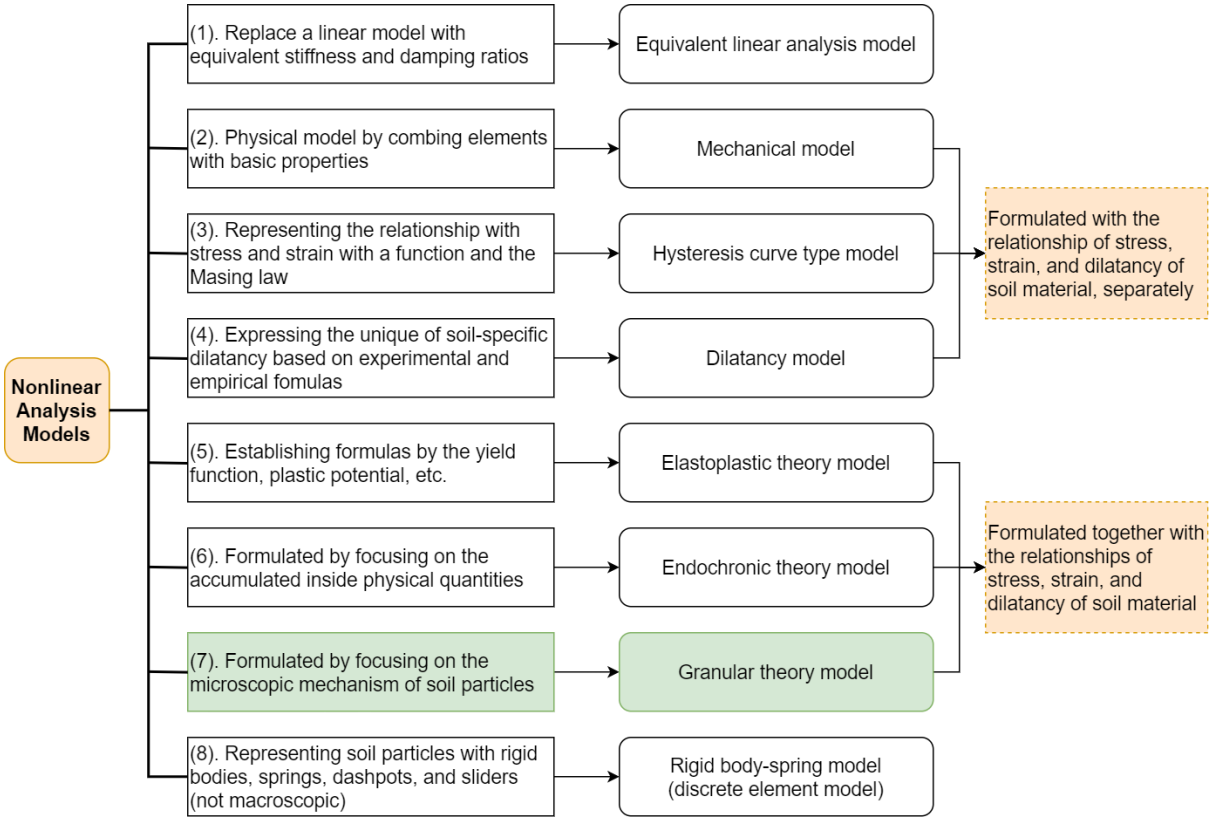

Fig. 6.1. Nonlinear analysis model of soil dynamic analysis [10]**.**

6.2. Theory of the Fukutake model

In the theory of Fukutake model, a hyperbolic model extending in three dimensions is used for the stress−strain−dilatancy relationship and is modeled as a Bowl function, i.e. a function that looks like a bowl. The hyperbolic stress−strain model parameters, G/G_{max}–γ and h–γ relationships, are determined from the dynamic deformation tests, as discussed in Chapter 5. The Bowl model parameters are determined from liquefaction resistance tests, which is obtained from the relationship between the stress ratio and cycle number [10,32].

6.2.1. Hyperbolic model and its parameters

The three dimensional stress used in the Fukutake model is shown in Fig. 6.1. In multi-dimensionalizing the hyperbolic model, the shear stress versus shear strain relationships for the shear component and the axial difference component, respectively, are defined by the following equations (Eqs. (6.1) and (6.2)).

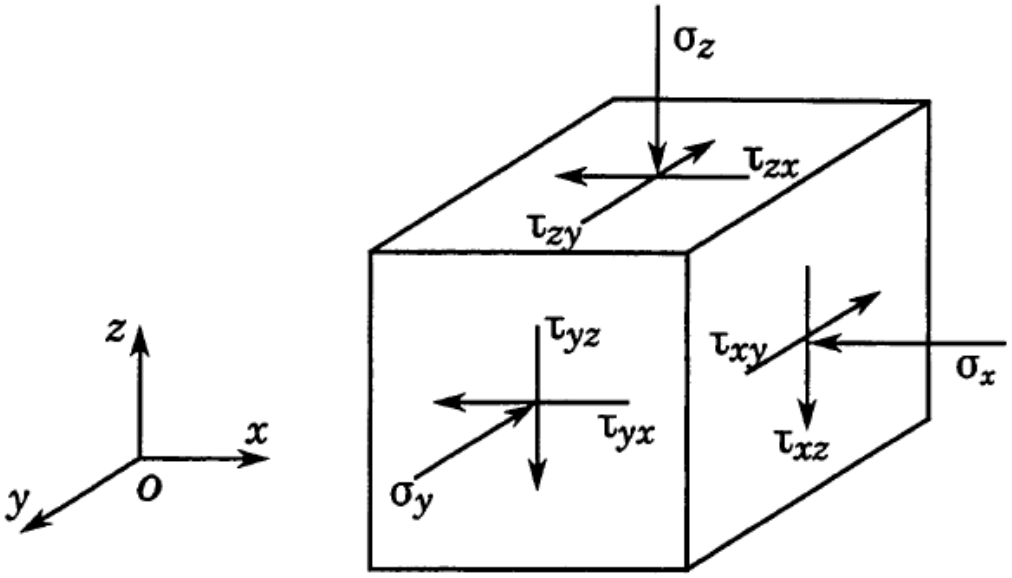

Fig. 6.1. Stress of three dimensional components in the Fukutake model [10]**.**

$$\tau_{xy} = \frac{G_{max} \times \gamma_{xy}}{1+\frac{\gamma_{xy}}{\gamma_r}}, \quad \tau_{xy} = \frac{G_{max} \times \gamma_{xy}}{1+\frac{\gamma_{xy}}{\gamma_r}}, \quad \tau_{xy} = \frac{G_{max} \times \gamma_{xy}}{1+\frac{\gamma_{xy}}{\gamma_r}} \tag{6.1}$$

$$\frac{\sigma_x-\sigma_y}{2} = \frac{G_{max} \cdot (\varepsilon_x-\varepsilon_y)}{1+\frac{(\varepsilon_x-\varepsilon_y)}{\gamma_r}}, \frac{\sigma_y-\sigma_z}{2} = \frac{G_{max} \cdot (\varepsilon_y-\varepsilon_z)}{1+\frac{(\varepsilon_y-\varepsilon_z)}{\gamma_r}}, \frac{\sigma_z-\sigma_x}{2} = \frac{G_{max} \cdot (\varepsilon_z-\varepsilon_x)}{1+\frac{(\varepsilon_z-\varepsilon_x)}{\gamma_r}} \tag{6.2}$$

where, G_{max} is the initial shear modulus, and γ_r is the reference strain. γ_r is obtained from the shear strength τ_f by the Eq. (6.3). The h–γ relationship was obtained by Eq. (6.4).

$$\gamma_r = \frac{\tau_f}{G_{max}} \tag{6.3}$$

$$h = h_{max} \cdot (1 - \frac{G}{G_{max}}) \tag{6.4}$$

where, h is the hysteretic damping parameter, h_{max} is the maximum damping ratio and G is the shear modulus.

There are three important parameters that are required to construct in the hyperbolic model, the G_{max}, h_{max}, and γ_r. G_{max} and h_{max} are functions of the effective stress. If we set the G_{max} and h_{max} at a certain reference effective stress (σ'_{mi}) are G_{maxi} and h_{maxi} , the the G_{max} and h_{max} can be obtained by Eq. (6.5).

$$G_{max} = G_{maxi}(\frac{\sigma'_m}{\sigma'_{mi}})^{0.5}, \ \gamma_r = \gamma_{ri}(\frac{\sigma'_m}{\sigma'_{mi}})^{0.5} \tag{6.5}$$

At every step, since the effective stress varies, these parameters are calculated over time from Eq. (6.5). At the same time, the relationship in Eq. (6.1) and (6.2) varies with time in accordance with the effective stress.

Applying the Masing rule to the hyperbolic model will result in excessive hysteretic damping. The hysteretic damping (h) is adjusted using the method of Ishihara et al [20].

Meaning of three parameters of the hyperbolic model was shown in Table 6.1 and Fig. 6.2. The G_{max} and h_{max} depend on the effective stress. The formulations of G_{maxi} and h_{maxi} are used when the mean effective stress σ'_m equals 1.0 kN/m^2. These parameters can be simply determined from the stiffness reduction curve (G/G_{max}–γ) and the damping increase curve (h–γ), obtained from the dynamic deformation tests.

Table. 6.1. Parameters of the hyperbolic model [32]**.**

Parameters	Physical meaning
G_{max}	Initial shear modulus. $G_{max} = \rho V_s^2$
h_{max}	Maximum damping ratio. As h_{max} increases the non-linearity becomes stronger
γ_r	Reference strain. $\gamma_r = \frac{\tau_f}{G_0}$ The shear strain when $\frac{G}{G_{max}} = 0.5$

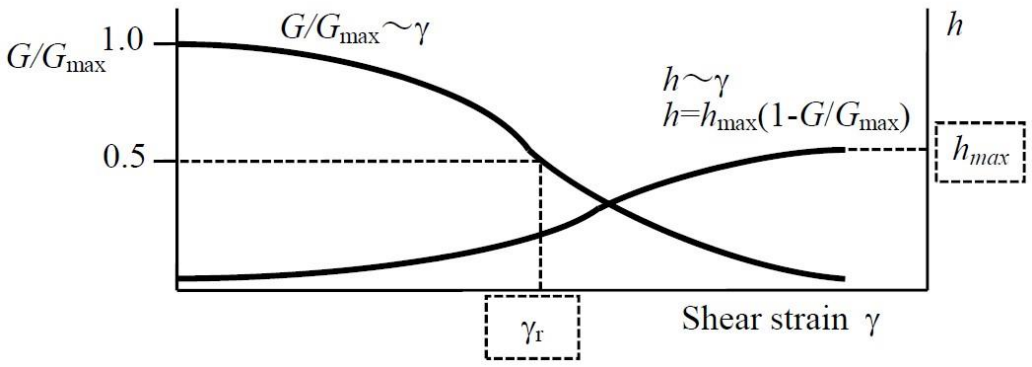

Fig. 6.2. Parameters of the hyperbolic model [10,32]**.**

6.2.2. Bowl model and its parameters

In order to model the deformation of soil in three dimensions, not only the equations for the shear strains representing the simple shearing deformation (γ_{xy}, γ_{yz}, γ_{zx}) and the axial shear strain differentials representing axial deformation differential (ε_x-ε_y, ε_y-ε_z, ε_z-ε_x), but also the equations for the

resultant shear strain (Γ) and cumulative shear strain (G^*) were needed, as shown in Eqs. (6.6) and (6.7).

$$\Gamma = \sqrt{\gamma_{zx}^2 + \gamma_{zy}^2 + \gamma_{xy}^2 + (\varepsilon_x - \varepsilon_y)^2 + (\varepsilon_y - \varepsilon_z)^2 + (\varepsilon_z - \varepsilon_x)^2} \quad (6.6)$$

$$G^* = \sum \Delta G^* = \sum \sqrt{\Delta\gamma_{zx}^2 + \Delta\gamma_{zy}^2 + \Delta\gamma_{xy}^2 + \Delta(\varepsilon_x - \varepsilon_y)^2 + \Delta(\varepsilon_y - \varepsilon_z)^2 + \Delta(\varepsilon_z - \varepsilon_x)^2} \quad (6.7)$$

The Bowl model focused on the resultant shear strain Γ and the cumulative shear strain G^*. Dilatancy (ε_v^S) results a certain soil particle repeatedly dropping into the valley between other soil particles (appears the negative dilatancy), and rising up on other soil particles (appears the positive dilatancy). This mechanism is represented by the superposition of the positive and negative dilatancy using Eq. (6.8).

$$\varepsilon_v^S = \varepsilon_\Gamma + \varepsilon_G = A \cdot \Gamma^{1.4} + \frac{G^*}{C + D \cdot G^*} \quad (6.8)$$

Where, A, C and D are parameters of the Bowl model. ε_G is the monotonic negative dilatancy (compressive strain). It is irreversible and represented as a hyperbolic function with respect to G^*. ε_Γ is the cyclic positive dilatancy (also called the swelling strain), and is reversible and represented as an exponential function with respect to Γ. The ε_G is the master curve and is the component that determines the basic dilatancy during cyclic shearing, while the ε_Γ component is an oscillating component associated with that. 1/D is the asymptotic line to the hyperbolic curve, corresponding to a relative density of 100%. The mechanism of the Bowl model is the movement of the soil particles in seven dimensional strain space with γ_{xy}, γ_{yz}, γ_{zx}, ε_x-ε_y, ε_y-ε_z, ε_z-ε_x, and ε_v^S as the axes. The case of unidirectional cyclic shearing model was illustrated in Fig. 6.3.

The consolidation term is taken into account in the stress−strain relationship, and the effective stress is modeled under the undrained condition (constant volume). The volumetric strain ε_v^S represented in Eq. (6.8) is the dilatancy component due to shearing, while an additional volumetric strain due to the variation in effective stress σ_m' has to be considered. The total volumetric strain increment of the soil $d\varepsilon_v$ is given by Eq. (6.9).

$$d\varepsilon_v = d\varepsilon_v^s + d\varepsilon_v^c \quad (6.9)$$

where, $d\varepsilon_v^s$ denote the shear component, and $d\varepsilon_v^c$ denote the consolidation component.

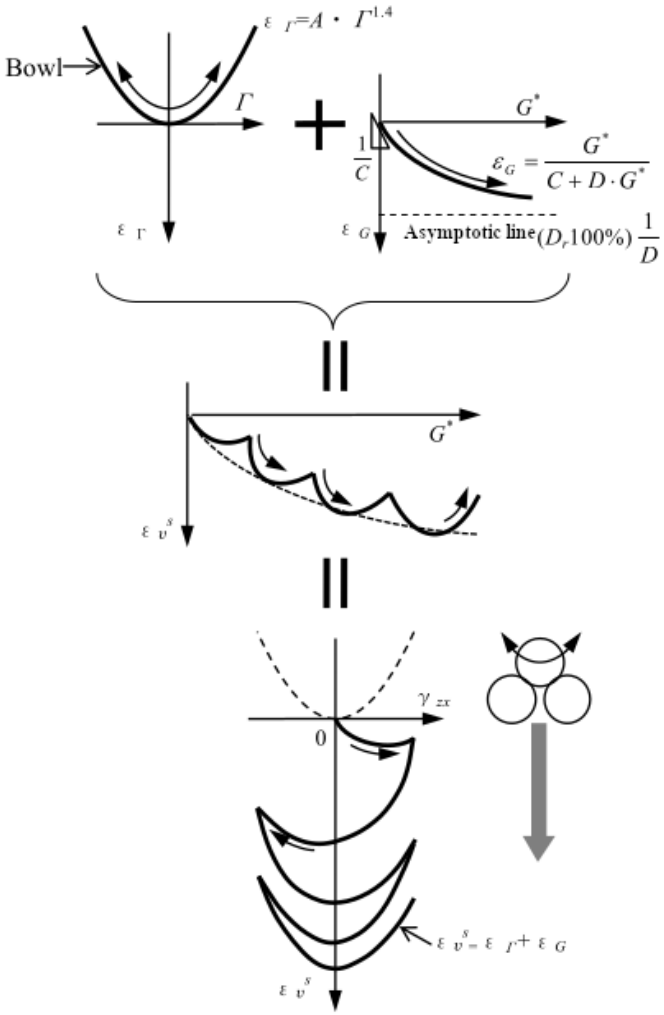

Fig. 6.3. Dilatancy in unidirectional cyclic shearing.

Eq. (6.10) is used to calculate the consolidation component $d\varepsilon_v^c$, assuming the 1D consolidation condition.

$$\begin{cases} d\varepsilon_v^c = \frac{0.434 \cdot C_s}{1+e_0} \cdot \frac{d\sigma_m'}{\sigma_m'}, & (for\ d\sigma_m' < 0) \\ d\varepsilon_v^c = \frac{0.434 \cdot C_c}{1+e_0} \cdot \frac{d\sigma_m'}{\sigma_m'}, & (for\ d\sigma_m' > 0) \end{cases} \tag{6.10}$$

where, C_s is the swelling index, C_c denotes the compression index, e_0 denote the initial void ratio of soil material. Under the undrained condition, the Eq. (6.11) could be obtained based on Eq. (6.10).

$$d\varepsilon_v^s + \frac{0.434 \cdot C_s}{1+e_0} \cdot \frac{d\sigma_m'}{\sigma_m'} = 0 \tag{6.11}$$

If the mean effective stress in the initial shearing stage equals σ'_{m0}, and if Eq. (6.11) is integrated under the condition: $\sigma'_m = \sigma'_{m0}$, the Eq. (6.12) could be obtained.

$$\varepsilon_v^s + \frac{C_s}{1+e_0} \cdot log \frac{\sigma'_m}{\sigma'_{m0}} = 0 \tag{6.12}$$

In Eq. (6.12), the effective stress under undrained shear σ'_m is given by Eq. (6.13).

$$\sigma'_m = \sigma'_{m0} \cdot 10^{\alpha}, \quad \alpha \equiv \frac{-\varepsilon_v^s}{\frac{C_s}{(1+e_0)}} \tag{6.13}$$

Substituting α frome Eq. (6.13), the effective stress reduction ratio is calculated by Eq. (6.14).

$$\left(\frac{\sigma'_{m0}-\sigma'_m}{\sigma'_{m0}}\right) = 1 - 10^{\alpha} \tag{6.14}$$

In order to suppress the occurrence of dilatancy under the small shear amplitude, a spherical region with the shear strain radius $\Gamma = R_e$ is considered in the strain space, in this region, there is no $d\varepsilon_G$. R_e is calculated by Eq. (6.15).

$$R_e = \frac{X_l \sigma'_{m0}}{G_{max} - \frac{X_l \sigma'_{m0}}{\gamma_r}} \tag{6.15}$$

where, σ'_{m0} denotes the mean effective stress in the initial shear. The positive excess pore water pressure does note increase when the amplitude of the stress ratio equals or less than X_l (the lower limit of liquefaction resistance). Fig. 6.4 presents the physical meaning of X_l and R_e.

Fig. 6.4(a) showed the liquefaction resistance curve and the relationship between liquefaction resistance of the lower limit value X_l. X_l is the liquefaction resistance after a lot of cycles. For simplicity, Fukutake assumed that the excess pore water pressure does not arise ($P_w = 0$) for repeated stress ratios less than the X_l.

Six important parameters of the Bowl model is listed in Table 6.2. These parameters were determined by fitting to the liquefaction resistance curves. Fig. 6.5 shows the physical meaning of them.

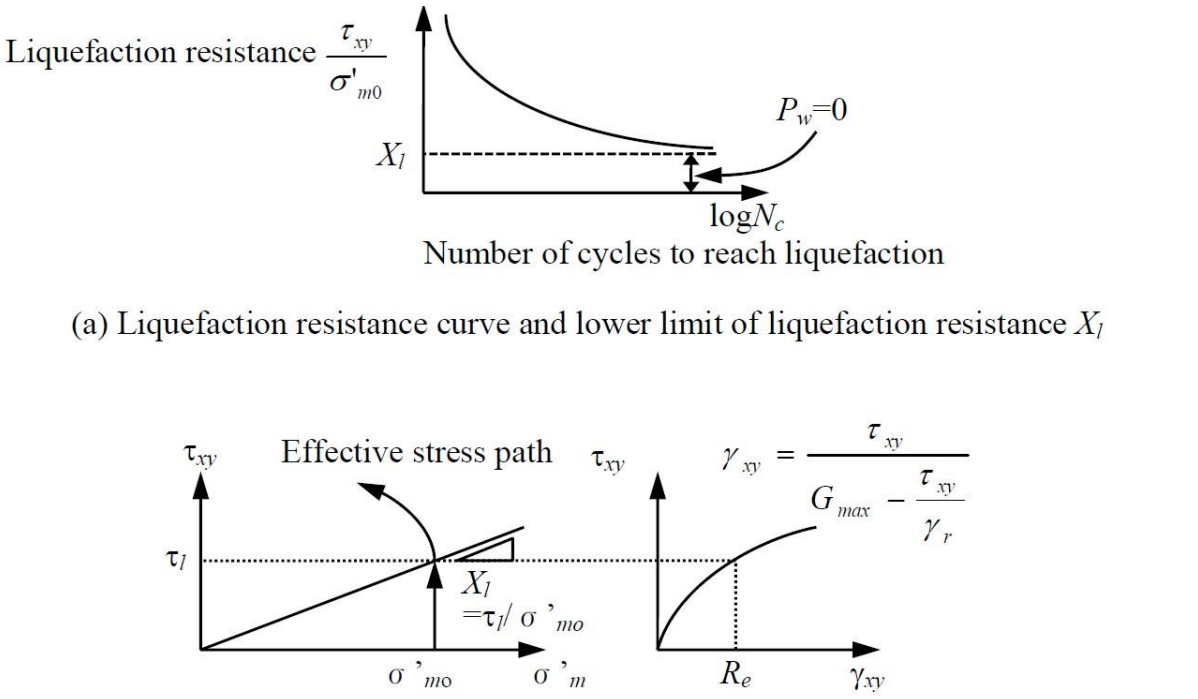

Fig. 6.4. Physical meaning of the lower limit of liquefaction resistance X_l and shear strain R_e [32].

Table. 6.2. Physical meaning of six important parameters in the Bowl model.

Parameter	Physical meaning of parameters
A	Parameter representing the swelling component ε_Γ of the dilatancy components. The larger the absolute value of A the greater the cyclic mobility.
C, D	Parameters representing the compression component ε_G of the dilatancy components. 1/C is the slope of the dilatancy in the initial stage of shear. 1/D is calculated from the minimum void ratio emin on the hyperbolic asymtotic line (maximum amount of compression).
$C_s/(1+e_0)$	C_s is the swelling index; e_0 is the initial void ratio.
$C_c/(1+e_0)$	C_c is the compression index; e_0 is the initial void ratio.
X_l	The lower limit value of the liquefaction resistance. In the relationship between stress ratio τ/σ'_{m0} and the number of cycles N_c, it is represented by τ/σ'_{m0} when N_c is sufficiently large. It appears power water pressure when $\frac{\tau}{\sigma'_{m0}} > X_l$.

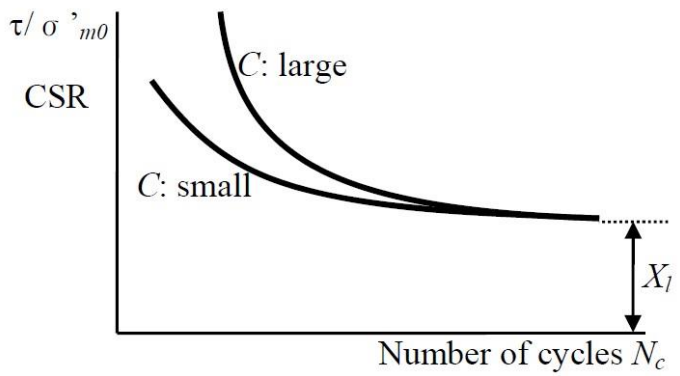

Fig. 6.5. Liquefaction resistance curves and the parameters of Bowl model.

6.3. Nonlinear response analysis of 592 sites in Mashiki

The software “SoilPlus” [33]was used to conduct nonlinear analysis of Mashiki subsurface layers. This software included the analysis program of RO model and Bowl model. For the RO model, it provides a curve fitting program to find the parameters which would be used in the RO model. In the Bowl model, the SoilPlus provides a program to study the important parameters which would be used in the Bowl model when performing the nonlinear analysis. Before the nonlinear analysis, the Rayleigh damping of every site is required. The workflow of nonlinear analysis for the Mashiki sites is shown in Fig. 6.6.

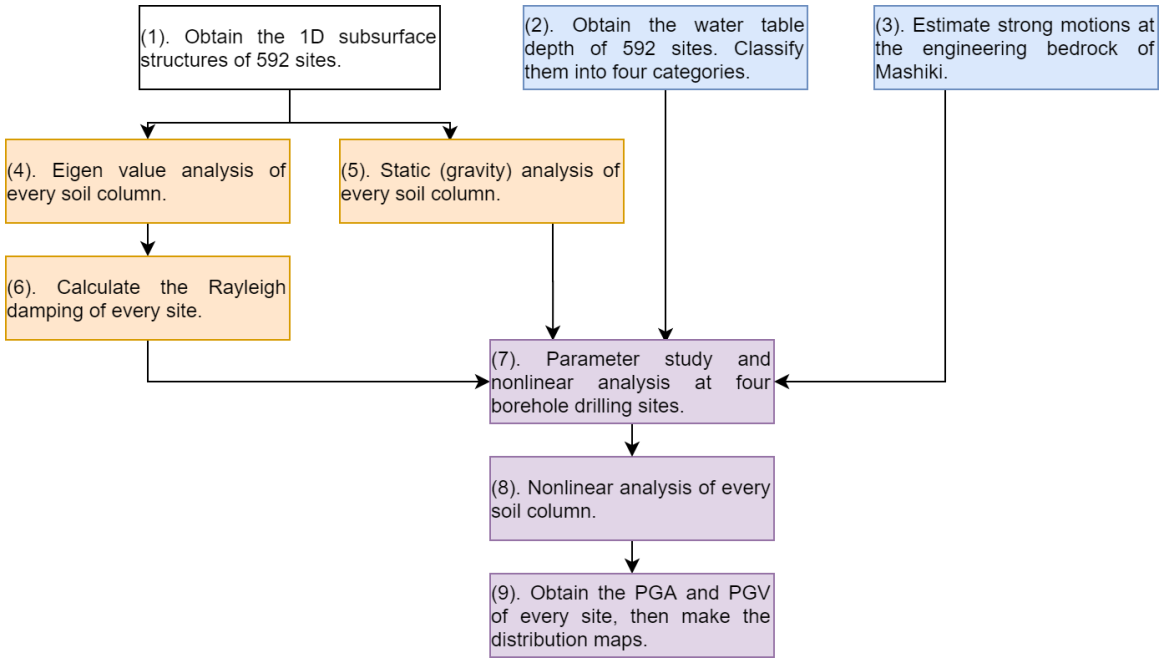

Fig. 6.6. Workflow of the nonlinear analysis for 592 sites at Mashiki.

In Chapter 5, the estimated motions of seismological bedrock during the mainshock at KMMH16 were used, which were obtained by Nagashima and Kawase [34]. These estimated motions were also applied for the nonlinear analysis. Since the tri-axis experimental data of the G/G_{max}–γ and h–γ relationships at four borehole drilling sites in Mashiki are available [35], the 592 1D subsurface structure sites were classified into four categories.

6.3.1. Water table depth of Mashiki

After the mainshock of the 2016 Kumamoto earthquake, researchers conducted borehole drilling in Mashiki, to study the soil materials of subsurface layers [35,36]. In this process, they published the water table depth of several sites, as listed in Table 6.3, the site names were referred to previous researches in Mashiki [4,36–38]. Akiba et al. [38] published the elevation of water table at Mashiki, then this results were inputted into the GIS system, as shown in Fig. 6.7. The elevations of ground surface in Mashiki were also obtained from the GSI (see Data and Resources), as shown in Fig. 6.8. The ground elevation map showed the ground surface is higher in the northeast and lower in the southwest. Also, ground elevation is usually low at the near river sites.

The water table depth can be obtained from the ground elevation minus the water table elevation, and the results are shown in Fig. 6.9. In Fig. 6.9, the water table depth is revised at several sites. The water depth larger than 14 m is corrected to be 14 m, and water depth less than 1 m is corrected to be 1 m. The water depths of five borehole drilling sites are listed in Table 6.3. It is found that the water depth is close to 1.5 m at sites near the river. In the north region of Mashiki, water table depth is larger.

Table. 6.3. Water table depth of five borehole drilling sites in Mashiki [35,36]**.**

Site Name	Longitude	Latitude	Water table depth (m)
Site_K	130.819901	32.796700	14.00
Site_Z	130.823043	32.794773	3.00
Site_M	130.816166	32.788029	1.60
Site_A	130.814234	32.786223	1.00
MSK3	130.808604	32.787203	4.00

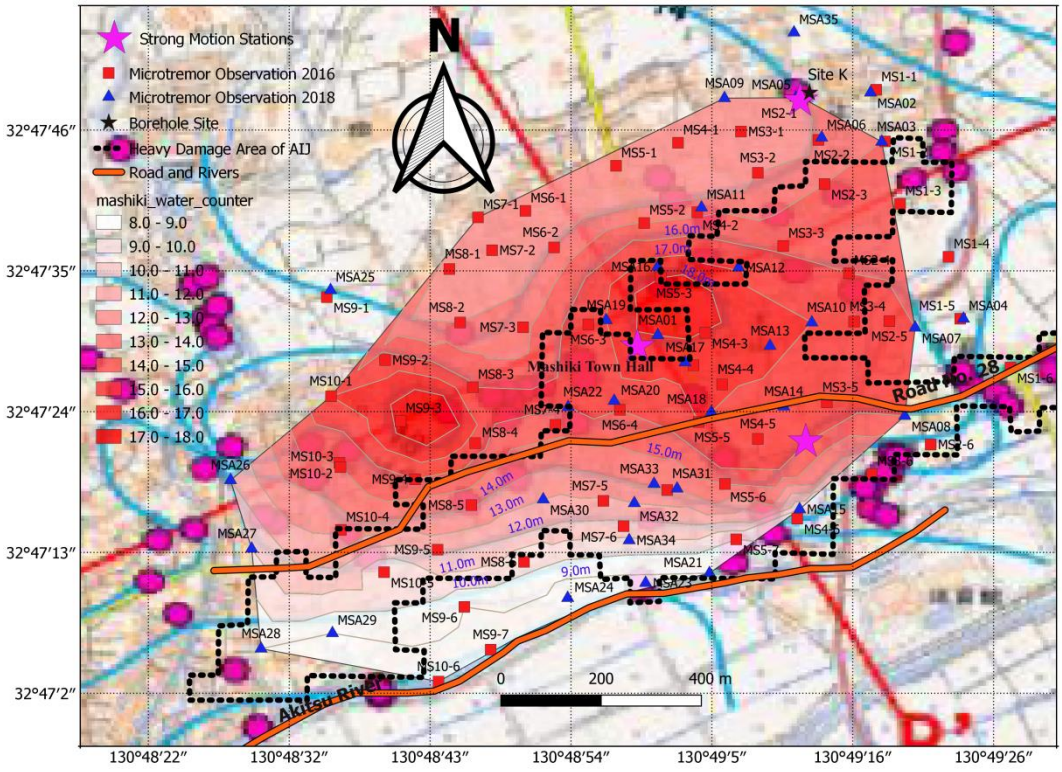

Fig. 6.7. Water table elevation of Mashiki [38]**. We made the contour map based on the previous results.**

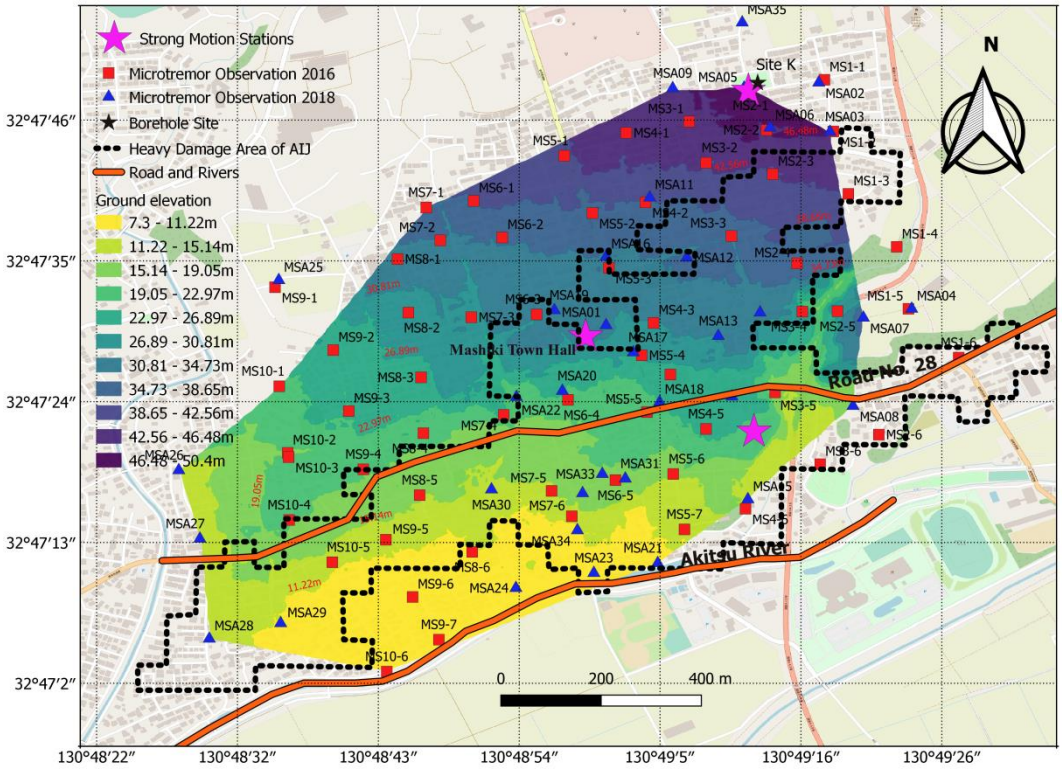

Fig. 6.8. Ground elevation of Mashiki. Original data was obtained from the GSI [39]**.**

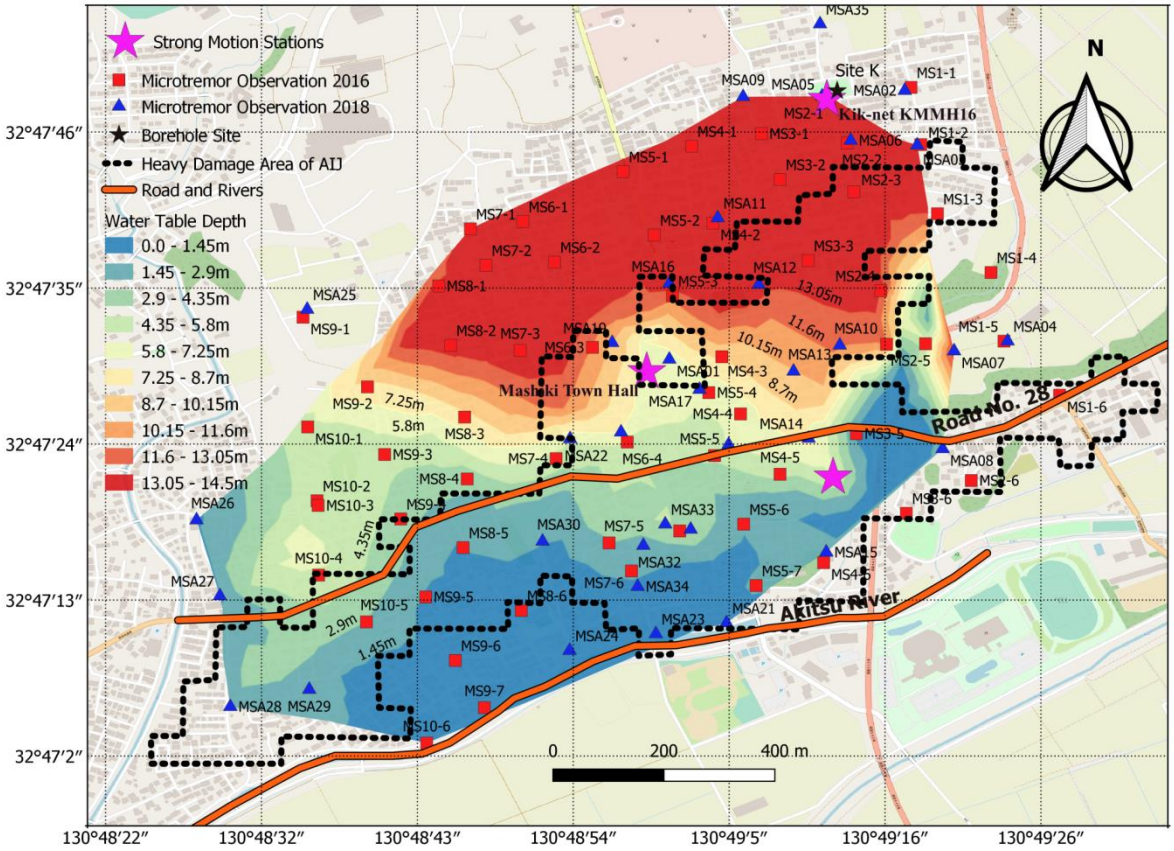

Fig. 6.9. Estimated water table depth of Mashiki.

6.3.2. Estimated seismic motions at engineering bedrock

The estimated seismic motions of three components (EW, NS, and UD) at the seismological bedrock (V_s=3400 m/s) of Nagashima and Kawase [33] is used. 1D subsurface velocity structures of Mashiki at 57 points were obtained in Chapter 4. Comparing the identified velocity structures with the borehole drilling data, the eighth layer (V_s=827.70 m/s) is determined as the engineering bedrock of Mashiki. For the layers between the engineering bedrock and seismological bedrock the linear analysis when inputting the estimated seismological bedrock motions at bottom of the model in three components (NS, EW, and UD). A cosine taper on the original estimated seismological bedrock motions was used, comparisons between the original and tapered versions are shown in Fig. 6.10. The accelerations of three panels are the input wave (E) of estimated motions.

In the linear analysis, the damping ratio of every subsurface layer was set to be 1.1% [40–42]. The seismic motions of 2E at the engineering bedrock were estimated using the “DYNEQ” software [43]. Comparison results of the engineering bedrock waves at three directions are shown in Fig. 6.11. Since the thickness of layers from the engineering bedrock to the seismological bedrock were the

same, as mentioned in Chapter 4, the engineering bedrock waves of all the sites in Mashiki were the same.

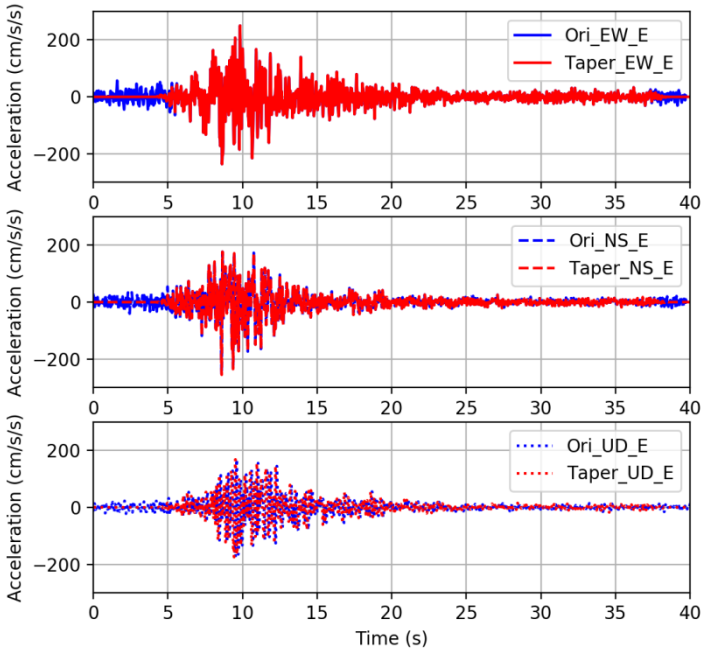

Fig. 6.10. Comparisons of the original and tapered accelerations of estimated seismological bedrock motions at KMMH16. Solid, dashed, and dotted lines denote the result of EW, NS, UD, respectively.

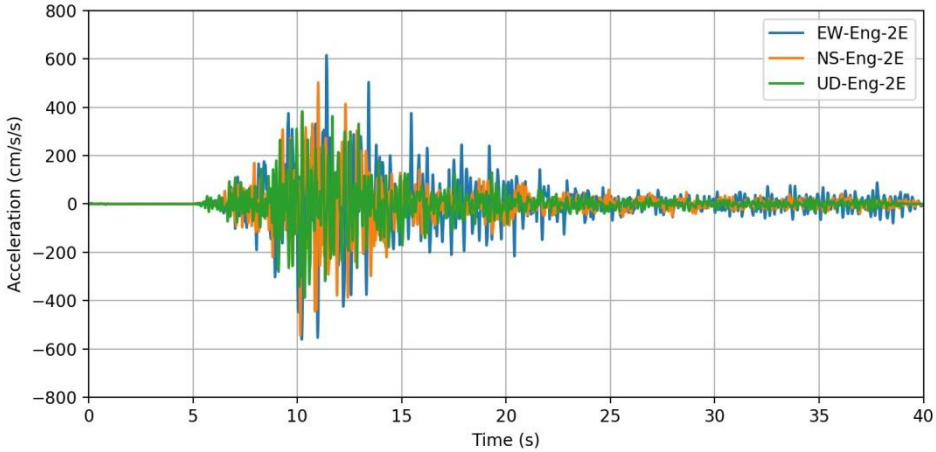

Fig. 6.11. Comparisons of estimated engineering bedrock waves of 2E in Mashiki.

6.3.3. Nonlinear analysis of soil column at KMMH16

First, the eigenvalue analysis of the soil column was carried out at KMMH16, to calculate the Rayleigh damping of the 1D subsurface structure. Eigenvalue analysis result is shown in Table 6.4. Analysis results of Rayleigh damping [44] of KMMH16 are shown in Fig. 6.12. α and β are the coefficient factors of stiffness and mass, Table 6.5 lists the coefficient factors of KMMH16.

Table.6.4. Eigenvalue analysis of KMMH16.

Mode	Frequency (Hz)	Period (s)	Participation factor			Effective mass ratio			Modal damping ratio
			x	y	z	x	y	z	
1	2.01260	0.49690	23.82800	-23.21100	0.00000	0.03180	0.03020	0.00000	0.011
2	2.01260	0.49690	-107.31000	-23.62200	0.00000	0.64510	0.03130	0.00000	0.011
3	2.01260	0.49690	18.61600	-106.46000	0.00000	0.01940	0.63490	0.00000	0.011
4	3.29850	0.30320	0.00000	0.00000	-111.17000	0.00000	0.00000	0.69230	0.011
5	4.06270	0.24610	18.84500	-3.11320	0.00000	0.01990	0.00050	0.00000	0.011
6	4.06270	0.24610	46.87600	9.27650	0.00000	0.12310	0.00480	0.00000	0.011
7	4.06270	0.24610	7.50400	-50.13000	0.00000	0.00320	0.14080	0.00000	0.011
8	6.64820	0.15040	0.00000	0.00000	-50.78300	0.00000	0.00000	0.14450	0.011
9	7.17900	0.13930	-21.50900	1.51710	-0.00009	0.02590	0.00010	0.00000	0.011
10	7.17900	0.13930	-16.95200	-24.31000	-0.00012	0.01610	0.03310	0.00000	0.011

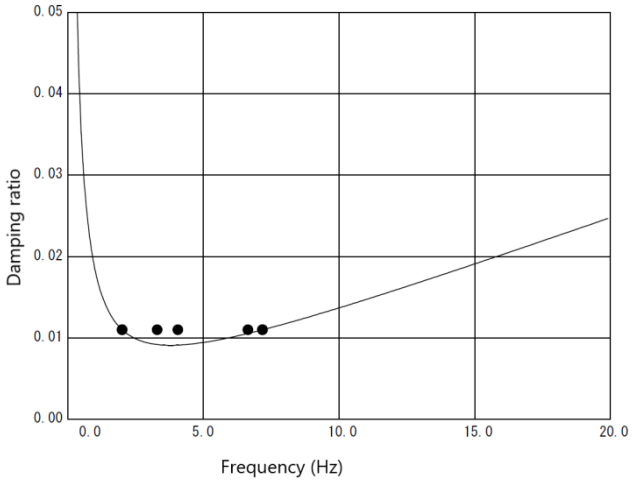

Fig. 6.12. Rayleigh damping calculation of KMMH16.

Table 6.5. Two coefficient factors of KMMH16.

α	3.81E-04
β	2.17E-01

Second, the curve fitting of the tri-axis experimental data of KMMH16 was applied. There were three sets of G/G_{max}–γ and h–γ relationships based on the experiment. Parameter of the RO model is shown in Fig. 6.13. Parameters of Soil 1, 2, and 3 were calculated by curve fitting of the experimental data, while Soil 4 parameters were obtained based on the experimental data provided by the SoilPlus for the Gravel material.

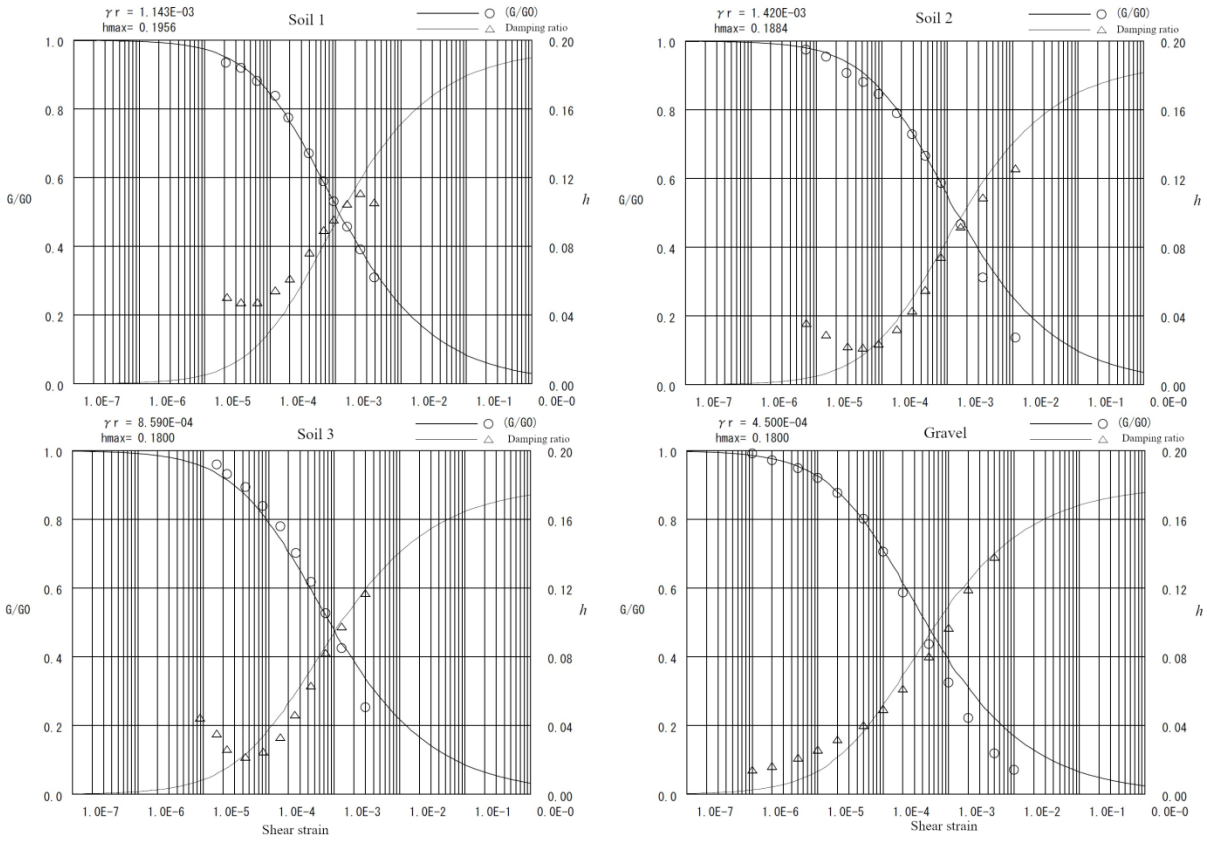

Fig. 6.13. RO parameters of KMMH16 by curve fitting of experimental data. Each panel includes the G/G_{max}–γ (left y-axis) and h–γ (right y-axis) relationships.

Third, the parameters of the Bowl model for KMMH16 were obtained. Comparing with the borehole drilling results near KMMH16, it was assumed that the third layer could be liquefied during the mainshock. Bowl model parameters are shown from Fig. 6.14. This figure shows the property of the Soil 3 as shown in Fig. 6.13.

All the parameters of subsurface layers from ground surface to the engineering bedrock were shown in Tables 6.6 and 6.7. Since the water table depth of KMMH16 is 14.0 m, the second layer was divided into two parts above and below the water table. The bottom layer (layer 9 as shown in Table 6.6) was set to be linear material.

After the nonlinear analysis, Figs. 6.15, 6.16, 6.17 show comparisons of properties of estimated ground motions and the observed strong ground motions at KMMH16 during the mainshock for EW, NS, and UD directions, respectively. Each subsurface layer was sliced into many pieces during the nonlinear analysis, Fig. 6.18 displays the response results of every layer. Fig. 6.19 shows the pore water pressure ratio of the layer using the Bowl model. Liquefaction does not occur if the with the maximum value is less than 100%.

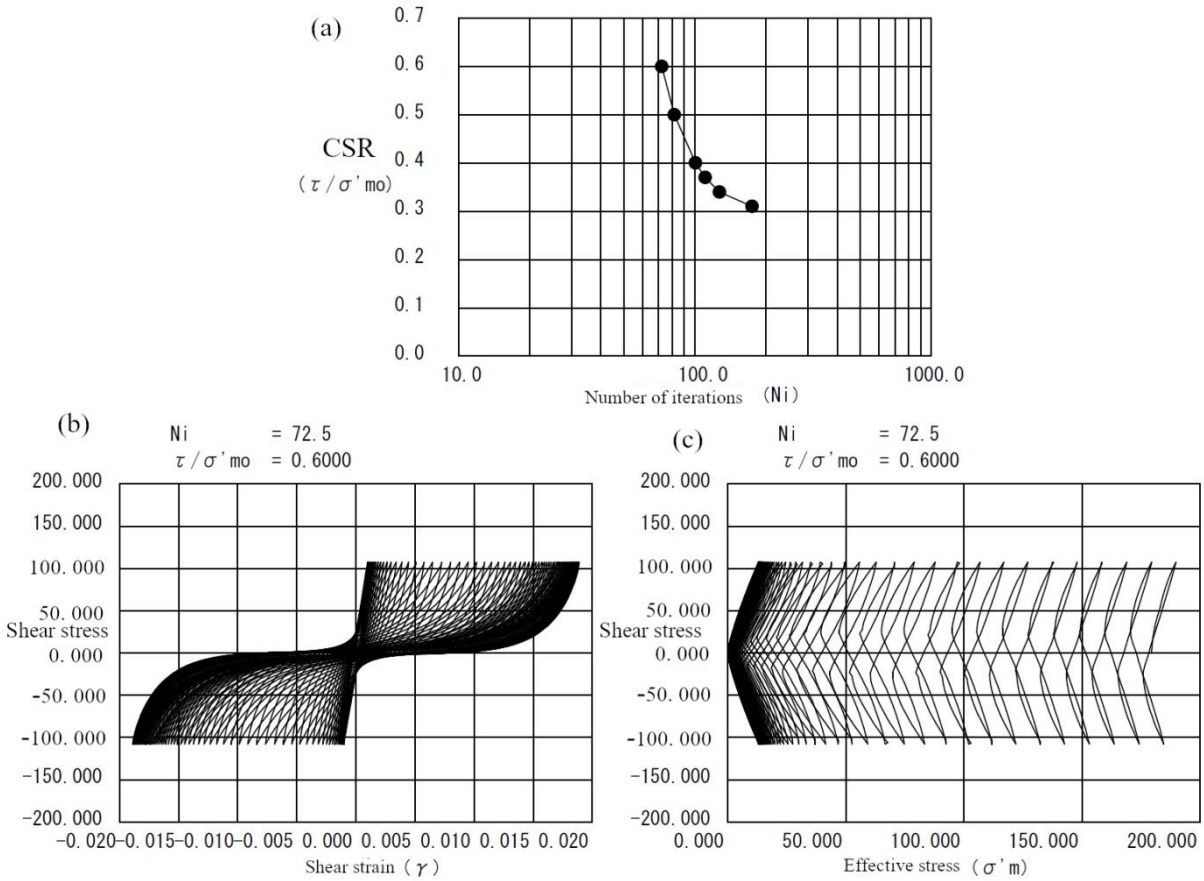

Fig. 6.14. Bowl parameters of the Soil 3 layer at KMMH16. (a) is the CRS curve, (b) is the relationship between shear stress and strain when Ni=72.5, (c) is the relationship of shear stress and effective stress when Ni=72.5.

Table. 6.6. Information of soil column at KMMH16 and RO parameters.

Layer number	Depth(m),	Soil type	γ_t (kN/m3)	V_s(m/s)	V_p (m/s)	G_0 (kN/m2)	G_{0i} (kN/m2)	σ'_{m0} (kN/m2)	Experiment, σ'_{m0} (kN/m2)	RO-Model		
										$\gamma_{0.5}$	h_{max}	$\gamma_{0.5i}$
1	3.00	KMMH16-Soil 1	16.60	154.87	296.56	40627.17	9971.55	16.60	35	1.14E-03	0.1956	1.93E-04
2	14.00	KMMH16-Soil 2	17.30	249.36	760.00	109767.46	11166.32	96.63	120	1.42E-03	0.1884	1.30E-04
3	15.00	KMMH16-Soil 2	17.30	249.36	1841.61	109767.46	8609.10	162.57	120	1.42E-03	0.1884	1.30E-04
4	20.29	KMMH16-Soil 3	17.90	337.07	1841.61	207523.44	15495.90	179.35	250	8.59E-04	0.18	5.43E-05
5	22.39	KMMH16-Soil 2	18.70	483.09	1918.07	445319.41	31499.65	199.86	120	1.42E-03	0.1884	1.30E-04
6	38.19	Gravel	19.20	598.03	1995.00	700682.22	43826.95	255.60	360	4.50E-04	0.18	2.37E-05
7	50.69	Gravel	19.70	733.19	1995.09	1080620.54	58064.66	346.36	360	4.50E-04	0.18	2.37E-05
8	75.99	Gravel	20.00	790.10	2529.23	1273995.94	58539.67	473.63	360	4.50E-04	0.18	2.37E-05
9	92.12	Linear	20.10	827.70	2558.47	1405128.01	56659.05	615.03				

Table. 6.7. Bowl parameters of the Soil 3 layer at KMMH16.

Layer	Bowl model						
	A	B	C	D	$C_s/(1+e_0)$	$C_c/(1+e_0)$	X_I
4	-3	1.4	15	50	0.006	0.00605	0.3

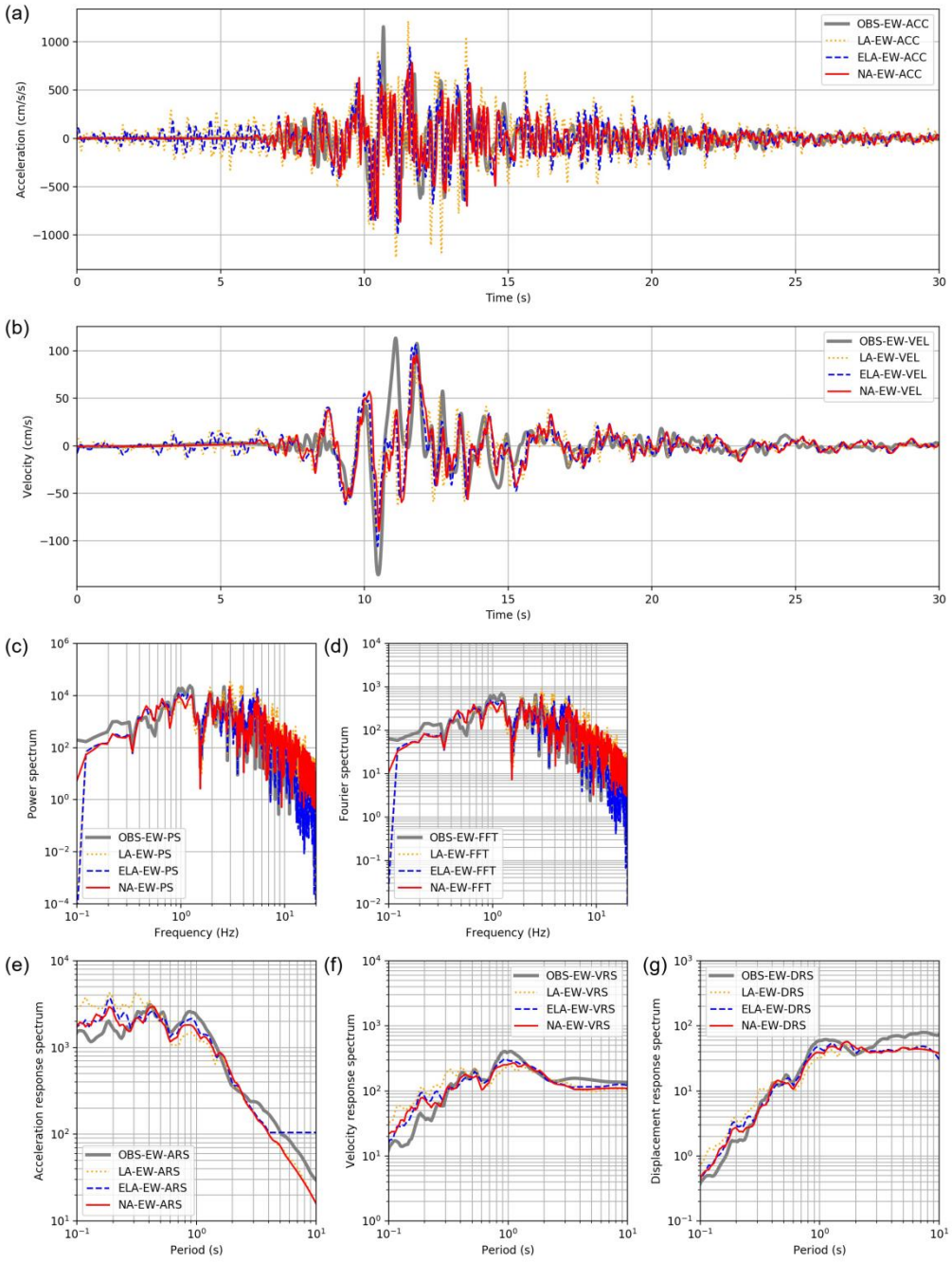

Fig. 6.15. Nonlinear dynamic analysis results of KMMH16 for the EW component. (a) Comparisons of the estimated and observed accelerations at KMMH16 for the EW component, grey, orange, blue and red lines denote the observed, LA, ELA, and NA estimated waves, respectively. (b) Comparisons of the estimated and observed velocity waveforms. (c) and (d) Comparisons of the power spectra and Fourier spectra of the estimated and observed acceleration waveforms. (e), (f), and (g) Comparisons of the acceleration response spectra, velocity response spectra, and displacement response spectra of the observed and estimated acceleration waveforms.

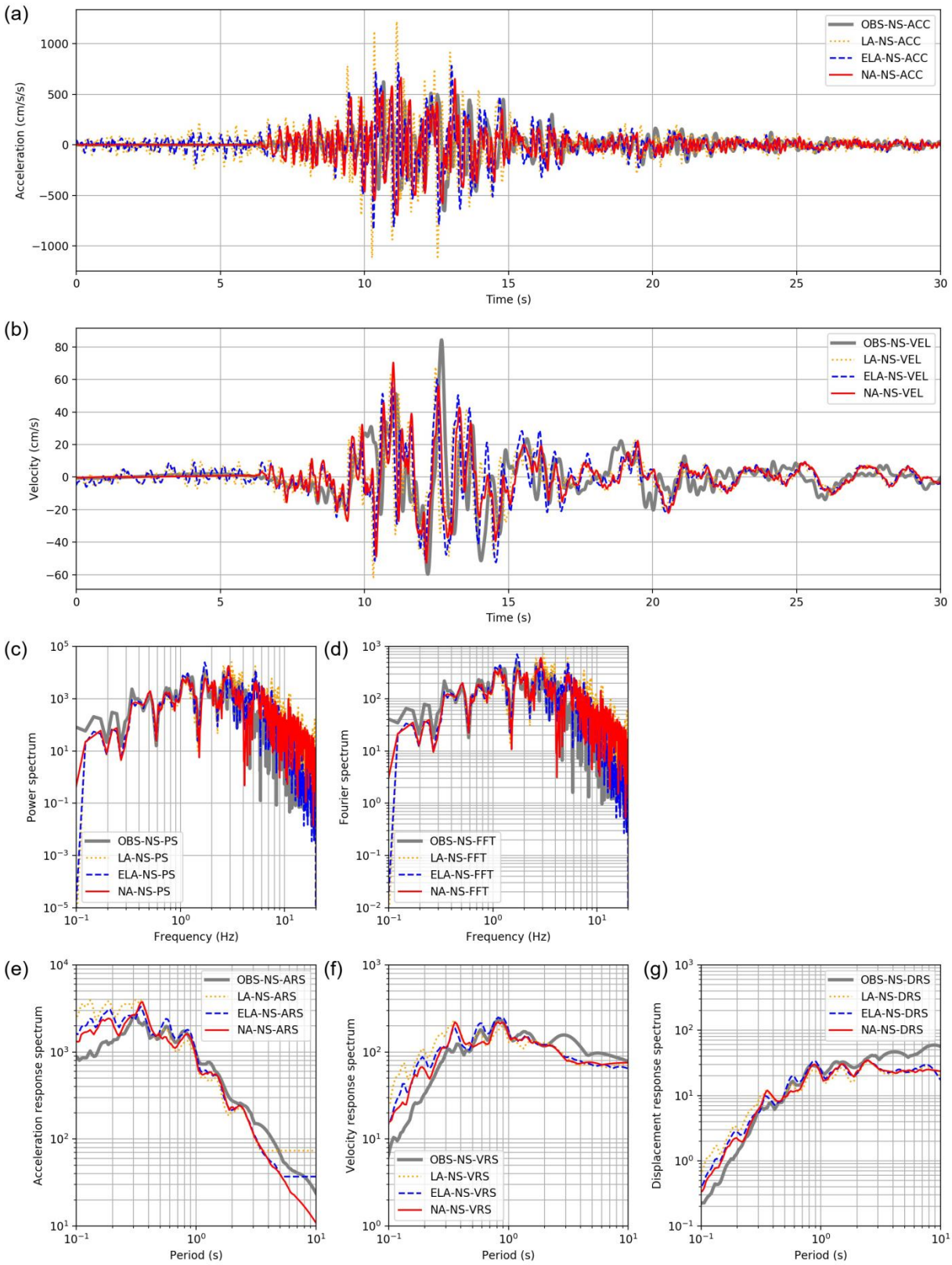

Fig. 6.16. Nonlinear dynamic analysis results of KMMH16 for the NS component. Meanings of each panel are similar to Fig. 6.15. Grey, orange, blue and red lines denote the observed, LA, ELA, and NA estimated results.

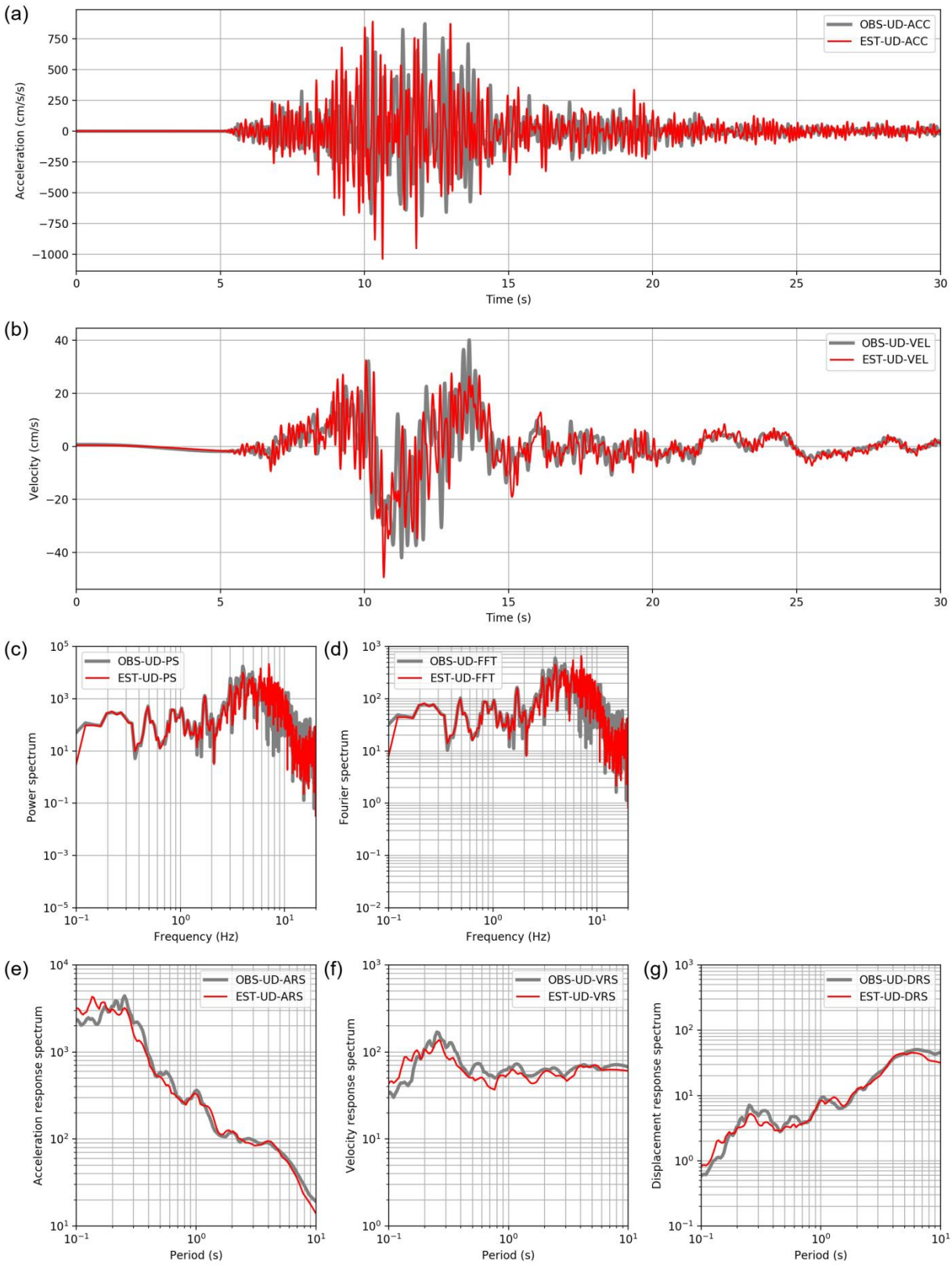

Fig. 6.17. Nonlinear dynamic analysis results of KMMH16 for the UD component. Meanings of each panel are similar to Fig. 6.15. Red and grey lines denote the results of estimation and observations.

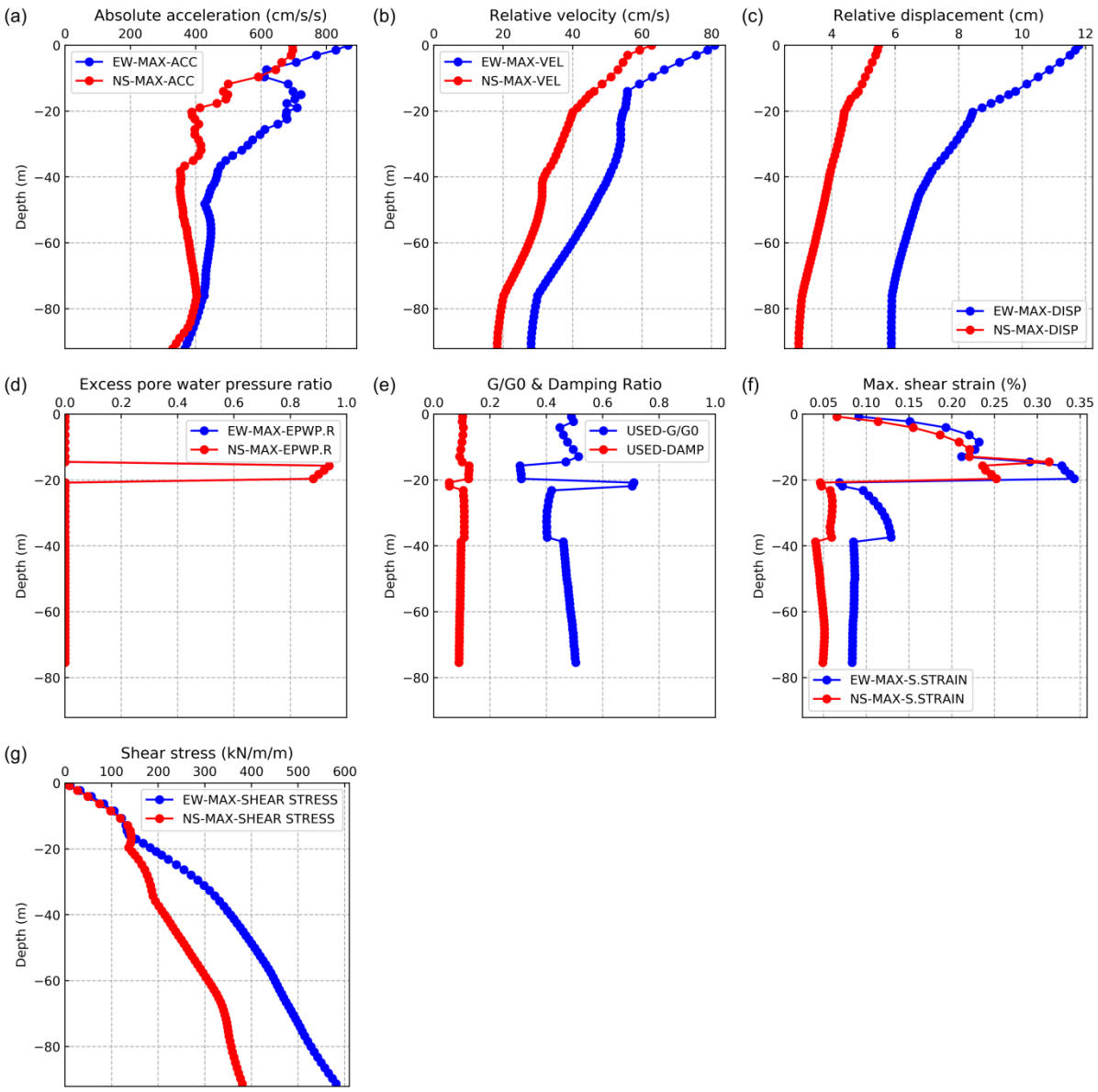

Fig. 6.18. Nonlinear response results of subsurface layers of soil column at KMMH16. Red and blue lines denote results of EW and NS directions, respectively. (a), (b), (c), (d), (e), (f), and (g) Estimated absolute peak acceleration of every layer, estimated relative peak velocity of every layer, estimated relative peak displacement of every layer, estimated pore water pressure ratio of every layer, G/G_{max} and damping ratio used in the calculation of every layer, maximum shear strain of every layer, estimated shear stress of every layer.

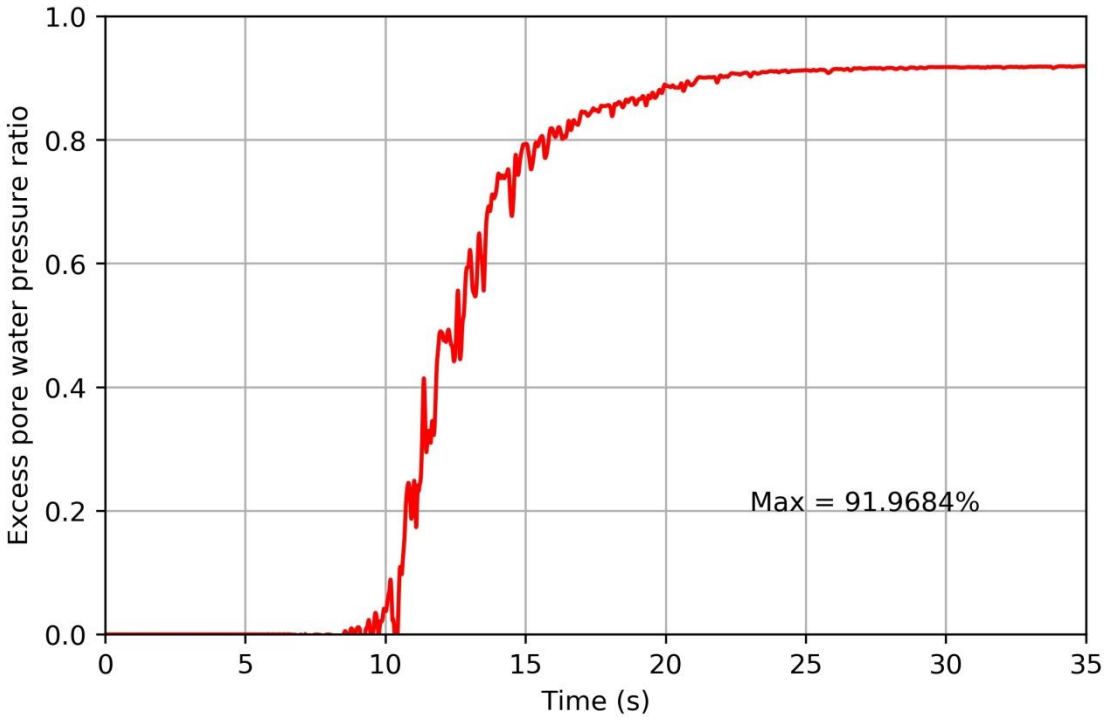

Fig. 6.19. Excess pore water pressure ratio of the Bowl model layer in time domain of KMMH16 soil. The maximum value was 91.9684%.

6.3.4. Nonlinear analysis of soil column at KMMP58

In the similar analysis procedure of KMMH16, eigenvalue analysis results is listed in Table 6.8, and calculation of Rayleigh damping coefficients is shown in Fig. 6.20 and Table 6.9. The RO parameters used for the soil column of KMMP58 is shown in Fig. 6.21, experimental data of Soil 1, 2, and 3 were obtained from the previous research, curve fitting results were obtained by the SoilPlus. At the second and third layers, the Bowl model was used, their parameters are shown in Fig. 6.22 (KMMP58−Soil 2) and Fig. 6.23 (KMMP58−Soil3). The inputting parameters of each subsurface layer is shown in Table 6.10. Since the water table depth at KMMP58 is 6.5 m, the second layer was split into two parts.

After nonlinear analyzing, the results of dynamic response is shown on Figs. 6.24 − 6.28. Liquefaction did not occur and the nonlinear effects at KMMP58 were not strong.

Table.6.8. Eigenvalue analysis of KMMP58.

Mode	Frequency (Hz)	Period (s)	Participation factor			Effective mass ratio			Modal damping ratio
			x	y	z	x	y	z	
1	2.48980	0.40160	-24.22600	50.04400	0.00000	0.05020	0.21400	0.00000	0.01100
2	2.48980	0.40160	81.08300	39.41600	0.00000	0.56190	0.13280	0.00000	0.01100
3	2.48980	0.40160	-31.09200	63.79700	0.00000	0.08260	0.34790	0.00000	0.01100
4	4.08410	0.24490	0.00000	0.00000	-89.77600	0.00000	0.00000	0.68890	0.01100
5	5.80480	0.17230	-18.52700	9.84800	0.00000	0.02930	0.00830	0.00000	0.01100
6	5.80480	0.17230	26.20600	30.54500	0.00000	0.05870	0.07970	0.00000	0.01100
7	5.80480	0.17230	24.86000	-24.86000	0.00000	0.05280	0.05280	0.00000	0.01100
8	9.49050	0.10540	0.00000	0.00000	40.25900	0.00000	0.00000	0.13850	0.01100
9	10.32040	0.09690	21.11900	5.24560	-0.00002	0.03810	0.00240	0.00000	0.01100
10	10.32040	0.09690	1.57940	-23.15500	0.00000	0.00020	0.04580	0.00000	0.01100

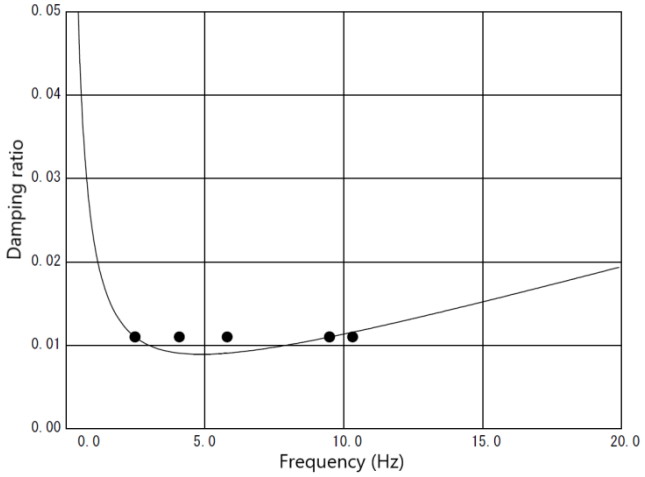

Fig. 6.20. Rayleigh damping calculation of KMMP58.

Table 6.9. Two coefficient factors of KMMP58.

α	2.9226 E-04
β	2.7264 E-01

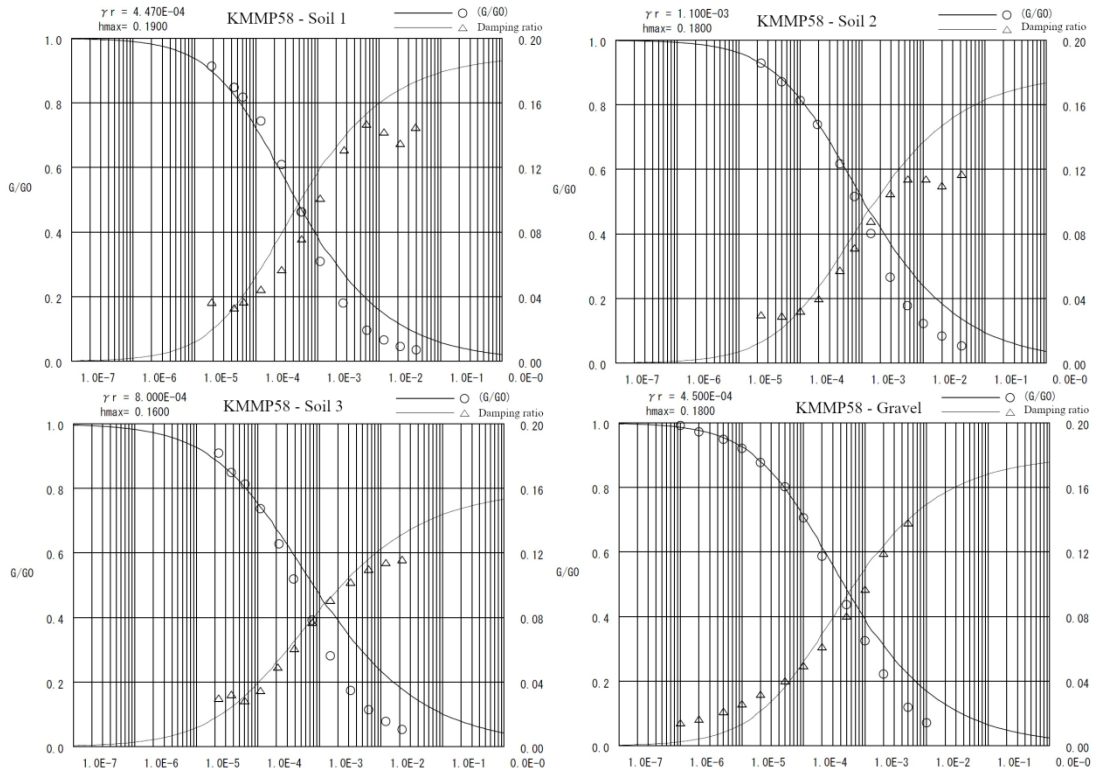

Fig. 6.21. RO model parameters of four soil materials at KMMP58. Each panel includes the G/G_{max}–γ (left y-axis) and h–γ (right y-axis) relationships.

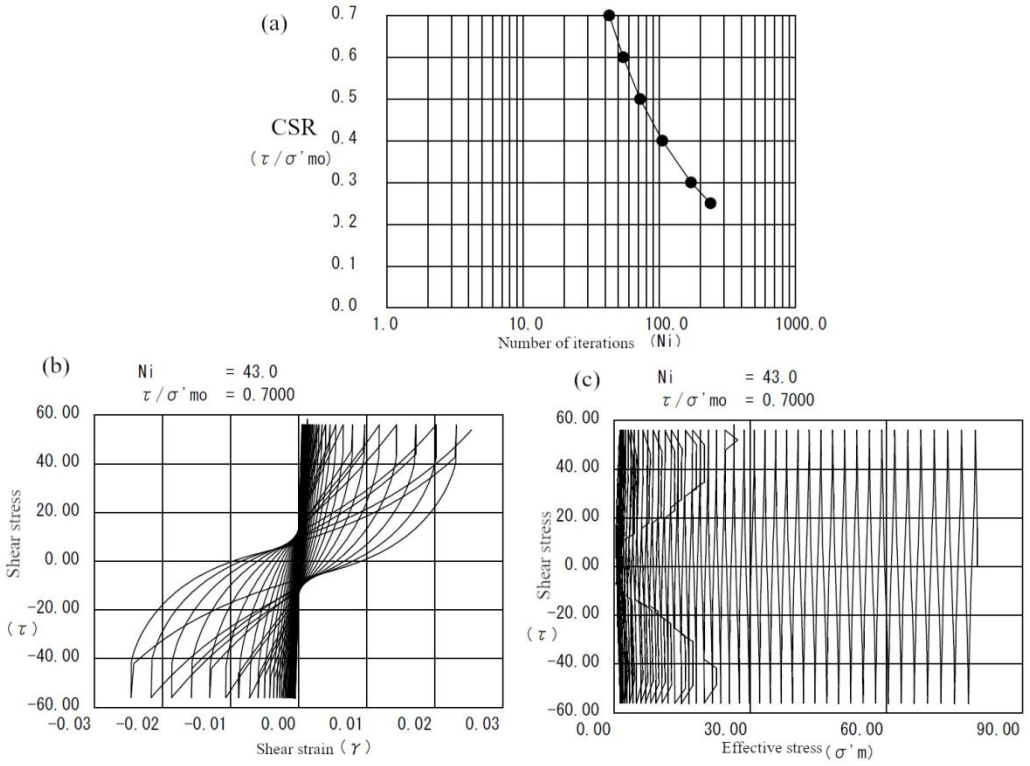

Fig. 6.22. Bowl model parameters of the KMMP58−Soil 2. (a) is the CRS curve, (b) is the relationship between shear stress and strain when Ni=43, (c) is the relationship of shear stress and effective stress when Ni=43.

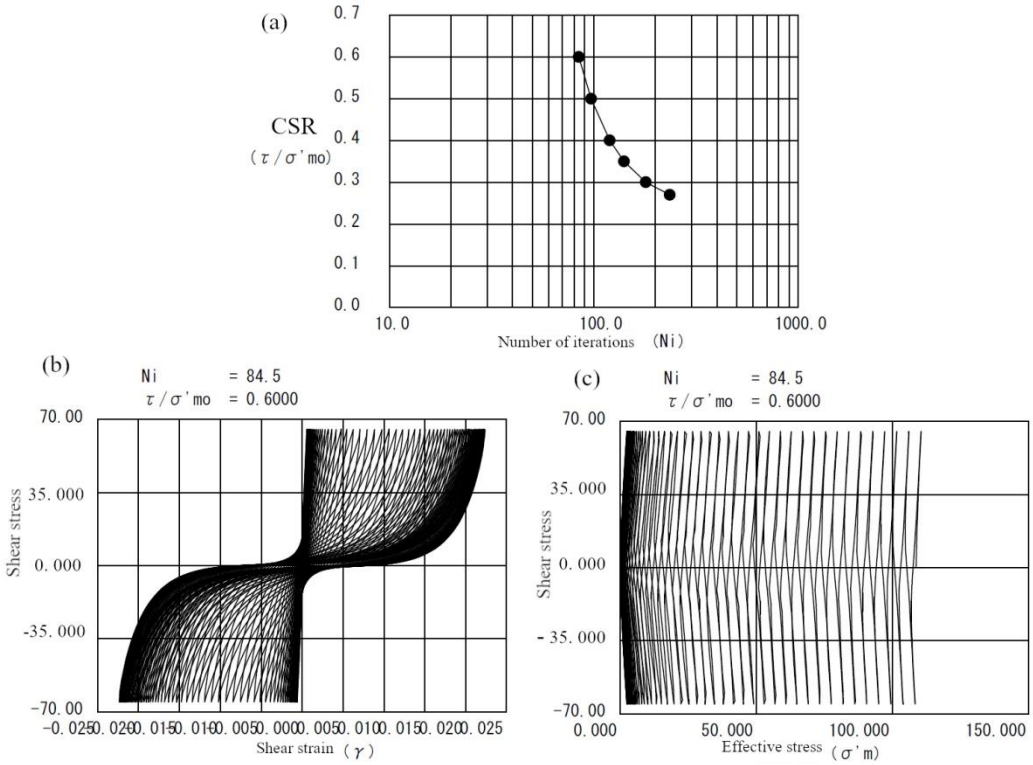

Fig. 6.23. Bowl model parameters of the KMMP58−Soil 3. (a) is the CRS curve, (b) is the relationship between shear stress and strain when Ni=84.5, (c) is the relationship of shear stress and effective stress when Ni=84.5.

Table. 6.10. Information of soil column at KMMP58 and RO model parameters.

Layer number	Depth(m),	Soil type	γ_t (kN/m3)	V_s(m/s)	V_p (m/s)	G_0 (kN/m2)	G_{0i} (kN/m2)	σ'_{m0} (kN/m2)	Experiment, σ'_{m0} (kN/m2)	RO-Model		
										$\gamma_{0.5}$	h_{max}	$\gamma_{0.5i}$
1	2.12	KMMP58-Soil 1	16.60	154.87	296.56	4.0627E+04	1.1862E+04	11.73	25	4.470E-04	0.19	8.940E-05
2	3.02	KMMP58-Soil 2	17.30	249.36	760.00	1.0977E+05	2.0507E+04	28.65	80	1.100E-03	0.18	1.230E-04
3	6.50	KMMP58-Soil 3	17.90	337.07	1841.61	2.0752E+05	2.8083E+04	54.61	110	8.000E-04	0.16	7.630E-05
4	18.81	KMMP58-Soil 3	17.90	337.07	1841.61	2.0752E+05	1.9913E+04	108.61	110	8.000E-04	0.16	7.630E-05
5	25.08	Gravel	18.70	483.09	1918.07	4.4532E+05	3.5157E+04	160.44	360	4.500E-04	0.18	2.372E-05
6	47.93	Gravel	19.20	598.03	1995.00	7.0068E+05	4.4258E+04	250.64	360	4.500E-04	0.18	2.370E-05
7	60.67	Gravel	19.70	733.19	1995.09	1.0806E+06	5.6618E+04	364.28	360	4.500E-04	0.18	2.370E-05
8	60.93	Gravel	20.00	790.10	2529.23	1.2740E+06	6.3134E+04	407.21	360	4.500E-04	0.18	2.370E-05
9	61.09	Linear	20.10	827.70	2558.47	1.4051E+06	6.9510E+04	408.64				

Table. 6.11. Bowl model parameters of soil material at KMMP58.

Layer	Bowl model						
	A	*B*	*C*	*D*	$C_s/(1+e_0)$	$C_c/(1+e_0)$	X_I
2	-1.5	1.4	5	15	0.02	0.021	0.15
3	-2.5	1.4	14	42	0.006	0.0061	0.25
4	-2.5	1.4	14	42	0.006	0.0061	0.25

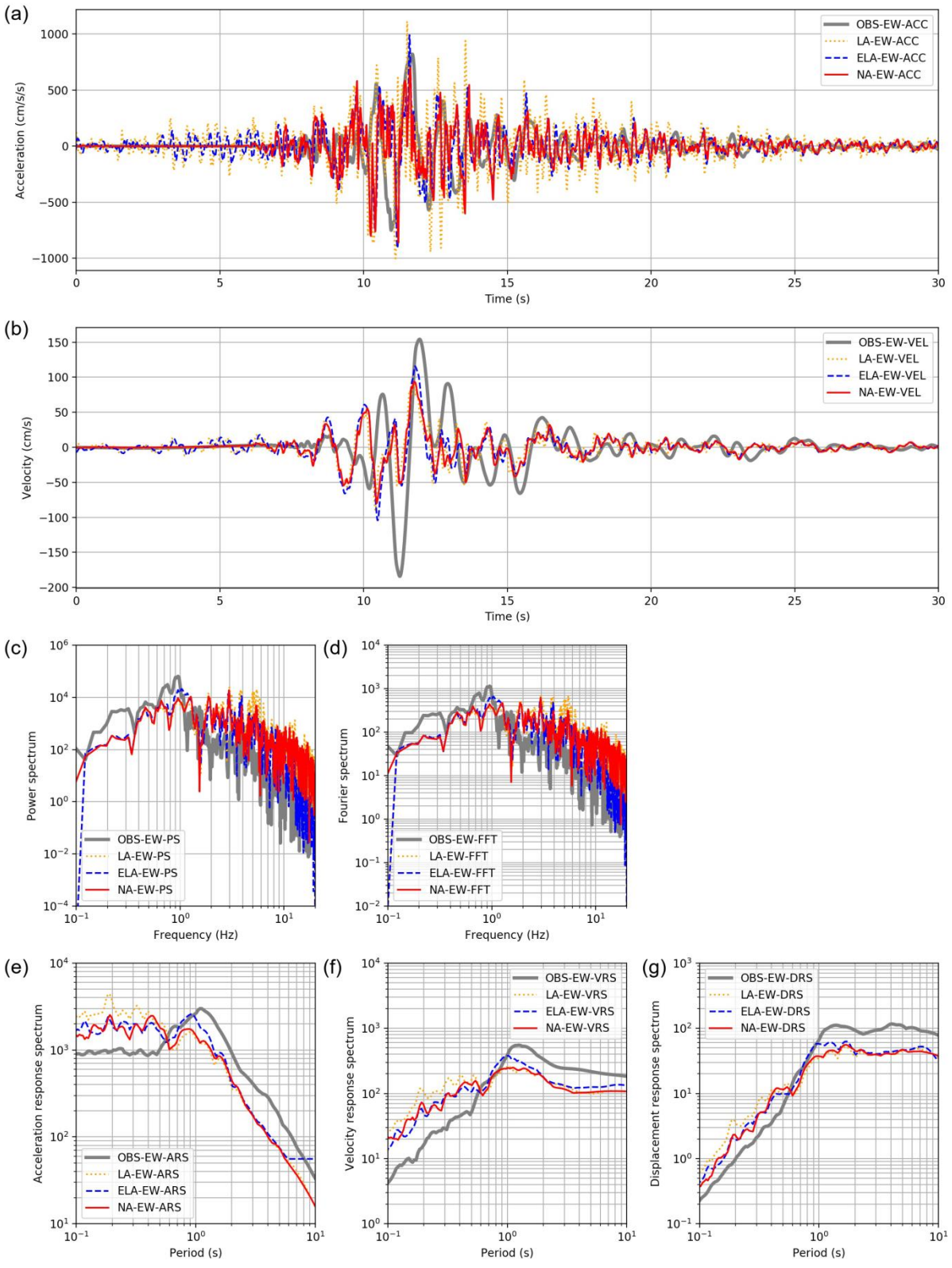

Fig. 6.24. Nonlinear dynamic analysis results of KMMP58 for the EW component. Meanings of each panel are similar to Fig. 6.15. Gray lines denote the results of observed ground motions at KMMP58

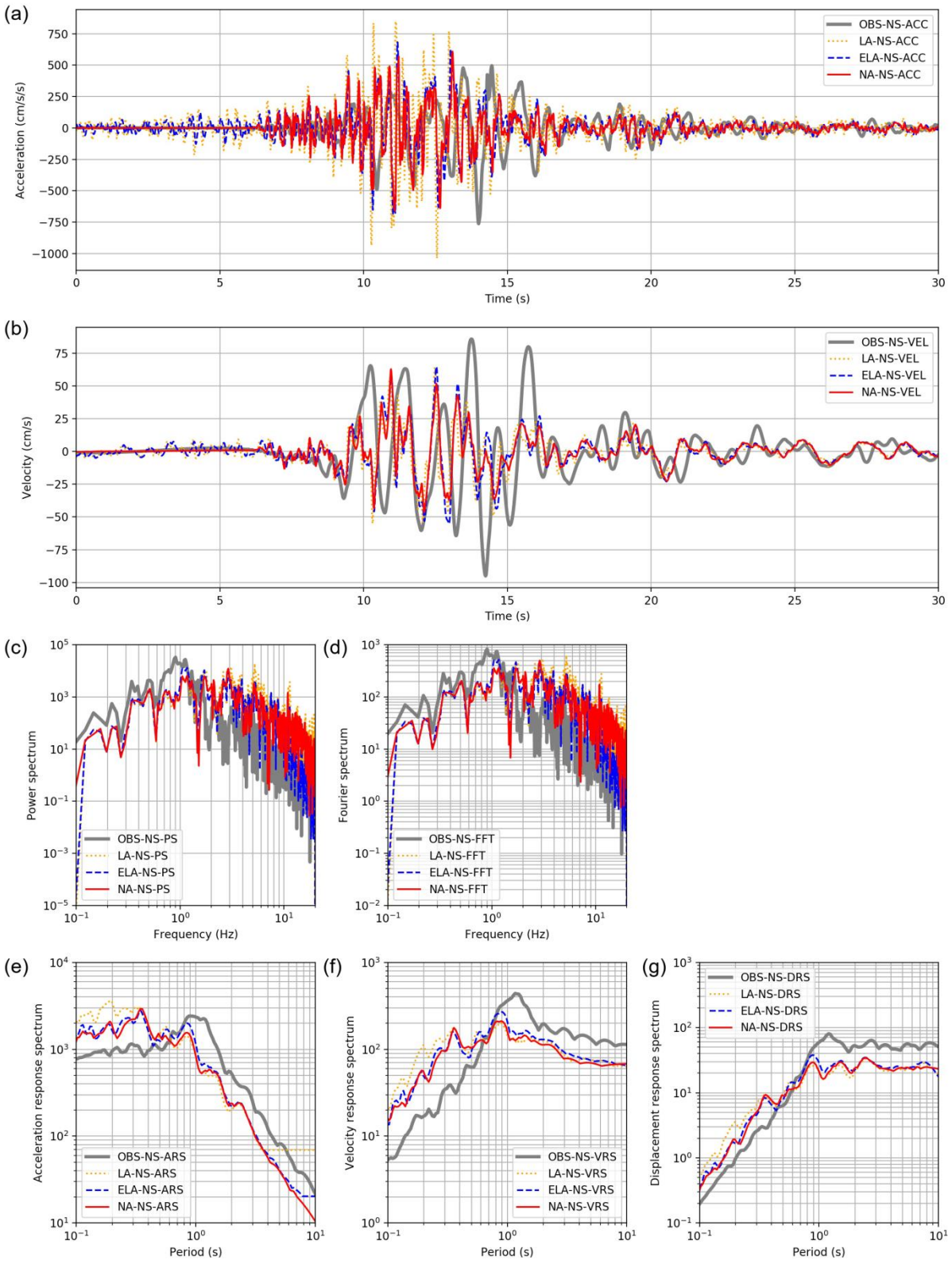

Fig. 6.25. Nonlinear dynamic analysis results of KMMP58 for the NS component. Meanings of each panel are similar to Fig. 6.15. Gray lines denote the results of observed ground motions at KMMP58

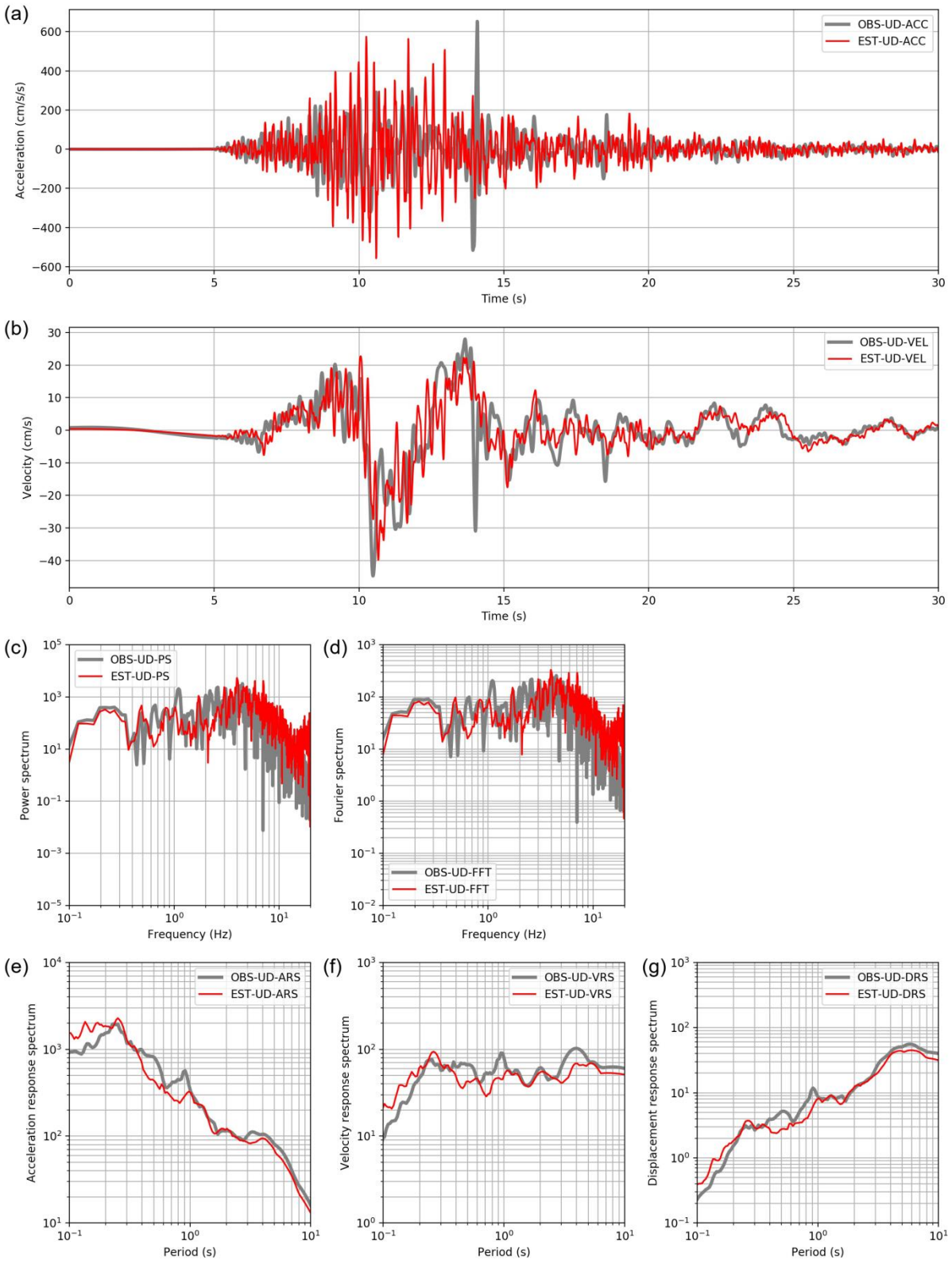

Fig. 6.26. Nonlinear dynamic analysis results of KMMP58 for the UD component. Meanings of each panel are similar to Fig. 6.15. Red and grey lines denote the results of estimation and observations.

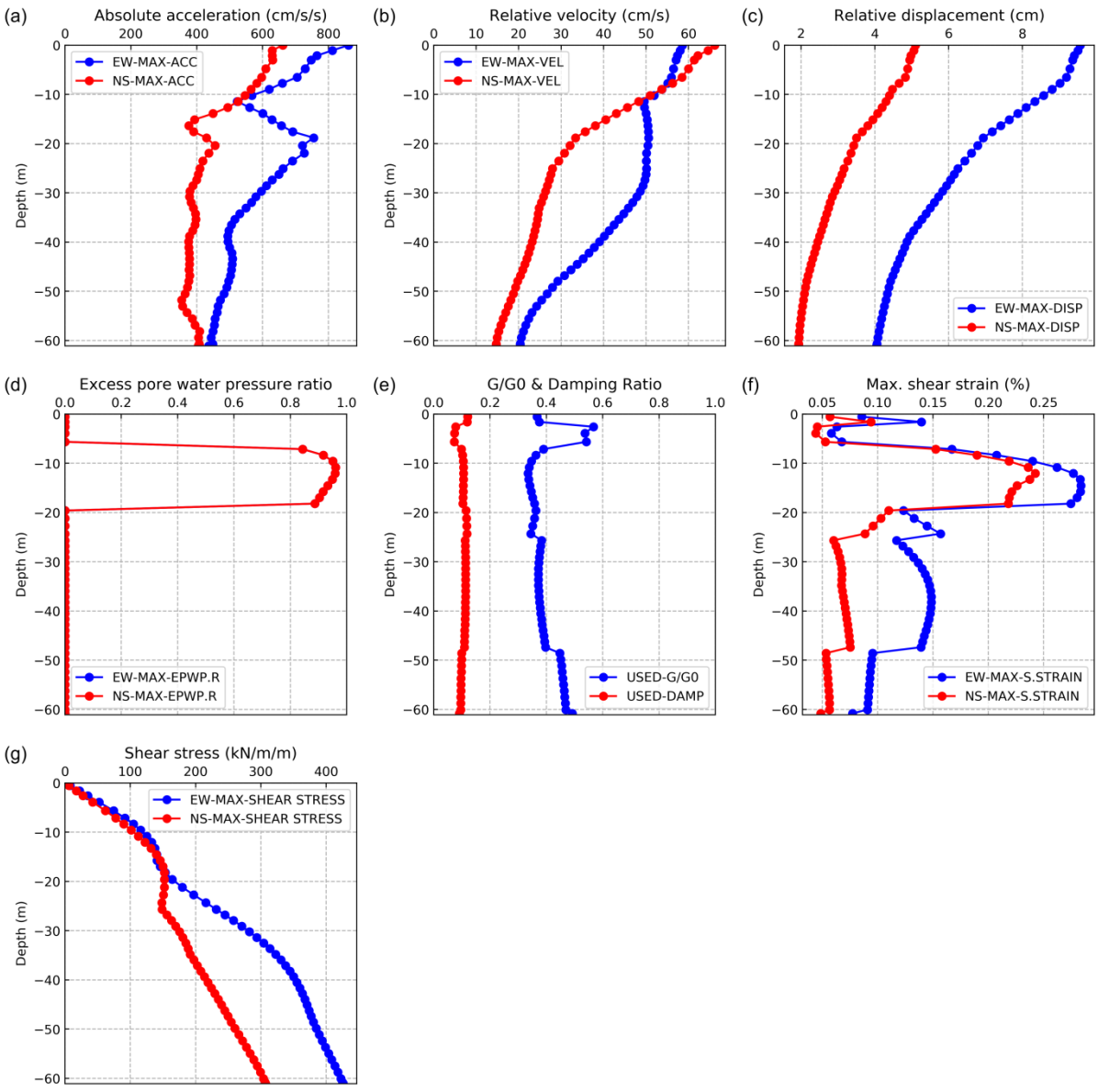

Fig. 6.27. Nonlinear response results of subsurface layers of soil column at KMMP58. Red and blue lines denote results of EW and NS directions, respectively. (a), (b), (c), (d), (e), (f), and (g) Estimated absolute peak acceleration of every layer, estimated relative peak velocity of every layer, estimated relative peak displacement of every layer, estimated pore water pressure ratio of every layer, G/G_{max} and damping ratio used in the calculation of every layer, maximum shear strain of every layer, estimated shear stress of every layer.

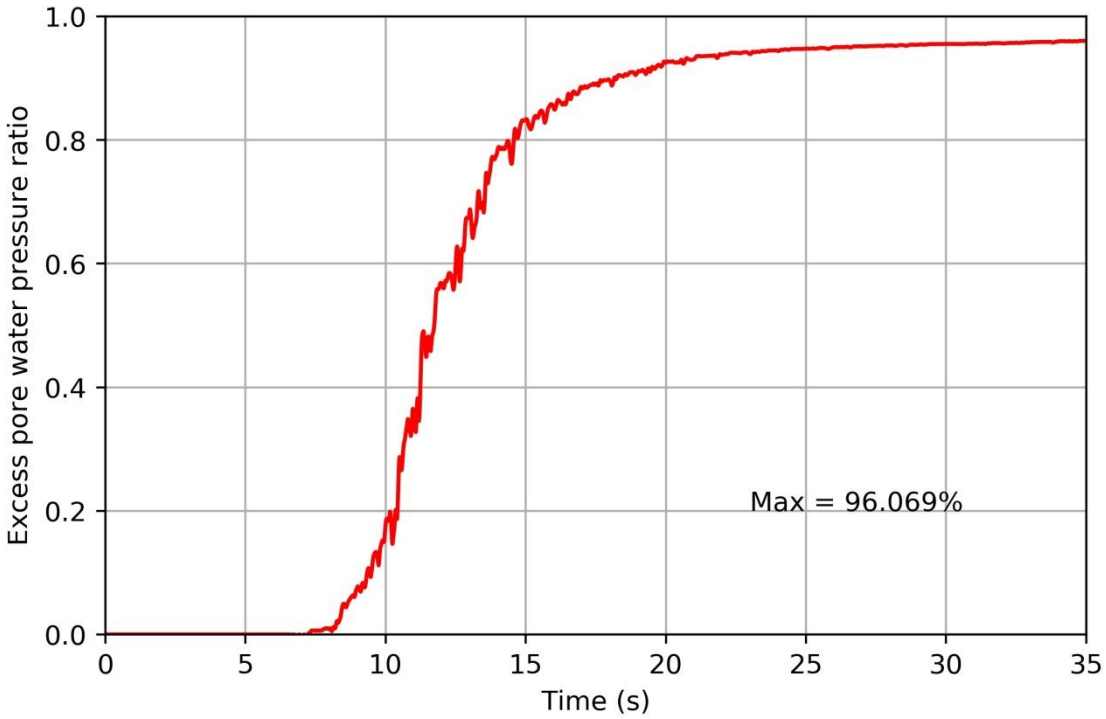

Fig. 6.28. Excess pore water pressure ratio of the Bowl model layer in time domain of KMMP58 soil. The maximum value was 96.069%.

6.3.5. Nonlinear analysis of soil column at MSA32

In the similar analysis procedure of KMMH16 and KMMP58, eigenvalue analysis results was listed in Table 6.12, and calculation of Rayleigh damping coefficients are shown in Fig. 6.29 and Table 6.13. MSA32 is close to the borehole drilling M in previous research [35]. The RO parameters used for the soil column of MSA32 are shown in Fig. 6.30, experimental data of Soil 1 and 2 were obtained from other research groups, curve fitting results were obtained by the SoilPlus. At the second and third layers, the Bowl model was used, parameters of them are shown in Fig. 6. 31 (MSA32−Soil 1) and Fig. 6. 32 (MSA32−Soil 2). The inputting parameters of each subsurface layer are shown in Tables 6.14 and 6.15, because the water table depth at MSA32 is 3.6 m, the second layer was split into two parts.

After nonlinear analyzing, the results of dynamic response are shown on Figs. 6.33 − 6.37. The liquefaction did not occur although the nonlinear effect at MSA32 was a little strong.

Table.6.12. Eigenvalue analysis of MSA32.

Mode	Frequency (Hz)	Period (s)	Participation factor			Effective mass ratio			Modal damping ratio
			x	y	z	x	y	z	
1	2.47280	0.40440	0.65786	-34.96100	0.00000	0.00000	0.07830	0.00000	0.01100
2	2.47280	0.40440	107.88000	-0.40894	0.00000	0.74560	0.00000	0.00000	0.01100
3	2.47280	0.40440	-0.65760	-102.06000	0.00000	0.00000	0.66730	0.00000	0.01100
4	4.05750	0.24650	0.00000	0.00000	-107.52000	0.00000	0.00000	0.74060	0.01100
5	5.33110	0.18760	-5.81340	5.49910	0.00000	0.00220	0.00190	0.00000	0.01100
6	5.33110	0.18760	-30.47700	-29.93900	0.00000	0.05950	0.05740	0.00000	0.01100
7	5.33110	0.18760	29.37100	-29.97800	0.00000	0.05530	0.05760	0.00000	0.01100
8	8.72310	0.11460	0.00000	0.00000	42.45700	0.00000	0.00000	0.11550	0.01100
9	9.57210	0.10450	-9.07660	-22.39600	0.00000	0.00530	0.03210	0.00000	0.01100
10	9.57210	0.10450	-25.87200	0.30030	0.00000	0.04290	0.00000	0.00000	0.01100

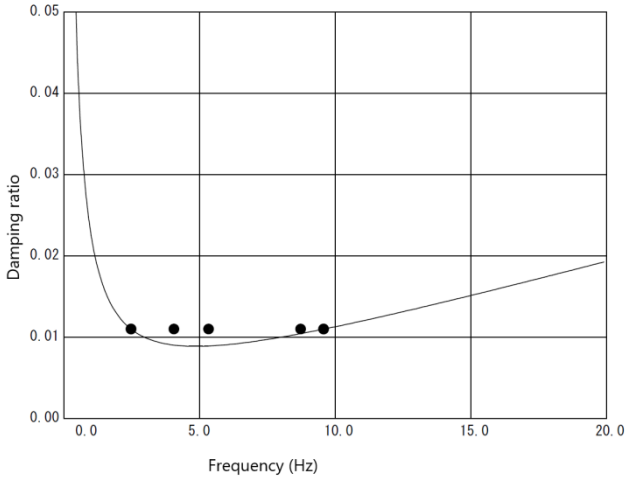

Fig. 6.29. Rayleigh damping calculation of MSA32.

Table 6.13. Two coefficient factors of MSA32.

α	2.9070 E-04
β	2.7164 E-01

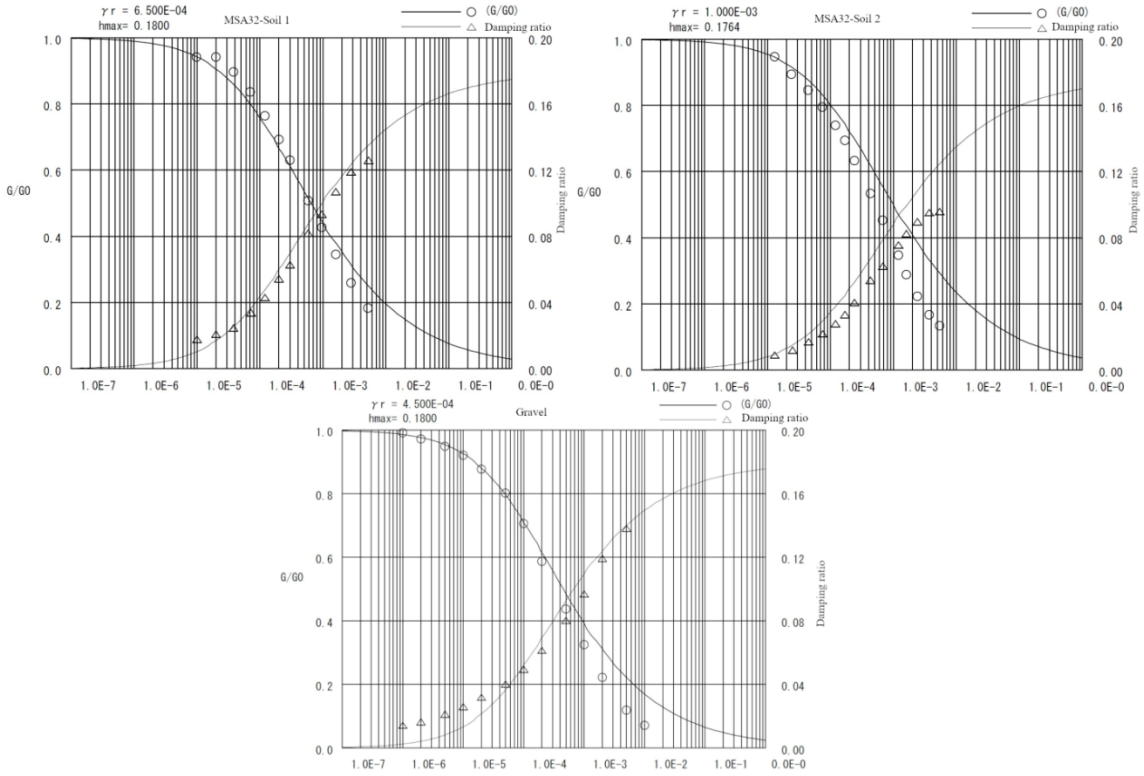

Fig. 6.30. RO model parameters of three soil materials at MSA32. Each panel includes the G/G_{max}–γ (left y-axis) and h–γ (right y-axis) relationships.

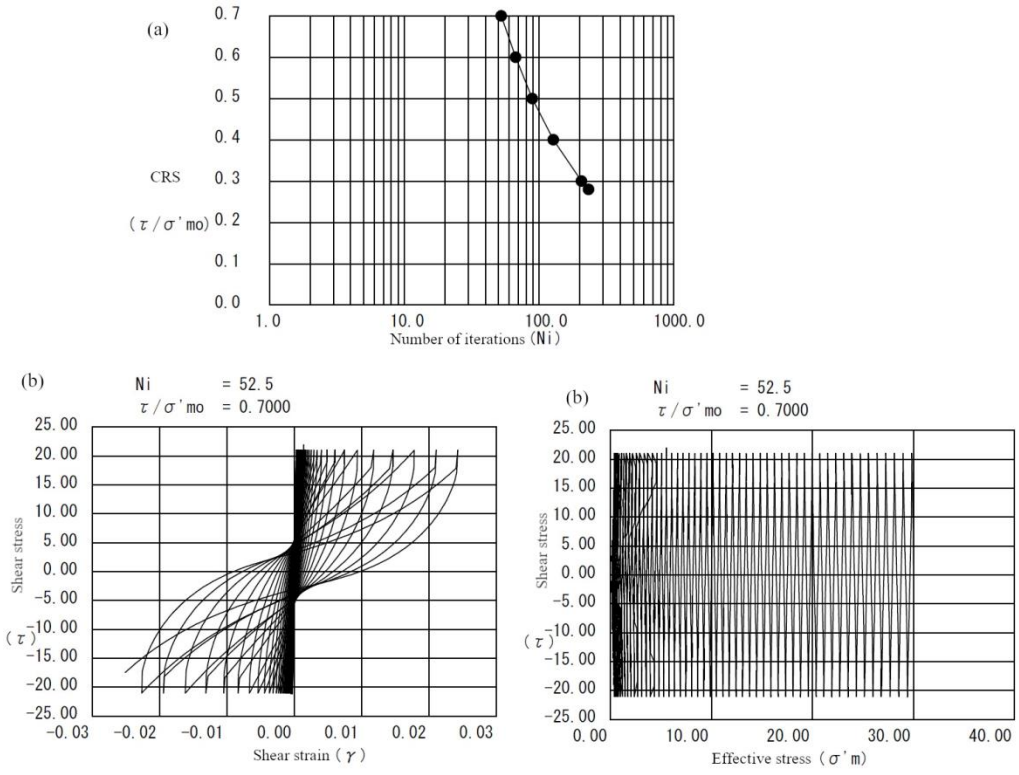

Fig. 6.31. Bowl model parameters of the MSA32−Soil 1. (a) is the CRS curve, (b) is the relationship between shear stress and strain when Ni=52.5, (c) is the relationship of shear stress and effective stress when Ni=52.5.

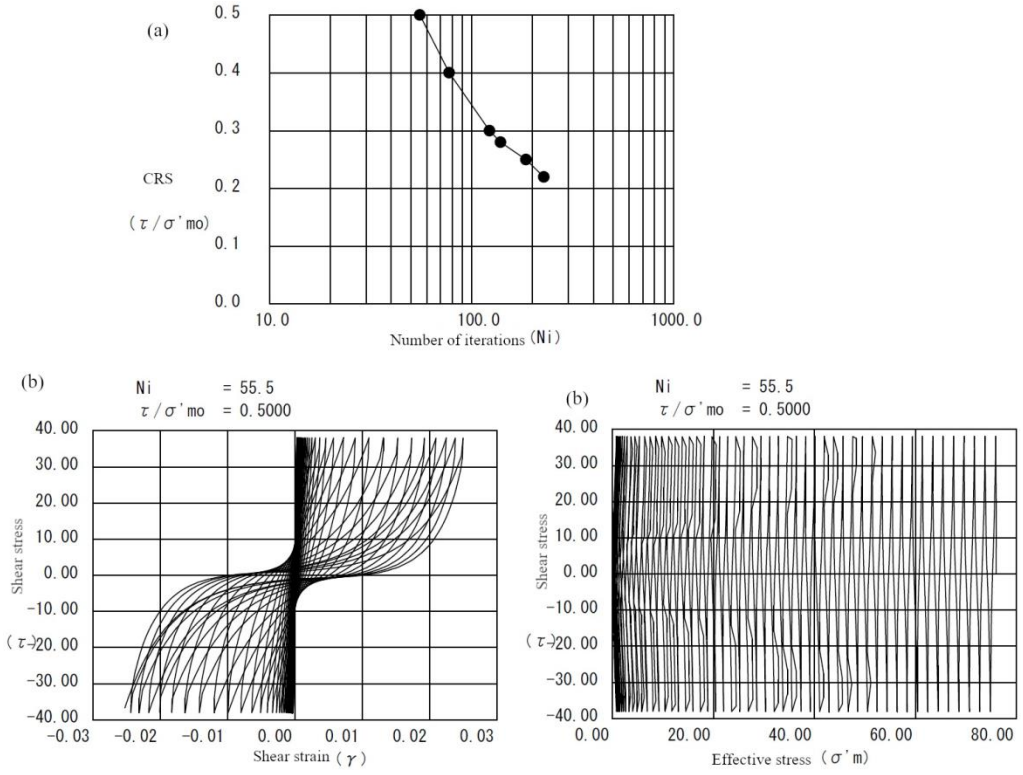

Fig. 6.32. Bowl model parameters of the MSA32−Soil 2. (a) is the CRS curve, (b) is the relationship between shear stress and strain when Ni=55.5, (c) is the relationship of shear stress and effective stress when Ni=55.5.

Table. 6.14. Information of soil column at KMMP58 and RO model parameters.

Layer number	Depth(m),	Soil type	γ_t (kN/m3)	V_s(m/s)	V_p (m/s)	G_0 (kN/m2)	G_{0i} (kN/m2)	σ'_{m0} (kN/m2)	Experiment, σ'_{m0} (kN/m2)	RO-Model		
										$\gamma_{0.5}$	h_{max}	$\gamma_{0.5i}$
1	2.05	MSA32-Soil 1	16.60	154.87	296.56	4.063E+04	1.206E+04	11.34	30	6.500E-04	0.18	1.187E-04
2	3.60	MSA32-Soil 1	17.30	249.36	760.00	1.098E+05	1.952E+04	31.63	30	6.500E-04	0.18	1.187E-04
3	3.91	MSA32-Soil 1	17.30	249.36	760.00	1.098E+05	1.707E+04	41.34	30	6.500E-04	0.18	1.187E-04
4	16.44	MSA32-Soil 2	17.90	337.07	1841.61	2.075E+05	2.381E+04	75.94	95	1.000E-03	0.1764	1.026E-04
5	22.71	Gravel	18.70	483.09	1918.07	4.453E+05	3.930E+04	128.38	360	4.500E-04	0.18	2.372E-05
6	23.17	Gravel	19.20	598.03	1995.00	7.007E+05	5.751E+04	148.42	360	4.500E-04	0.18	2.370E-05
7	23.30	Gravel	19.70	733.19	1995.09	1.081E+06	8.815E+04	150.29	360	4.500E-04	0.18	2.370E-05
8	52.63	Gravel	20.00	790.10	2529.23	1.274E+06	8.050E+04	250.44	360	4.500E-04	0.18	2.370E-05
9	79.60	Linear	20.10	827.70	2558.47	1.405E+06	6.678E+04	442.76				

Table. 6.15. Bowl model parameters of soil material at KMMP58.

Layer	Bowl model						
	A	*B*	*C*	*D*	$C_s/(1+e_0)$	$C_c/(1+e_0)$	X_l
2	-1.5	1.4	4	15	0.02	0.021	0.14
3	-1.5	1.4	4	15	0.02	0.021	0.14
4	-1.6	1.4	11	35	0.006	0.00615	0.17

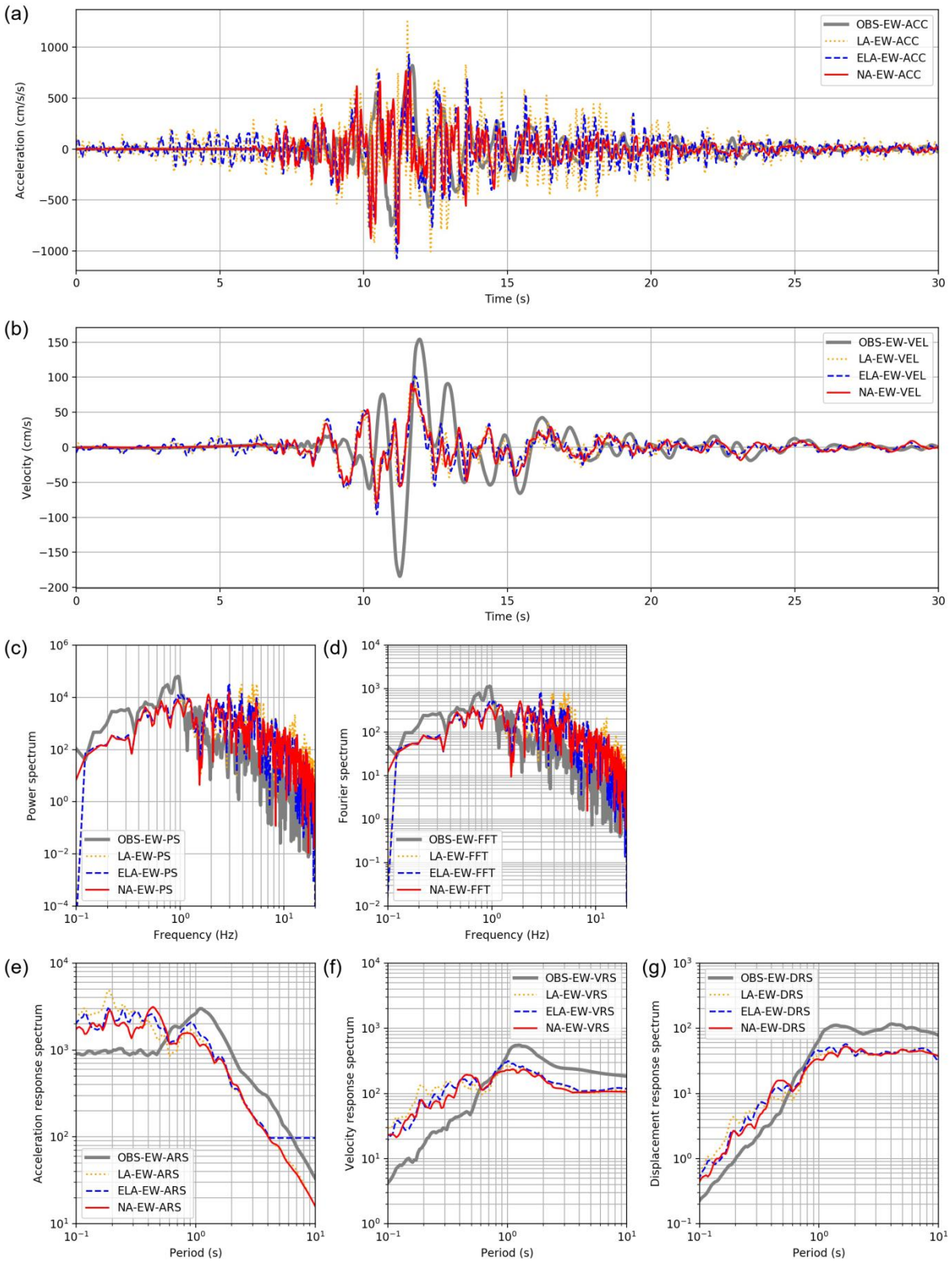

Fig. 6.33. Nonlinear dynamic analysis results of MSA32 for the EW component. Meanings of each panel are similar to Fig. 6.15. Gray lines denote the results of observed ground motions at KMMP58.

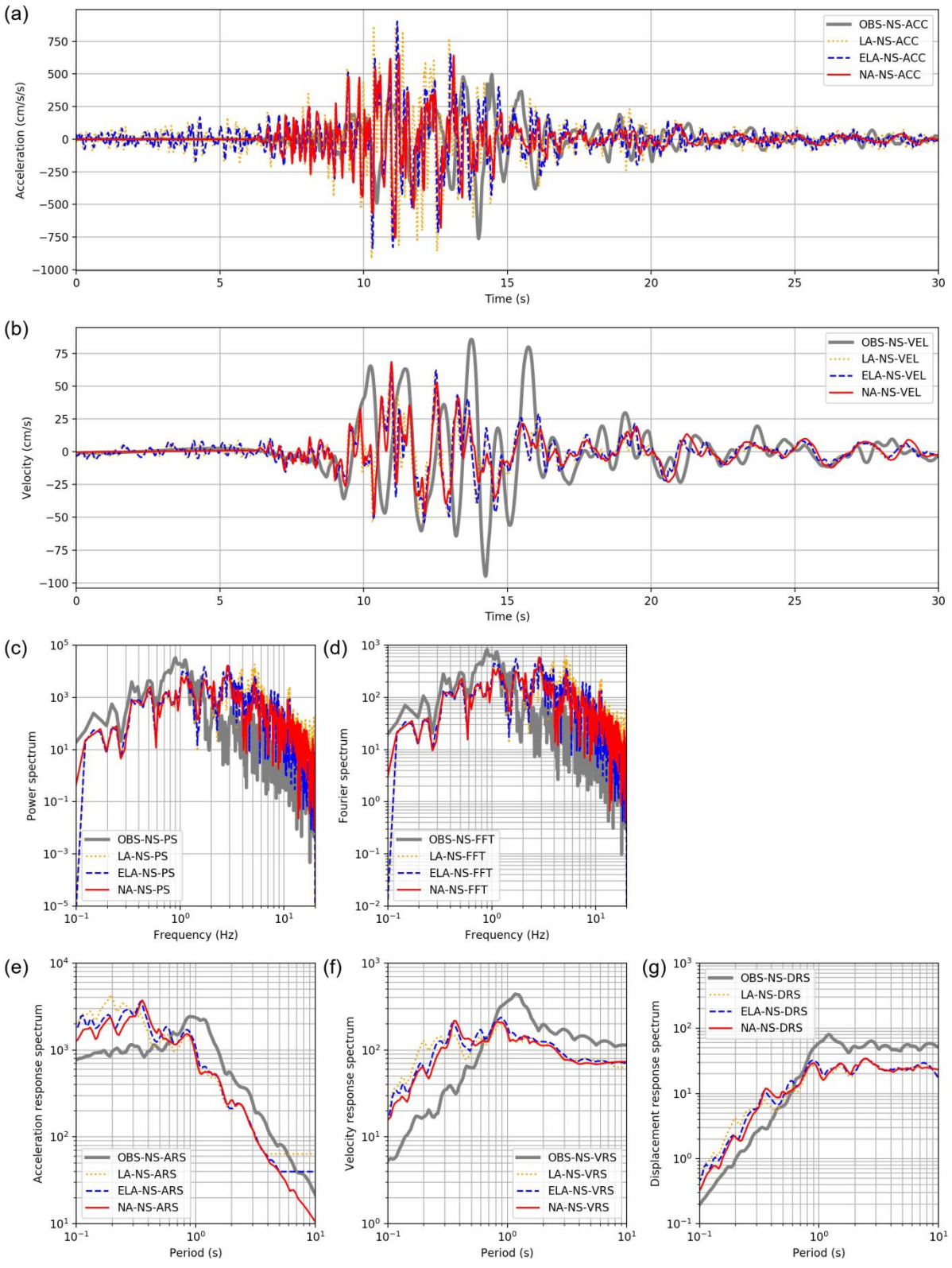

Fig. 6.34. Nonlinear dynamic analysis results of MSA32 for the NS component. Meanings of each panel are similar to Fig. 6.15. Red and blue lines denote the results of estimation and observations.

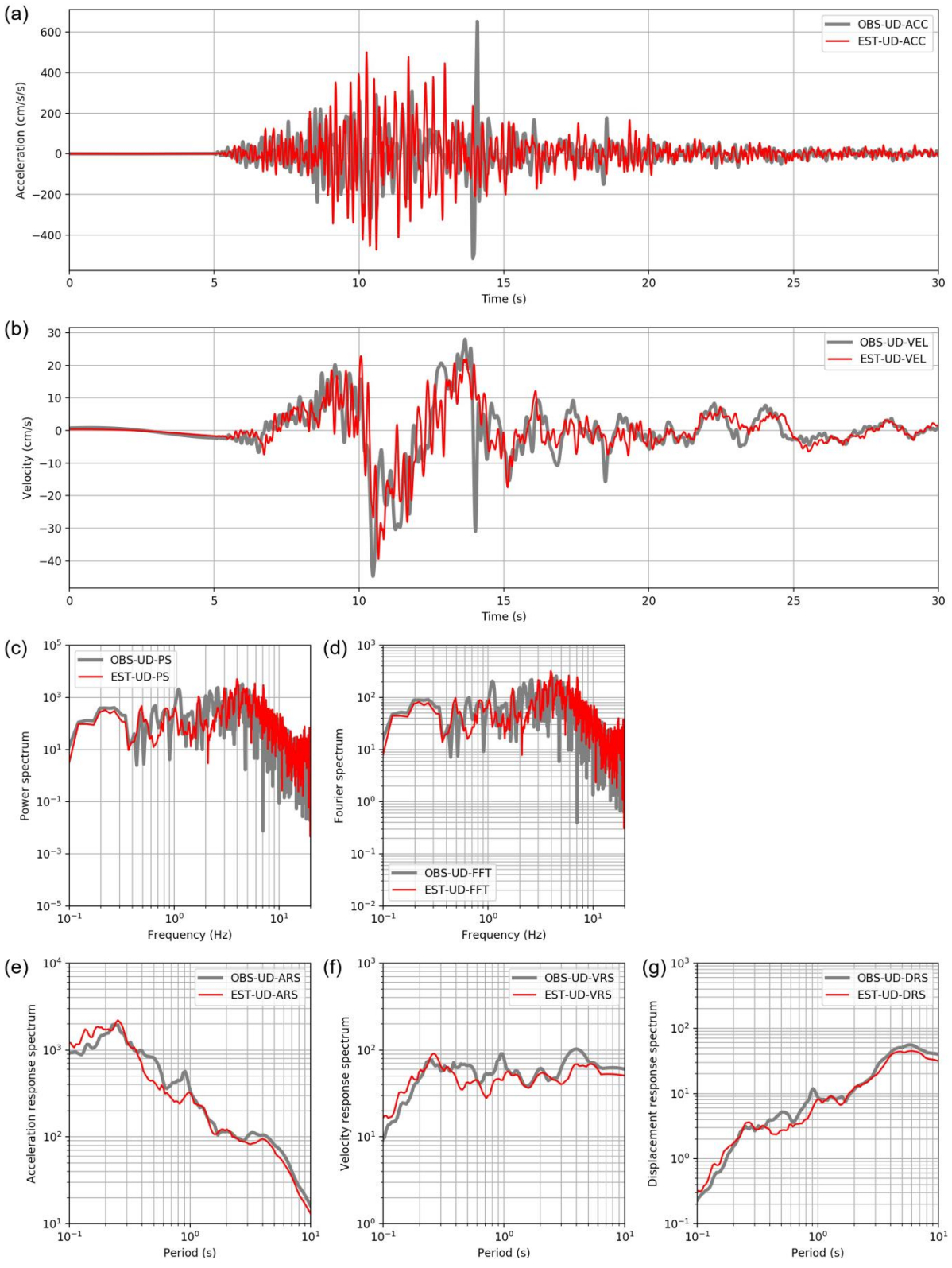

Fig. 6.35. Nonlinear dynamic analysis results of MSA32 for the UD component. Meanings of each panel are similar to Fig. 6.15. Red and grey lines denote the results of estimation and observations.

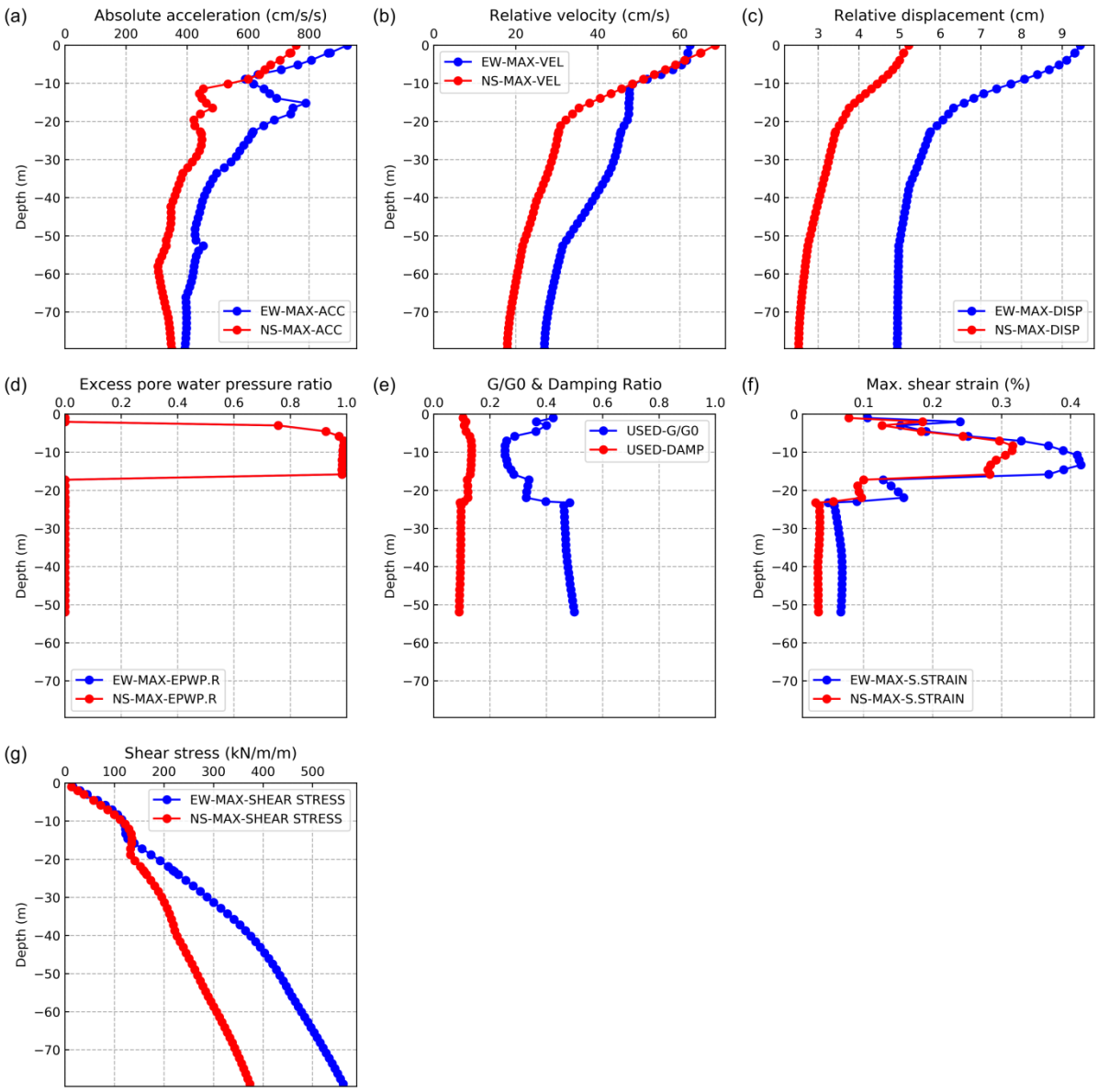

Fig. 6.36. Nonlinear response results of subsurface layers of soil column at MSA32. Red and blue lines denote results of EW and NS directions, respectively. (a), (b), (c), (d), (e), (f), and (g) Estimated absolute peak acceleration of every layer, estimated relative peak velocity of every layer, estimated relative peak displacement of every layer, estimated pore water pressure ratio of every layer, G/G_{max} and damping ratio used in the calculation of every layer, maximum shear strain of every layer, estimated shear stress of every layer.

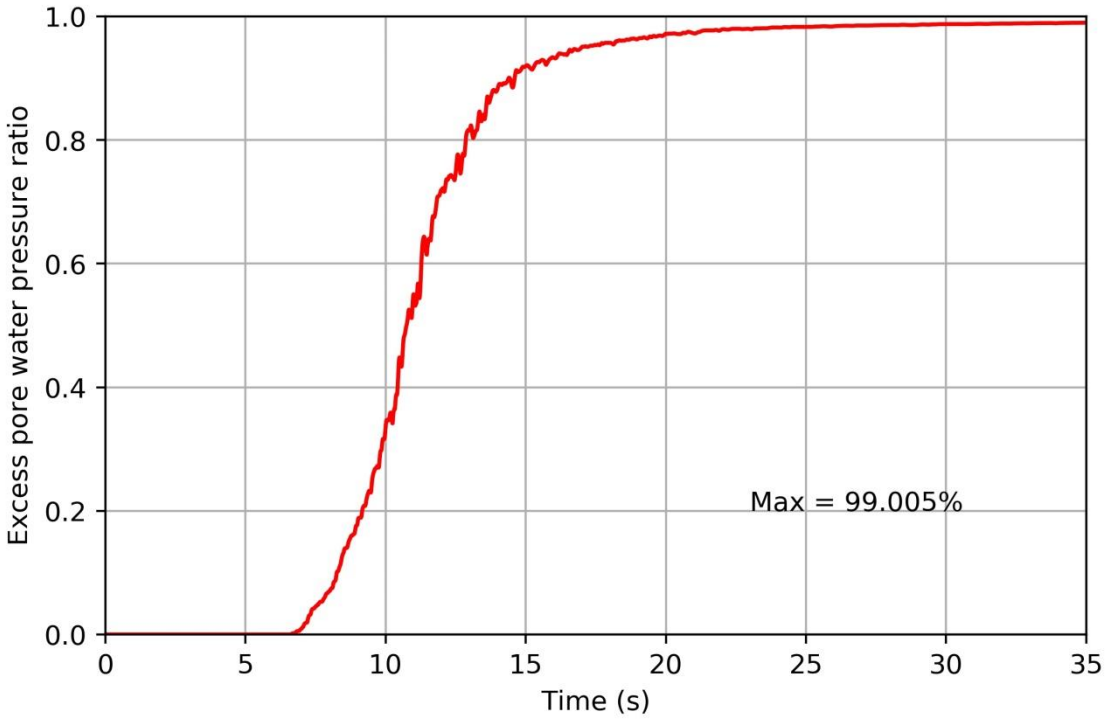

Fig. 6.37. Excess pore water pressure ratio of the Bowl model layer in time domain of MSA32 soil. The maximum value was 99.005%.

6.3.6. Nonlinear analysis of soil column at MS9-6

MS9-6 is a site near the Akitsu River, in the similar analysis procedure of KMMH16 and KMMP58, eigenvalue analysis results was listed in Table 6.16, and calculation of Rayleigh damping coefficients is shown in Fig. 6.38 and Table 6.17. MS9-6 is close to the borehole drilling A in previous research [35]. The RO parameters used for the soil column of MS9-6 is shown in Fig. 6.39, experimental data of Soil 1 and 2 were obtained from other research groups, curve fitting results were obtained by the SoilPlus. At the second and third layers, the Bowl model was used, parameters of them are shown in Fig. 6.40 (MS9-6−Soil 1) and Fig. 6.41 (MS9-6−Soil 2). The inputting parameters of each subsurface layer are shown in Tables 6.18 and 6.19, because the water table depth at MSA32 is 1.0 m, the first layer was split into two parts.

After nonlinear analyzing, the results of dynamic response are shown on Figs. 6.42 − 6.46. The liquefaction occurs and the nonlinear effect at MSA32 was a strong.

Table.6.16. Eigenvalue analysis of MS9-6.

Mode	Frequency (Hz)	Period (s)	Participation factor			Effective mass ratio			Modal damping ratio
			x	y	z	x	y	z	
1	0.91620	1.09150	60.59100	-76.93100	0.00000	0.10080	0.16250	0.00000	0.01100
2	0.91620	1.09150	-106.58000	-104.80000	0.00000	0.31200	0.30160	0.00000	0.01100
3	0.91620	1.09150	86.66000	-75.09900	0.00000	0.20620	0.15490	0.00000	0.01100
4	1.49800	0.66760	0.00000	0.00000	149.94000	0.00000	0.00000	0.61740	0.01100
5	1.84100	0.54320	54.20700	-54.25900	0.00000	0.08070	0.08090	0.00000	0.01100
6	1.84100	0.54320	65.56900	58.97600	0.00000	0.11810	0.09550	0.00000	0.01100
7	1.84100	0.54320	-24.57400	37.67300	0.00000	0.01660	0.03900	0.00000	0.01100
8	3.00970	0.33230	0.00000	0.00000	-88.35400	0.00000	0.00000	0.21440	0.01100
9	3.33900	0.29950	26.95500	-12.03000	0.00000	0.02000	0.00400	0.00000	0.01100
10	3.33900	0.29950	-20.49500	25.74400	0.00000	0.01150	0.01820	0.00000	0.01100

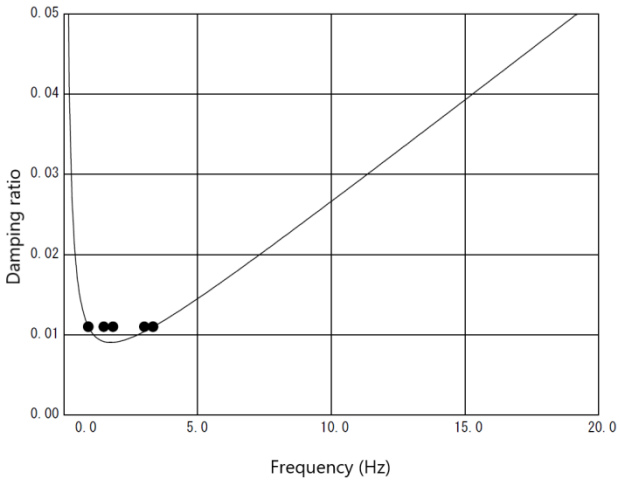

Fig. 6.38. Rayleigh damping calculation of MS9-6.

Table 6.17. Two coefficient factors of MS9-6.

α	8.2285 E-04
β	9.9378 E-01

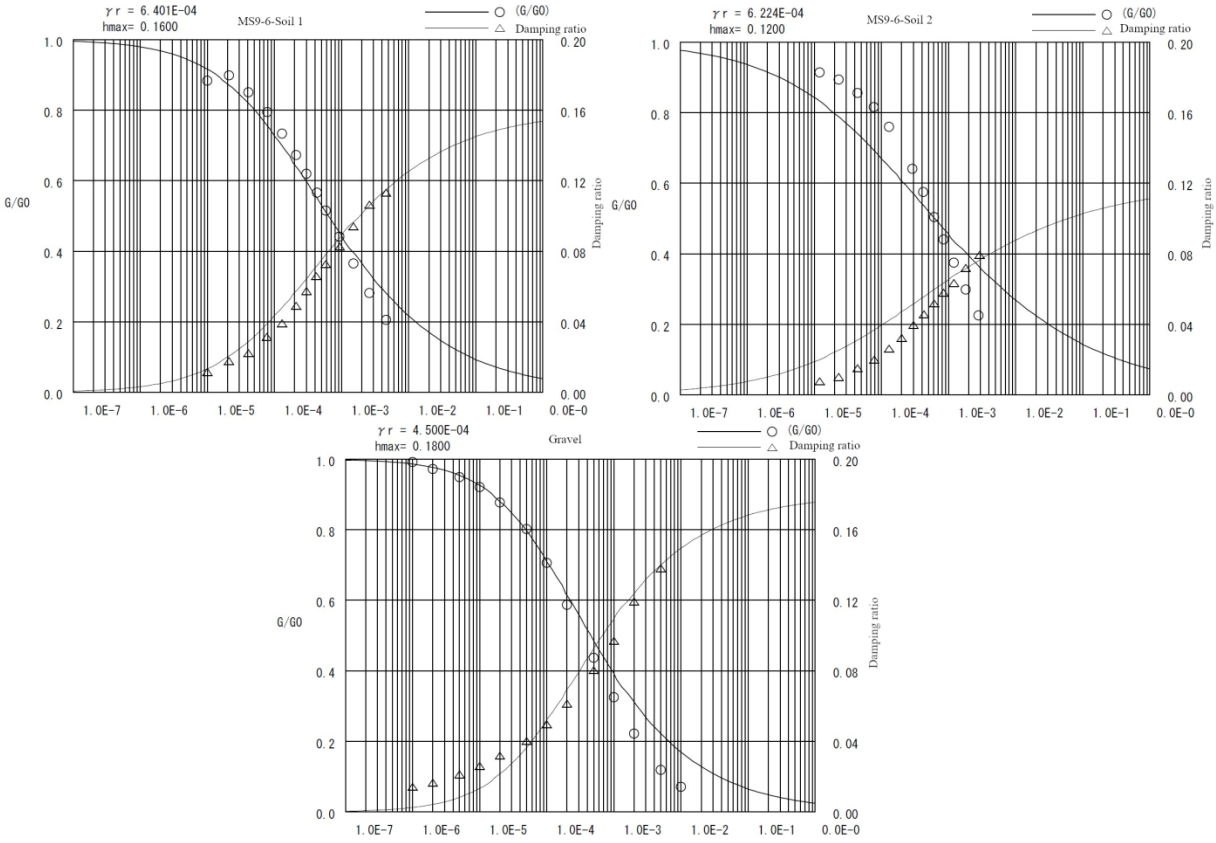

Fig. 6.39. RO parameters of three soil materials at MS9-6. Each panel includes the G/G_{max}–γ (left y-axis) and h–γ (right y-axis) relationships.

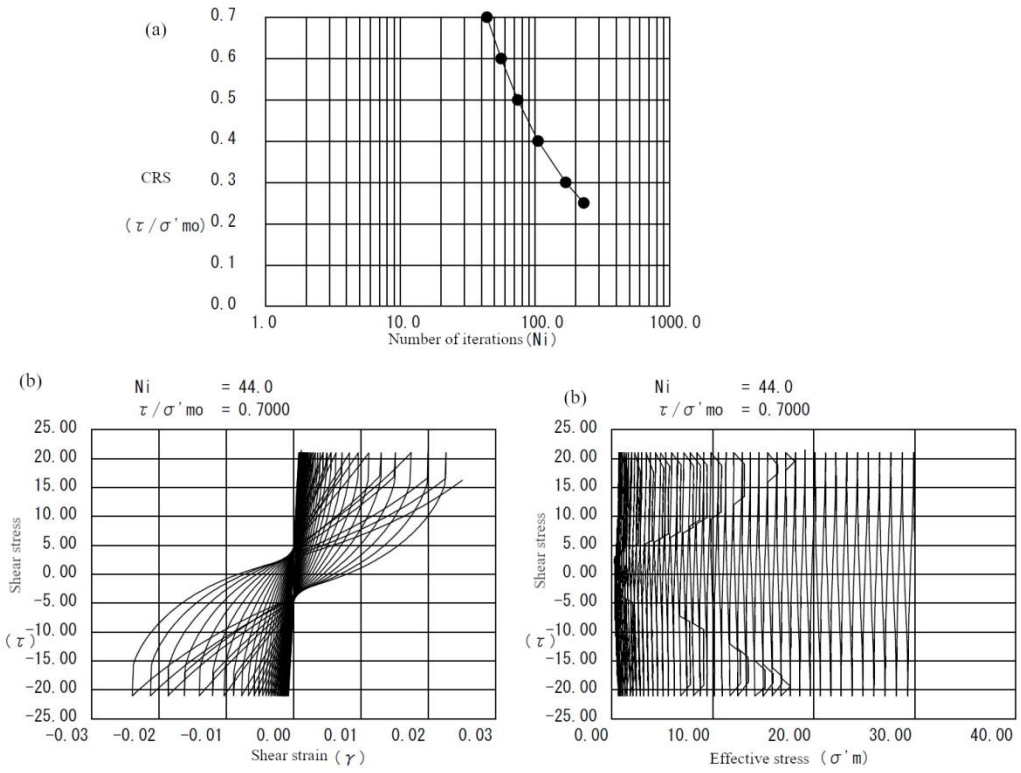

Fig. 6.40. Bowl parameters of the MS9-6−Soil 1. (a) is the CRS curve, (b) is the relationship between shear stress and strain when Ni=44.0, (c) is the relationship of shear stress and effective stress when Ni=44.0.

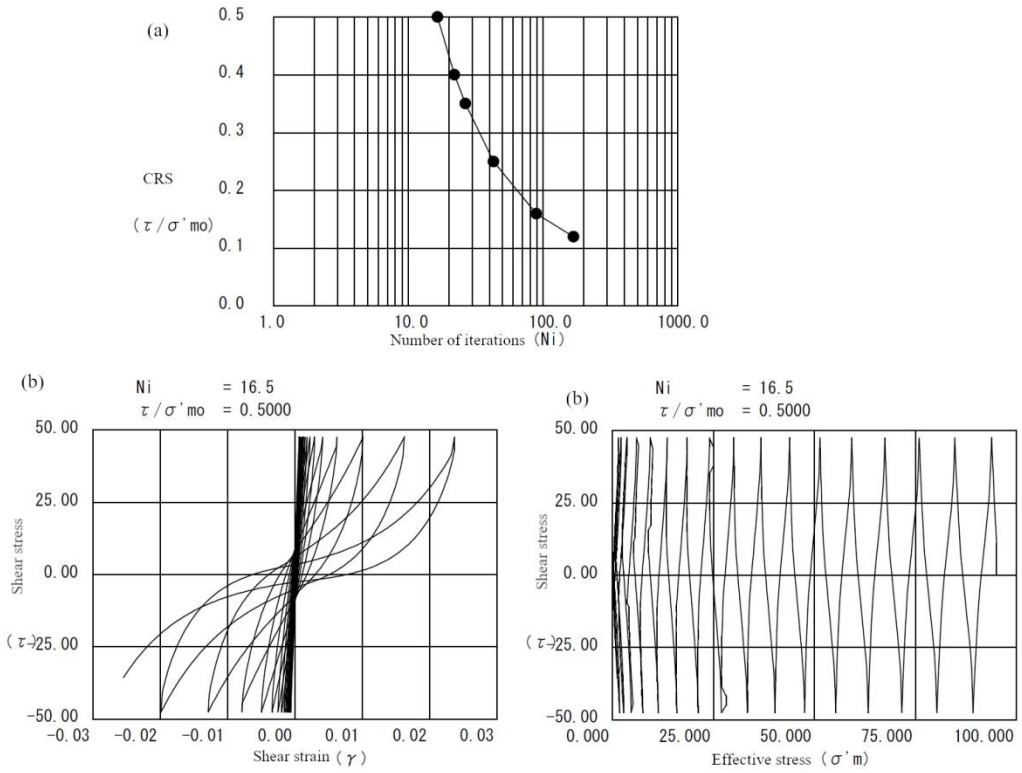

Fig. 6.41. Bowl parameters of the MS9-6−Soil 2. (a) is the CRS curve, (b) is the relationship between shear stress and strain when Ni=16.5, (c) is the relationship of shear stress and effective stress when Ni=16.5.

Table. 6.18. Information of soil column at MS9-6 and RO parameters.

Layer number	Depth(m),	Soil type	γ_t (kN/m3)	V_s(m/s)	V_p (m/s)	G_0 (kN/m2)	G_{0i} (kN/m2)	σ'_{m0} (kN/m2)	Experiment, σ'_{m0} (kN/m2)	RO-Model		
										$\gamma_{0.5}$	h_{max}	$\gamma_{0.5i}$
1	1.00	MS9-6_Soil 1	16.60	154.87	296.56	4.06E+04	1.73E+04	5.53	30	6.401E-04	0.16	1.169E-04
2	2.29	MS9-6_Soil 1	16.60	154.87	296.56	1.05E+05	2.82E+04	13.99	30	6.401E-04	0.16	1.169E-04
3	38.11	MS9-6_Soil 1	17.30	249.36	760.00	2.01E+05	1.94E+04	106.46	30	6.401E-04	0.16	1.169E-04
4	53.90	MS9-6_Soil 2	17.90	337.07	1841.61	2.08E+05	1.34E+04	238.65	95	1.400E-03	0.1507	1.436E-04
5	60.17	Gravel	18.70	483.09	1918.07	4.45E+05	2.57E+04	299.88	360	4.500E-04	0.18	2.372E-05
6	86.34	Gravel	19.20	598.03	1995.00	7.01E+05	3.50E+04	400.48	360	4.500E-04	0.18	2.370E-05
7	105.51	Gravel	19.70	733.19	1995.09	1.08E+06	4.63E+04	545.74	360	4.500E-04	0.18	2.370E-05
8	155.86	Gravel	20.00	790.10	2529.23	1.27E+06	4.56E+04	780.19	360	4.500E-04	0.18	2.370E-05
9	187.96	Linear	20.10	827.70	2558.47	1.41E+06	4.31E+04	1061.59				

Table. 6.19. Bowl parameters of soil material at MS9-6.

Layer	Bowl model						
	A	*B*	*C*	*D*	$C_s/(1+e_0)$	$C_c/(1+e_0)$	X_l
3	-1.2	1.4	8	15	0.02	0.022	0.12
4	-1	1.4	8	30	0.006	0.0062	0.1

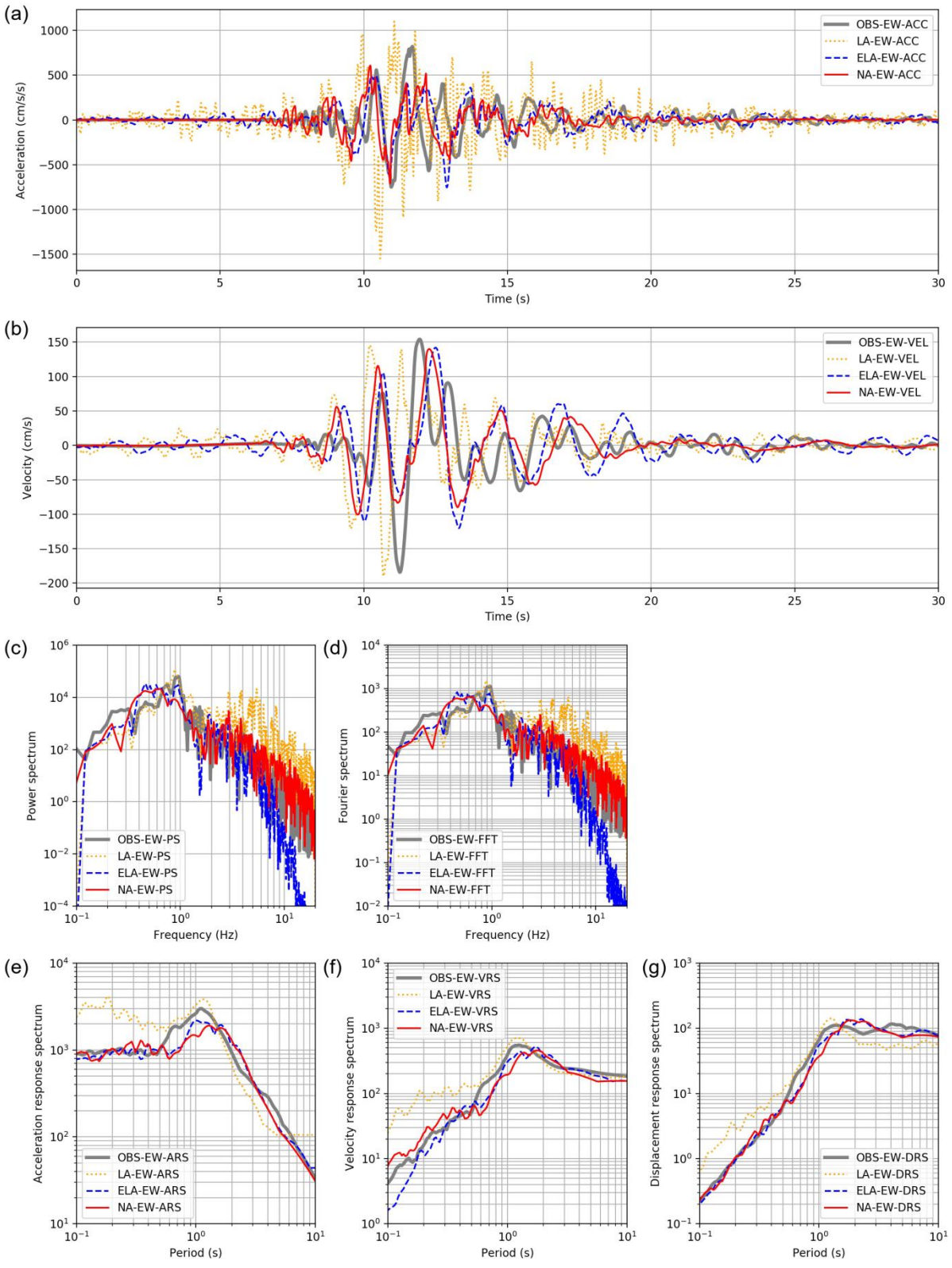

Fig. 6.42. Nonlinear dynamic analysis results of MS9-6 for the EW component. Meanings of each panel are similar to Fig. 6.15. Gray lines denote the results of observed ground motions at KMMP58.

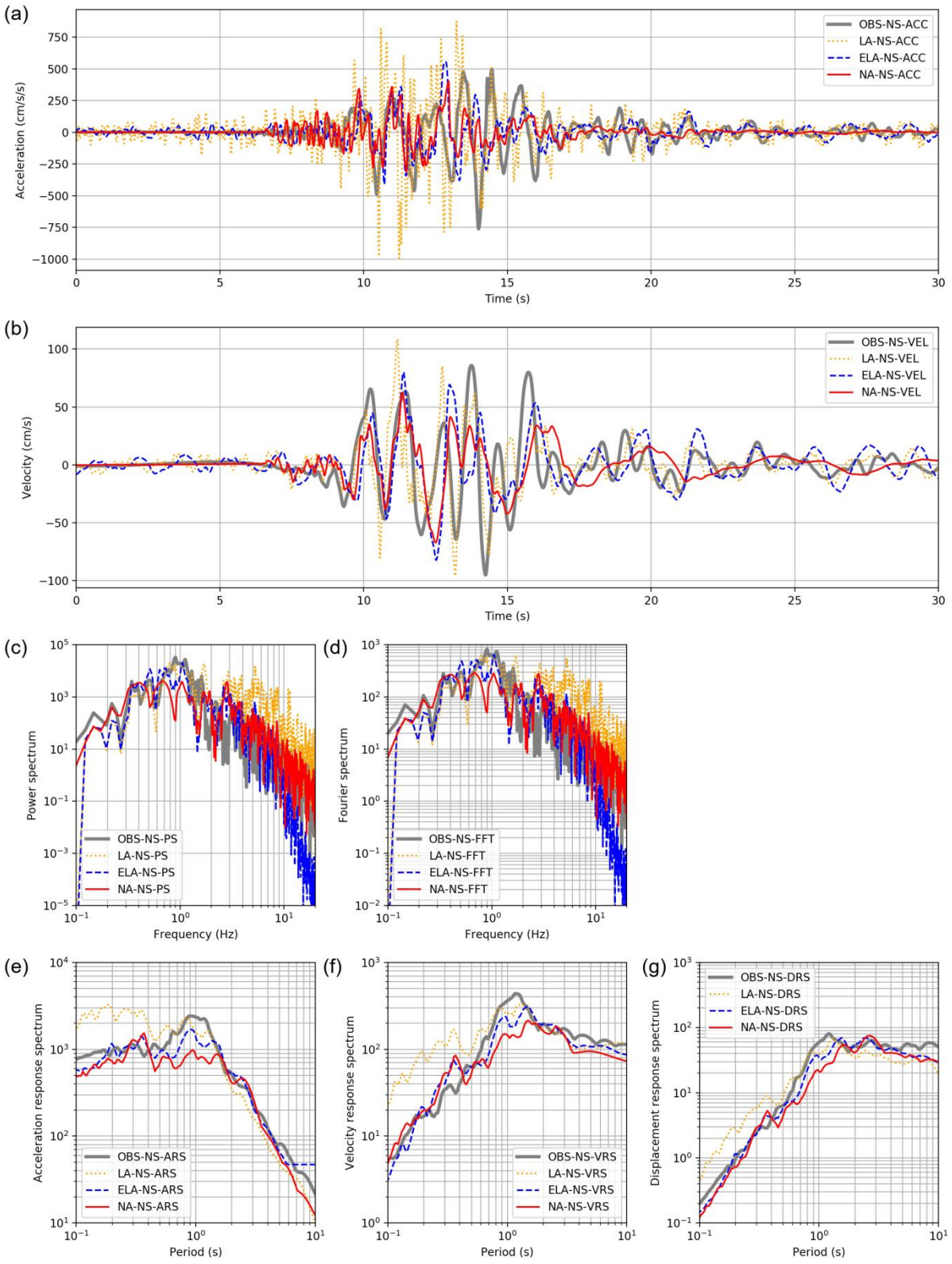

Fig. 6.43. Nonlinear dynamic analysis results of MS9-6 for the NS component. Meanings of each panel are similar to Fig. 6.15. Gray lines denote the results of observed ground motions at KMMP58.

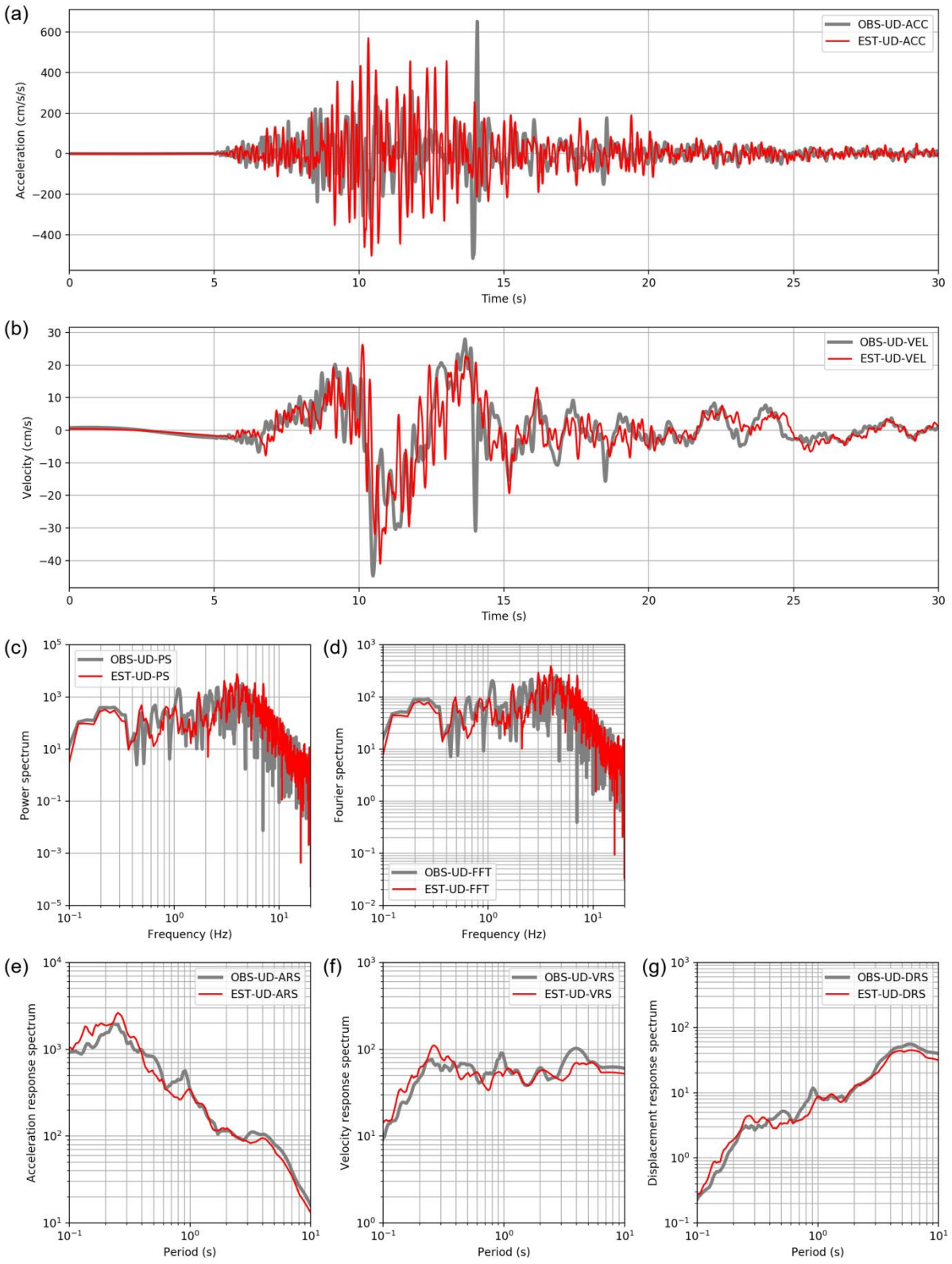

Fig. 6.44. Nonlinear dynamic analysis results of MS9-6 for the UD component. Meanings of each panel are similar to Fig. 6.15. Red and grey lines denote the results of estimation and observations.

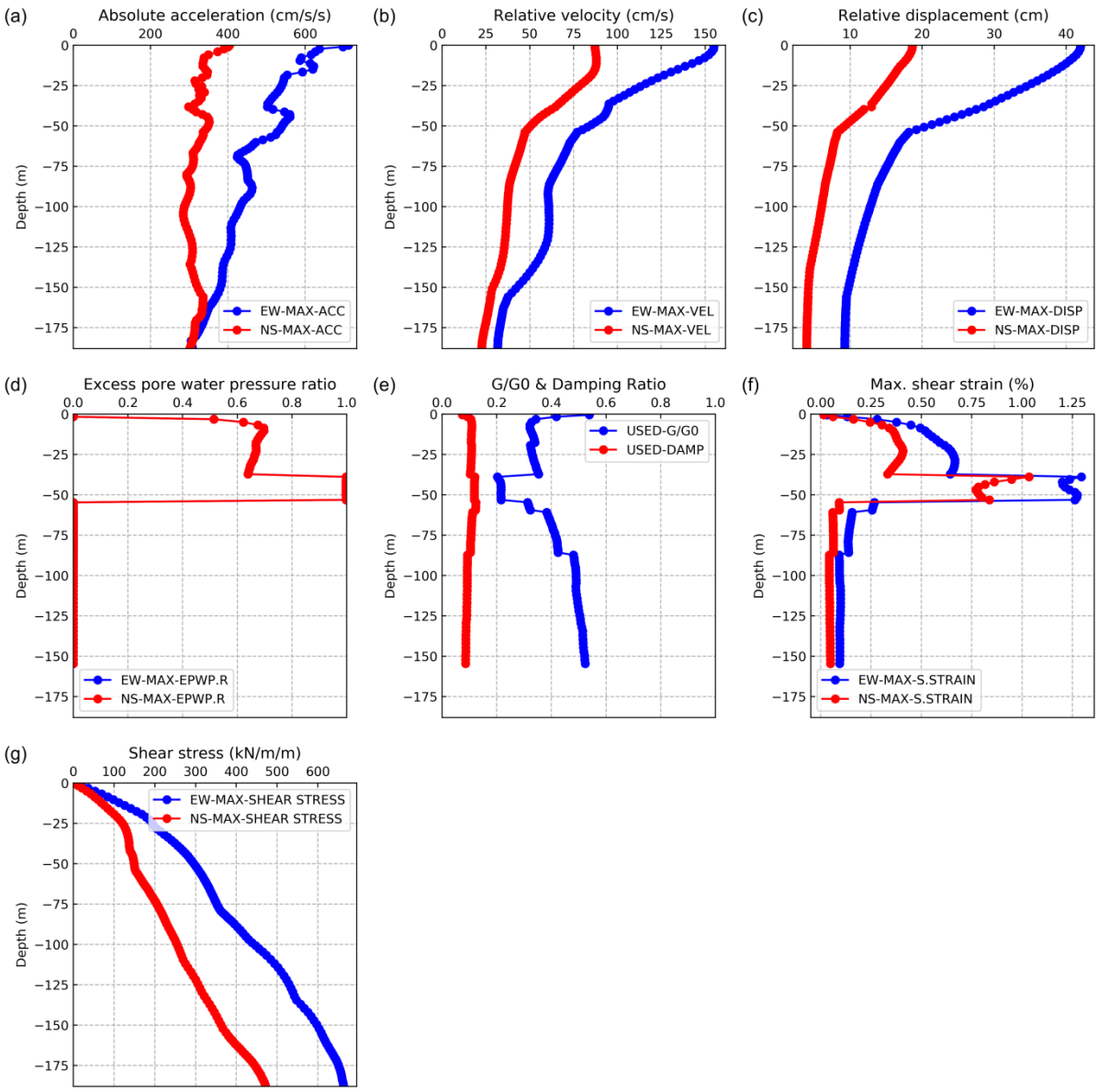

Fig. 6.45. Nonlinear response results of subsurface layers of soil column at MS9-6. Red and blue lines denote results of EW and NS directions, respectively. (a), (b), (c), (d), €, (f), and (g) Estimated absolute peak acceleration of every layer, estimated relative peak velocity of every layer, estimated relative peak displacement of every layer, estimated pore water pressure ratio of every layer, G/G_{max} and damping ratio used in the calculation of every layer, maximum shear strain of every layer, estimated shear stress of every layer.

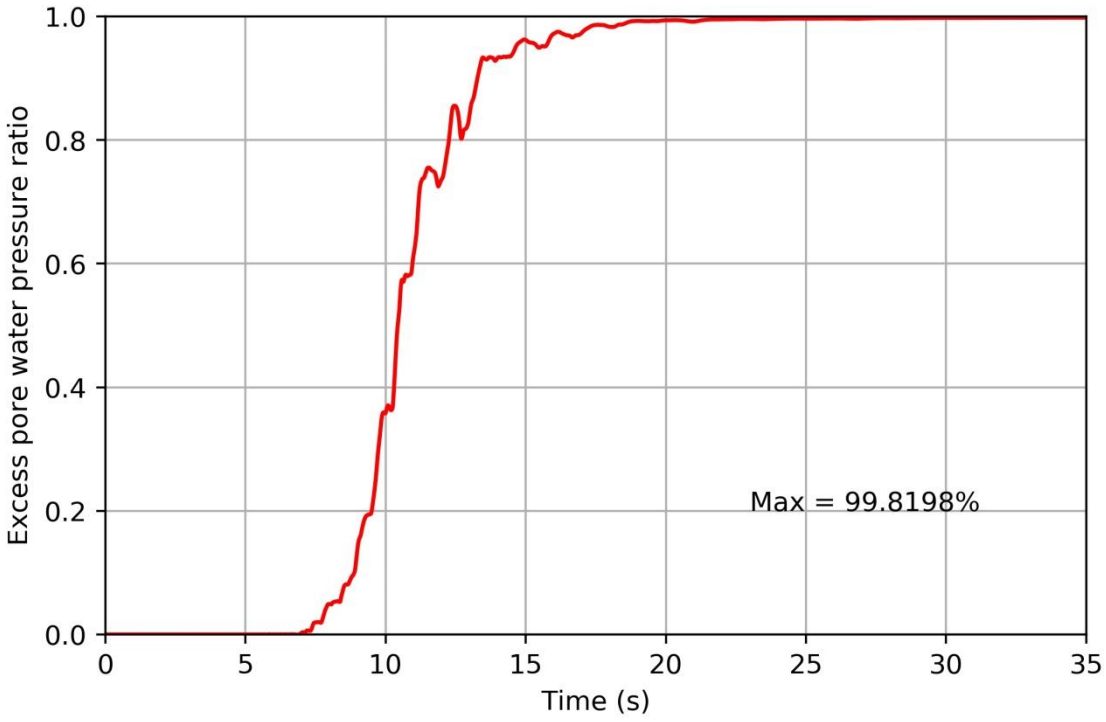

Fig. 6.46. Excess pore water pressure ratio of the Bowl model layer in time domain of MS9-6 soil. The maximum value was 99.8198%.

6.3.7. PGA and PGV distribution of Mashiki based on the NA

Because the results of site response with NA fit the reports of the mainshock of the 2016 Kumamoto earthquake, the 1D velocity structure of 592 sites with were classified into four categories, which correspond to the location relative to the four borehole drilling sites and subsurface velocity structures at these sites. It was also found that the water table depth have some relationship with the shallow stratigraphic classification of Mashiki [45,46]. Sites of every classification would be better to located in one region, the classification of southern part would be better to fit the flooding area near rivers in Mashiki, and make sure one borehole site located into one different category. Four categories of site classification are shown in Fig. 6.47.

Then, the NA was applied for soil columns of 592 sites. Soil property of each category was the same as the borehole drilling site as discussed above. Finally, the PGA and PGV distributions of Mashiki were obtained, based on the estimated 592 sets of seismic motions on the ground surface. According to Fig. 6.48, large PGAs were concentrated in two north regions, it was much clear when checking the PGA of NS direction. The PGV distribution was similar to the ELA estimated results, while the NA results showed more clear that the large PGV are and building heavy damaged area were in the same region. That explained the PGV is an important parameter to evaluate site risk in

Mashiki town. Also, the PGV is considered to be an important factor to evaluate the building damage in Japan wooden houses. Fig. 6.49 shows distribution of the maximum pore water pressure ratio in Mashiki. Sites near the river showed more likely to produce liquefaction at both the southern area sites and some eastern sites. This result is consistent with the Ministry of Land, Infrastructure and Transportation (MLIT) survey report and some other research results of liquefaction study in Mashiki.

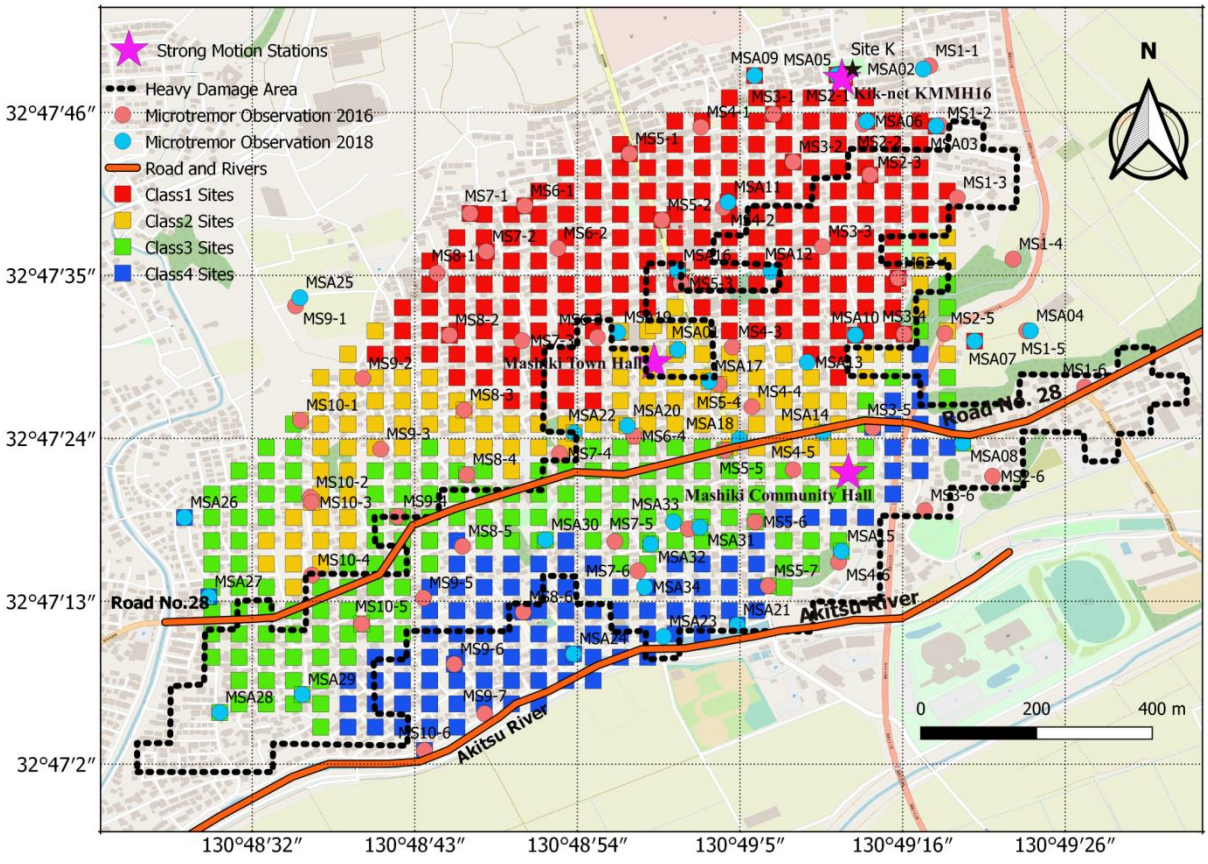

Fig. 6.47. Four categories of 592 sites in Mashiki. Red, yellow, green, blue regions denote water depth of these sites are 10.0−14.0 m, 5.0−10.0 m, 1.5−5.0 m, 1.0−1.5 m.

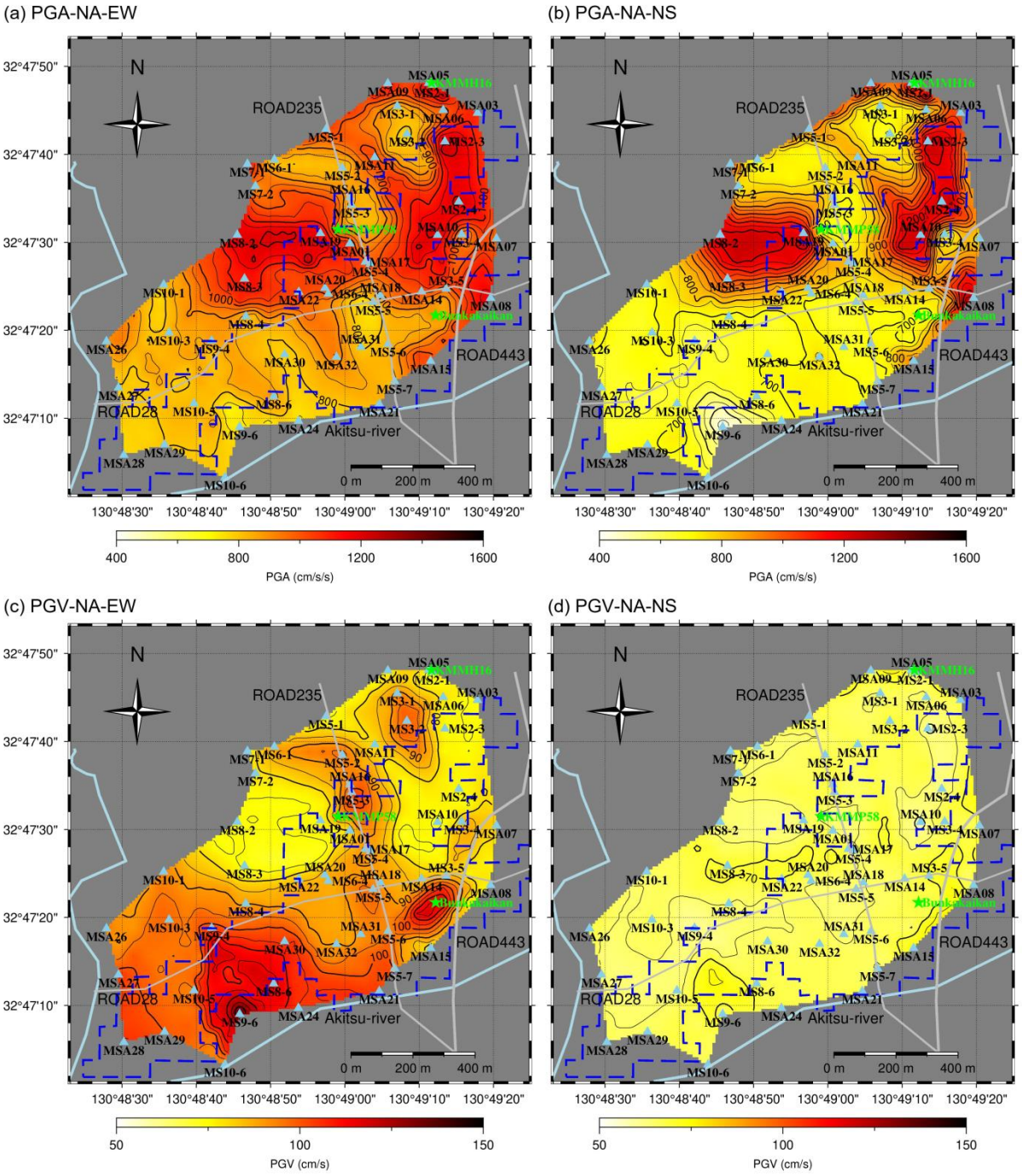

Fig. 6.48. PGA and PGV distribution of Mashiki by using NA. (a) and (b) The PGA distribution for EW and NS components, respectively. (c) and (d) The PGV distribution for EW and NS components, respectively.

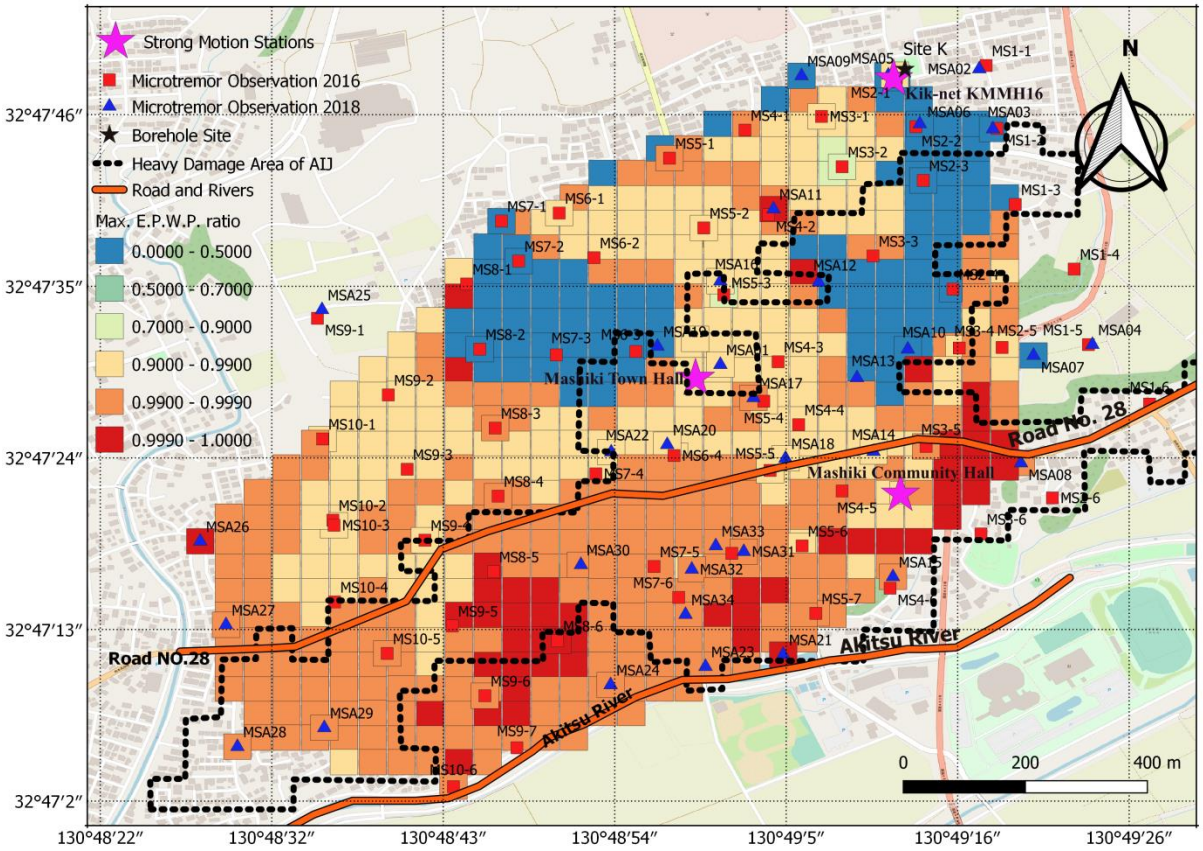

Fig. 6.49. Maximum pore water pressure of 592 sites in Mashiki.

6.4. Conclusion

Nonlinear analysis method including the RO and Bowl models are introduced in this Chapter. Soil nonlinear properties of four borehole drilling sites were obtained. Obviously, the characteristics of soil are different in different regions from northeast to southwest. Distribution of water table depth in Mashiki was investigated, and it gets shallower from northeast to southwest, which showed the similar tendency as the soil nonlinear properties in Mashiki. According to the estimated ground motions of KMMH16 by NA, the estimations fit observed ground motions very well. The results also confirmed that the influence of EW ground motions were stronger than that of NS during the mainshock. Associated with the comparison of estimated ground motions at MS9-6 and the observed ground motions at KMMP58, the estimated results were close to the observed ones. Soil liquefaction effect may be one of the reasons to cause the strong ground motions at KMMP58. As shown by the PGA and PGV distributions of NA results, NA-PGVs were closely related to the distribution of building damage distribution observed by the AIJ, while NA-PGAs did not appear the similar relations. According to the distribution map of the excess pore water pressure ratio in Mashiki, the highest ratios appeared along the river, especially near the Akitsu River, where has shallower water

table depth and soft soil materials. The estimated soil liquefaction site distribution showed close relationship to the distribution observed by MLIT and previous studies (Figs. 1.3 and 1.4), which showed all soil liquefaction sites were located in the southern area near the river. Influences of soil liquefactions were also obtained according to the comparisons of estimated ground motions. Comparing to the ELA results, the NA estimated ground motions were slightly smaller than the ELA results both in EW and NS directions. The difference showed the strong effects of soil liquefactions to the ground motions in Mashiki during the mainshock. In the southwestern area, NA estimations showed strong effects of soil nonlinear properties of shallow layers. Thus, NA is a better choice than the ELA to analyze site response for the region where happens soil liquefaction during a strong shake.

Reference (Chapter 6)

[1] KURITA T. NONLINEARITY AMPLIFICATION OF SUBSURFACE GROUND AT KIK-NET MASHIKI SITE DURING THE 2016 KUMAMOTO EARTHQUAKE. Journal of Japan Society of Civil Engineers, Ser A1 (Structural Engineering & Earthquake Engineering (SE/EE)) 2017;73:I_74-I_82. https://doi.org/10.2208/jscejseee.73.I_74.

[2] NAKANO T, MIYAMOTO Y, KAWABE H. NONLINEAR SOIL-STRUCTURE INTERACTION OF MASHIKI TOWN OFFICE SUBJECTED TO CONTINUOUS STRONG MOTIONS DURING THE 2016 KUMAMOTO EARTHQUAKE. Journal of Structural and Construction Engineering (Transactions of AIJ) 2018;83:781–91. https://doi.org/10.3130/aijs.83.781.

[3] KAGAMI Y, KIYOTA T, IKEDA T, MUHAMMAD U, KATAGIRI T. Study on ground subsidence of volcanic soil caused by the Kumamoto Earthquake. SEISAN KENKYU 2019;71:1071–4. https://doi.org/10.11188/seisankenkyu.71.1071.

[4] YASUHARA K, WATANABE M, KOBAYASHI K, ARAI Y, SATO K, HYODO M, et al. Residential instability caused by earthquake-induced degradation of volcanic ash cohesive soils. Japanese Geotechnical Journal 2020;15:225–39. https://doi.org/10.3208/jgs.15.225.

[5] Introduction of Landslide Disaster in the 2016 Kumamoto Earthquake. Ministry of Land, Infrastructure, Transport and Tourism; 2016.

[6] WAKAMATSU K, SENNA S, OZAWA K. Liquefaction and its Characteristics during the 2016 Kumamoto Earthquake. Journal of Japan Association for Earthquake Engineering 2017;17:4_81-4_100. https://doi.org/10.5610/jaee.17.4_81.

[7] Dafalias YF, University of California, California Institute of Technology. Overview of constitutive models used in VELACS. Verification of numerical procedures for the analysis of soil liquefaction problems, California: Balkema A; 1993, p. 1293–304.

[8] Iai S. Symposium on ground liquefaction countermeasures, section 4: Simultaneous calculation on liquefaction. 1991.

[9] Ishihara K. Symposium on the behavior of ground and soil structures during earthquakes, Committee report: 2. Effective stress analysis of ground and soil structures. 1989.

[10] Fukutake K. Research on three-dimensional liquefaction analysis of ground and structure systems considering multi-directional repeated shear characteristics of soil. PhD thesis. Nagoya Institute of Technology, 1997.

[11] Hakuno M, Tarumi Y. A GRANULAR ASSEMBLY SIMULATION FOR THE SEISMIC LIQUEFACTION OF SAND. Doboku Gakkai Ronbunshu 1988;1988:129–38. https://doi.org/10.2208/jscej.1988.398_129.

[12] Ogawa Y. Soil mechanical model for seismic response analysis, Japan: Proceedings of the 24th Soil Engineering Research presentation; 1989, p. 987–90.

[13] Jennings PC. Periodic response of a general yielding structure. Proc of ASCE 1964:131–63.

[14] Liou GP. Numerical model for liquefaction. vol. 103, Proc. ASCE; 1977, p. 589–606.

[15] Hara A. Dynamic deformation characteristics of soils and seismic response analysis of the ground. Japan: University of Tokyo; 1980.

[16] Hardin B, Drnevich V. Shear Modulus and Damping in Soils: Design Equations and Curves. J Soil Mech Found Div 1972;98.

[17] Iwasaki T. Analytical study of the effect of soil nonlinearity on the seismic response of the subsurface layers. Public Works Research Institute; 1980.

[18] Takura T, Shimizu K, Sato M, Hirose T, Yokota H. Study on nonlinear seismic response characteristics of the soil. Tokyo, Japan: Shimizu Corporation; 1988.

[19] Kenji I, Ikuo T. Ground response analysis considering dynamic pore water pressure, Japan: Proceedings of the 14th Soil Engineering Research Presentation; 1979, p. 1305–8.

[20] Towhata I, Ishihara K. Modeling Soil Behavior Under Principal Axes Rotation, Nagoya, Japan: Fifth International Conference on Numerical Methods in Geomechanics; 1985, p. 523–30.

[21] Bonilla L. NOAH: User's Manual, 2005.

[22] Martin GR, Finn WDL, Seed HB. Fundamentals of liquefaction under cyclic loading GED. ASCE 1975;101:423–38.

[23] Tanaka T, Tani S. Liquefaction Analysis of Cyclic Triaxial Test of Sand using the Endochronic Theory. Transactions of The Japanese Society of Irrigation, Drainage and Reclamation Engineering 1987;1987:51-61,a2. https://doi.org/10.11408/jsidre1965.1987.132_51.

[24] Zienkiewicz OC, Chang CT, Hinton E. Non-linear seismic response and liquefaction. International Journal for Numerical and Analytical Methods in Geomechanics 1978;2:381–404. https://doi.org/10.1002/nag.1610020407.

[25] Matsuoka G, Nakai T. Introduction to soil constitutive equation, section 6, granule theory and application. SOILS AND FOUNDATIONS 1984;32:83–91.

[26] Oda M. Introduction to constitutive equations of soil. 7: Microscopic structures and constitutive equations-Part 1 for granules. SOILS AND FOUNDATIONS 1984;32:67–73.

[27] Matsuoka H, Sakakibara K. A constitutive model for sands and clays evaluating prinsipal stress rotation. SOILS AND FOUNDATIONS 1987;27:73–88. https://doi.org/10.3208/sandf1972.27.4_73.

[28] MATSUOKA H, GEKA H. A STRESS-STRAIN MODEL FOR GRANULAR MATERIALS CONSIDERING MECHANISM OF FABRIC CHANGE. SOILS AND FOUNDATIONS 1983;23:83–97. https://doi.org/10.3208/sandf1972.23.2_83.

[29] Matsuoka G, Nakai T. A new three-dimensional stress-strain model for soil. SOILS AND FOUNDATIONS 1985;33:p15-23.

[30] Nakai T. Study on Deformation Strength Characteristics of Soil and Application to Deformation Analysis of Soil. PhD thesis. Kyoto University, 1981.

[31] Fukutake K, Ohtsuki A, Sato M, Shamoto Y. Analysis of saturated dense sand-structure system and comparison with results from shaking table test. Earthquake Engineering & Structural Dynamics 1990;19:977–92. https://doi.org/10.1002/eqe.4290190705.

[32] Fukutake K, Kiriyama T. LEAP-2017 Centrifuge Test Simulation using HiPER. Report on Institute of Technology, Shimizu Corporation 2017:18.

[33] engineering-eye: SoilPlus. engineering-eye 2021. http://www.engineering-eye.com/SOILPLUS/ (accessed February 12, 2021).

[34] Nagashima F, Kawase H. Estimation of the incident spectrum at the seismic bedrock by using the observed vertical motion at the ground surface based on diffuse field theory, Proceedings of the 15th Japan Earthquake Engineering Symposium; 2018.

[35] Arai H. Influence of ground characteristics in the center of Mashiki-cho on strong ground motion in the 2016 Kumamoto earthquake. BRI-H29 lecture; 2017.

[36] Nakazawa T, Sakata K, Sato Y, Hoshizumi H, Urabe A, Yoshimi M. Stratigraphy and distribution patttern of volcanogenic sediments beneath downtown Mashiki, Kumamoto, SW Japan, seriously damaged by the 2016 Kumamoto Earthquake. Jour Geol Soc Japan 2018;124:347–59. https://doi.org/10.5575/geosoc.2017.0077.

[37] Shingaki Y, Yoshimi M, Goto H, Kurata T, Sato K, Hosoya T, et al. Physical and dynamic properties of the volcanic ash soil in the heavily damaged site of the 2016 Kumamoto earthquake, Mashiki town. Journal of Japan Society of Civil Engineers, Ser A1 (Structural Engineering & Earthquake Engineering (SE/EE)) 2017;73:552–9. https://doi.org/10.2208/jscejseee.73.552.

[38] Akiba S, Murakami T, Hanyu K, Sato S, Torii M. The shallow subsurface structure of Mashiki town. 54th Geotechnical Research Presentation, Japan: 54th Geotechnical Research Presentation; 2019, p. 1905~1906.

[39] Geospatial Information Authority of Japan. Geospatial Information Authority of Japan. Geospatial Information Authority of Japan 2020. https://www.gsi.go.jp/ENGLISH/.

[40] Kawase H, Sanchez-Sesma FJ, Matsushima S. The optimal use of horizontal-to-vertical spectral ratios of earthquake motions for velocity inversions based on diffuse-field theory for plane waves. Bulletin of the Seismological Society of America 2011;101:2001–14. https://doi.org/10.1785/0120100263.

[41] Nagashima F, Matsushima S, Kawase H, Sanchez-Sesma FJ, Hayakawa T, Satoh T, et al. Application of Horizontal-to-Vertical Spectral Ratios of Earthquake Ground Motions to Identify Subsurface Structures at and around the K-NET Site in Tohoku, Japan. Bulletin of the Seismological Society of America 2014;104:2288–302. https://doi.org/10.1785/0120130219.

[42] Sun J, Nagashima F, Kawase H, Matsushima S. Site effects analysis of shallow subsurface structures at Mashiki town, Kumamoto, based on microtremor horizontal-to-vertical spectral

ratios. Bulletin of the Seismological Society of America 2020. https://doi.org/10.1785/0120190318.

[43] Yoshida N. DYNEQ - A computer program for Dynamic response analysis of level ground by Equivalent Linear Method. 2014.

[44] Bathe KJ. Finite Element Procedures. Prentice Hall; 2006.

[45] NILIM, BRI. Quick report of the field survey and the building damage by the 2016 Kumamoto earthquake. National Institute for Land and Infrastructure Management; 2016.

[46] Report on safety measures for the reconstruction of Mashiki Town for the 2016 Kumamoto Earthquake (final report). Ministry of Land, Infrastructure, Transport and Tourism; 2017.

Chapter 7

Investigation of building construction period in Mashiki

7.1. Introduction

7.2. Investigation of building construction period in Mashiki

7.3. Conclusion

References (Chapter 7)

7.1. Introduction

Buildings are usually constructed following the temporal building codes in Japan. After the 1995 Kobe earthquake, some studies showed the building seismic resistance behavior had a correlation with the building construction period [1–5]. Buildings constructed in accordance with the new building codes tend to have a better performance during the strong earthquake. After the 2011 Tohoku earthquake, some researchers also pointed out that the newly constructed buildings had better seismic properties [6–11]. Especially the buildings built after the 1995 Kobe earthquake had relatively less damage. During the 2016 Kumamoto earthquake, heavy damage on wooden houses were reported in downtown Mashiki, where researchers of the Architectural Institute of Japan (AIJ) made the field survey after the mainshock [12]. According to their results, 27% of wooden houses appeared heavy damage during the mainshock, and 65.8% of these heavy damaged wooden buildings were constructed before 1981, which means they were built in accordance with the old building codes in Japan. It is noted that the heavy damage of wooden buildings were evaluated in accordance with the earthquake damage standard for wooden buildings by Takai and Okada [13,14]. Thus, the building construction period is an important parameter when evaluate the building damage probability. Especially, Nagato and Kawase [3] developed the damage evaluation model and considering the building construction period as an important parameter in the model. Then Yoshida et al. [4,15] perfected their model and distinguished the construction period more finely.

Because it was expacted to use the damage evaluation model of Yoshida (Yoshida model) in the next section, to estimate the damage probability of wooden houses in Mashiki, the construction period of every building is required to be figured out in downtown Mashiki in accordance with the regulations of the Yoshida model.

7.2. Investigation of building construction period in Mashiki

Yamada et al. [16] used the aerial photos of Mashiki taken before and after the foreshock and mainshock to identify the collapsed buildings and building ages. They divided all buildings in to the follow categories: (1) before 1967, (2) 1967–1975, (3) 1975–1982, (4) 1982–1986, (5) 1986–1997, (6) 1997–2008, and (7) after 2008. This research method was applied, and aerial photo taken in 1947 and 1956 were obtained from the Geospatial Information Authority of Japan (GSI, see Data and Resources). The research steps were as follows.

1) Obtaining the coordinates of all building centroids in the target area by referring to OpenStreetMap (OSM, see Data and Resources). The green dots on Fig. 7.1 represent the location of building center points in Mashiki.
2) Checking the building construction periods by referring to Yamada et al. [16]. They had defined construction periods of as before 1967, 1968–1975, 1976–1981, 1982–1986, 1987–1997, 1998–

2008, and after 2008. These results were obtained through an analysis of aerial photos shared by the Geospatial Information Authority of Japan (GSI). Then, the construction periods of our target area as before 1967, 1967–1981, and after 1982 were re-checked and re-defined. Here, I showed the building construction periods by referring to results of Yamada et al in Figure 6.2. The black, carmine, blue, and green dots denote the re-checked building locations of before 1967, 1967–1981, after 1981.

3) The geographical coordinates of buildings in the AIJ survey with a construction period after 1982 was obtained. All of the buildings were located within the heavy black dashed line as shown in Fig. 7.1. We checked all of these buildings and corrected any information contradicting the AIJ survey data.
4) For buildings with construction periods before 1967, their locations were compared with aerial photos captured in 1947 and 1956 (GSI, see Data and Resources). The building locations before 1967 and aerial photo which was taken at 1947 are presented in Fig. 7.3. For buildings with a 1967–1981 construction period, the locations in aerial photos captured in 1964 and 1975 (GSI) were re-checked. Fig. 7.4 presents the building locations before 1975 and the aerial photo captured at 1975. After this step, the database of construction period as before 1947, 1947–1956, 1956–1967, 1967–1975, 1975–1981, and after 1981 was obtained.
5) Comparing the results with Moya et al. [17] to correct and confirm the database for buildings between Road No.28 and Akitsu River in Mashiki. Then, a database was established for the actual construction period of each building in Mashiki.
6) According to the Yoshida model, 1951, 1971, and 1981 are important transitions for construction periods. Because aerial photos captured exactly in 1951 and in 1971 were difficult to obtain, we assumed construction periods for the database to correspond with the construction periods used in the Yoshida model, as given in Table 7.1. Finally, a distribution map of the construction periods was obtained for the target area following the same standards as those used in the research of Yoshida et al. [4,15], as shown in Fig. 7.5.

The statistics analysis results of building construction periods of the new database was compared with those of Yamazaki et al. [18], as depicted in Fig. 7.6. The overall matching was satisfactory. A slightly lower percentage of buildings constructed before 1950 was obtained than Yamazaki et al. because it counted buildings based on an aerial photo that was captured in 1947, so 3 years were missed. A larger percentage of buildings constructed during 1951–1970 were obatained because this period included buildings constructed during 1947–1975. A slightly larger percentage of buildings constructed before 1950 and during 1951–1970 than Yamazaki et al were presented. This may be because the number of older buildings built before 1970 in the target area was slightly more than that of the entire downtown Mashiki. For buildings built after 1982, our result was close to those of Yamazaki et al.

Table 7.1. Comparison of real construction periods and those used in the Yoshida model.

Real Construction Period	Building Construction Period used in the Yoshida Model
Before 1947	Before 1950
1947-1956	1951-1970
1956-1967	
1967-1975	
1975-1981	1971-1981
After 1981	After 1982

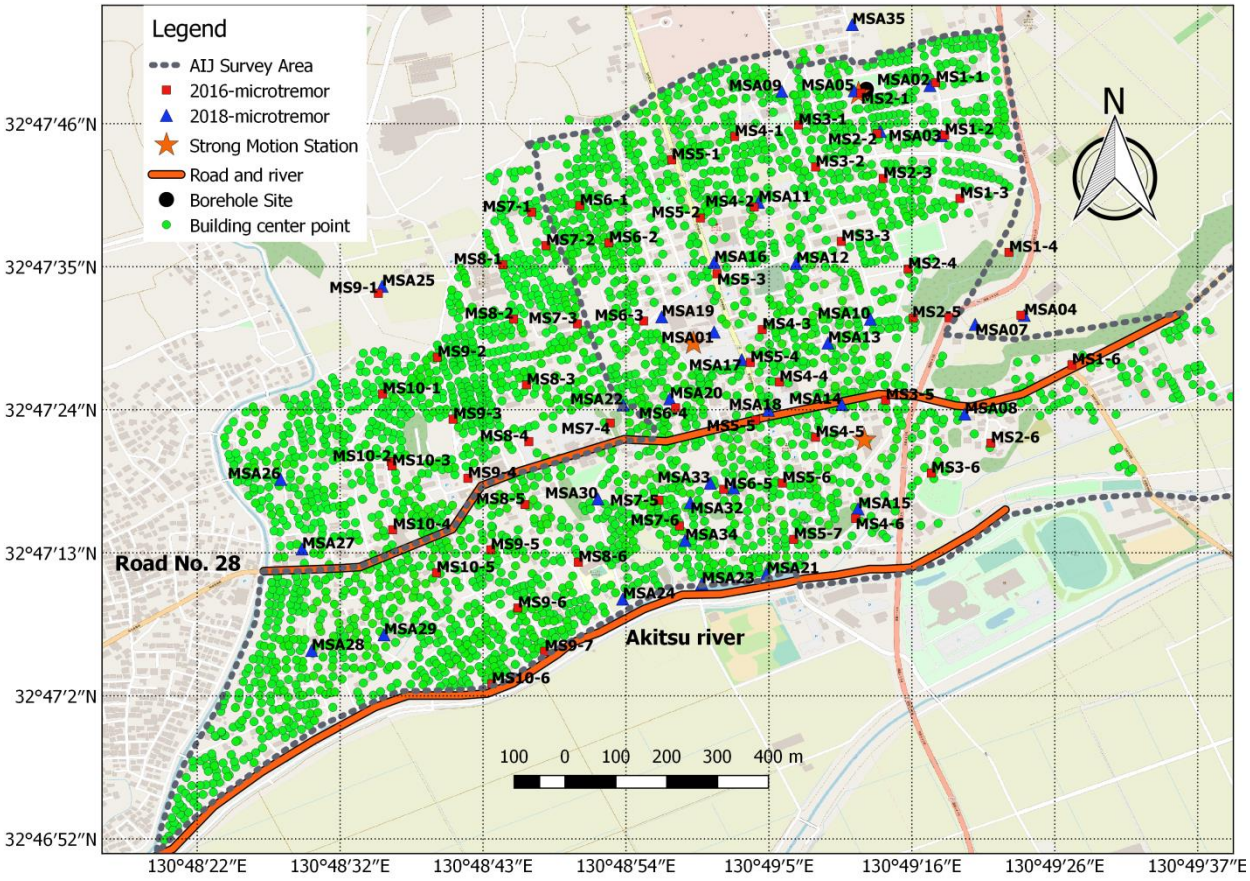

Fig. 7.1. Center point locations of buildings in Mashiki. Green dots denote the locations of building center points, black dashed lines denotes the AIJ survey area, blue triangles denote the location of 2018 microtremor observation sites, red rectangles denote the location of 2016 microtremor observation sites. Background map was obtained from the OpenStreetMap (see Data and Resources).

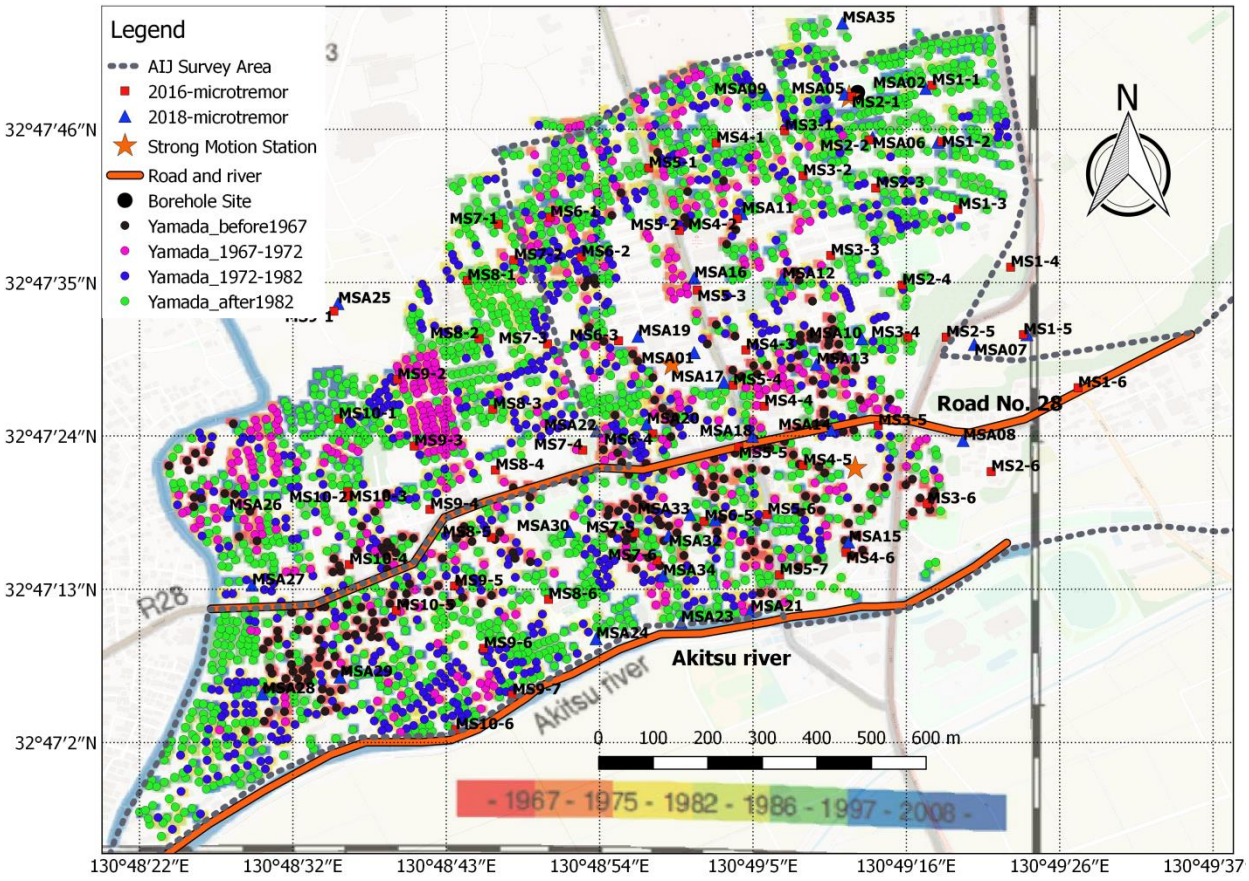

Fig. 7.2. Building locations re-checked based on the results of Yamada et al. [16]. The black, carmine, blue, and green dots denote the re-checked building locations of before 1967, 1967–1981, after 1981. Other markers have the same meaning as Fig. 6.1. Background maps were obtained from the results of Yamada et al. and the OpenStreetMap.

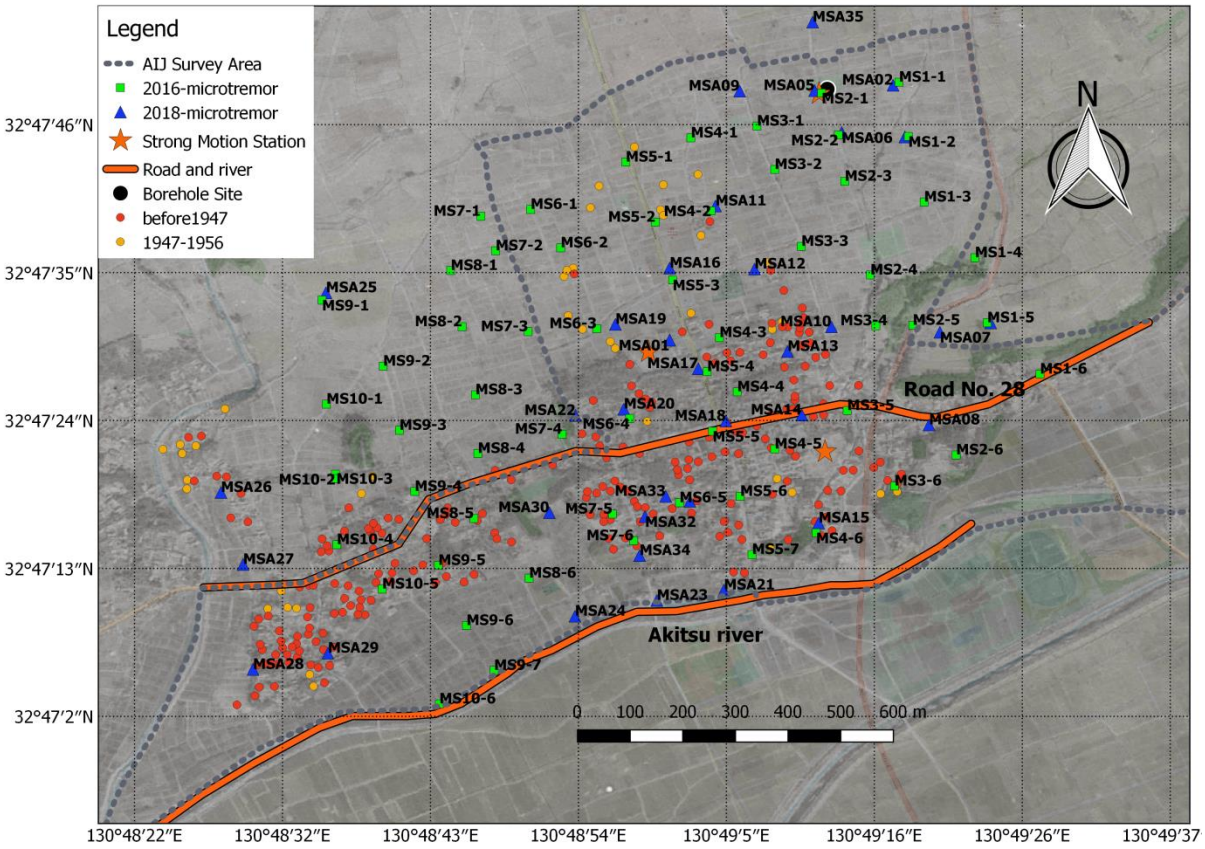

Fig. 7.3. Classification of buildings before 1967. The red dots denote the building before 1947, and the yellow dots denote the building 1947–1967. Building locations were obtained from buildings before 1967 as shown in Fig. 6.2. Background maps were aerial photo taken at 1947 obtained from the GSI and the OpenStreetMap.

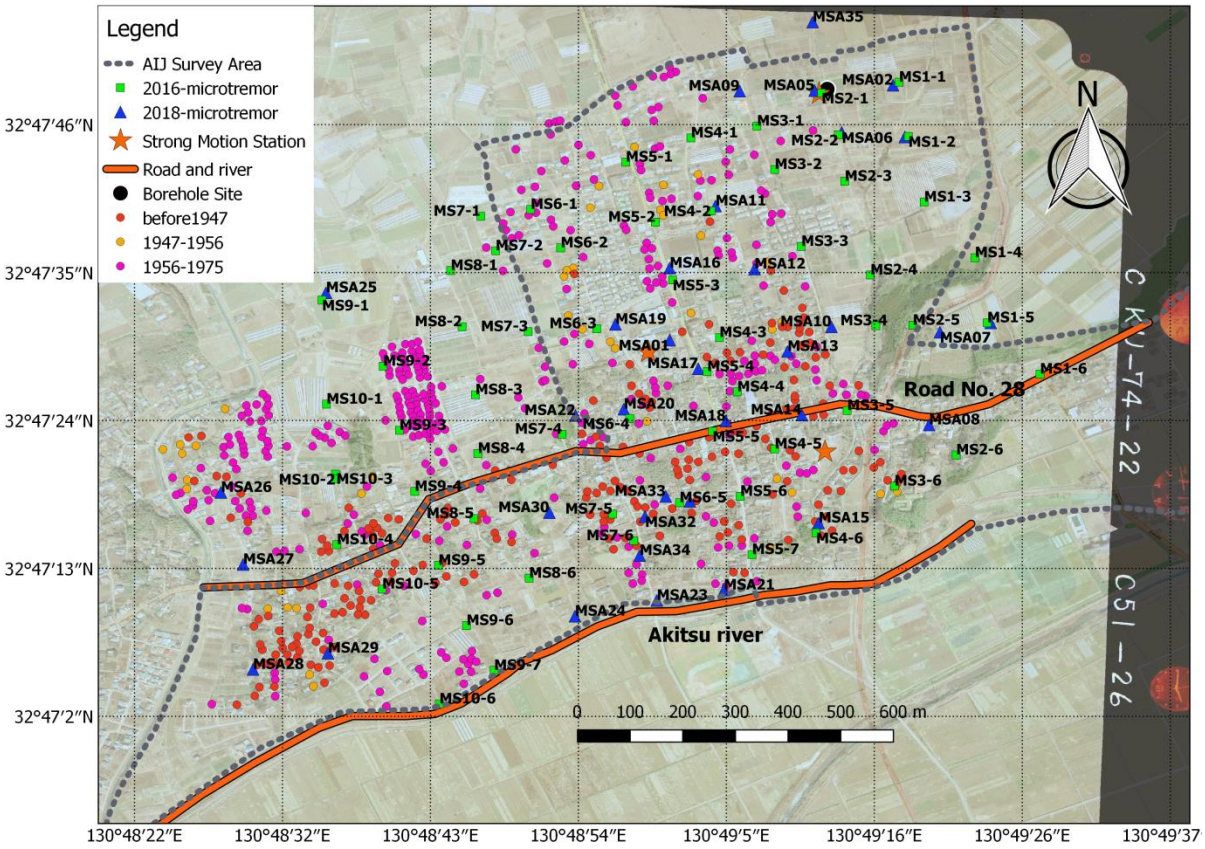

Fig. 7.4. Classification of buildings before 1975. The red, yellow, and purple dots denote the building before 1947, 1947–1967, and 1967–1975. Background maps were the aerial photo captured at 1975 and the OpenStreetMap.

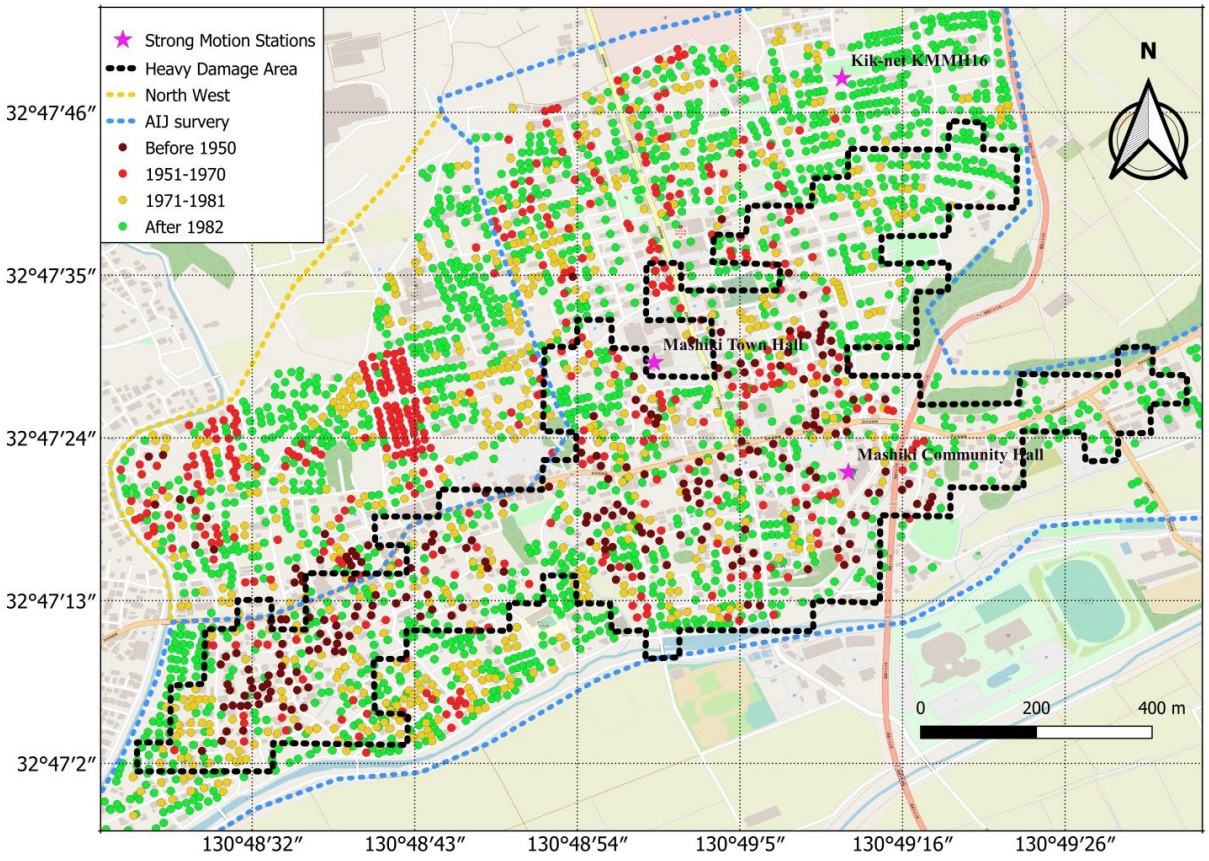

Fig. 7.5. Definition of the construction periods for all buildings in the target area. The black, blue, and yellow dashed lines denote the heavily damaged area, AIJ field survey area, and northwestern part not surveyed by the AIJ, respectively. The three stars mark the strong motion stations, as in Fig. 1. The dark red, red, yellow, and green dots mark buildings built before 1950, during 1951–1970, during 1971–1981, and after 1982, respectively. The background was taken from OpenStreetMap.

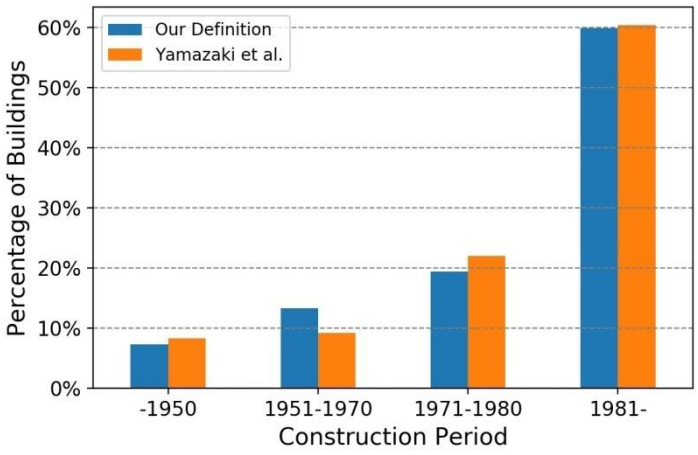

Fig. 7.6. Statistical analysis of construction periods. The blue and orange columns denote our results and those of Yamazaki et al., respectively.

7.3. Conclusion

Construction periods of buildings in Mashiki were investigated based on the historical aerial photos and several previous studies. Four categories of buildings based on the construction period associated to the Yoshida model were obtained. According to the comparisons with Yamazaki et al.[18], the new investigated buildings in this Chapter of before 1970 were slightly more than theirs, while the buildings of 1971−1981 were slightly less than theirs. It means that there are slightly more old buildings in the central Mashiki than in other areas. Comparison results indicate the investigated construction periods of wooden houses in the central Mashiki were suitable to use for the next step.

Reference (Chapter 7)

[1] NIED. Study on seismic fragilities of categorized wooden houses. NIED; 2004.

[2] Murao O, Yamazaki F. Development of fragility curves for buildings based on damage survey data of a local government after the 1995 Hyogoken-Nanbu earthquake. Journal of Structural and Construction Engineering (Transactions of AIJ) 2000;65:189–96. https://doi.org/10.3130/aijs.65.189_1.

[3] Nagato K, Kawase H. Damage evaluation models of reinforced concrete buildings based on the damage statistics and simulated strong motions during the 1995 Hyogo-ken Nanbu earthquake. Earthquake Engineering & Structural Dynamics 2004;33:755–774. https://doi.org/10.1002/eqe.376.

[4] Yoshida K, Hisada Y, Kawase H. Construction of damage prediction model for wooden buildings considering construction age, Hokkaido: 2004.

[5] Hayashi Y, Miyakoshi J, Tasai A, Ohno Y. Seismic performance of RC buildings during Hyogo-Ken Nanbu earthquake. Journal of Structural and Construction Engineering (Transactions of AIJ) 2000;65:135–42. https://doi.org/10.3130/aijs.65.135_1.

[6] Building Research Institute, National Institute for Land and Infrastructure Management. 2011 Tohoku-Pacific ocean earthquake damage survey report by Building Research Institute. 2017.

[7] Wu H, Masaki K, Irikura K, Kurahashi S. Empirical Fragility Curves of Buildings in Northern Miyagi Prefecture During the 2011 off the Pacific Coast of Tohoku Earthquake. Journal of Disaster Research 2016;11:1253–70. https://doi.org/10.20965/jdr.2016.p1253.

[8] Yu J, Kanakubo T, Yasojima A. Damage Tendency of Public School Buildings in Ibaraki Prefecture Suffered in 2011 Off The Pacific Coast of Tohoku Earthquake. Journal of Japan Association for Earthquake Engineering 2014;14:2_164-2_180. https://doi.org/10.5610/jaee.14.2_164.

[9] Motosaka M, Mitsuji K. Building damage during the 2011 off the Pacific coast of Tohoku Earthquake. Soils and Foundations 2012;52:929–44. https://doi.org/10.1016/j.sandf.2012.11.012.

[10] Japan Meteorological Agency. Report on the 2011 off the Pacific coast of Tohoku Earthquake by Japan Meteorological Agency. Tokyo: Japan Meteorological Agency; 2012.

[11] MIDORIKAWA S, ITO Y, MIURA H. Vulnerability Functions of Buildings based on Damage Survey Data of Earthquakes after the 1995 Kobe Earthquake. Journal of Japan Association for Earthquake Engineering 2011;11:4_34-4_47. https://doi.org/10.5610/jaee.11.4_34.

[12] NILIM, BRI. Quick report of the field survey and the building damage by the 2016 Kumamoto earthquake. National Institute for Land and Infrastructure Management; 2016.

[13] Takai N, Okada S. Classifications of damage patterns of reinforced concrete buildings for earthquake field investigation. Journal of Structural and Construction Engineering (Transactions of AIJ) 2001;66:67–74. https://doi.org/10.3130/aijs.66.67_4.

[14] Okada S, Takai N. Classifications of structural types and damage patterns of buildings for earthquake field investigation. Journal of Structural and Construction Engineering (Transactions of AIJ) 1999;64:65–72. https://doi.org/10.3130/aijs.64.65_5.

[15] Yoshida K, Hisada Y, Kawase H, Fushimi M. Study of damage rate function and destructive force index of wooden buildings based on seismic response analysis, Kinki: Abstracts of the 2005 Architectural Institute of Japan Conference; 2005, p. 161–2.

[16] Yamada M, Ohmura J, Goto H. Wooden building damage analysis in Mashiki town for the 2016 Kumamoto earthquakes on April 14 and 16. Earthquake Spectra 2017;33:1555–1572. https://doi.org/10.1193/090816EQS144M.

[17] Moya L, Mas E, Koshimura S, Yamazaki F. Synthetic building damage scenarios using empirical fragility functions: A case study of the 2016 Kumamoto earthquake. International Journal of Disaster Risk Reduction 2018;31:76–84. https://doi.org/10.1016/j.ijdrr.2018.04.016.

[18] Yamazaki F, Suto T, Matsuoka M, Horie K, Inoguchi M, Liu W. Statistical analysis of building damage in Japan based on the 2016 Kumamoto earthquake. 17th US-Japan-New Zealand Workshop on the Improvement of Structural Engineering and Resilience 2018.

Chapter 8

Damage probability estimations of Mashiki wooden houses using estimated ground motions of linear, equivalent linear, and nonlinear analyses

8.1. Introduction
8.2. Nonlinear response models of wooden building
8.3. Building damage probability estimation of KMMH16
    8.3.1. Using the ELA ground motions
    8.3.2. Using the NA ground motions
8.4. Damage probability estimation of Mashiki
    8.4.1. Damage probability estimation results of ELA
    8.4.2. Damage probability estimation results of NA
8.5. Conclusion
References (Chapter 8)

8.1. Introduction

Earthquakes will cause a large amount of economic losses and casualties, while a major part of seismic losses are contributed by building damages under strong ground motions [1,2]. Therefore, an accurate prediction of seismic damage to buildings on a reginal scale is important for modern city planning and post-earthquake rescue, which will help to mitigate direct/indirect seismic losses [3,4]. In global wise view, existing approaches for seismic damage evaluation of buildings on a reginal scale mainly include the damage probability matrix method [5,6], the spectrum method [7], and methods based on time history analysis [8–10]. The damage probability matrix method relies greatly on historical damage data, which are not easily adopted for areas without sufficient statistical data. The capacity spectrum method can, to some extent, consider the seismic resistance of individual buildings and the spectral characteristics of different ground motions. However, the effects of duration and pulse-like ground motions, or high-order vibration modes of buildings, cannot be fully considered by this method. The dynamic analysis of structures can fully consider the nonlinear response characteristics of buildings as well as intensity, frequency content, and duration characteristics of ground motions, thus, this method is suitable for seismic damage simulation of buildings [8,11,12].

Nagato and Kawase [8] developed a seismic response analysis model (i.e., Nagato-Kawase model) for multi-story structures, based on the building damage statistics for the Kobe city after the 1995 Kobe earthquake. They consider the construction period is an important factor for estimate building damage. They establish a set of models for damage evaluation that can be used to explain the observed damage data in Kobe city after the mainshock. They successfully reproduced the damage belt in Kobe, based on the estimated ground motions of Kawase [13], and Matsushima and Kawase [14]. This work established a standard model of the common two-story wooden houses in the Kobe area associated with the Japanese building code. Further, Yoshida et al. [11,15] enhanced the standard model of Japanese wooden houses to consider four construction periods (i.e. Yoshida model) before 1950, 1951–1970, 1971–1981, and after 1982. Thus, the local ground motions and construction period should be considered when estimating the damage to wooden houses.

A statistical analysis of the damage to wooden houses obtained from the AIJ survey report is depicted in Fig. 8.1. The buildings were classified into six categories based on the main construction material: wooden structure, steel structure, reinforced concrete (RC) structure, hybrid structure, others, and unknown [16]. For the hybrid structure, the main building material varied between different floors; for example, RC or steel was used in the first floor of the building, whereas wood was on the second floor. The other structures used steel or other materials in certain parts of the building. In total, the AIJ surveyed 2,340 buildings: 1,955 wooden, 276 steel, 52 RC, 32 hybrid, 21 other, and 4 unknown. Thus, most of the buildings in this area were wooden (83.5%). Because Japan updated the seismic code for buildings in June 1981, the AIJ survey results are separated as before and after 1981 in Fig. 8.1. D0 to D6 indicate the damage level according to the damage grade used by the AIJ [16–18]. Fig. 8.2 defines

different damage grades and how they compare to each other for each damage level. The meanings of each damage level for the 2016 Mashiki building damage survey was followed the Damage Grade #4 in Fig. 3. Sugino et al. [19] and Murase et al. [20] also did the study of building damage investigations in the central Mashiki. The heavily damaged buildings were also located in the area between the Road No.28 and Akitsu River in the southern part.

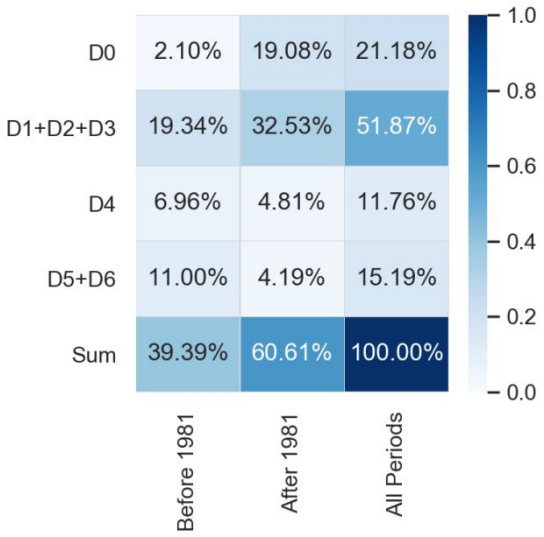

Fig. 8.1. Statistical analysis of the damage to the wooden houses in Mashiki [16]**. The x-axis denotes the construction period, and the y-axis denotes the damage grade used in the AIJ survey and the corresponding damage index.**

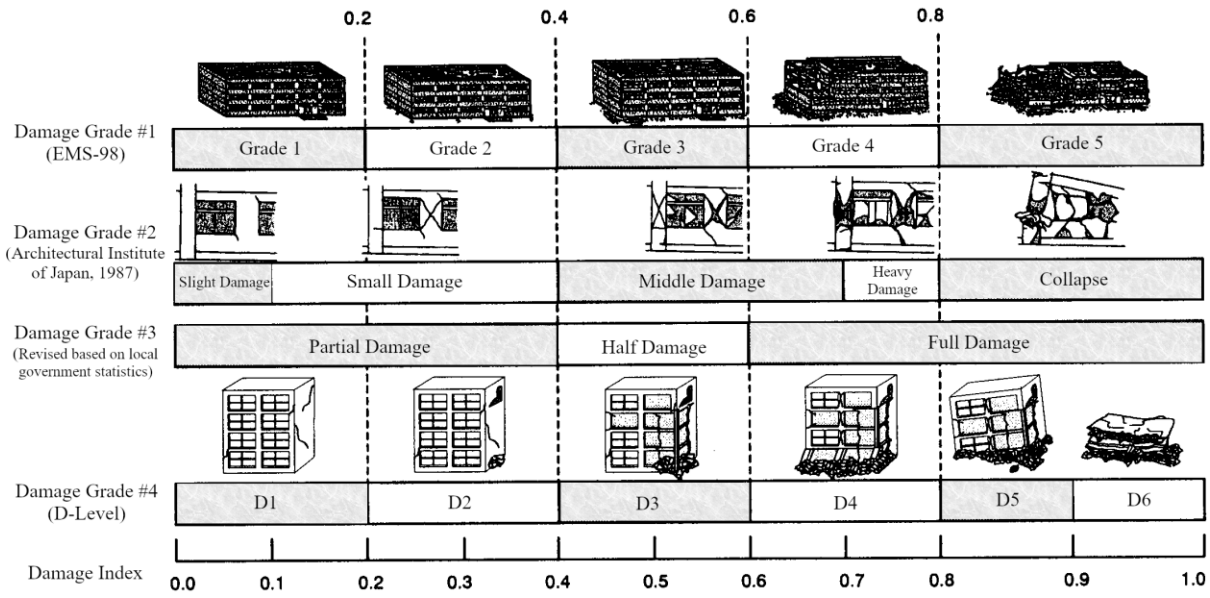

Fig. 8.2. Four damage grade standards and damage index used in Japan. Damage Grade #1 is the European Macroseismic Scale 1998 [21]**. Damage Grade #2 is the AIJ 1987 standard. Damage Grade #3 is used in the Yoshida model. Damage Grade #4 was used for the AIJ survey after the 2016 Kumamoto earthquakes. This figure is edited based on the results of Takai and Okada** [18]**.**

In Chapter 7, the construction period of every building in Mashiki were investigated. In Chapter 5, the strong ground motions of 592 sites in Mashiki during the mainshock were calcluated using the equivalent linear analysis (ELA). In Chapter 6, the strong ground motions of 592 sites in Mashiki during the mainshock were obtained using the nonlinear analysis (NA). Therefore, all preparations for the building damage probability evaluation in Mashiki have been completed. The Yoshida model would be used to estimate damage probability of Mashiki buildings. The analysis workflow is shown in Fig. 8.3.

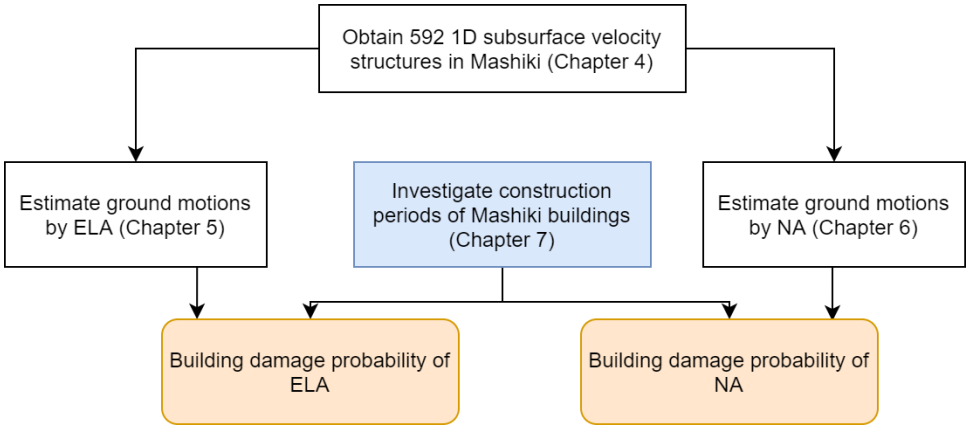

Fig. 8.3. Workflow of estimation of building damage probability in Mashiki.

8.2. Nonlinear response models of wooden building

Nagato and Kawase constructed a model for estimating the damage probabilities of the group buildings in an area, including wooden, RC, and steel structures [8]. They calculated the observed damage ratios (ODRs) based on statistical data for Kobe after the 1995 Kobe earthquake. They then established building models by referring to the Japanese building code (except for wooden houses, for which the dependence on the construction period was not obtained). Subsequently, they analyzed the seismic responses of the building models and obtained the calculated damage ratios (CDRs, the CDR is a value of the calculated damage probability of a building) by assuming log-normal distributions of the yield capacities. They compared the ODRs and CDRs, modified the strength of the building model, and performed the analysis until the deviation between the ODRs and CDRs was sufficiently small. Finally, they established the Nagato–Kawase model, which they applied to successfully reproducing the special building damage belt caused by the 1995 Kobe earthquake. Nagato and Kawase [8] used multi-degree-of-freedom models with non-linear springs for their seismic response analysis model. They assumed that RC buildings are characterized by the degrading trilinear hysteresis type (D-tri type) of nonlinear springs [8,22–24]. Kawase and Masuda [25] applied this model to predicting the building damage in the Yatsushiro City, Japan. In particular, Japanese wooden houses were estimated to be twice as strong on average, compared to the building standard.

Yoshida et al. [22] followed the construction procedure of the Nagato–Kawase model and updated parameters related to the four construction periods to analyze the dynamic response of the standard models, for a more detailed damage estimation of Japanese wooden houses. They used 24 representative models for the two-floor wooden houses of different strengths. For the first floor, eight representative strength factors relative to the standard strength and the existing ratio were used. These eight strength factors are shown in Fig. 8.4. For the second floor, they used a ratio between the structural wall sufficiency rate (i.e. a ratio between the existing structural wall quantity and necessary

structural wall quantity) of the second and first stories, which are 1.0, 1.5 , and 2.0 [8,22], respectively. The strength of the standard wooden model was defined by the necessary structural wall quantity for a wooden house according to the Japanese building code. The necessary structural wall quantity is satisfied when the base shear coefficient is 0.2 and the angle of deformation is 1/120 rad. [8,22,25]. They also set the parameter α, which is the ratio between the structural strength of a wooden house for a specific construction period and that of the standard wooden model, as given in Table 8.1 [11,22]. They successfully expanded the Nagato–Kawase model to consider different construction periods because they used the damage statistics for tax evaluation by municipal governments which requires the construction period of each house (Damage Grade #3 in Fig. 8.2).

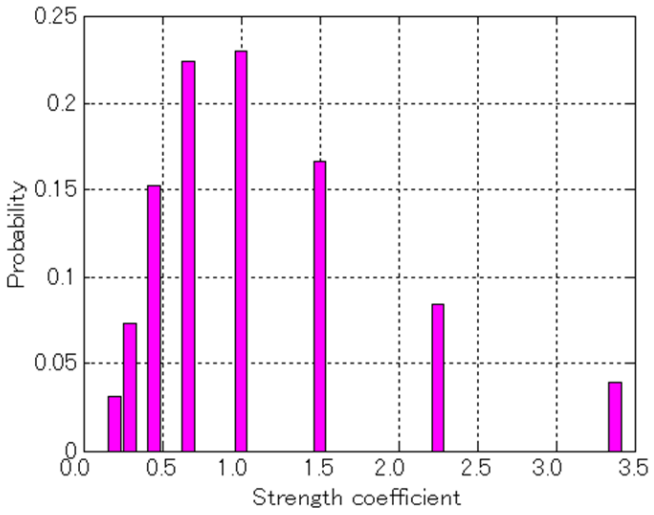

Fig. 8.4. Log-normal distribution of existing probability with different strength coefficient (normalized strength with reference to the average) for the two-floor wooden house of Yoshida model [8,22]**.**

Table 8.1. Parameter α for every construction period in the Yoshida model.

Construction Period	Before 1950	1951-1970	1971-1981	After 1982
α	1.80	2.15	2.90	4.70

8.3. Building damage probability estimation of KMMH16

8.3.1. Using the ELA ground motions

Because most of the wooden houses in Mashiki were two-story structures, we used the two-story wooden model of Yoshida model for analyzing the target area. The Newmark–β analysis method was applied, with β = 0.25 and a time increment Δt = 0.005 s. Instantaneous stiffness proportional-type damping was applied with a damping ratio of 5%. For the standard model constructed according to the Japanese building code, the mass of the first floor was set to 15.88 tons and that of the second floor was 11.52 tons. Both floors were set to a height of 2.9 m. A log-normal distribution was assumed with the standard deviation based on the measured resonant frequency distribution of wooden houses. Because the damage ratios shown in Fig. 1 are those for damage levels of D4 and higher, the damage criterion for the nonlinear building response analysis was set to a story drift angle of greater than 1/30. This threshold was used by Yoshida et al. [22] to represent the total damage level in the survey for property tax evaluation; this should be similar to a damage level of D4 or higher, although it is not an exact match.

The average yield capacities of the Nagato–Kawase model and Yoshida model, were obtained by using synthetic seismograms of the ground surface in Kobe simulated by the 3D finite difference method for a frequency range of up to 1.5 Hz [26]. Thus, a high-cut filter of 1–2 Hz to the estimated strong motions of the ground surface at Mashiki was used. Even though high-frequency components from the input waves were filterred, the damage still occurs because the structural period will be prolonged owing to the strong nonlinearity of the model. Figs. 8.5 and 8.6 show representative results for the dynamic response analysis of a wooden house model with a weaker yield strength (construction period of 1971–1981, strength coefficient factor of the first and second floors respectively are 0.29648 and 0.59296) among the 24 representative models. The filtered estimated ground motions at KMMH16 were applied to this model. The maximum story drift angles of the EW and NS components were 0.167 and 0.038 *rad*, respectively. Full damage was considered to occur because both were greater than 1/30 *rad*. Table 8.2 lists the maximum response accelerations, velocities, and displacements of the ground floor (0F), first floor (1F), and second floor (2F) with the EW and NS components.

Table 8.2. Maximum response accelerations, velocities, and displacements of the ground floor (0F), first floor (1F), and second floor (2F) of a building model, using the ELA ground motions.

	0F_EW	0F_NS	1F_EW	1F_NS	2F_EW	2F_NS
Acceleration (cm/s^2)	410.58	270.40	493.05	368.04	496.71	443.60
Velocity (cm/s)	95.14	47.58	81.19	66.38	100.29	84.37
Displacement (cm)	24.74	11.62	48.36	11.08	66.44	13.25

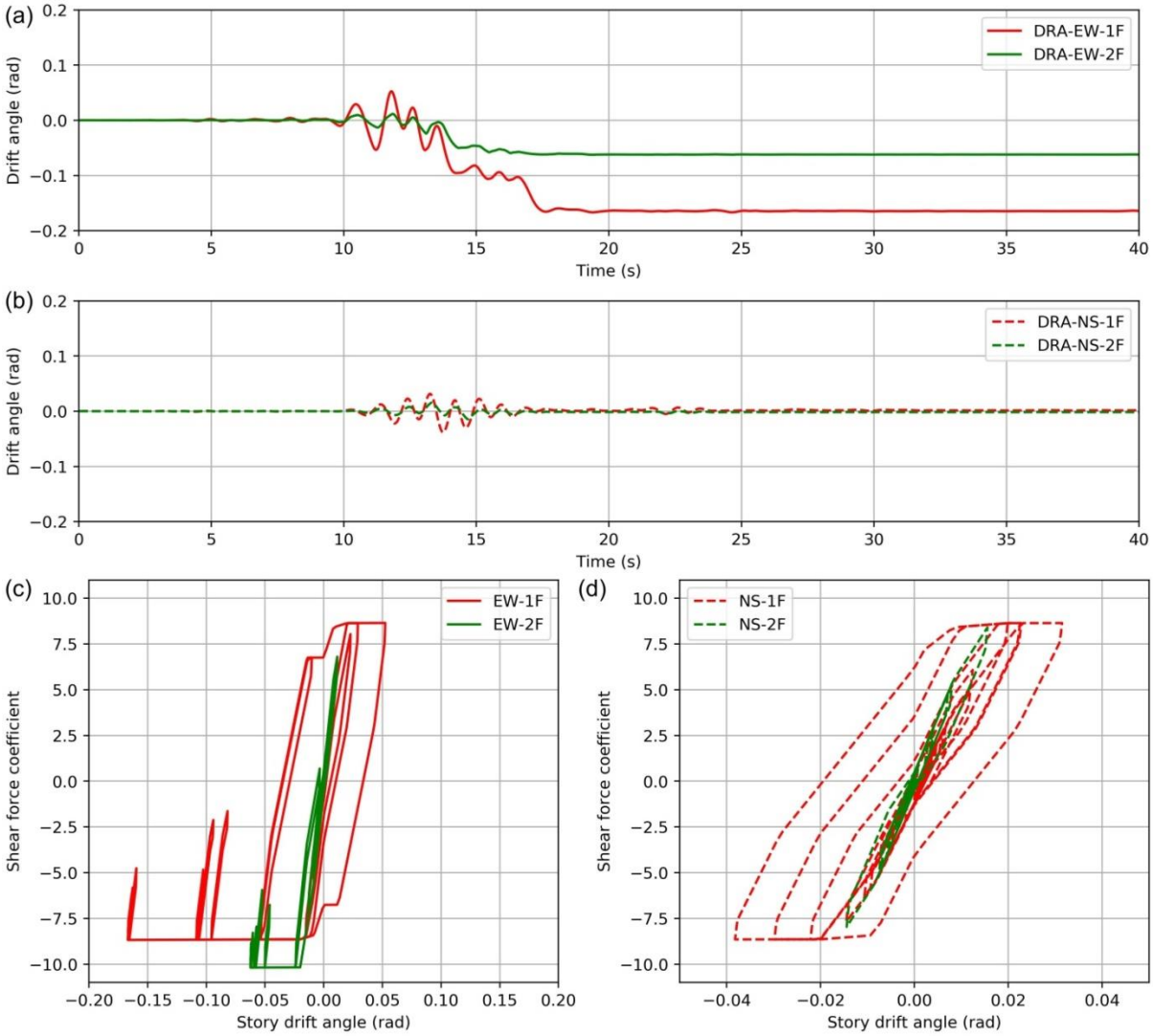

Fig. 8.5. Dynamic response of the damaged model for two-floor wooden house using the ELA ground motions at KMMH16. Story drift angles for (a) EW and (b) NS components in the time domain. Hysteresis curves for (c) EW and (d) NS components. The red and green lines (solid and dashed) denote the results of the first and second floors, respectively.

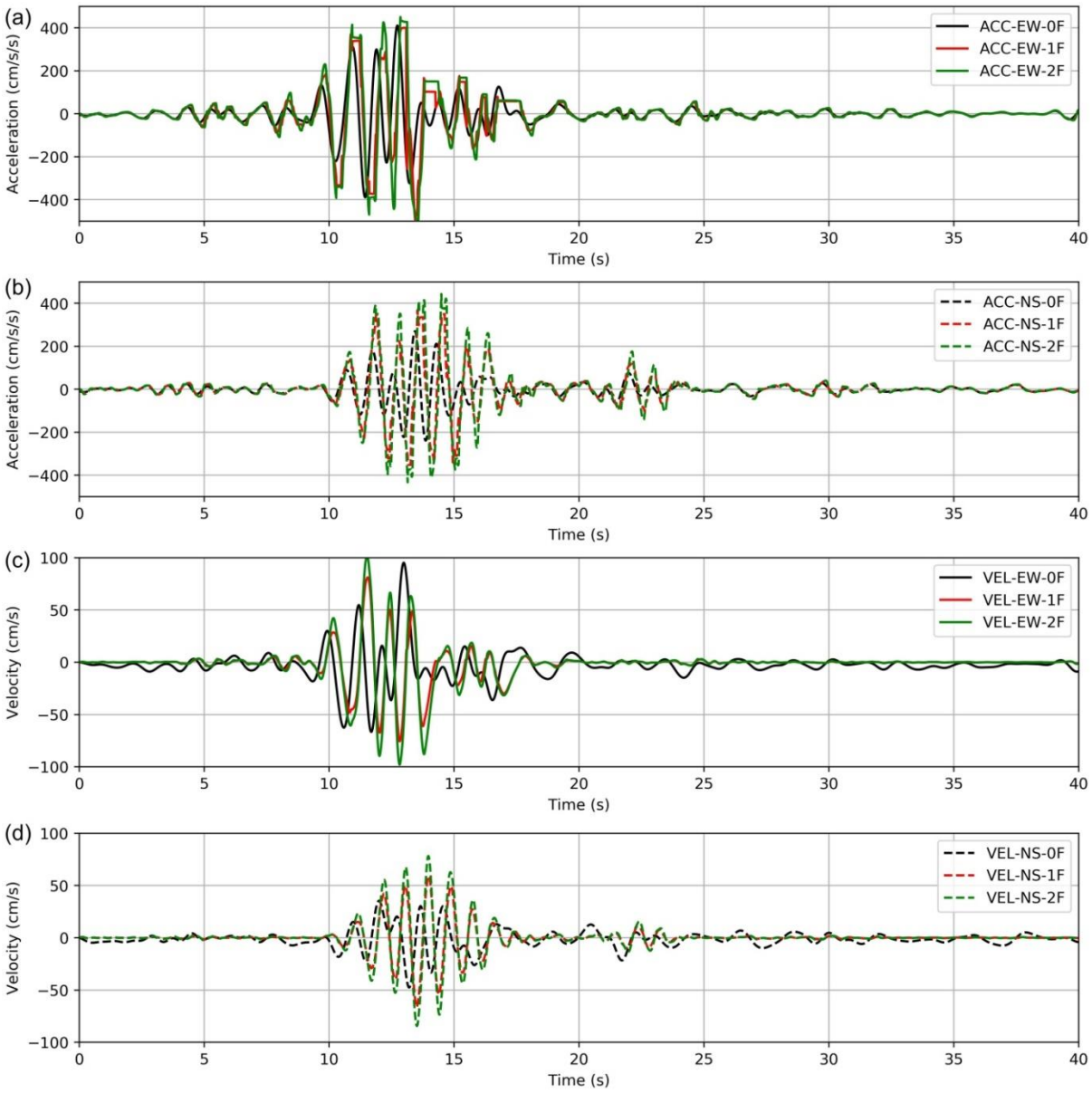

Fig. 8.6. Response accelerations of the damage model for the (a) EW and (b) NS components using the ELA ground motions at KMMH16. Response velocities of the (c) EW and (d) NS components. The black, red, and green lines denote the results of the ground floor, first floor, and second floor, respectively. Figs. 8.5 and 8.6 show the response results of the same model.

8.3.2. Using the NA ground motions

Then the estimation of building damage probability was performed for the same wooden model by using the NA ground motions. The maximum story drift angles of the EW and NS components were 0.059 and 0.036 *rad*, respectively. Full damage was considered to occur because

both were greater than 1/30 *rad*. Table 8.3 shows the maximum response accelerations, velocities, and displacements of the ground floor (0F), first floor (1F), and second floor (2F) with the EW and NS components. The nonlinear structure response results are shown in Figs. 8.7 and 8.8.

According to the comparisons of Tables 8.2 and 8.3, the ELA results of EW component are usually larger than the NA results, while difference is not significant for the NS component. It means that the nonlinearity of the subsurface soil structure will greatly reduce the surface response motions under strong motions. However, this wooden house model will be damaged even under the estimated NS ground motion.

Table 8.3. Maximum response accelerations, velocities, and displacements of the ground floor (0F), first floor (1F), and second floor (2F) of a building model, using the NA ground motions.

	0F_EW	0F_NS	1F_EW	1F_NS	2F_EW	2F_NS
Acceleration (cm/s^2)	371.98	260.22	364.28	374.08	450.05	439.26
Velocity (cm/s)	90.77	44.52	73.12	61.41	90.77	79.18
Displacement (cm)	24.74	14.74	17.12	10.31	20.16	12.7

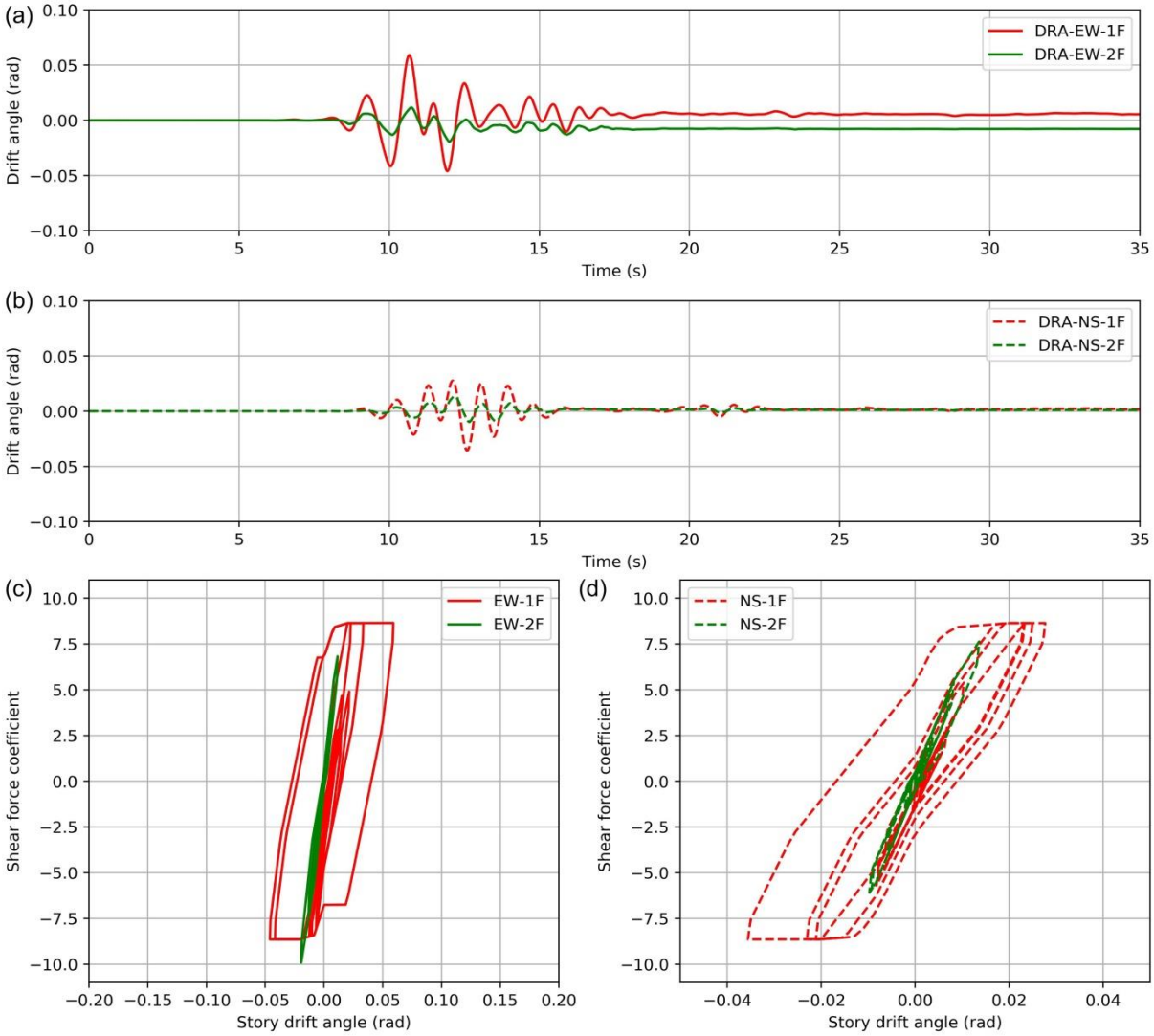

Fig. 8.7. Dynamic response of the damaged model for two-floor wooden house using the NA ground motions at KMMH16. Story drift angles for (a) EW and (b) NS components in the time domain. Hysteresis curves for (c) EW and (d) NS components. The red and green lines (solid and dashed) denote the results of the first and second floors, respectively.

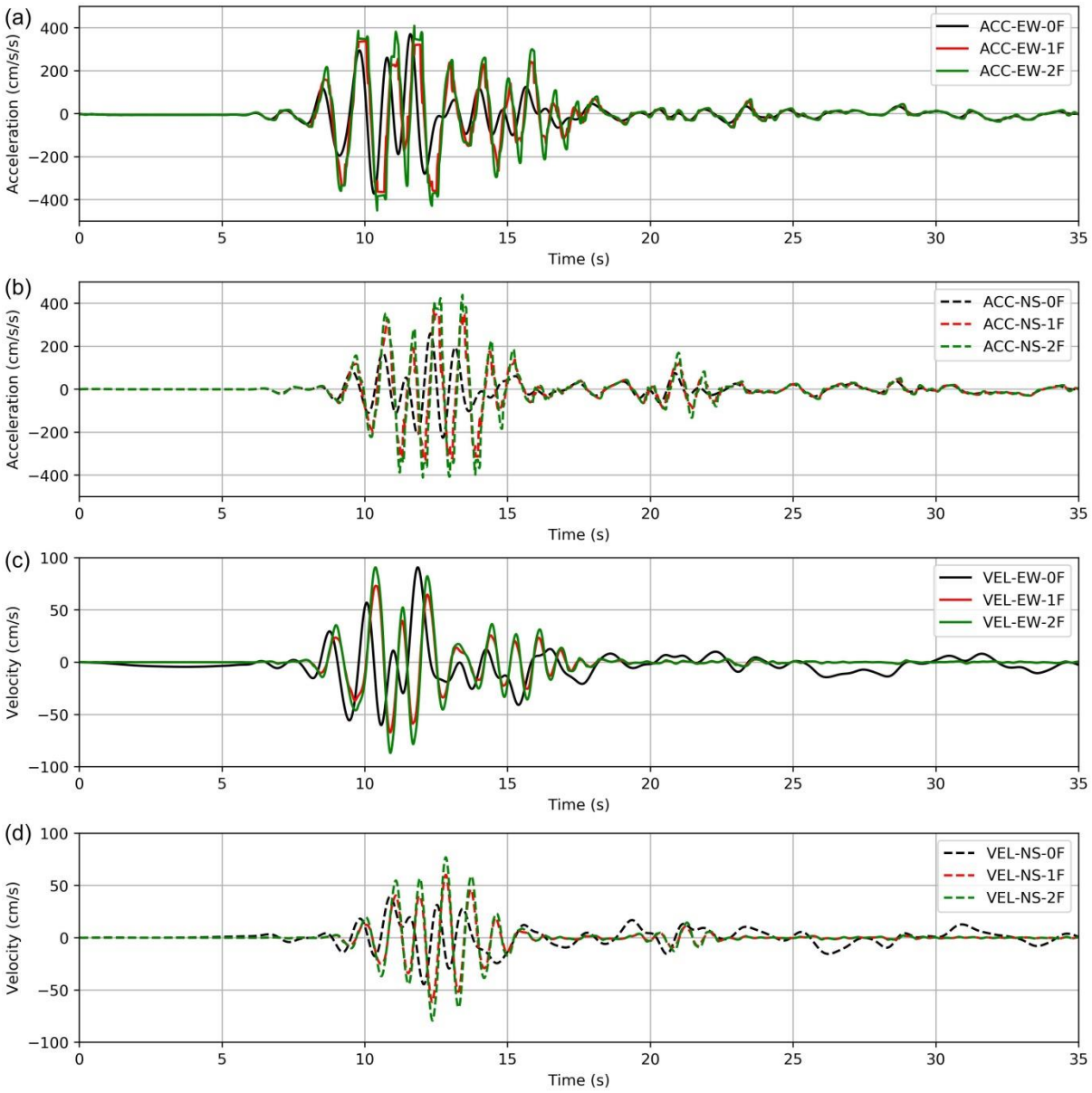

Fig. 8.8. Response accelerations of the damage model for the (a) EW and (b) NS components using the NA ground motions at KMMH16. Response velocities of the (c) EW and (d) NS components. The black, red, and green lines denote the results of the ground floor, first floor, and second floor, respectively. Figs. 8.7 and 8.7 show the response results of the same model.

8.4. Damage probability estimation of Mashiki

8.4.1. Damage probability estimation results of ELA

Next, the building damage probabilities of 592 sites in Mashiki were calculated, through the similar studying procedure as KMMH16. The damage probabilities corresponding to the construction periods of before 1950, 1951–1970, 1971–1981, and after 1982 are designated as DP_{950}, DP_{970}, DP_{980}, and DP_{990}, respectively. We created distribution maps of these damage probabilities through ELA. Fig. 8.9 presents the estimated damage probability distributions of Mashiki for the four construction periods with the estimated ground motions by ELA.

After obtaining the damage probabilities for four different construction periods at every grid point, the damage probability of each individual building was calculated. Within a 30×30 grid, each wooden house is surrounded by four grid points, as shown in Fig. 8.10. The distance between a grid point and a wooden house was denoted as *Dis(i)* (House1 – grid point). In other words, a building is affected by the estimated ground motions at the four surrounding grid points. Then, an influence coefficient (IC) related to the distance between the building and four grid points was defined, as shown in Eq. (8.1). IC was used to calculate the damage probability of every building with Eq. (3). For example, if House1 is one building as shown in Fig. 7.5 with a construction period of after 1982, then $DP(B2)_{990}$, $DP(B3)_{990}$, $DP(C2)_{990}$, and $DP(C3)_{990}$ are the damage ratio of B2, B3, C2, and C3 respectively, with a construction period of after 1982 (Fig. 16(d)). By considering *IC(B2)*, *IC(B3)*, *IC(C2)*, and *IC(C3)* of the four grid points, the damage ratio of this building could be obtained with Eq. (8.2).

$$Power\ (i) = \frac{1}{Dis(i)}; \quad IC(i) = \frac{Power(i)}{\sum_{i=1}^{4} Power(i)} \tag{8.1}$$

where, *Power(i)* denotes the inverse of each distance, and *IC(i)* represents the influence coefficient of each grid point.

$$DP_{building} = \sum_{i=1}^{4} IC(i) \times DP(i)_{period} \tag{8.2}$$

where, $DP_{building}$ denotes the damage probability of the target building, and $DP(i)_{period}$ is the estimated damage probability of the four surrounding grid points with the same construction period as the target building.

Although the damage probability of every building in the target area was estimated, the results were not presented here because it is the private information of the house owner. To compare the estimated damage of houses with the AIJ survey results, we created a new grid similar to the AIJ survey and calculated the averaged damage probabilities of each cell (DP_{cell}) with Eq. (8.3). Fig. 8.11 is the distribution map of DP_{cell} using the estimated ground motions of ELA.

$$DP_{cell} = \frac{\sum_{i=1}^{N} DP(i)_{building}}{N} \quad (8.3)$$

where, N is the number of buildings located in the cell, and $DP(i)_{building}$ is the estimated damage probability of each building in the cell. The size of the new grid is approximately equal to that used in the AIJ survey results.

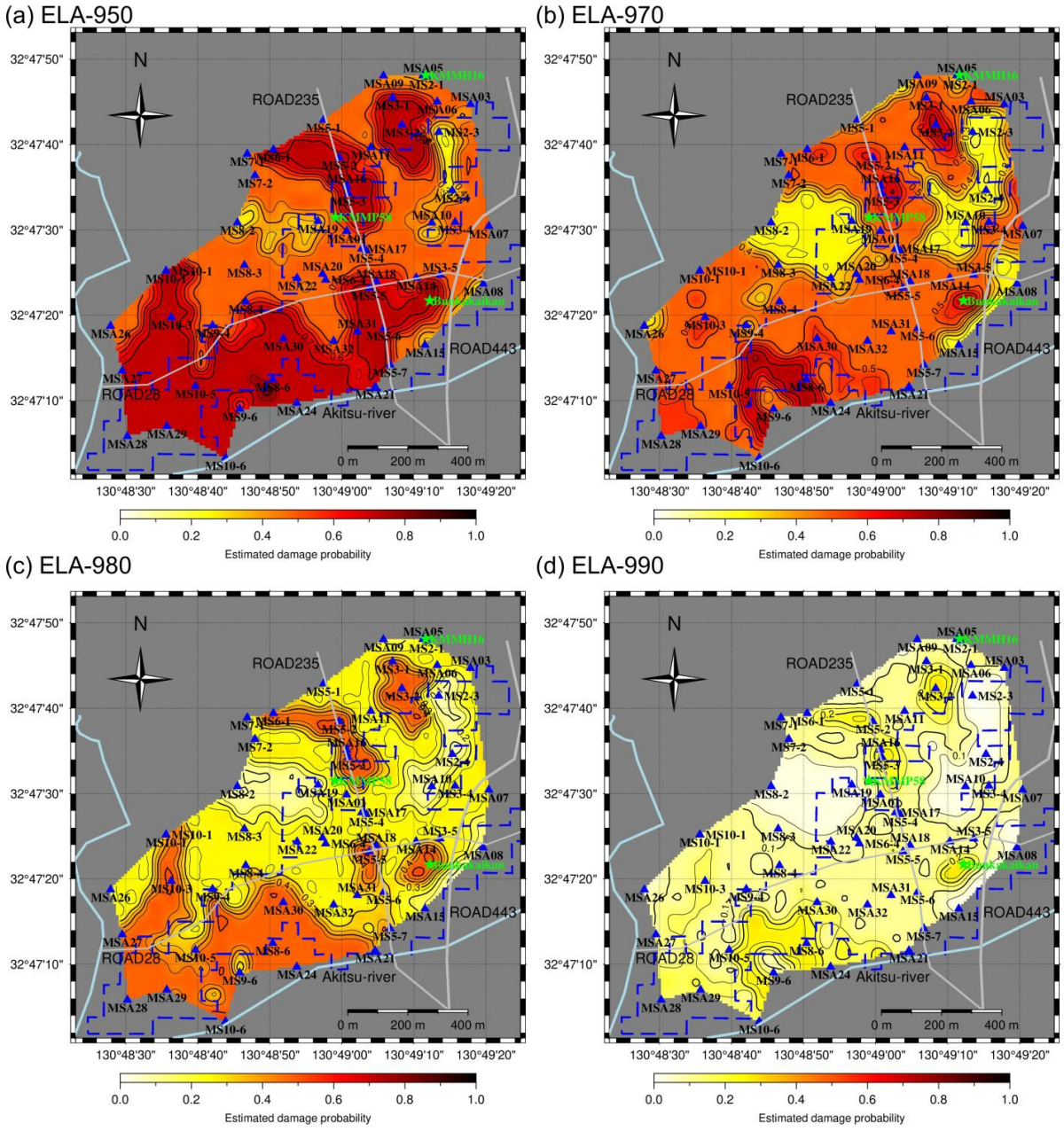

Fig. 8.9. Estimated damage probability distribution maps of wooden buildings from different construction periods according to the Yoshida model, based on the estimated horizontal ground motions using the ELA: (a) DP_{950}, (b) DP_{970}, (c) DP_{980}, and (d) DP_{990}.

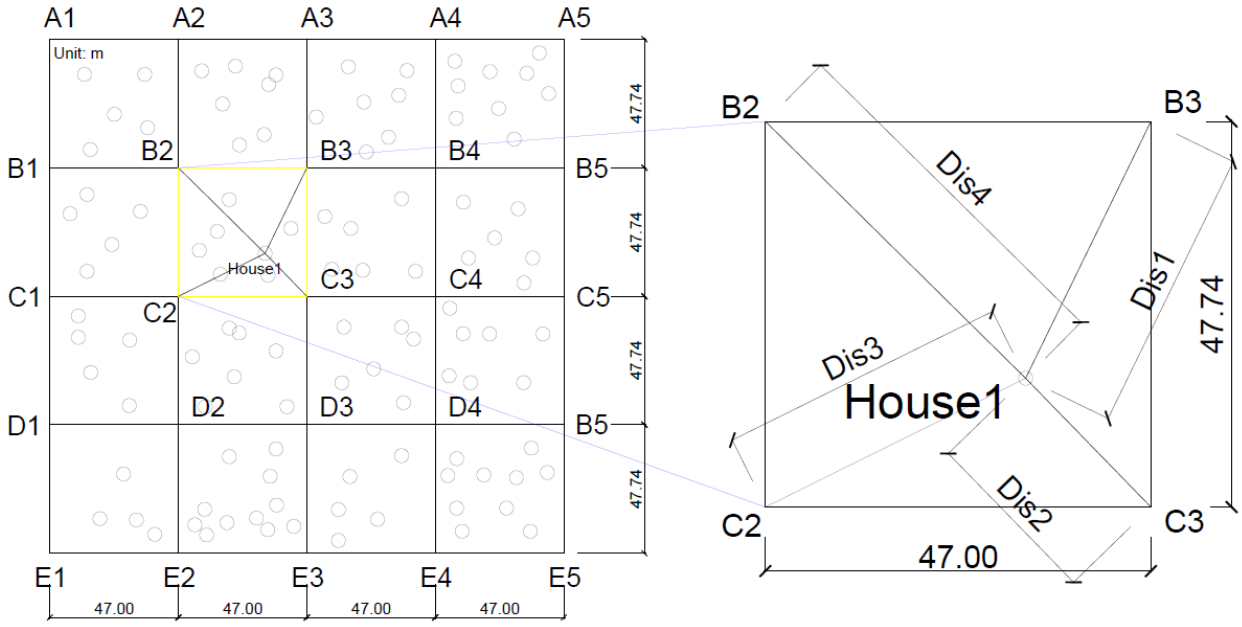

Fig. 8.10. Schematic map of locations of wooden houses and surrounding grid points. A1–E5 are the grid points corresponding to the grids shown in Fig. 5.14. The small circles are the building locations (unit: m).

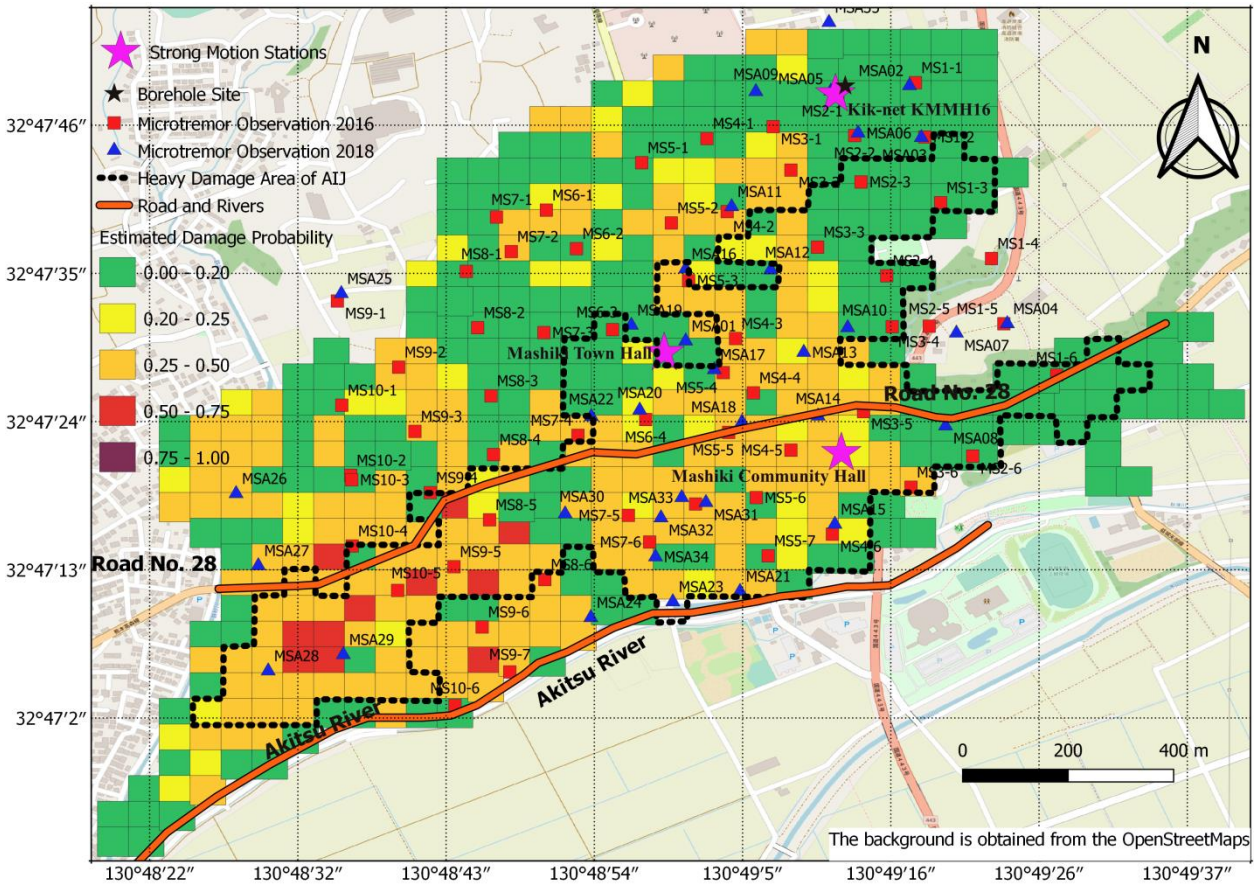

Fig. 8.11. Averaged damage probability of each cell based on the estimated ground motions of the ELA. The green, yellow, orange, red, and dark red colors denote damage probabilities of 0–20%, 20–25%, 25–50%, 50–75%, and greater than 75%, respectively.

8.4.2. Damage probability estimation results of NA

Using the same research process as the ELA analysis, the DPs of 592 sites were calculated by inputting the estimated ground motions of NA. Fig. 8.12 presents the estimated DP_{950}, DP_{970}, DP_{980}, and DP_{990}. Comparisons of LA, ELA, and NA results in the area surrounding MSA32 and MS7-6with the results of Sugino et al. [19] are shown in Fig. 8.13(c). It shows the DPs of before 1981 were higher than the DPs of after 1981, which was not the same as results of Sugino et al. [19]. Maybe stronger ground motions were occurred in this area comparing with other places in Mashiki during the mainshock. Moreover, maybe most of buildings were constructed during a narrow period of 20 years in this area, which resulted in the similar average damage ratios of before 1982 and after 1982 periods.

Fig. 8.14 shows the estimated DP_{cell} of NA. Comparing the NA DP with ELA DP, the NA analysis results were found to be better than the ELA to the AIJ survey results in some areas. At the near river sites, such as MS9-6 and MS8-6, the ELA DP was larger than surrounding sites, while the NA DP was estimated to be more real to the AIJ survey. It was consided that the results were resulted

by the nonlinearity of soil structure According to the DP_{950}, NA DP shows more real than the ELA DP, not all the old buildings were collapsed in Mashiki. As for the DP_{970} of two methods, NA simulated much better than the ELA, because the building damage were mainly concentrated in the southern part of Mashiki. Both ELA DP and NA DP showed the damage occurred in the northwestern part, especially for the near river area.

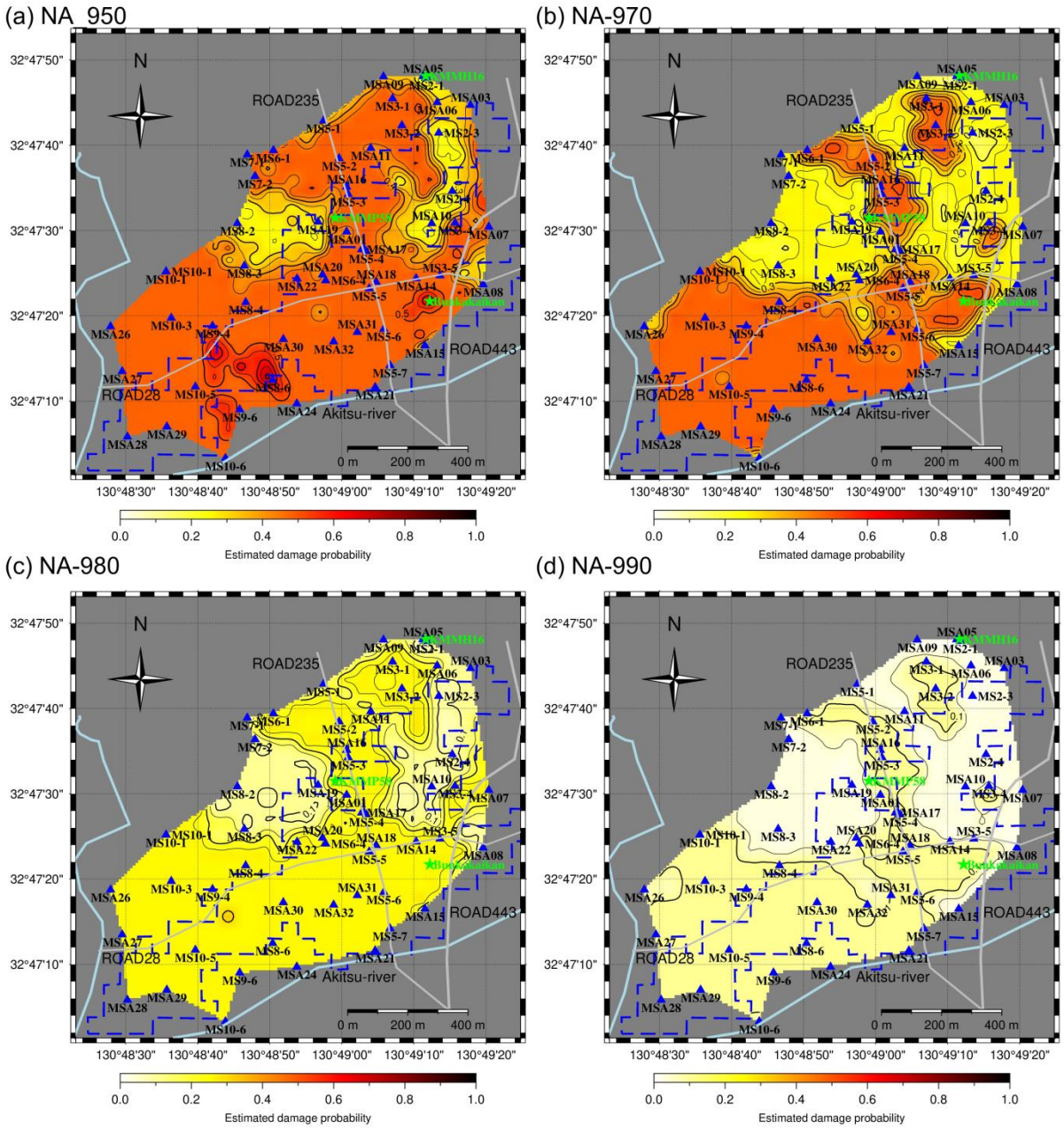

Fig. 8. 12. Estimated damage probability distribution maps of wooden buildings from different construction periods according to the Yoshida model, based on the estimated horizontal ground motions using the NA: (a) DP_{950}, (b) DP_{970}, (c) DP_{980}, and (d) DP_{990}.

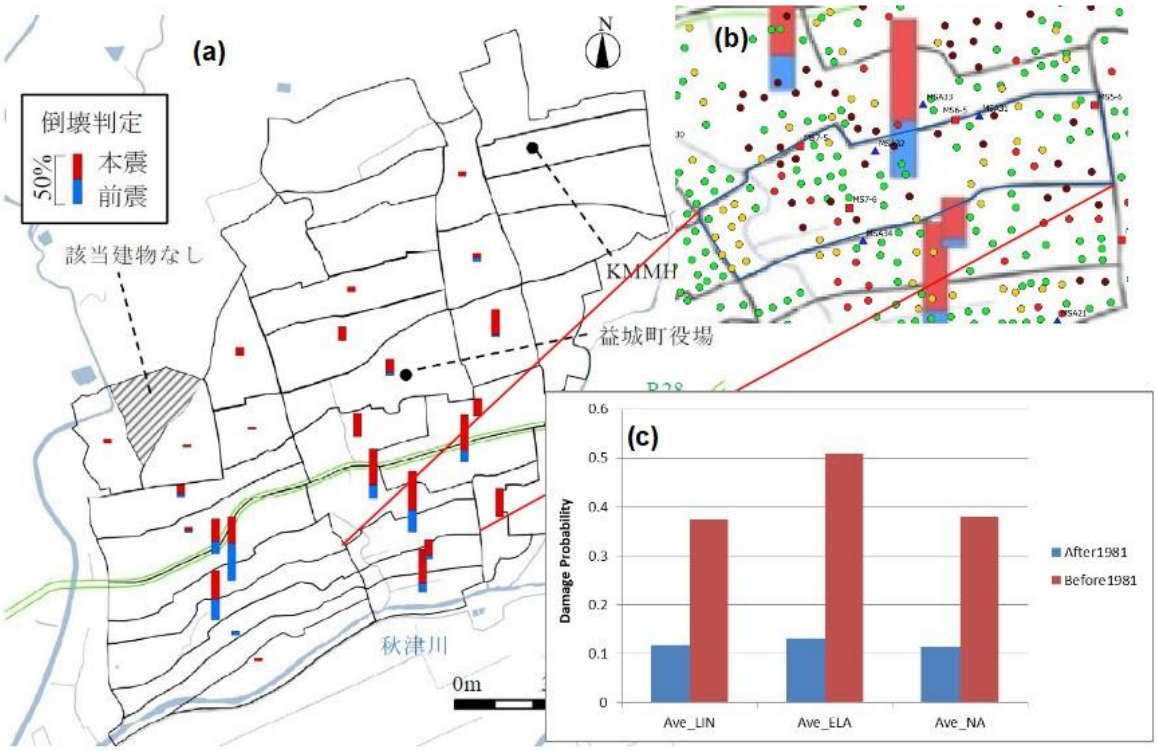

Fig. 8.13. Comparison of the average DP of LA, ELA, and NA with Sugino et al. [19] in the special area. (a) the research results of Sugino et al.; (b) construction periods in the special region; (c) averaged DP of after 1981 (blue) and before 1981 (red) of LA (left columns), ELA (middle columns), NA (right columns).

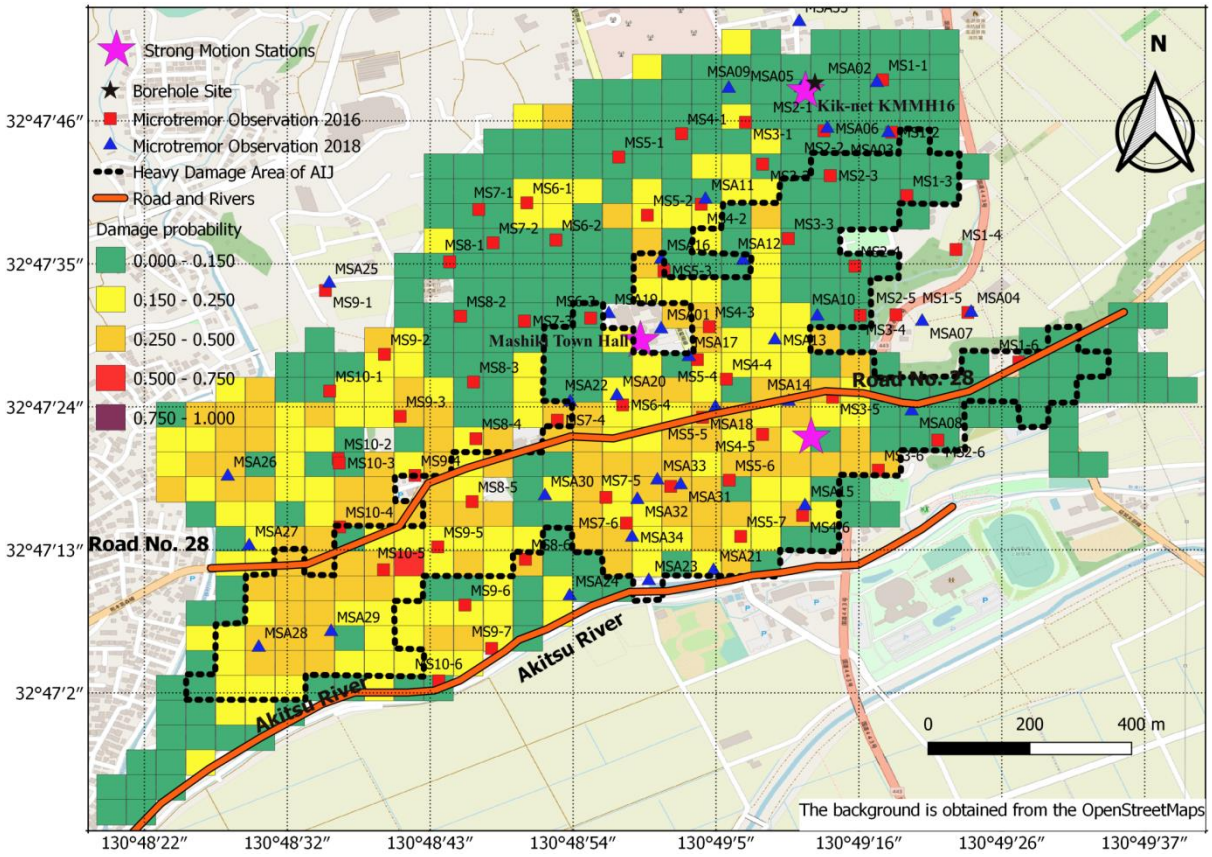

Fig. 8.14. Averaged damage probability of each cell based on the estimated ground motions of the NA. The green, yellow, orange, red, and dark red colors denote damage probabilities of 0–15%, 15–25%, 25–50%, 50–75%, and greater than 75%, respectively.

8.5. Conclusion

Building damage probability estimations were adopted in this chapter, and multiple useful estimations were obtained. The new method to calculate the damage probability considering ground motions of four surrounding sites was proposed. Damage probabilities considering the local site–specific ground motions were calculated based on the time history dynamic analysis of structures. Estimated DPs using the ELA ground motions were slightly larger than that using the NA ground motions. Both the ELA–DP and NA–DP distribution maps showed close relationship to the AIJ survey results. Large DP also occurred in the northwestern region. Obviously, most of the heavy damage was concentrated on the area between the Road No.28 and Akitsu River. Moreover, the NA–DPs of soil liquefied sites were decreased because of the influence of liquefactions in the near river areas. Besides, the ELA–DPs were slightly larger than the NA–DPs, which confirmed the nonlinear soil properties of shallow layers in Mashiki, especially in the southern parts. According to both the ELA–DP and NA–DP distribution maps, construction period of building also showed strong influence

on the estimated DP. Study results of this chapter showed the building construction period and site ground motions were two important factors when estimating the DP of wooden houses. In the northwestern region, non-negligible heavy damage was also found in the estimation results.

Reference (Chapter 8)

[1] Lu X, McKenna F, Cheng Q, Xu Z, Zeng X, Mahin SA. An open-source framework for regional earthquake loss estimation using the city-scale nonlinear time history analysis. Earthquake Spectra 2020:8755293019891724. https://doi.org/10.1177/8755293019891724.

[2] Zeng X, Lu X, Yang TY, Xu Z. Application of the FEMA-P58 methodology for regional earthquake loss prediction. Natural Hazards 2016;83:177–92. https://doi.org/10.1007/s11069-016-2307-z.

[3] Lu X, Han B, Hori M, Xiong C, Xu Z. A coarse-grained parallel approach for seismic damage simulations of urban areas based on refined models and GPU/CPU cooperative computing. Advances in Engineering Software 2014;70:90–103. https://doi.org/10.1016/j.advengsoft.2014.01.010.

[4] Hori M. Introduction to Computational Earthquake Engineering. IMPERIAL COLLEGE PRESS; 2011. https://doi.org/10.1142/p644.

[5] Rojahn C, Sharpe RL, Council AT, Agency USFEM. Earthquake Damage Evaluation Data for California. Applied Technology Council; 1985.

[6] Yakut A, Ozcebe G, Yucemen M. Seismic vulnerability assessment using regional empirical data. Earthquake Engineering & Structural Dynamics 2006;35:1187–202. https://doi.org/10.1002/eqe.572.

[7] FEMA. Multi-hazard loss estimation methodology: earthquake model 2012.

[8] Nagato K, Kawase H. Damage evaluation models of reinforced concrete buildings based on the damage statistics and simulated strong motions during the 1995 Hyogo-ken Nanbu earthquake. Earthquake Engineering & Structural Dynamics 2004;33:755–774. https://doi.org/10.1002/eqe.376.

[9] Nagato K, Kawase H. A SET OF DYNAMIC MODELS OF STEEL BUILDINGS FOR DAMAGE EVALUATION. Journal of Structural and Construction Engineering (Transactions of AIJ) 2002;67:101–6. https://doi.org/10.3130/aijs.67.101_7.

[10] Lu X, Guan H. Earthquake Disaster Simulation of Civil Infrastructures: From Tall Buildings to Urban Areas. 2017. https://doi.org/10.1007/978-981-10-3087-1.

[11] Yoshida K, Hisada Y, Kawase H, Fushimi M. Study of damage rate function and destructive force index of wooden buildings based on seismic response analysis, Kinki: Abstracts of the 2005 Architectural Institute of Japan Conference; 2005, p. 161–2.

[12] Lu X, Tian Y, Guan H, Xiong C. Parametric sensitivity study on regional seismic damage prediction of reinforced masonry buildings based on time-history analysis. Bulletin of Earthquake Engineering 2017;15:4791–820. https://doi.org/10.1007/s10518-017-0168-9.

[13] Kawase H. The cause of the damage belt in kobe: “the Basin-Edge effect,” constructive interference of the direct s-wave with the basin-induced diffracted/rayleigh waves. Seismological Research Letters 1996;67:25–34. https://doi.org/10.1785/gssrl.67.5.25.

[14] Matsushima S, Kawase H. Multiple Asperity Source Model of the Hyogo-Ken Nanbu Earthquake of 1995 and Strong Motion Simulation in Kobe. Journal of Structural and Construction Engineering (Transactions of AIJ) 2000;65:33–40. https://doi.org/10.3130/aijs.65.33_3.

[15] Yoshida K, Hisada Y, Kawase H. Construction of damage prediction model for wooden buildings considering construction age, Hokkaido: 2004.

[16] NILIM, BRI. Quick report of the field survey and the building damage by the 2016 Kumamoto earthquake. National Institute for Land and Infrastructure Management; 2016.

[17] Okada S, Takai N. Classifications of structural types and damage patterns of buildings for earthquake field investigation. Journal of Structural and Construction Engineering (Transactions of AIJ) 1999;64:65–72. https://doi.org/10.3130/aijs.64.65_5.

[18] Takai N, Okada S. Classifications of damage patterns of reinforced concrete buildings for earthquake field investigation. Journal of Structural and Construction Engineering (Transactions of AIJ) 2001;66:67–74. https://doi.org/10.3130/aijs.66.67_4.

[19] Sugino M, Yamamuro R, Kobayashi S, Murase S, Ohmura S, Hayashi Y. Analyses of Building Damages in Mashiki Town in the 2016 Kumamoto Earthquake. Journal of Japan Association for Earthquake Engineering 2016;16:10_69-10_83. https://doi.org/10.5610/jaee.16.10_69.

[20] MURASE S, OHMURA S, SUGINO M, HAYASHI Y. Relationship between Characteristics of Ground Motions and Ratio of Collapsed Wooden Houses in the 2016 Kumamoto Earthquake. Journal of Japan Association for Earthquake Engineering 2018;18:2_147-2_165. https://doi.org/10.5610/jaee.18.2_147.

[21] Grunthal G. European Macroseismic Scale 1998 1998.

[22] Yoshida K, Hisada Y, Kawase H. Construction of Damage Prediction Model for Wooden Buildings Considering Construction Age, Hokkaido: the 2004 Architectural Institute of Japan; 2004.

[23] Fukada Y. Study on hysteretic characteristics of reinforced concrete buildings, Part 1, Establishment and response calculations of the degrading stiffness tri-linear model. Proceedings of the 40th Meeting of AIJ Kanto Branch, 1969, p. 121–4.

[24] Otani S. Hysteresis models of reinforced concrete for earthquake response analysis. Journal of Faculty of Engineering, University of Tokyo 1981:407–41.

[25] Kawase H, Masuda A. Damage prediction of yatsushiro city and its vicinity due to a hyoptehsized Hinagu fault earthquake. Journal of Structural and Construction Engineering (Transactions of AIJ) 2004;69:39–46. https://doi.org/10.3130/aijs.69.39_3.

[26] Kawase H, Matsushima S, Graves RW, Somerville PG. Strong motion simulation of Hyogo-Ken Nanbu (Kobe) earthquake considering both the heterogeneous rupture process and the 3-D basin structure, 2000, p. 8.

Chapter 9

Simulation of strong ground motions in Mashiki during the mainshock of 2016 Kumamoto earthquake using rupture dynamics model

9.1. Introduction

9.2. Parameter study of the rupture dynamic simulation model for a M6.7 earthquake

- 9.2.1. Numerical modeling and parameterization
- 9.2.2. Simulation result of no-basin structure
- 9.2.3. Simulation result of basin structure
- 9.2.4. Slip velocity function of dynamic rupture simulations

9.3. Simulation of mainshock of 2016 Kumamoto earthquake.

- 9.3.1. Fault property distributions of the mainshock
- 9.3.2. Comparisons between estimated and observed ground motions in Mashiki
- 9.3.3. Distributions of PGV and PGD

9.4. Conclusion

Reference (Chapter 9)

9.1. Introduction

Irikura and Miyake [1] proposed a two-stage scaling relationship of source parameters for crustal earthquakes in Japan, which combined source parameters obtained from the waveform inversion of strong-motion data [2,3] with those obtained from geological and geomorphological surveys, selecting only reliable data from the source parameter catalog compiled by Wells and Coppersmith [4]. They found that there is a strong correlation between source parameters from the waveform inversion results and those from geological and geomorphological data for crustal earthquakes of magnitudes larger than 7 [5]. Since the observed peak ground acceleration (PGA) and peak ground velocity (PGV) of two stations in Mashiki, the Kik-net KMMH16 and KMMP58 (Mashiki townhall station), were very different. Also, the heavy damaged buildings were located in a belt parallel to the Hinagu fault zone associating with the fault directions [5–7]. It is necessary to understand whether the source effects of the mainshock affected the observed ground motions in Mashiki.

Dynamic rupture modeling of crustal earthquakes has been helpful in understanding earthquake rupture process and its implication in generation of seismic energy and near-fault ground motion, for fault under different initial stress conditions and material frictional properties. Analysis of simulated spontaneous rupture for crustal faults can be used to guide the development and improvement of rupture models that are used in strong ground motion simulations for scenario earthquakes. The motivation of our study is inspired by recent analysis of rupture kinematics and damage to buildings observed during the M_{JMA} 7.3 2016 Kumamoto, Japan earthquake. The earthquake caused substantial damage to wooden houses in a large area concentrated near the fault. Several investigations of the recorded ground motion and damage distribution characteristics have concluded that the large near-fault ground motion was caused by the local rupture process [8]. Moreover, this strong event was one of the largest earthquakes since the 1995 Hyogo-ken Nanbu earthquake in Japan. A lot of strong ground motions from this earthquake were recorded by dense and accurate strong−motion networks, such as the K-net, Kik-net, and the seismic intensity meters network of the Japan metrological agency (JMA) [7].

9.2. Parameter study of the rupture dynamic simulation model for a M6.7 earthquake

This work was completed with researcher from the Lawrence Livermore National Laboratory (LLNL) in 2018. Our investigation is mainly focused on bridging the kinematic rupture characteristics and rupture dynamics for crustal earthquakes that rupture the surface, similar to the Kumamoto earthquake [8]. Because numerical rupture dynamics simulations are still computationally expensive, and to clear understanding the kinematic analysis, the investigation was started with performing spontaneous rupture modeling for a moderate size strike-slip earthquake of M6.7 on a vertical fault

rupturing the free surface. In the following sections, the stress drop models used in the simulations were described, and show their validation against empirical relations between the magnitude and fault slip and near-fault ground motion peak velocity. Finally, preliminary results of effects of rupture dynamics on rupture kinematics and near-fault ground motion for a characterized M6.7 earthquake rupture scenario were presented in this chapter.

9.2.1. Numerical modeling and parameterization

The spontaneous rupture simulations were performed using a staggered-grid finite difference code FDM_SPLIT1.6 [9] that uses the staggered-grid split-node method of Dalguer and Day [10]. The grid spacing in the finite-difference calculations is 100 m. The maximum modeled frequency is 1Hz. A layout of the modeled area, and fault and stations locations are shown in Figs. 9.1 and 9.2 illustrate the stress drop model used in one of the many spontaneous rupture simulations.

A stochastic characterization of the spatial complexity of earthquake rupture stress drop was adopted in which the stress drop distribution is described by a power spectral density function in the wavenumber domain, parameterized by two characteristic length scales, along the strike and dip directions, respectively [2]. The spectral decay above the corner wavenumber along the strike and dip directions is proportional to k^{-1} where k is the wavenumber [11]. This model produces ω^{-2} type near-fault ground motion. The linear slip weakening friction law was used [12,13]. The velocity strengthening in the weak layer was represented using the slip-weakening friction law by setting values the dynamic friction coefficient values at appropriate elevated levels to yield depth-varying negative to zero stress drop. In the weak zone the slip-weakening distance Dc increases linearly from its background level of 50cm at the bottom to 75 cm at the free surface. The dynamic friction coefficient follows a linear decay that causes the stress drop to linearly decrease from around 5 MPa at the bottom of the weak layer to an average value of zero at the surface. The stress drop in the asperity areas is 13 MPa based on IM2011 recipe [14]. Two series parameterization simulation were carried out. First, the 1D velocity model used in the simulations is shown in Table 9.1 and Fig. 9.3(a). Second, a shallow basin was added to the 1D velocity model, as shown in Fig. 9.3(b). In the basin layer, thickness = 170 m, V_p = 1300 m/s, V_s = 400 m/s, and Density = 1.9 g/cm^3.

In order to validate our stress drop model parameterization, rupture dynamics for 56 earthquake scenarios were computed for which the asperities offset were varied, the asperities depth, and rupture initiation point. Based on these simulations, the maximum fault slip and ground motion peak velocity averaged all rupture scenarios were calculated. The simulated average slip on the fault is 1.4 km. The computed the average peak ground motion velocity and average maximum slip velocity are 57 cm and 113 cm, respectively. In Figs. 9.4 (a) and (b), they are compared with empirical relationships for fault slip [15], and ground motion prediction equation for velocity for a

V_s=680 m/s [16]. Our simulated average values of both slip and peak ground motion velocity fit the empirical predictions very well.

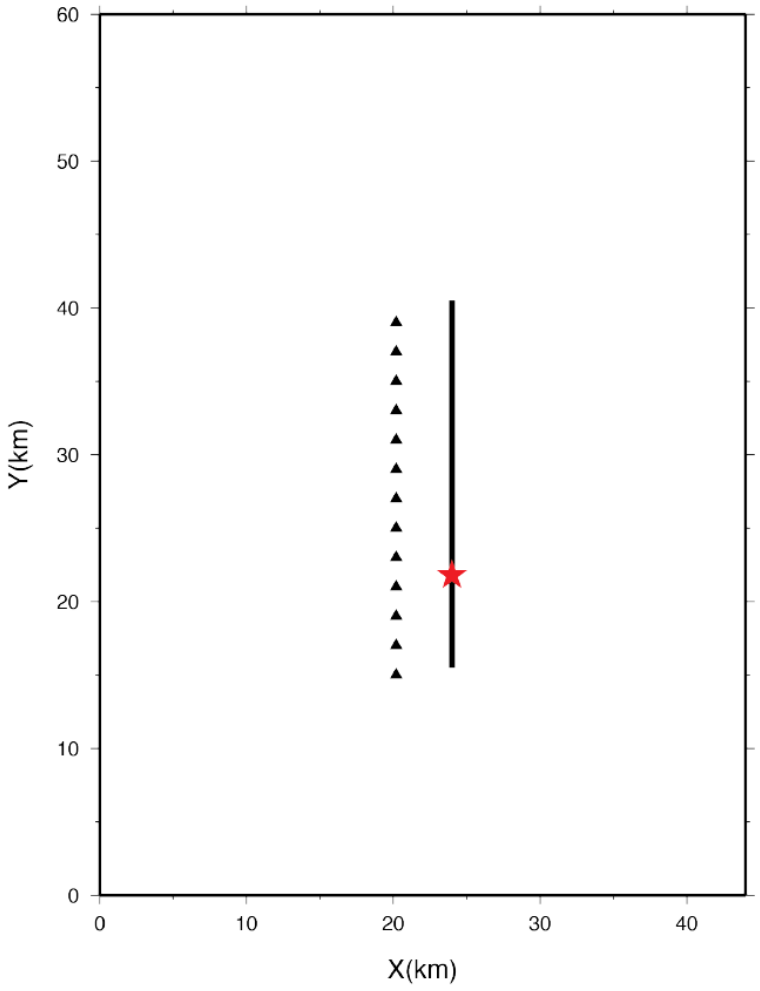

Fig. 9.1. Map view of the computation domain showing the fault and stations (triangle) locations. Star indicates the rupture initiation point.

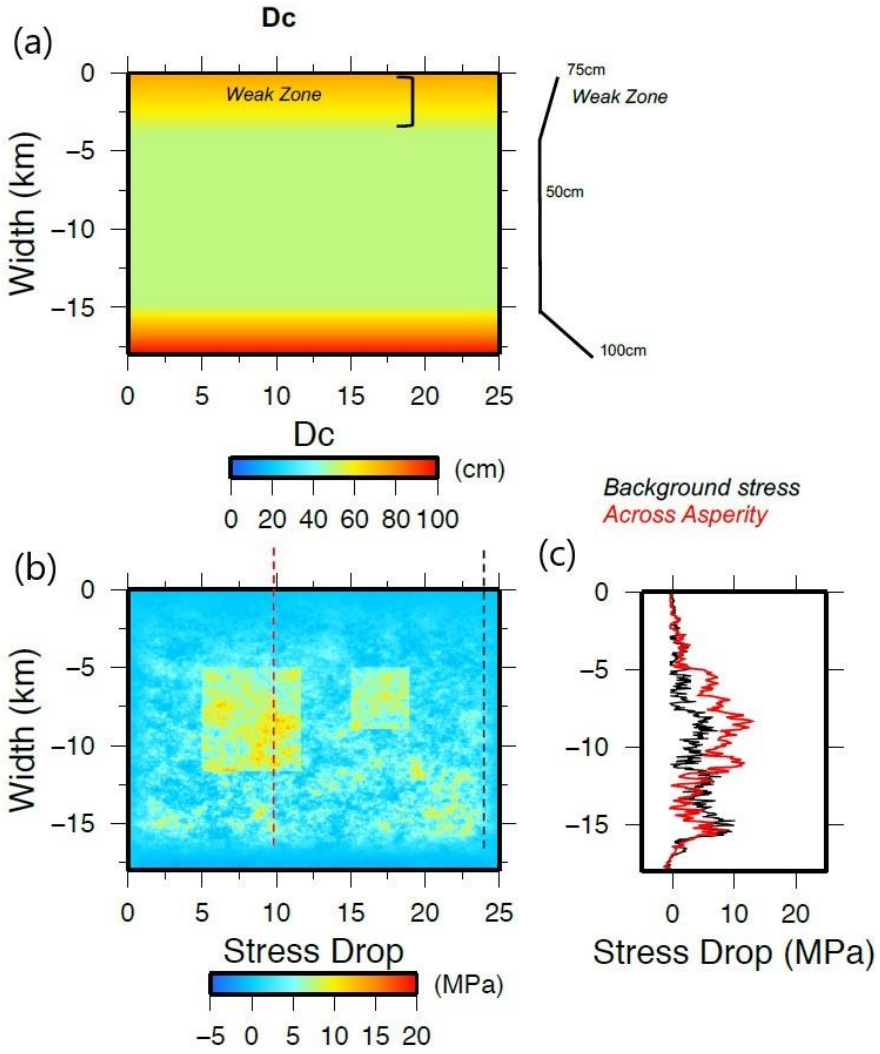

Fig. 9.2. Stress parameters in rupture dynamics modeling. (a) Dc and its depth variation in the fault zone. (b) and (c) Stress drop and depth variation of stress drop. On panel (c), red line indicates the depth variation of stress drop cross the asperity, as the red dashed line showed on panel (b); black line indicate the depth variation of stress drop cross the background area, as the black dashed line showed on (b).

Table 9.1. 1D velocity structure used in the first series of rupture dynamics simulations.

Number	***Depth* (m)**	**V_p (m/s)**	**V_s (m/s)**	***Density* (g/cm^3)**	**Q_p**	**Q_s**
Layer 1	500	1200	680	2.1	160	80
Layer 2	1000	1900	1000	2.2	200	100
Layer 3	5000	4800	2800	2.4	400	200
Layer 4	30000	6000	3464	2.67	2000	1000

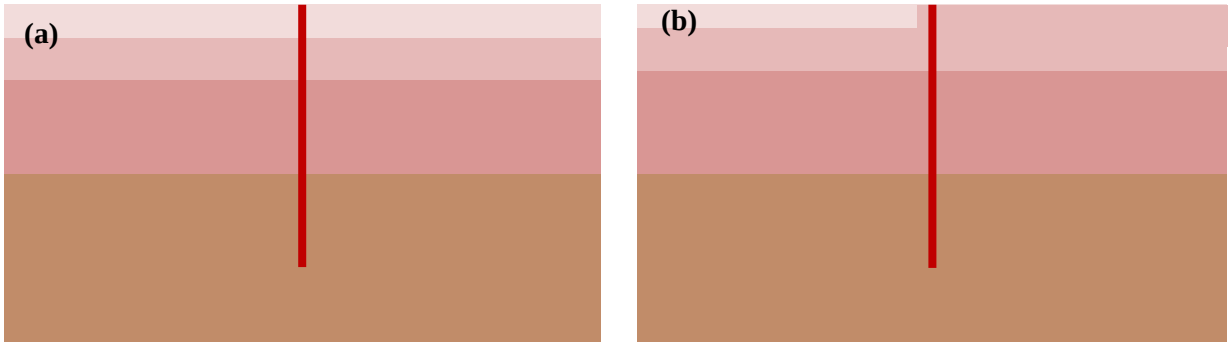

Fig. 9.3. 1D velocity structures according to Table 9.1. (a) and (b) indicate the models we used in the first and second series simulations.

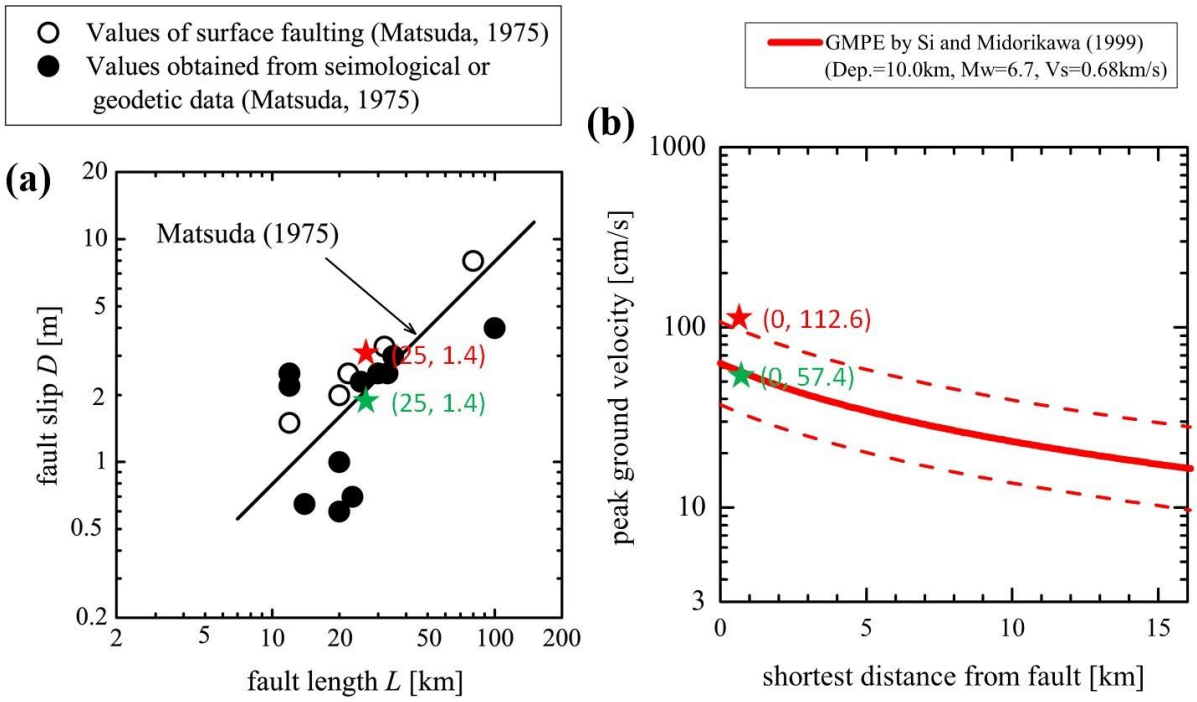

Fig. 9.4. Comparisons of our estimated results with previous research results. (a) Comparing with Matsuda's scaling law of fault slip as a function of fault length [15]**. Green star denotes the fault slip derived from our estimation averaged over several rupture scenarios for which we varied the asperity and rupture initiation, and red star denotes mean value of the maximum fault slip. (b) Comparing with prediction equation for peak ground motion velocity proposed by Si and Midorikawa for Japanese earthquakes** [16]**. Red star indicates the maximum and green star the average peak ground motion velocity computed over 13 stations and several rupture scenarios with various asperity locations and rupture initiation.**

9.2.2. Simulation result of no-basin structure

Calculations using many different fault rupture models with different parameter settings were performed. The quantitative results regarding the estimated maximum slip amount, average slip amount, maximum PGV and average ground surface velocity in previous studies were presented [17,18]. 13 cases of the results of many parametric analyses are displayed, as listed in Table 9.2. The asperities depth is aligned, and the depth is basically changed as a parameter in three stages of 6 km, 8 km, and 10 km (only the Case10_31 is 4 km). Parameter of the asperity offset was set as 1.4 km, 3.4 km, 5.4 km, and 7.4 km. Among all these cases, we considered the model (Case 9_2) with an asperity top depth of 6 km and an asperity interval of 3.4 km as the standard model.

Table 9.2. Selected cases of results of dynamic rupture simulations.

Case	Asperity top depth Da (km)	Asperity distance La (km)	Moment (dyne*cm)	Magnitude (Mw)	Maximum slip(cm)	Average slip for entire fault (cm)	Max. PGV (cm/s)	Average PGV (cm/s)
10_31	4	3.4	1.76E+26	6.80	302.0	142.0	157.5	87.2
9_2	6	3.4	1.71E+26	6.79	294.4	136.4	127.6	59.7
9_22	8	3.4	1.70E+26	6.79	283.7	134.1	125.5	60.5
9_23	10	3.4	1.66E+26	6.78	265.2	130.3	126.9	52.2
9_24	6	1.4	1.73E+26	6.79	298.0	138.0	126.9	58.1
9_25	8	1.4	1.70E+26	6.79	286.5	135.2	126.7	60.9
9_26	10	1.4	1.66E+26	6.78	267.0	131.0	126.4	57.8
10_27	6	5.4	1.71E+26	6.79	280.8	137.0	85.0	51.2
10_28	8	5.4	1.68E+26	6.78	264.2	135.6	79.3	45.8
10_29	10	5.4	1.73E+26	6.79	297.1	132.6	107.0	56.2
9_30	6	7.4	1.69E+26	6.79	291.4	134.8	133.4	61.9
9_31	8	7.4	1.67E+26	6.78	290.0	132.7	125.8	54.3
10_33	10	7.4	1.69E+26	6.79	278.9	133.4	89.8	43.8
Ave.	-	-	1.70E+26	6.79	284.6	134.8	118.3	57.7

First, the effect of asperities offset on rupture dynamics and rupture kinematics were investigated. Figs. 9.5 and 9.6 show results for two selected rupture scenarios in which the offset between the two asperities is 1.4 km and 5.4 km, respectively. In addition to the stress drop model, Figs. 9.5 and 9.6 show the computed final slip and rupture time resulted from the spontaneous rupture modeling.

Several interesting features on both final slip and rupture time were observed. The slip is mainly concentrated in an area that includes both asperities and near the free surface. Based on our previous experience with simulations of ruptures that break the surface, the amount of shallow slip depends on the asperity depth and shear modulus in the near-surface material. Similarly, the peak slip velocity correlates with areas of larger stress drop, however it is stronger along the asperity edges, as well as in the soft shallow layer. The rupture slightly accelerates as it crosses the largest asperity. It slows down as it penetrates the weak zone, in the top 4 km. This is clearly seen in Fig. 9.5 (1.4 km offset) and Fig. 9.6 (5.4 offset). The reduction of rupture speed near the free surface increases the slip rise time, which affects the near-fault ground motion at long periods (>1s). A larger separation between the two asperities creates a larger area with elevated slip. However the peak slip value is reduced.

Fig. 9.7 shows time histories of simulated velocity, computed at near-fault stations, shown in Fig. 9.1, low-pass filtered at 1 Hz. The effect of rupture dynamics enhanced by the rupture directivity effect is expressed as larger peak ground motion on the fault normal component, especially toward the north end of the fault (Fig. 9.8). In contrast the largest ground motion on the fault parallel component is observed at sites above the main asperity and near the epicenter. This is a manifestation of upward rupture directivity effect, which mainly amplifies the fault parallel component of motion.

Fig. 9.9 summarizes the results of our numerical experiments in investigating effects of asperity offset on peak ground motion velocity and fault slip. 35 simulations were performed in which the asperity offset varies from 1.4 to 7.6 km. It was found that the asperity offset has no effect on both average slip and maximum slip. However its effect is not negligible on peak ground motion velocity. In general, larger asperities offsets reduce the peak ground motion velocity.

After that, it was necessary to look at the asperities depth effects. Fig. 9.10 and Fig. 9.11 show stress drop models and the resulting slip and rupture time distributions for a rupture scenario with shallow asperities (depth = 5km), and a second scenario with deep asperities (depth=10km). The resulting rupture kinematics are very different. Shallow asperities create a rather single shallow slip patch, whereas deep asperities create distinct slip concentrations in the asperities area. They also produce much larger shallow slip. Also in terms of rupture kinematics, the deep asperities create a much complex rupture time pattern, which is dominated by a very slow initial rupture and gradually faster rupture at depth. The very different rupture kinematics produces much different ground motion as well. This is illustrated in Fig. 9.12 where synthetics ground motion velocity at linear arrays parallel to the fault was compared. There is a tendency that the shallow asperities generate slightly stronger ground motion on the fault normal direction. This feature which is a manifestation of rupture directivity effect, is probably controlled by the rupture initiation depth. The slight tendency of increased peak ground motion velocity with decreasing asperity depth is clearly seen in Fig. 9.13 where peak velocity and fault slip obtained with 32 rupture scenarios was compared for which the asperity depth is varied from 4 to 10 km. It is interesting to see in both Fig. 9.13 and Fig. 9.9 that

shallow asperities tend to generate larger slip. This is mainly due to the rupture interaction with the free surface.

Finally, through rupture dynamics simulations, the effects of increased stress drop fluctuations with depth on fault slip and peak ground motion velocity were investigated. Fig. 9.14 illustrate stress drop profiles for three different rupture scenarios in which the stress drop spatial variation increases with depth. The final results in terms of peak ground motion velocity and fault slip are shown in Fig. 9.15. Our simulations show that both average peak velocity and fault slip increases when stress drop variations increase with depth.

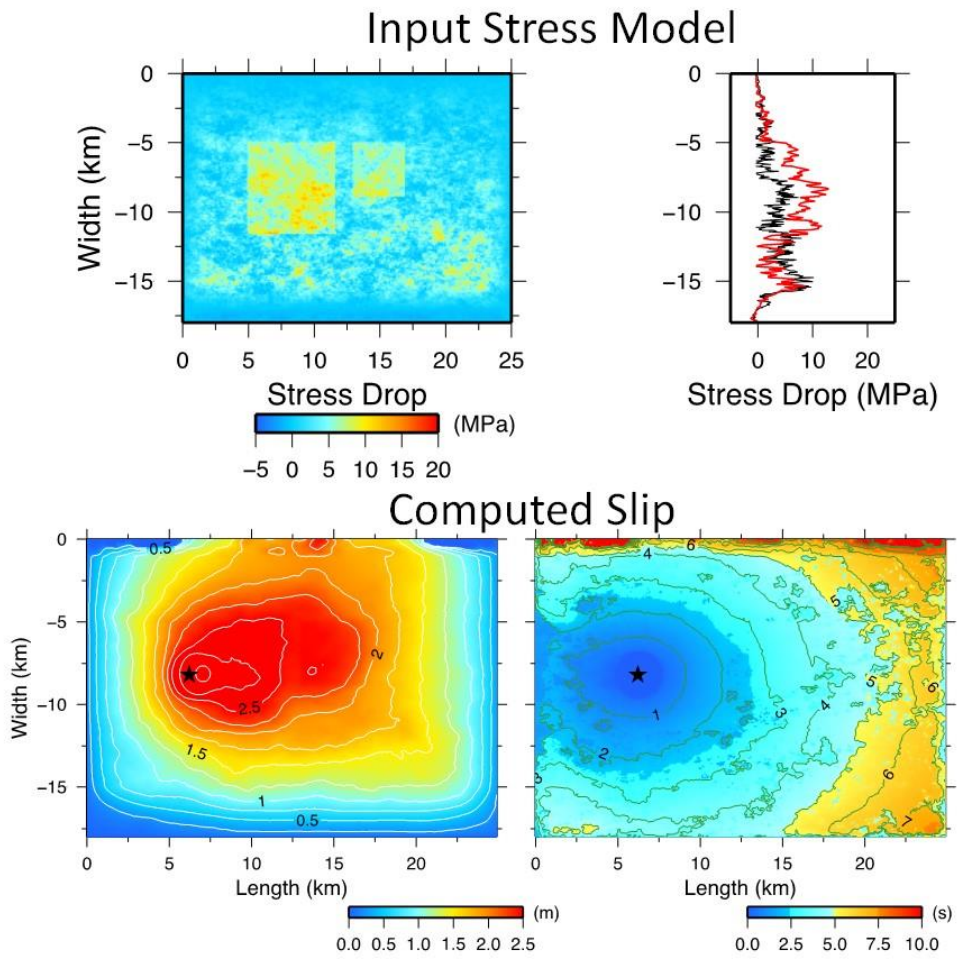

Fig. 9.5. Rupture kinematics derived from the spontaneous rupture modeling for a stress drop model with 1.4km asperities offset. Top left panel: Imposed stress drop. Top right panel: depth profiles of stress drop across the large asperity (red trace) and in the background area (black trace). Left bottom panel: derived fault slip. Bottom right panel: Rupture time. The black star indicates the rupture initiation.

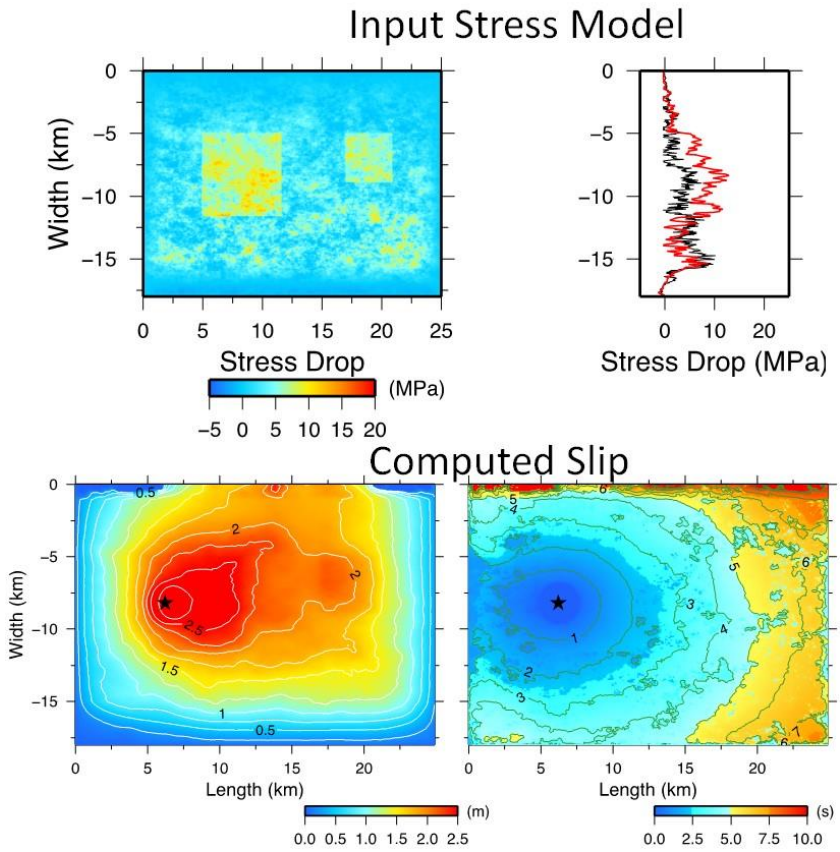

Fig. 9.6. Rupture kinematics derived from the spontaneous rupture modeling for a stress drop model with 1.4km asperities offset. Meaning on each panel is the same as in Fig. 9.5.

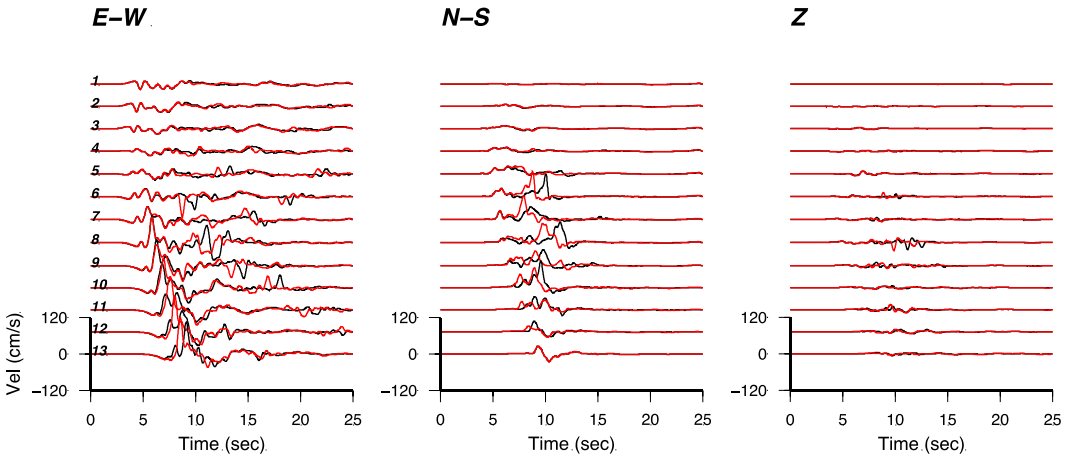

Fig. 9.7. Effects of asperities offset on simulated near-fault ground motion velocity computed at the linear array of stations parallel to the fault shown in Fig. 9.1. Given the fault orientation EW is the fault normal component, and the NS is the fault parallel component. Red traces correspond to the rupture model with asperity offset of 1.4 km, and black traces correspond to the rupture model with asperity offset of 5.4 km.

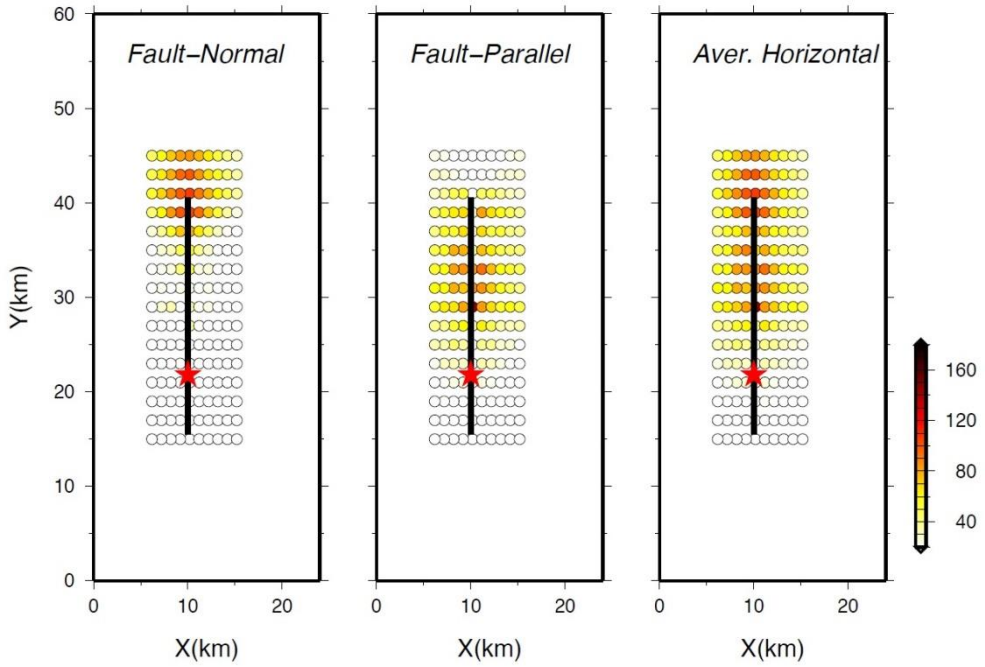

Fig. 9.8. Peak ground motion velocity. Full colored circles indicate the location of the receivers and the amount of maximum ground motion velocity in cm/s.

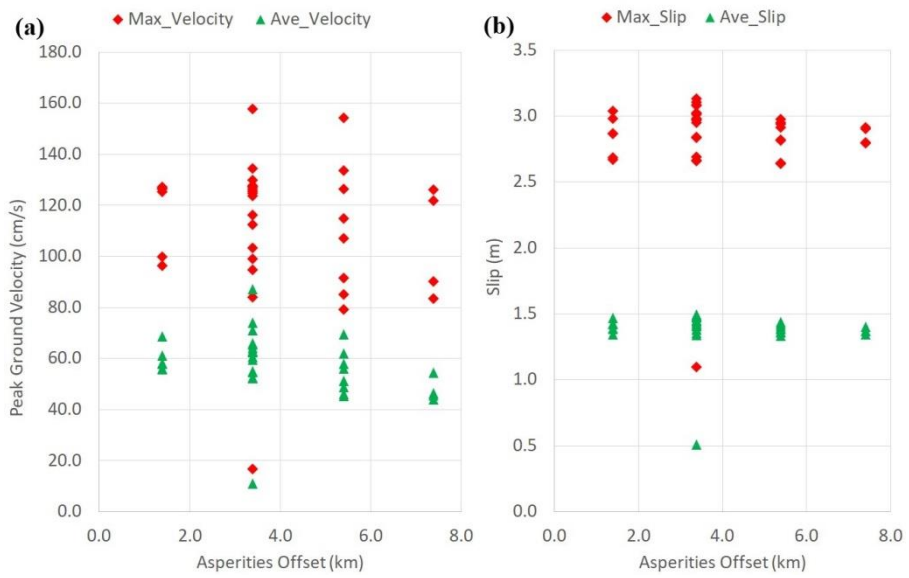

Fig. 9.9. Effects of asperities offset on computed ground motion velocity (a) and total fault slip (b). For each rupture scenario the maximum peak velocity is shown by red diamonds and average peak ground motion velocity is shown by green triangles. Same symbols are used to show the maximum fault slip and average fault slip, shown on the left panel.

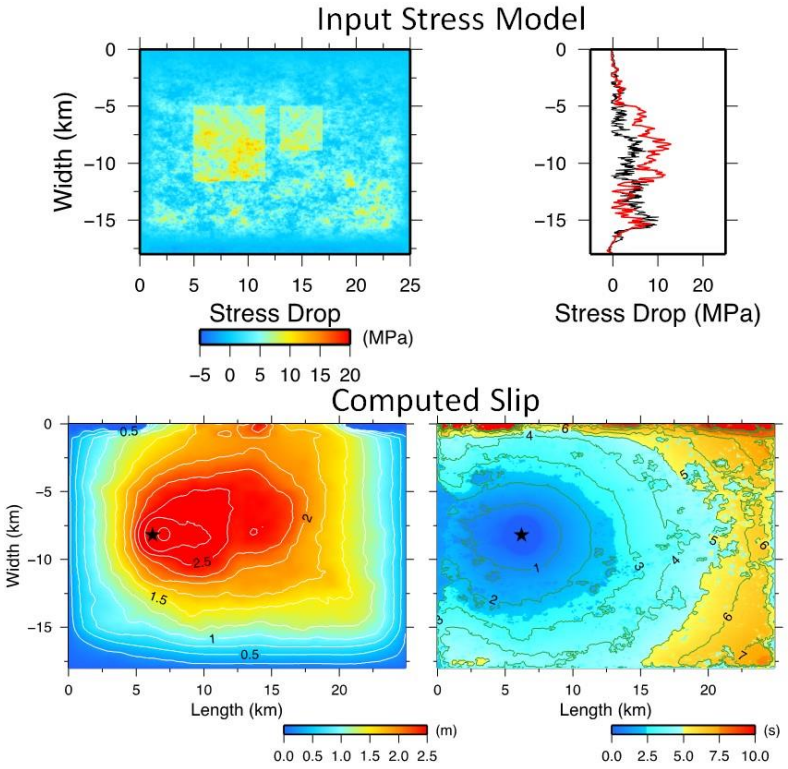

Fig. 9.10. Effects of asperities depth on rupture kinematics. Asperity depth = 5 km.

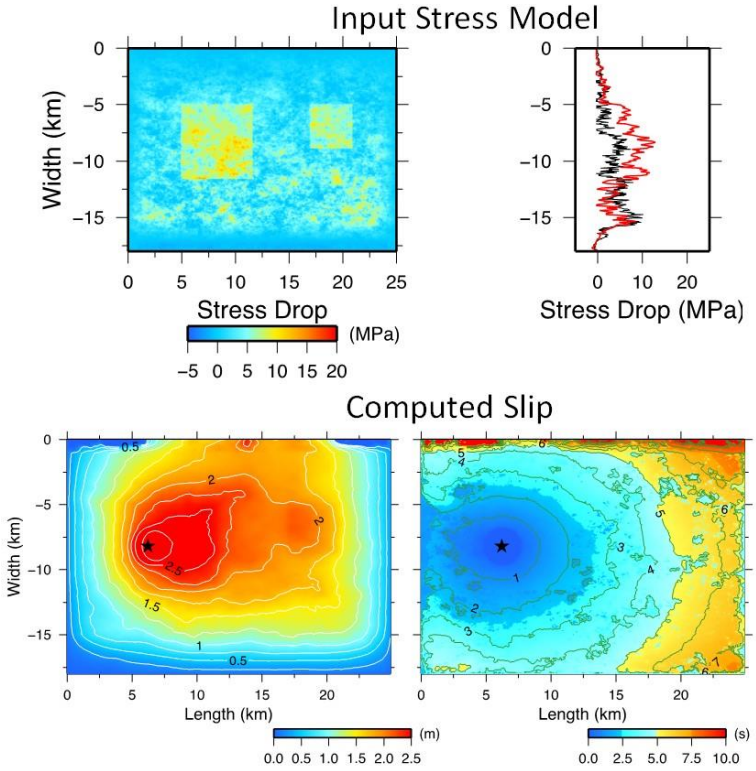

Fig. 9.11. Effects of asperities depth on rupture kinematics. Asperity depth = 10 km.

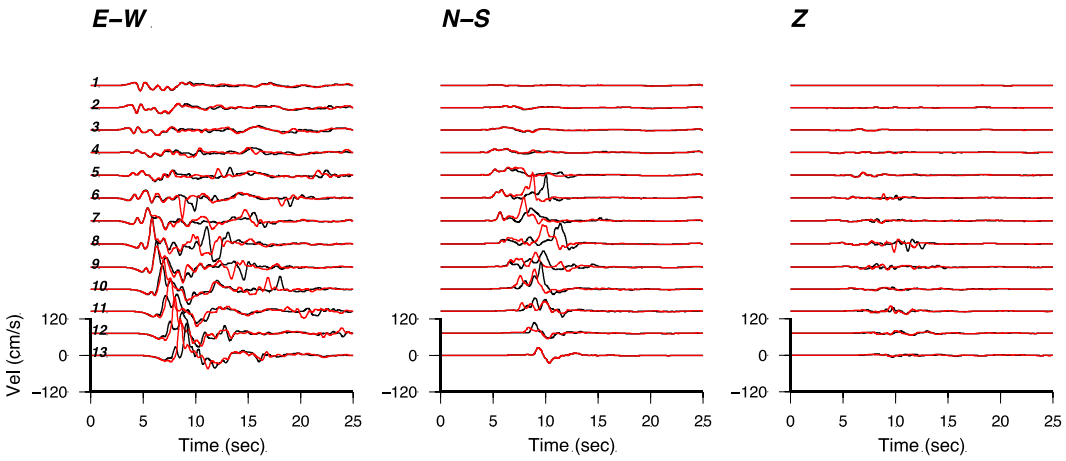

Fig. 9. 12. Effects of asperities depth on simulated near-fault ground motion velocity computed at the linear array of stations parallel to the fault shown in Figure 1. Given the fault orientation EW is the fault normal component, and the NS is the fault parallel component. Red traces correspond to the rupture model with asperity depth of 5 km, and black traces correspond to the rupture model with asperity depth of 10 km.

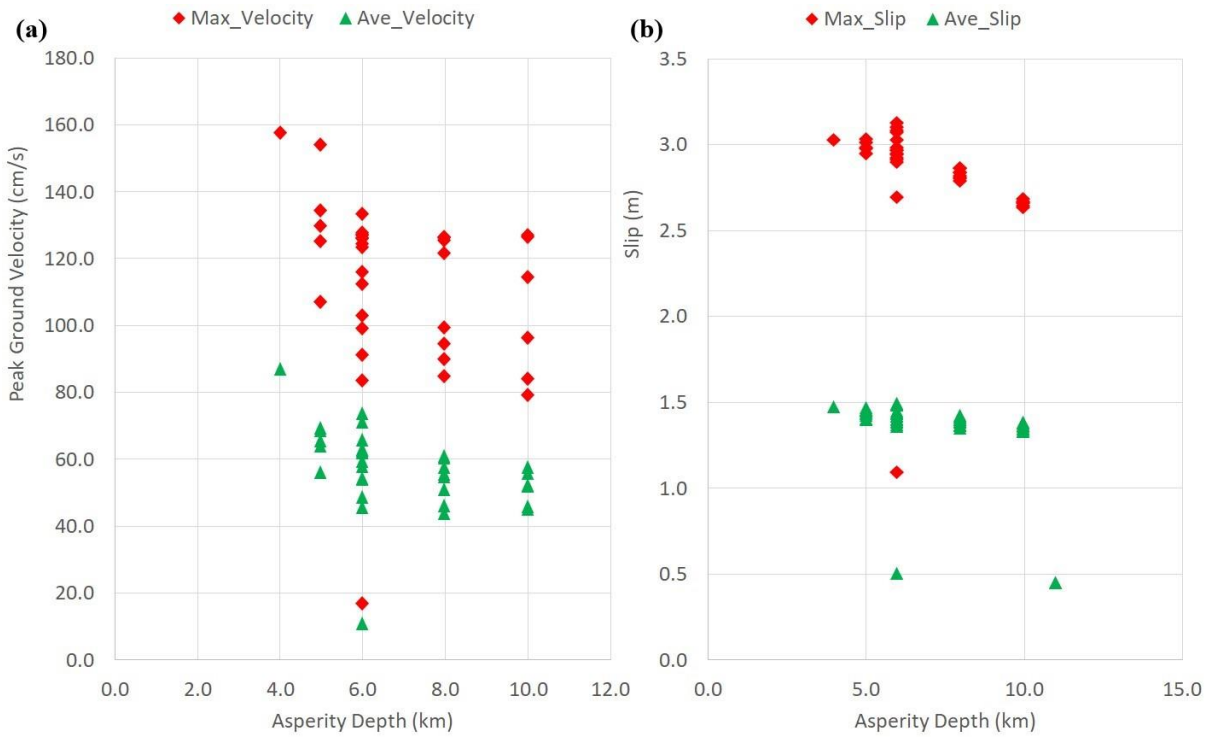

Fig. 9.13. Effects of asperity depth on computed ground motion velocity (a) and total fault slip (b). For each rupture scenario the maximum peak velocity is shown by red diamonds and average peak ground motion velocity is shown by green triangles. Same symbols are used to show the maximum fault slip and average fault slip, shown on the left panel.

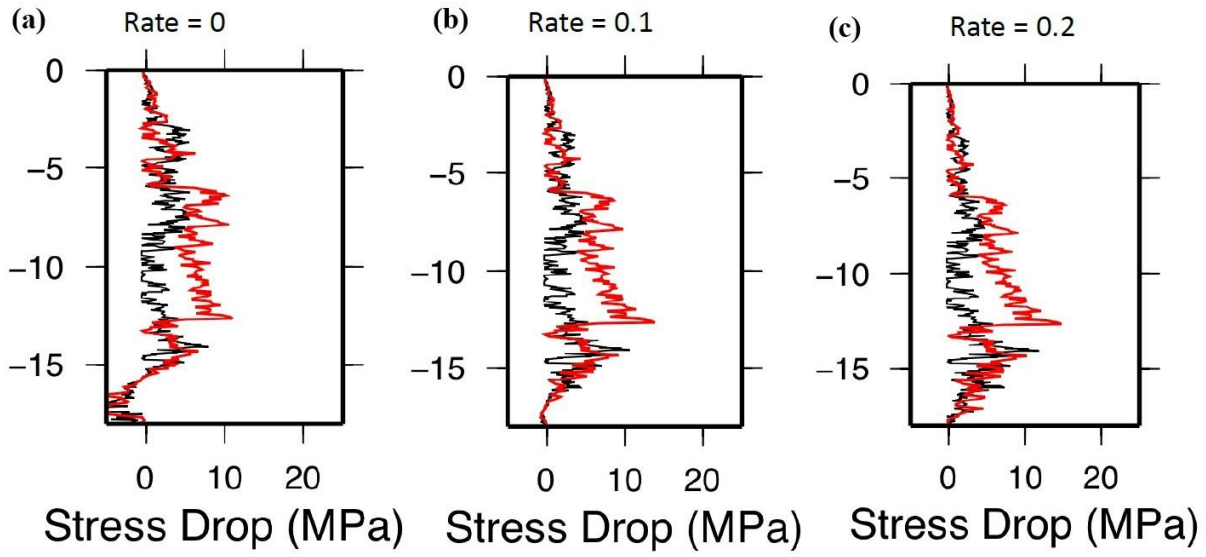

Fig. 9.14. Effect of increased stress drop fluctuations with depth. The three panels show three different rupture scenarios in which the rate of stress drop fluctuations with depth is gradually increased.

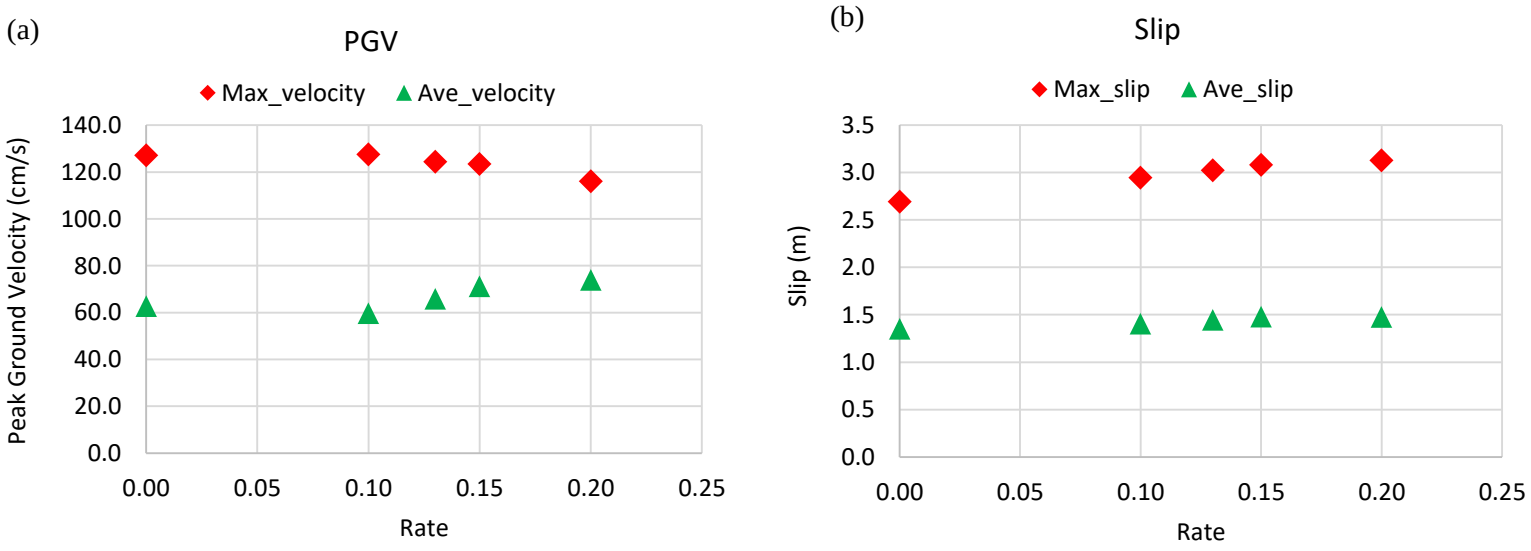

Fig. 9.15. (a) Correlation of maximum and average ground motion amplitudes with stress rate increase with depth. (b) Correlation of maximum fault slip average fault slip with stress rate increase with

9.2.3. Simulation result of basin structure

Rupture dynamics simulations are also done using two asperities based on the basin structure as shown in Fig. 9. 3 (b). The forward directivity effect is very clear for asperities depth at both 5 km

and 10 km, as shown in Fig. 9.16 and Fig. 9.17. Especially in the fault normal cases, surface peak velocities were large in the basin area. The effects of asperity offset are shown in Fig. 9.18 and Fig. 9.19. Larger surface ground velocity were estimated when asperities offset equals 1.4 km. Fig. 9.18 shows stronger directivity effect than Fig. 9.19.

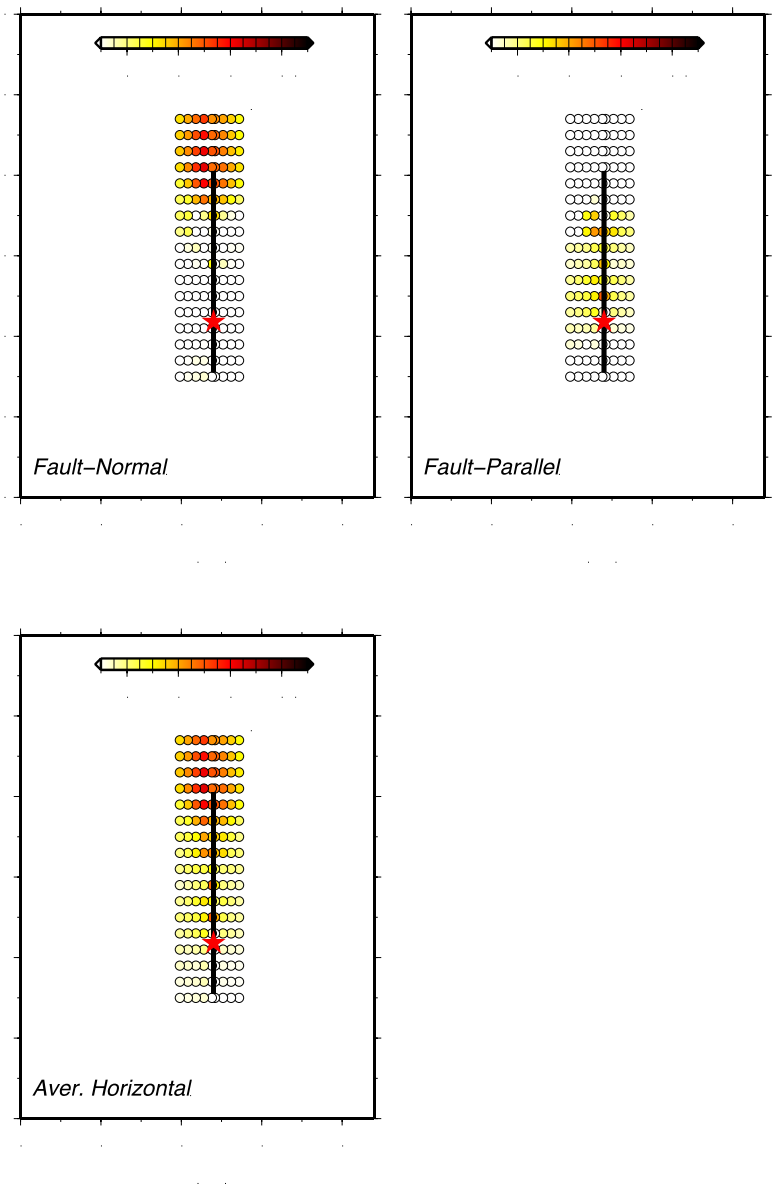

Fig. 9.16. Surface peak velocity distribution for scenario of asperities depth at 5 km (asperity offset = 3.4 km). Red star is the epicenter location on ground surface. Left area of the black line is the basin area.

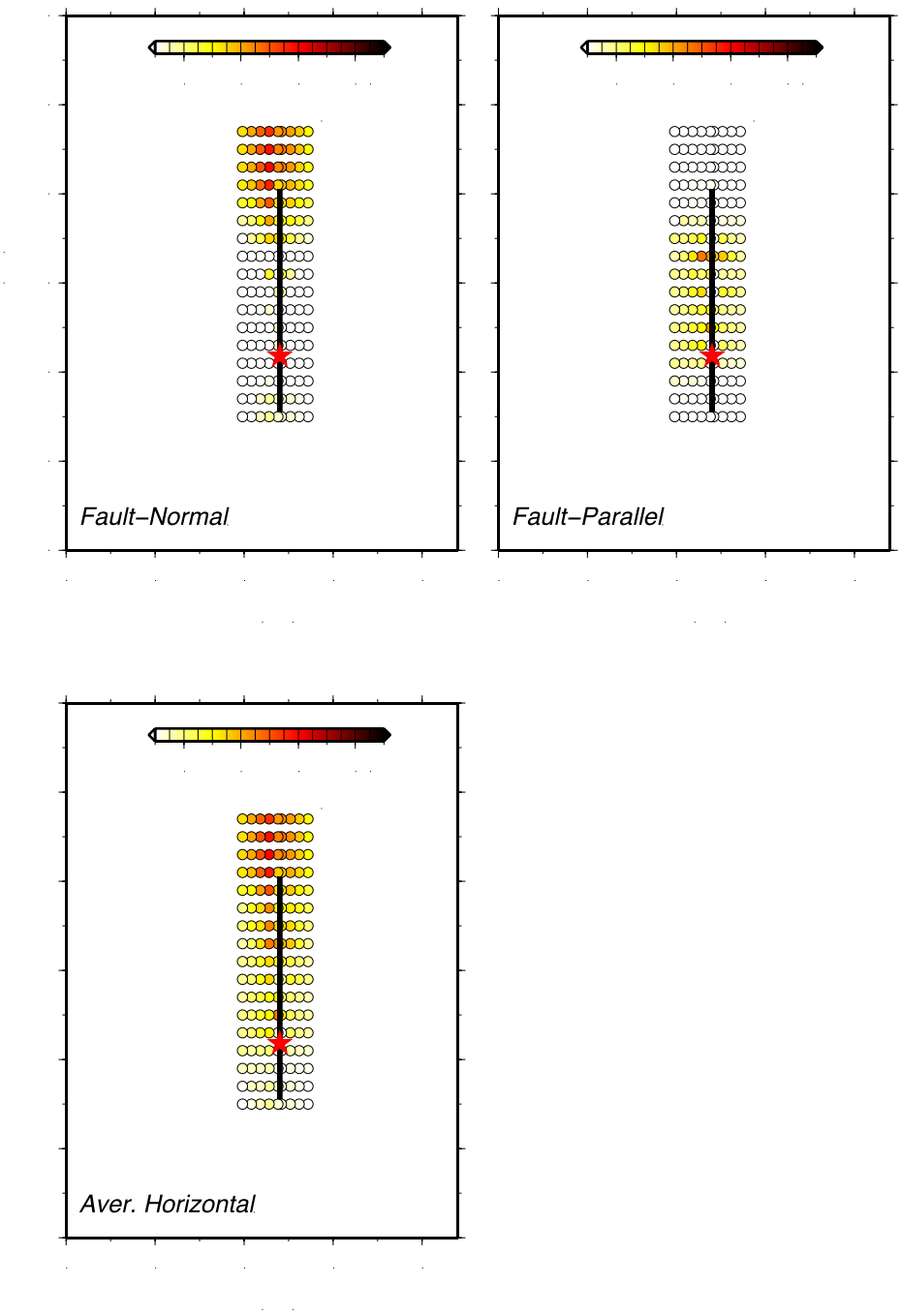

Fig. 9.17. Surface peak velocity distribution for scenario of asperities depth at 10 km (asperity offset = 3.4 km). Red star is the epicenter location on ground surface.

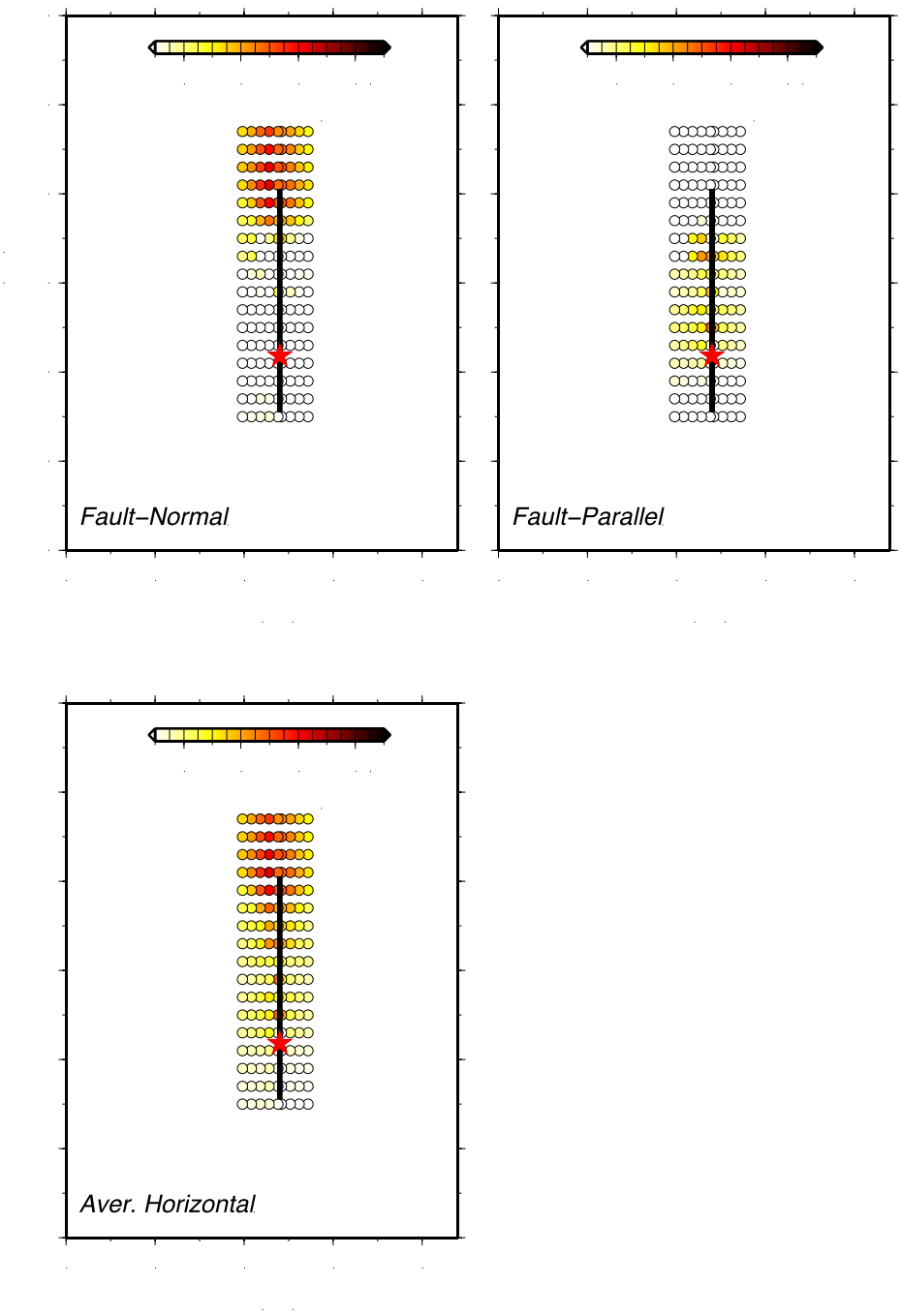

Fig. 9.18. Surface peak velocity distribution for the scenario of asperities offset equals 1.4 km (asperity depth = 6 km).

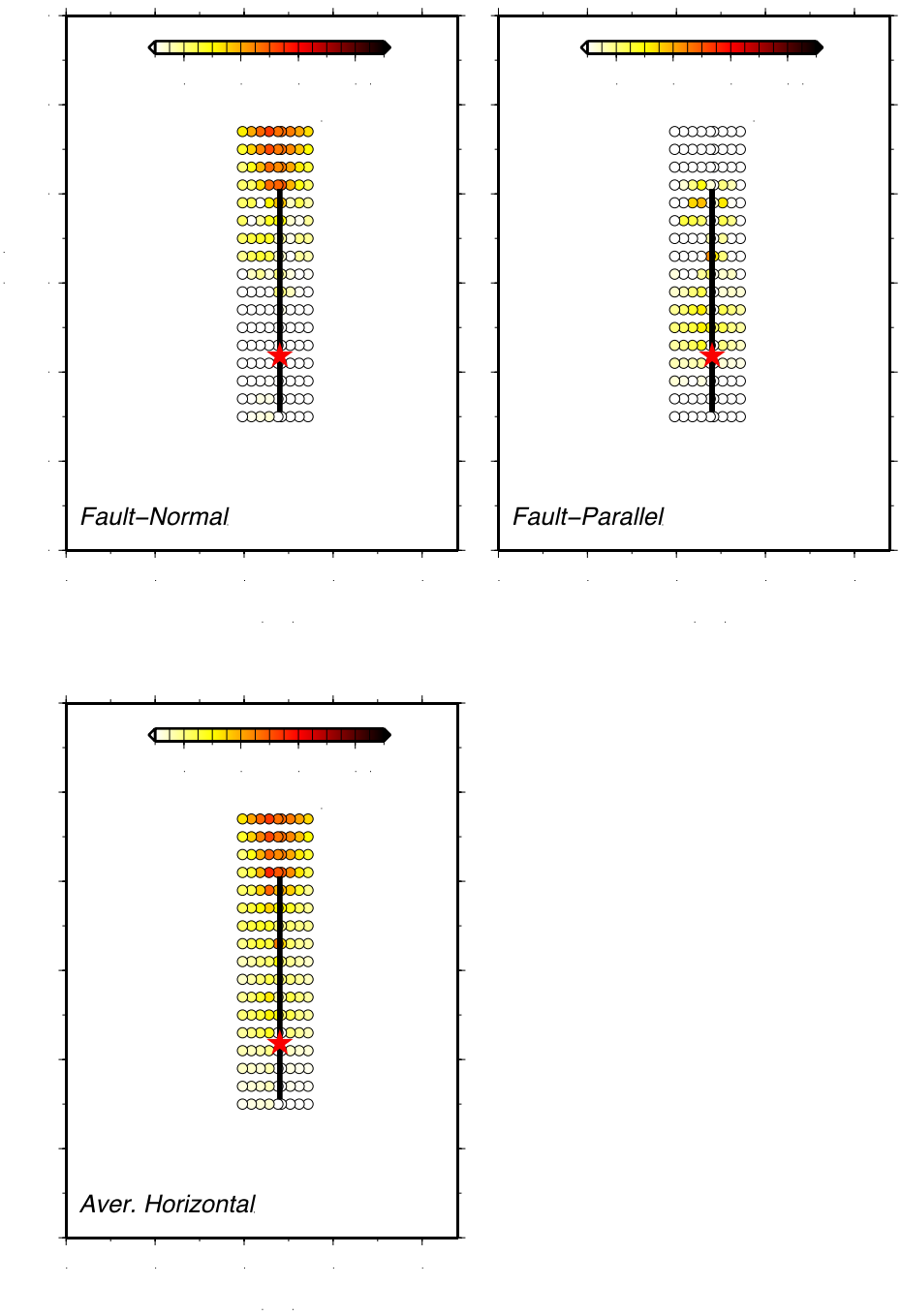

Fig. 9.19. Surface peak velocity distribution for the scenario of asperities offset equals 5.4 km (asperity depth = 6 km).

9.2.4. Slip velocity function of dynamic rupture simulations

The final slip amount obtained by our dynamic rupture simulation shows smooth variability compared to the spatial distribution of the final slip amount of the kinematic source inversion. The slip velocity function on the fault plane is a so-called Kostrov-type slip velocity function with a steep rise and a large peak slip velocity in the region where has a large amount of stress drop. It is important to understand the relationship between the spatial distribution and the region with a large stress drop.

Fig. 9.20 shows the results of the standard model (asperity depth = 6 km, asperity offset = 3.4 km, Case 9_2 in Table 9.2), the slip velocity functions were taken out in a straight line in the depth direction at the strike direction of 8 km (sampled at a pitch of about 2 km). The bottom panels showed the vertical extraction line on the slip amount distribution and stress drop distribution. The shallow sedimentary layers had a smooth rising ramp function or the shape of a normalized Yoffe function, whereas the asperity layers appeared the shape of a steep rising Kostrov function. It can also be seen that the duration was relatively longer at the upper end, but shorter in the deeper part where the crack progressed. It should be noted that the forward rupture directivity in the direction of rupture propagation was very clear and can be found in other cases.

Fig. 9.21 shows the slip velocity function (sampled pitch of 2 km) of the results of Case 9_2, forward the strike direction at the depth of 8 km. The bottom panels showed the horizontal extraction data line. The properties of the slip velocity functions were the same as that shown in the depth direction. Within the asperity, the peak slip velocity at the rising edge increased rapidly because the rupture progresses, and once outside the asperity, the rupture velocity decreased and the peak slip velocity also decreased. However, when the rupture progressed to the second asperity, the rupture was accelerated and the peak slip velocity increased. Since the rupture progressed unilaterally towards right except for the left 5 km area, due to the forward rupture directivity, the slower the rupture reaches, the steeper the rise of slip velocity function would be.

Fig. 9.22 shows the distribution of the peak slip velocity and the final slip amount on the strike direction crossed line. Arrow markers on each panel denote the region of stress drop asperities. Although the final slip amount showed a correlation with the asperity position, the overall distribution shape was smooth. The peak slip velocity showed a high correlation with the asperity position and increased towards the direction of rupture progress.

The slip velocity function appeared a Kostrov shape within the asperity, while it showed a triangular shape in the shallow part and the region between two asperities. In particular, the peak slip velocity did not appear at the center of the asperity, it shifted to the direction of rupture progress, due to the effect of rupture orientation on the shape of the slip velocity function. Since the analysis results reproduced the empirical values of the surface velocity near the epicenter, it can be pointed out that the slightly short-period pulse near the epicenter may be not caused by the sudden spatial fluctuation of the slip amount but by the rapid spatial fluctuation of the slip velocity.

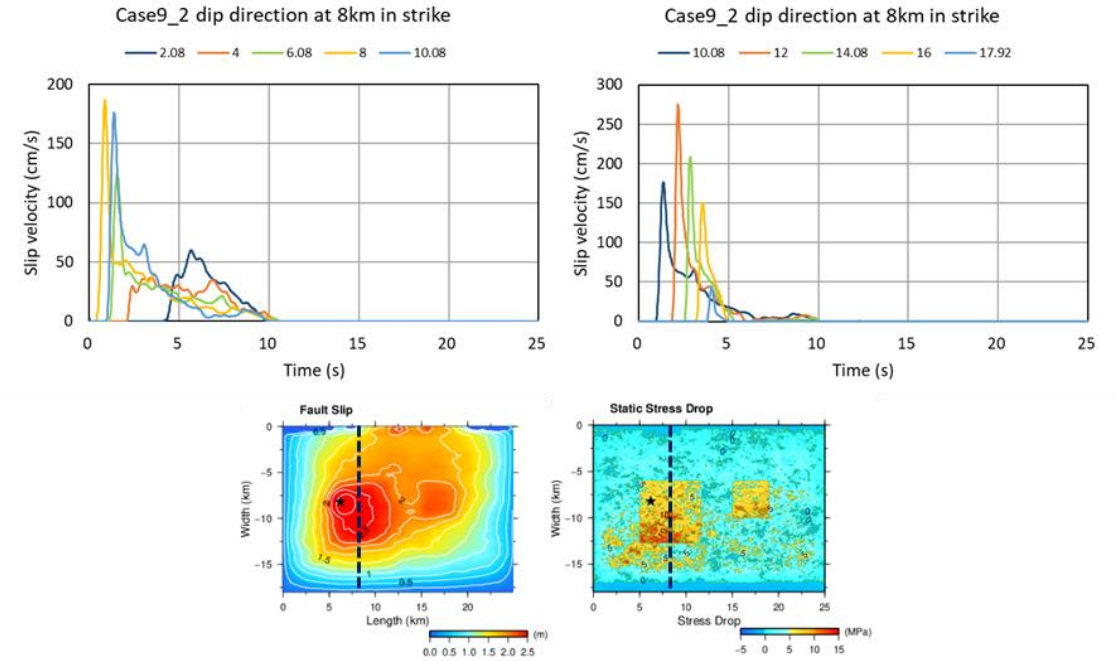

Fig. 9.20. The slip velocity function recorded in the depth direction at the strike direction of 8 km, referring to the dynamic rupture analysis of Case 9_2 (asperity depth = 6 km, asperity offset = 3.4 km).

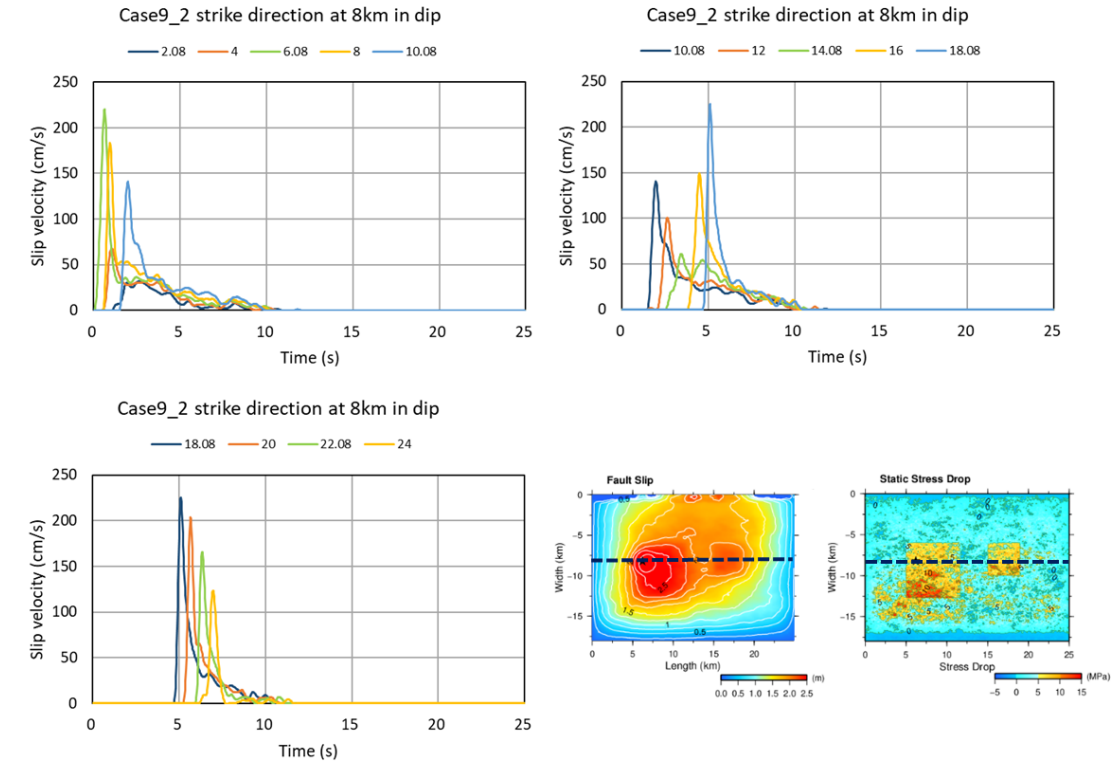

Fig. 9.21. The slip velocity function recorded in the strike direction at the depth direction of 8 km, referring to the dynamic rupture analysis of Case 9_2.

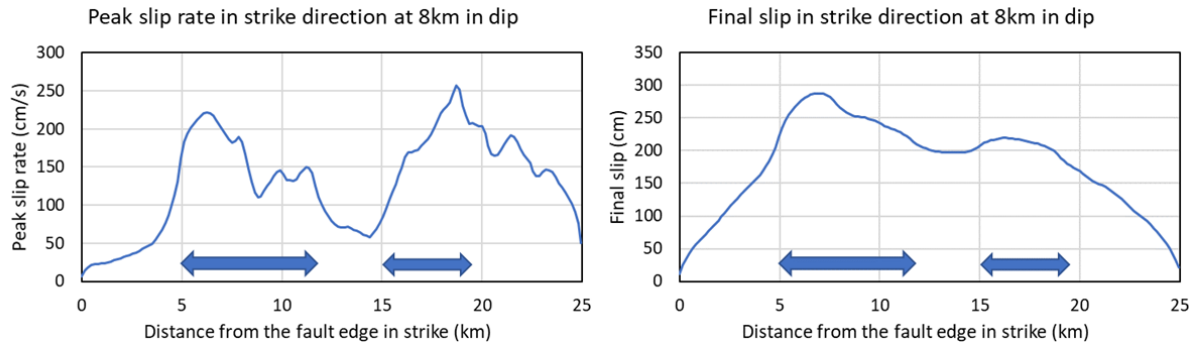

Fig. 9.22. Peak slip velocity and final slip amount in the strike direction of Case 9_2 (the horizontal cross section at the depth of 8 km)

9.3. Simulation of mainshock of 2016 Kumamoto earthquake.

Yoshida et al. have estimated source process of the 2016 Kumamoto earthquake from strong motion data by using the multiple-time window linear kinematic waveform inversion method to discuss generation of strong motions and to explain crustal deformation pattern with a seismic source inversion model [7]. A four-segment fault model was assumed based on the aftershock distribution, active fault traces, and interferometric synthetic aperture radar data, as shown in Fig. 9.23. Three western segments were set to be northwest-dipping planes, and the most eastern segment under the Aso caldera was examined to be a southeast-dipping plane (as shown in Fig. 9.23). A scenario of three asperities was defined based on the previous research results of Yoshida et al. [7] and Pitarka et al. [19], while the eastern end rupture segment was not considered. The fault geometry and location are decided based on the distribution of aftershocks after the mainshock, and also refer to the results of InSAR [20]. Velocity models used in the rupture dynamics analysis is shown in Table 9.3. It was obtained from previous studies on strong motion simulation for the 2016 Kumamoto earthquake [5–7,19].

Table 9.3. Velocity model used in the rupture dynamic analysis of the mainshock.

	Vp	Vs	Den (g/cm^3)	Qs	Dep (km)
Layer 1	1.6	0.6	1.92	60	0.1
Layer 2	2.4	1.1	2.13	100	0.2
Layer 3	4.1	2.4	2.3	200	4.8
Layer 4	5.7	3.2	2.6	280	13.5
Layer 5	6.4	3.77	2.82	1000	-

9.3.1. Fault property distributions of the mainshock

The rupture models of the mainshock are shown in Fig. 9.24. Locations of four corner sites of Mashiki are shown in Fig. 9.25. Rupture model in 3D space is: 26 km wide, 65 km long, and 25 km deep. Rupture segment is 45 km wide and 20 km deep. Fig. 9.26 presents the distributions of stress drop relative strength, and Dc of the rupture zone. Larger stress drop are concentrated in the second asperity surrounding 12 km deep. Locations of three asperities (A_2, A_3, and A_H) are displayed on the left panel, which were consistent with the fault segment on Fig. 9.23 (F2, F3, and H). In the rupture dynamics model, A_2, A_3, and A_H were located between 25 − 38 km, 21 − 31 km, and 21 − 31 km in the fault parallel direction. Fig. 9.27 shows the results of simulated slip distribution (a), slip-rate distribution (b), t0 distribution (c), the moment when the peak slip-rate appears, and rupture time distribution and rupture time distribution (d).

Largest fault slip is concentrated in the large asperity (A_2, as shown in Fig. 9.23 and Fig. 9.26), and it achieved more than 4 m. Additionally, the large fault slip on the ground occurs above A_2. In A_3, the fault final slip was not large in the deeper part, approximately below 15 km, while the 12 − 15 km deep region in A_3 was occurred larger fault slip. Moreover, the shallower the site was, the larger the slip amount in A_3. In A_H, from left to right, the final fault slip became larger and larger. It also generated a large fault final slip area surrounding the hypocenter. The large fault final slip appeared in the region between three asperities, especially for the area near A_2.

According to the distribution of peak slip-rate result, the largest peak slip-rate was concentrated in the top–right area of A_2, which was as large as 6 m/s. On the ground, large peak slip-rate occurred above A_2, which was similar as the fault final slip distribution on the ground. In the deeper part of A_2, even though peak slip-rate decreased to approximate 3.5 m/s in most area, it was larger than that of other two asperities. In A_3, large peak slip-rate was generated in the top-right area, which was as large as 4 km/s. However, in the top-left area of A_3, peak slip-rate decreased to less than 1 km/s which was similar to that of background areas. Peak slip-rate was small even if in the near hypocenter area in A_3. In A_H, the peak slip-rate was between 1~2 m/s in most areas. Additionally, in the top-left of A_H, peak slip-rate was larger than other regions. The rupture dynamic model also generated a large area with peak slip-rate equals approximately 2~3 m/s right to A_2, which might be resulted by the rupture directivity effect.

In the contour of peak slip rate time (t_0) distribution, short t_0 was concentrated in A_2 and the fault forward direction (the right area to A_2). On the ground above A_2, t_0 was also shorter than 0.2 s. It reached to the peak slip-rate quickly during the mainshock in this region.

Rupture time was shorter in the area close to the hypocenter, and longer in the area close to the hypocenter. Moreover, the rupture time decreased slightly when it passes through the asperity areas. Shorter rupture time also appeared at the left boundary region surrounding A_3.

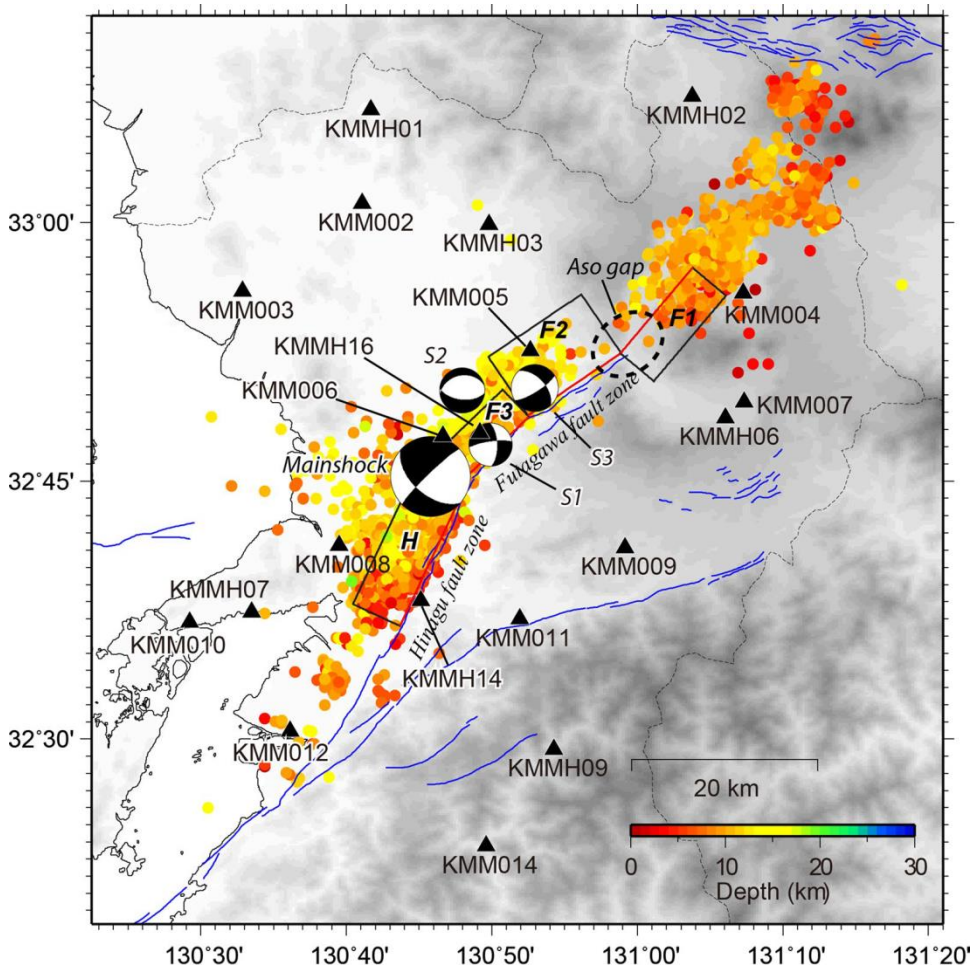

Fig. 9.23. Map showing aftershocks (after the JMA unified hypocenter catalogue) that occurred during the first 24 h after the mainshock, and the location of active faults (blue line, National Institute of Advanced Industrial Science and Technology 2012). Triangles show the seismic stations [7]**.**

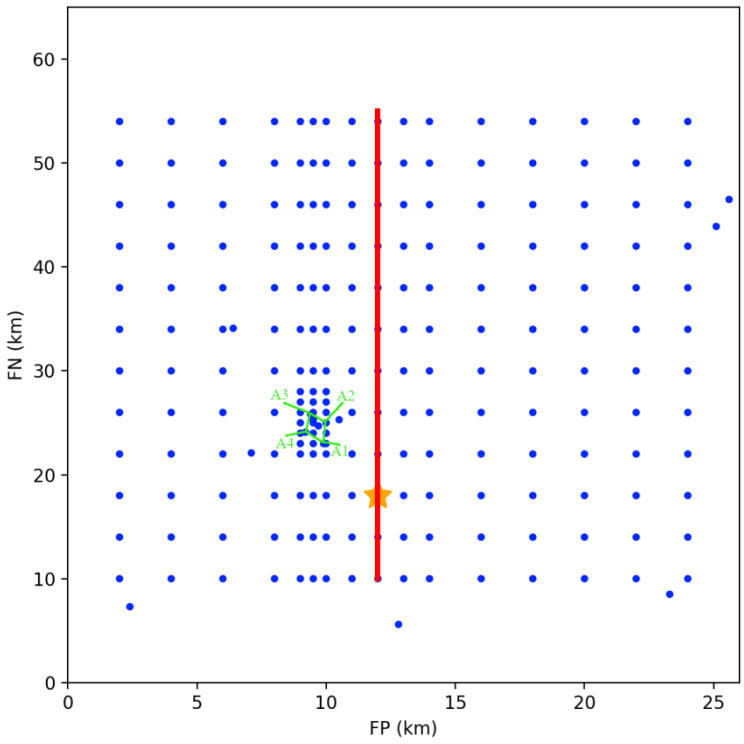

Fig. 9.24. Top view of the rupture modeling. Red solid line denotes the fault zone, large orange star denotes the epicenter location of mainshock, blue dots denote the recording locations set on the ground surface, green polygon shows roughly the location of Mashiki. X-axis and Y-axis are the fault parallel (FP) and fault normal (FN) directions, respectively. Mashiki NE and SW points means the northeastern (A1) and southwestern (A3) points of my research area, as shown in Fig. 9.25.

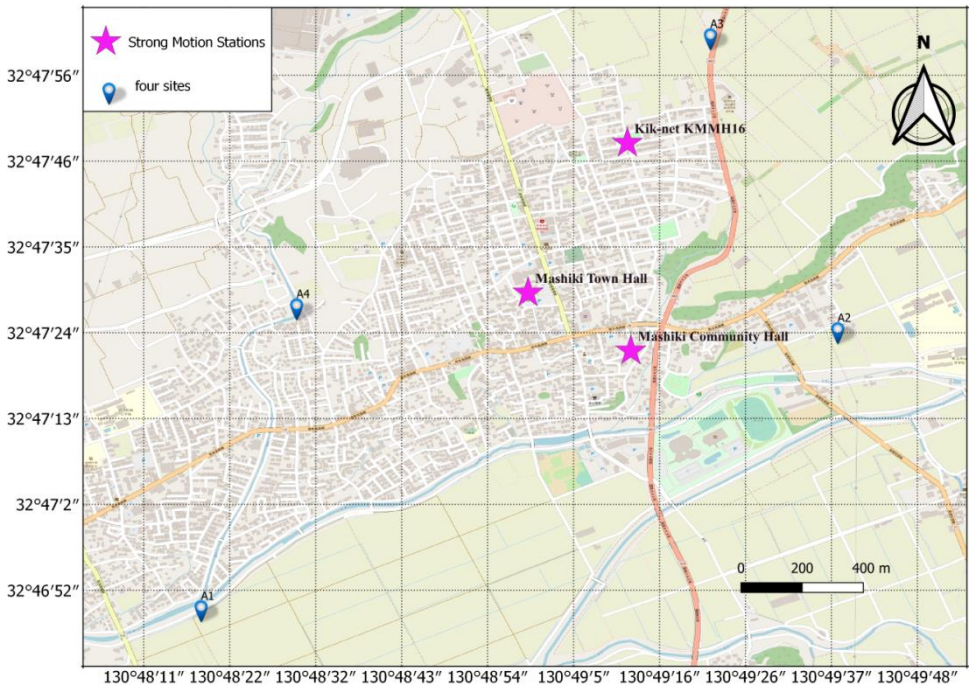

Fig. 9.25. Four corner points of Mashiki. A1, A2, A3, A4 denote the southwestern, southeastern, northeastern, and northwestern corner points of Mashiki, respectively. Locations of these sites are consistent with the green polygon in Fig. 9.24.

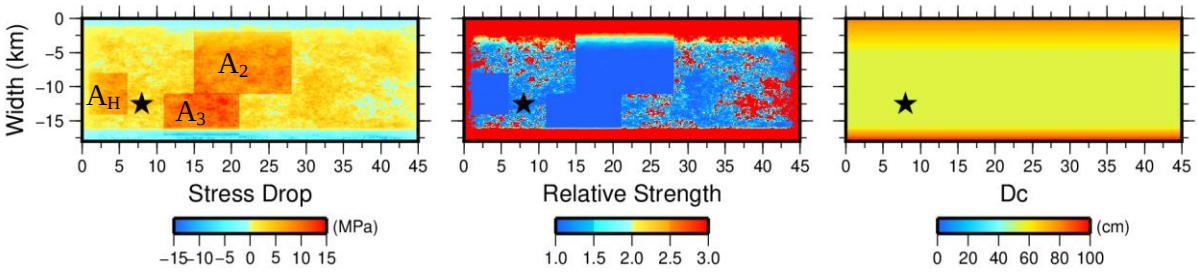

Fig. 9.26. Stress drop, relative strength, and Dc of our simulation scenario for the 2016 Kumamoto earthquake.

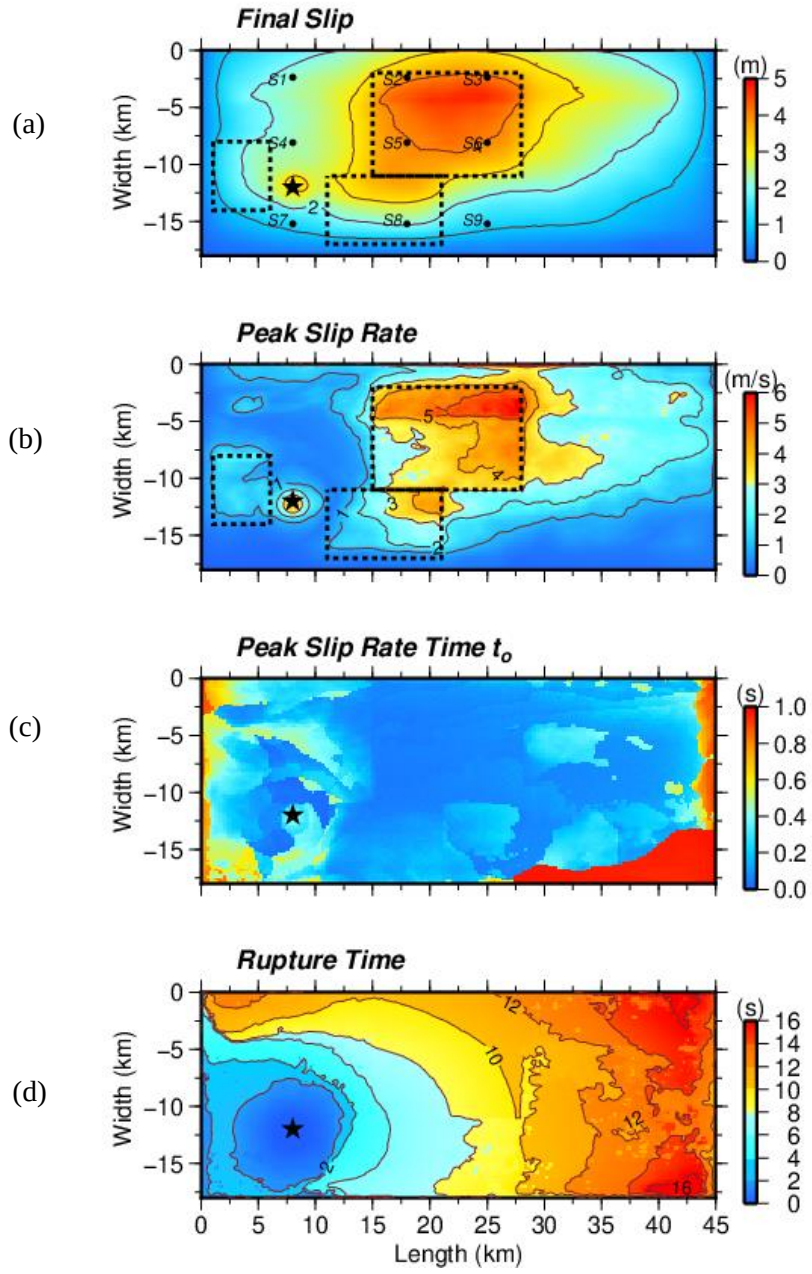

Fig. 9.27. Estimated fault slip distribution (a), slip-rate distribution (b), peak slip-rate distribution (c) t_0 (when the peak slip-rate appears), and rupture time distribution (d) of the fault model in Fig. 9.26.

9.3.2. Comparisons between estimated and observed ground motions in Mashiki

Comparisons of the estimated ground motions of EW, NS, and UD at KMMH16 are shown in Figs. 9.27, 9.28, 9.29. Both observed and estimated waveforms were adopted a 0.1~1.0 Hz butterworth filter. According to the EW and NS comparison results, the estimated velocity waveforms

and displacement waveforms were close to the observed ones. As for the UD comparison results, the estimated velocities and displacements were smaller than the observed one.

Comparisons of the estimated ground motions of three components at KMMP58 are shown in Figs. 9.30, 9.31, 9.32. The 0.1~1.0 Hz butterworth filter was also adopted in these results. Shapes of estimated curves fit the observed ones seems well. However, the estimated ground motions were approximate half of the observed ones in three directions. Maybe because the KMMP58 strong motion station was set at the first floor of a RC building with a basement, the combined effects of RC structure and site effect resulted in such large recordings during the mainshock.

After obtaining the ground motions at KMMH16 and KMMP58 by the rupture dynamics analysis, the seismological bedrock motions were calculated by the linear analysis (LA) method [21]. According to the identified velocity model at KMMH16 and KMMP58, the velocity models used in the LA to estimate the seismological bedrock motions are listed in Table 9.4, from ground surface (0.0 m) to -4252m for KMMH16, and 0.0 − -4221 m for KMMP58. Figs. 9.33 − 9.35 show comparisons of the LA inverted seismological bedrock motions at KMMH16 and KMMP58. It was clearly to find that two estimated seismological bedrock motions at KMMH16 and KMMP58 were very close to each other, and results of KMMH16 were slightly larger than the KMMP58 results. Associating with the ray path analysis in Chapter 5, the seismological bedrock motions in Mashiki have a very little difference between different sites. In this case, the same seismological bedrock waves were suitable to use in the site response analysis in Mashiki.

Table 9.4. Velocity model used in the LA to estimate the seismological bedrock motions.

	Vp	**Vs**	**Den (g/cm^3)**	**Qs**	**Depth of KMMH16 (km)**	**Depth of KMMH58 (km)**
Layer 1	1.6	0.6	1.92	60	0.1	0.1
Layer 2	2.4	1.1	2.13	100	0.2	0.2
Layer 3	4.1	2.4	2.3	200	4.252	4.221
-	5.7	3.2	2.6	280	-	-

After that, the ground motions with correction of shallow velocity structures at KMMH16 and KMMP58 were carried out. The linear analysis (LA), equivalent linear analysis (ELA) and nonlinear analysis (NA) were adopted with the soil columns of two sites. The same nonlinear soil properties of KMMH16 and KMMP58 as in the Chapter 6 were used in NA. Shallow subsurface structures of two sites are also the same as in Chapter 6, as shown in Table 9.5. The input seismological bedrock motioned were the ones inverted from the estimated ground motions by the rupture dynamics analysis. Comparisons of the LA, ELA, NA, rupture dynamic estimated results and the observed ground motions at KMMH16 are shown in Figs. 9.36 − 9.38, for EW, NS and UD directions, respectively.

Moreover, comparisons of the estimated and results and observed motions at KMMP58 are presented in Figs. 9.39 − 9.41, for EW, NS, and UD directions, respectively. The LA, ELA, and NA results were very close to each other. The LA, ELA, and NA results were close to the rupture dynamics analysis results at KMMH16 and KMMP58. It was also noted that the LA, ELA, and NA results of horizontal components of velocities and displacements were similar to the observed motions at KMMH16. In the UD direction at KMMH16, all the estimated results were a little smaller than the observed ones. It is undeniable than the estimated accelerations were quite different from the observations, while the most important properties in rupture dynamics analysis were velocity and displacement. Thun, the estimated ground motions were similar to the observations at KMMH16. The soil nonlinearity had slightly effect to change the ground motions for the frequency range of 0.1−1.0 Hz. At KMMP58, although curve shapes of estimated displacements were similar to the observations, the observed motions were quite larger than the estimated ground motions. The joint effects of RC building and soil properties may be the reason to cause it.

Table 9.5. Shallow subsurface structures of KMMH16 and KMMP58. These models were used for the LA analyses, to estimate the ground motions.

Layer	**V_p**	**V_s**	**Density**	**KMMH16 Depth**	**KMMP58 Depth**
Number	(m/s)	(m/s)	(g/cm^3)	(m)	(m)
1	296.56	154.87	1.66	3.00	2.12
2	760.00	249.36	1.73	15.00	3.02
3	1841.61	337.07	1.79	20.29	18.81
4	1918.07	483.09	1.87	22.39	25.08
5	1995.00	598.03	1.92	38.19	47.93
6	1995.09	733.19	1.97	50.69	60.67
7	2529.23	790.10	2.00	75.99	60.93
8	2558.47	827.70	2.01	92.12	61.09
9	2768.98	990.51	2.07	137.04	106.01
10	4078.39	1172.19	2.13	166.27	135.24
11	4796.23	1468.35	2.21	230.87	199.84
12	4813.21	1790.20	2.30	246.39	215.36
13	5776.98	1871.20	2.32	1152.17	1121.14
14	5786.36	3264.74	2.61	4252.48	4221.45
15	6000.00	3400.00	2.64	4252.48	4221.45

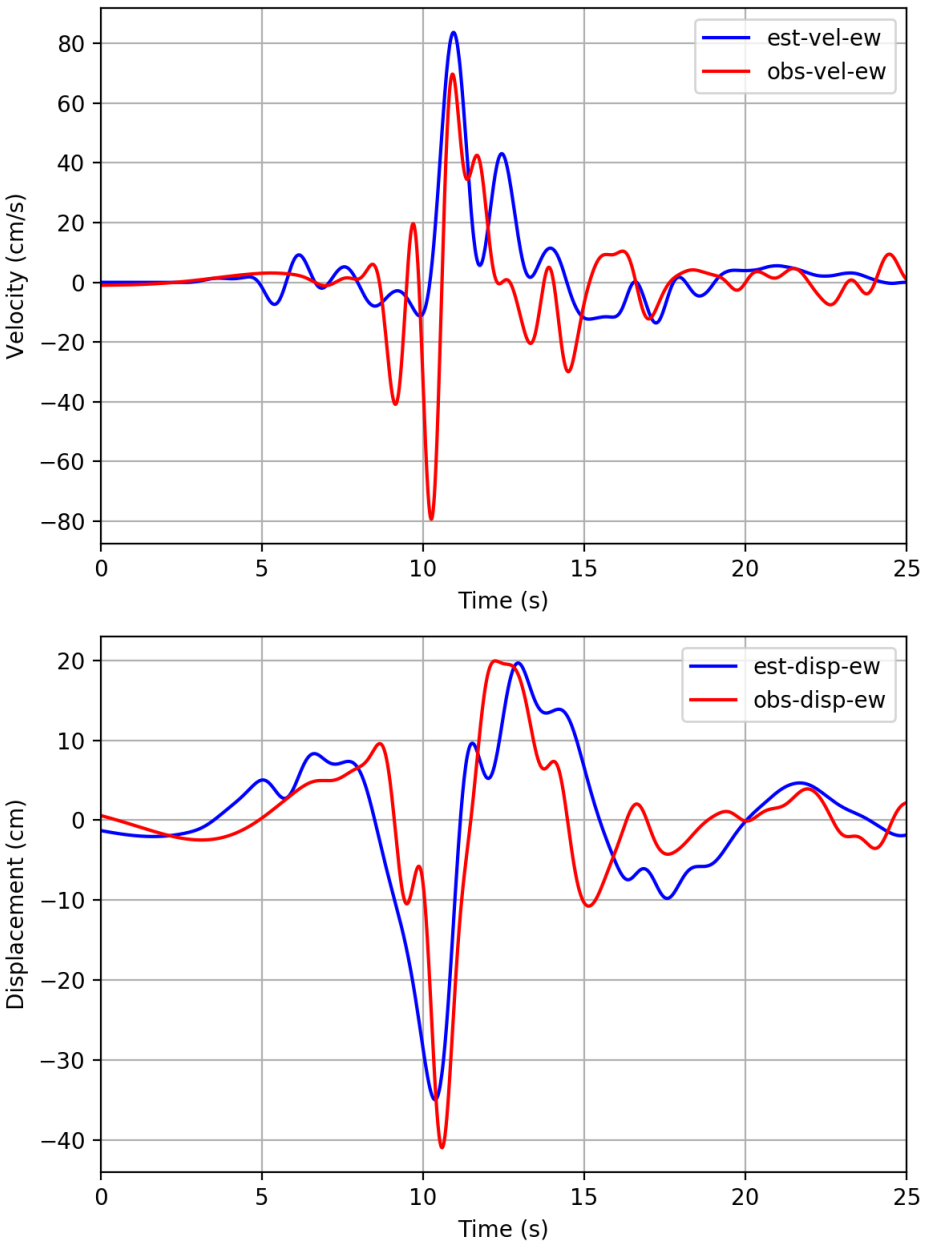

Fig. 9.27. Comparisons between the estimated EW ground motion by rupture dynamics analysis and observed EW ground motion at KMMH16. Panel above is the comparison of velocity waveforms, and panel below is the comparison of displacement waveforms. Red and blue lines denote the observed and estimated EW components at KMMH16, respectively.

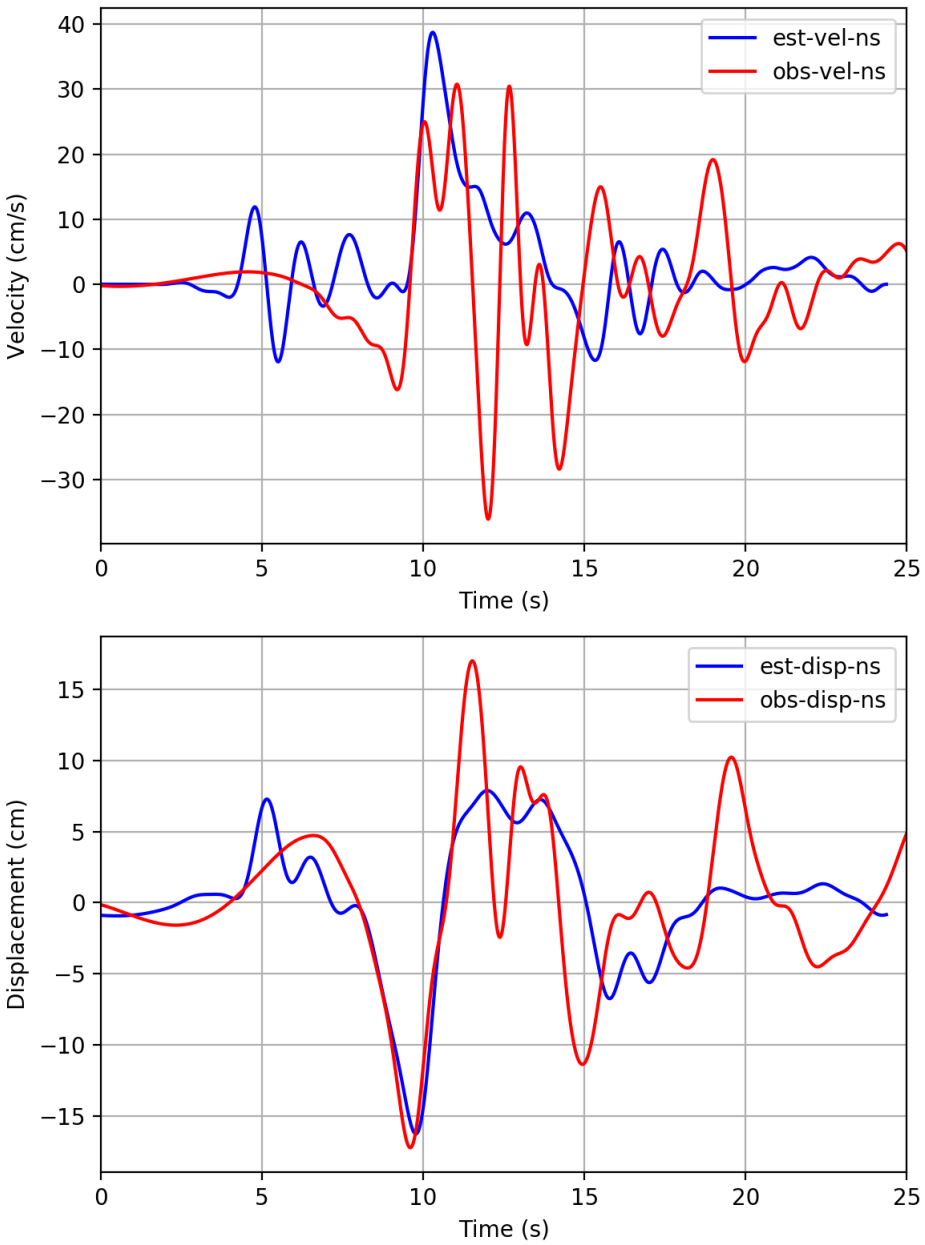

Fig. 9.28. Comparisons between the estimated NS ground motion by rupture dynamics analysis and observed NS ground motion at KMMH16. Each panel and line denotes the same meaning as Fig. 9.27, but all in the NS direction.

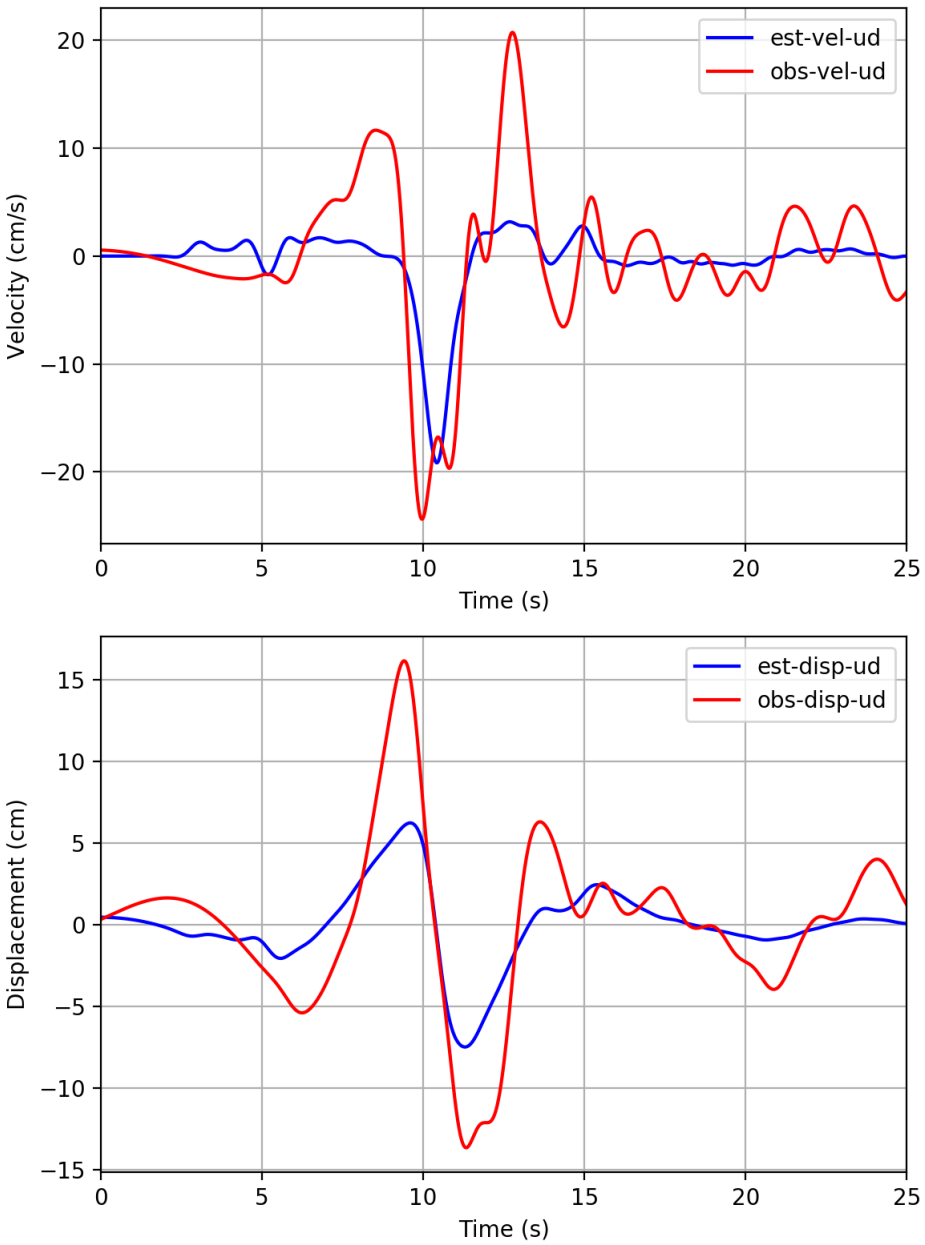

Fig. 9.29. Comparisons between the estimated UD ground motion by rupture dynamics analysis and observed UD ground motion at KMMH16. Each panel and line denotes the same meaning as Fig. 9.27, but all in the UD direction.

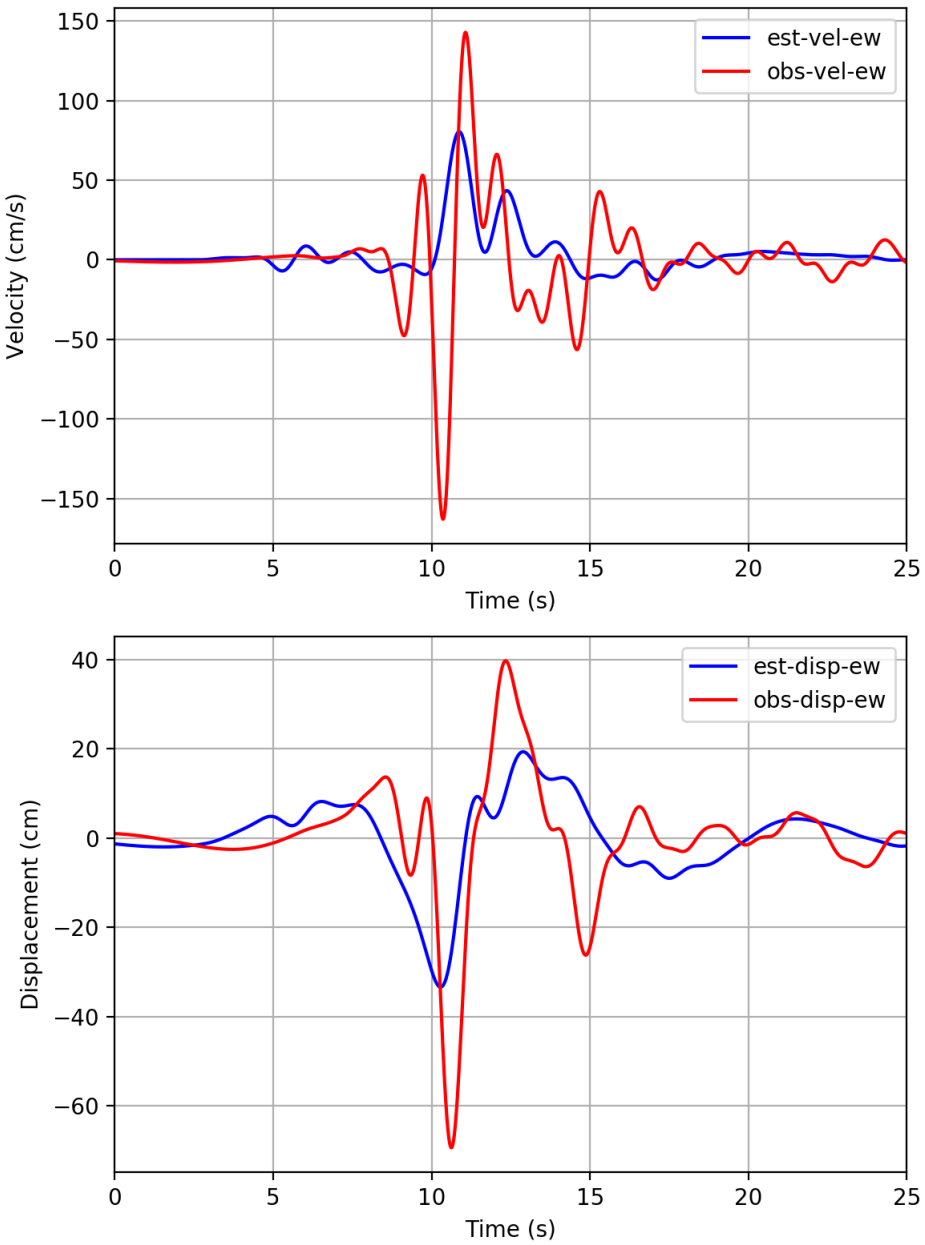

Fig. 9.30. Comparisons between the estimated EW ground motion by rupture dynamics analysis and observed EW ground motion at KMMP58. Each panel and line denotes the same meaning as Fig. 9.27, but all are for KMMP58 EW component.

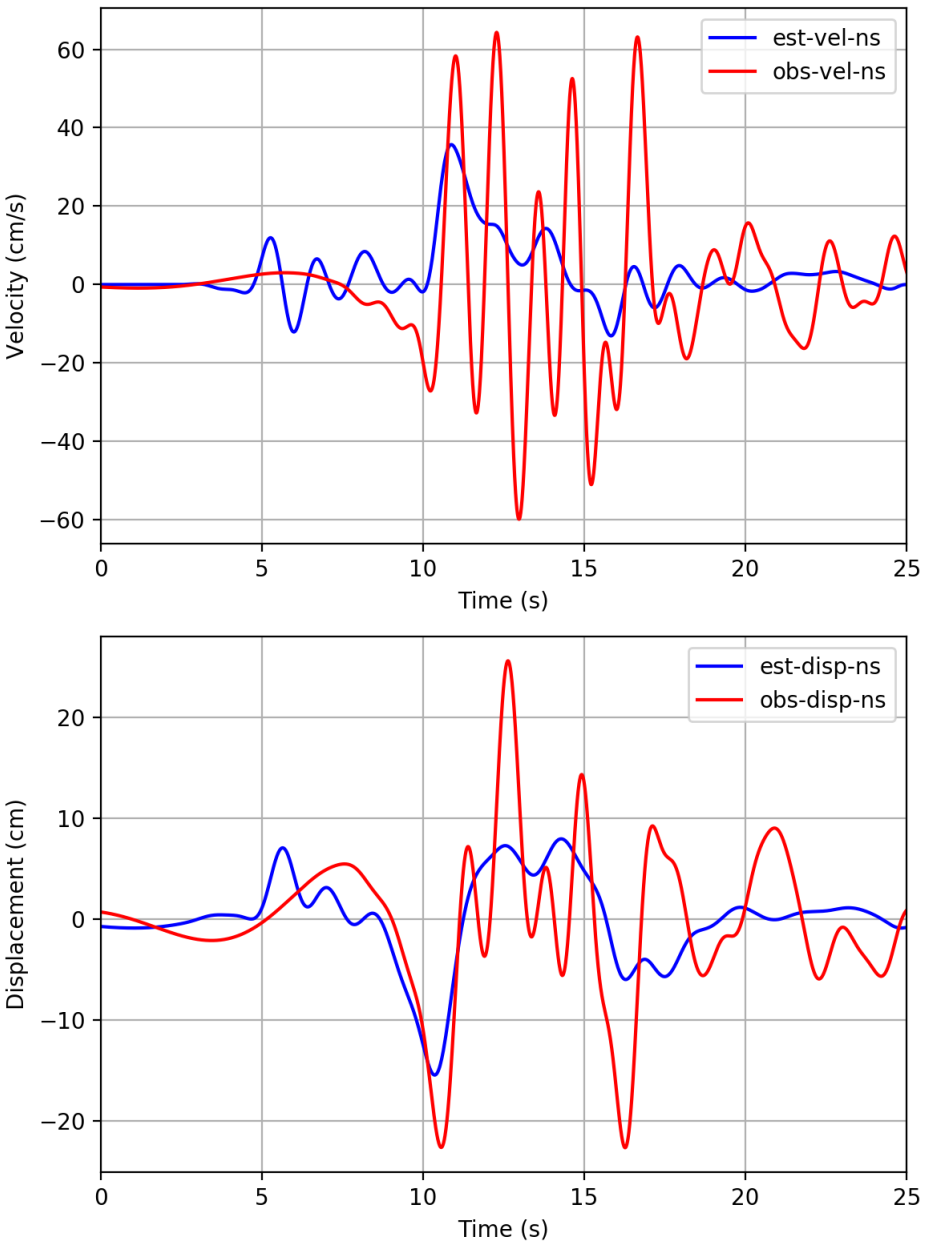

Fig. 9.31. Comparisons between the estimated NS ground motion by rupture dynamics analysis and observed NS ground motion at KMMP58. Each panel and line denotes the same meaning as Fig. 9.27, but all are for KMMP58 NS component.

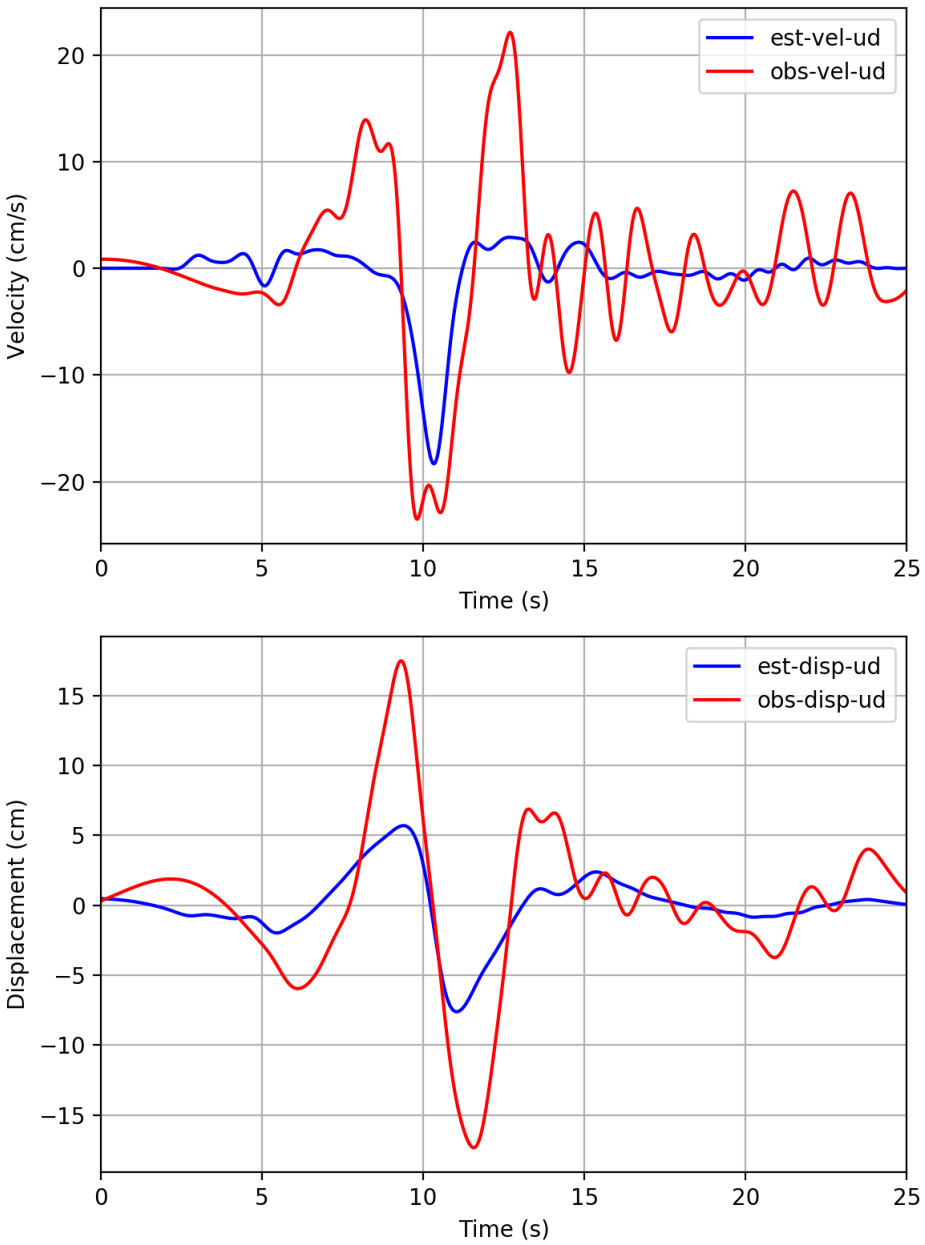

Fig. 9.32. Comparisons between the estimated UD ground motion by rupture dynamics analysis and observed UD ground motion at KMMP58. Each panel and line denotes the same meaning as Fig. 9.27, but all are for KMMP58 UD component.

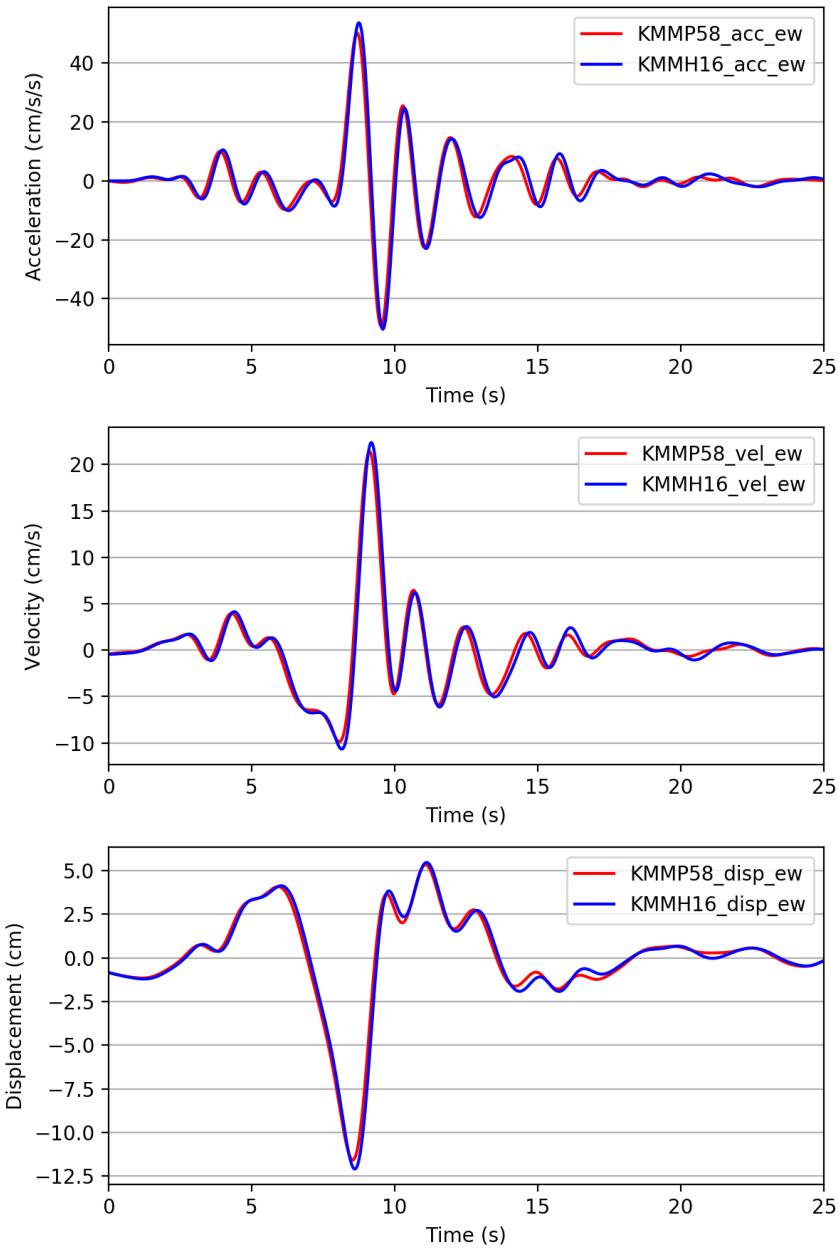

Fig. 9.33. Comparisons of LA analyzed seismological bedrock motions at KMMH16 and KMMP58. Above, middle, and below panels denote the results of accelerations, velocities and displacements, respectively. Blue and red lines denote the estimated results at KMMH16 and KMMP58, respectively. All these result are in the EW direction.

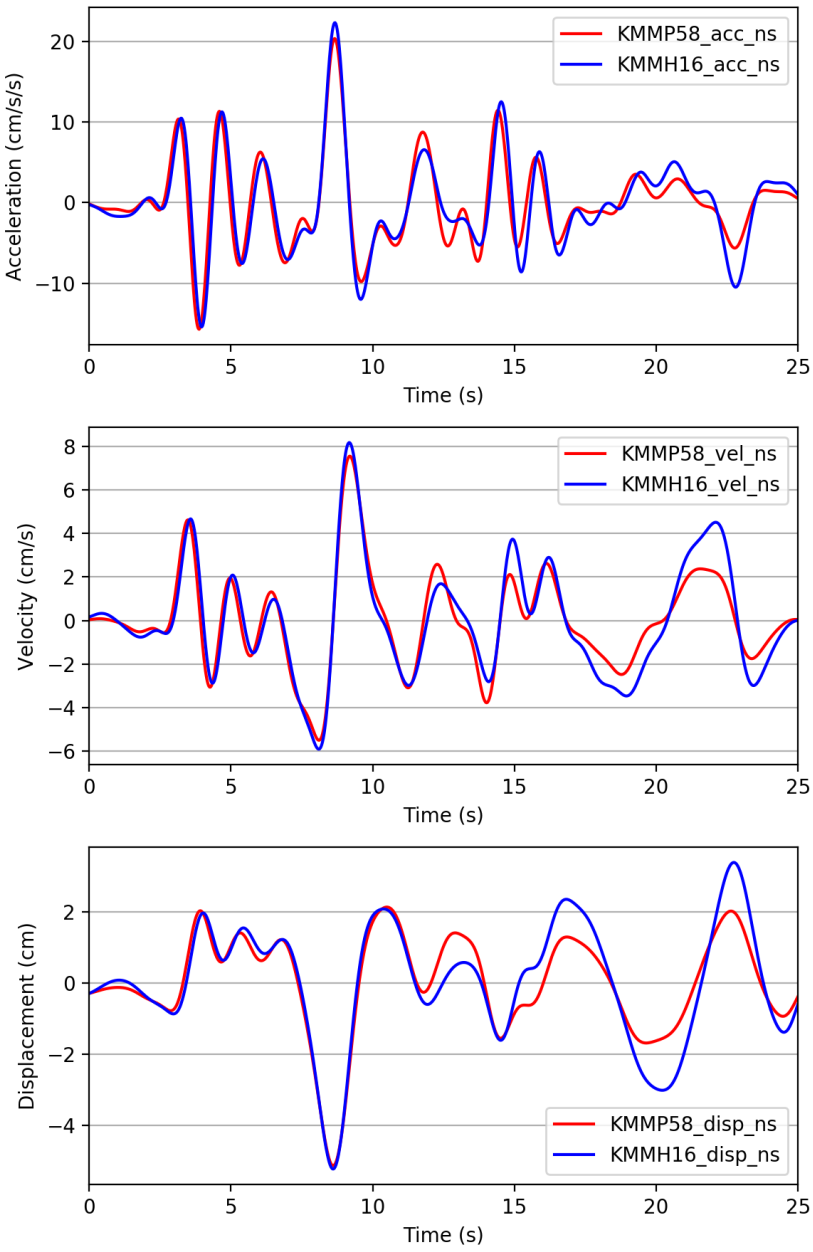

Fig. 9.34. Comparisons of LA analyzed seismological bedrock motions at KMMH16 (blue) and KMMP58 (red). Each panel and colored lines denote the similar meaning as in Fig. 9.33, but all these results are in the NS direction.

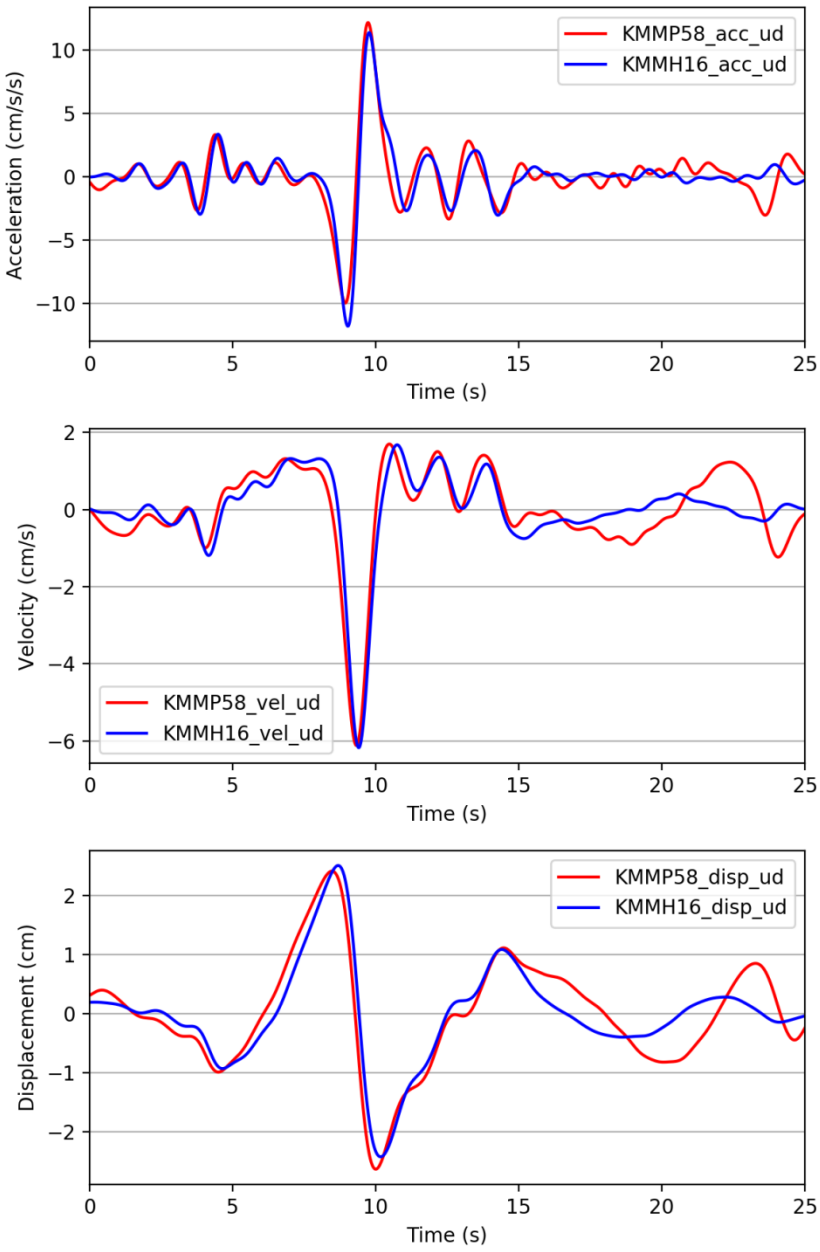

Fig. 9.35. Comparisons of LA analyzed seismological bedrock motions at KMMH16 (blue) and KMMP58 (red). Each panel and colored lines denote the similar meaning as in Fig. 9.33, but all these results are in the UD direction.

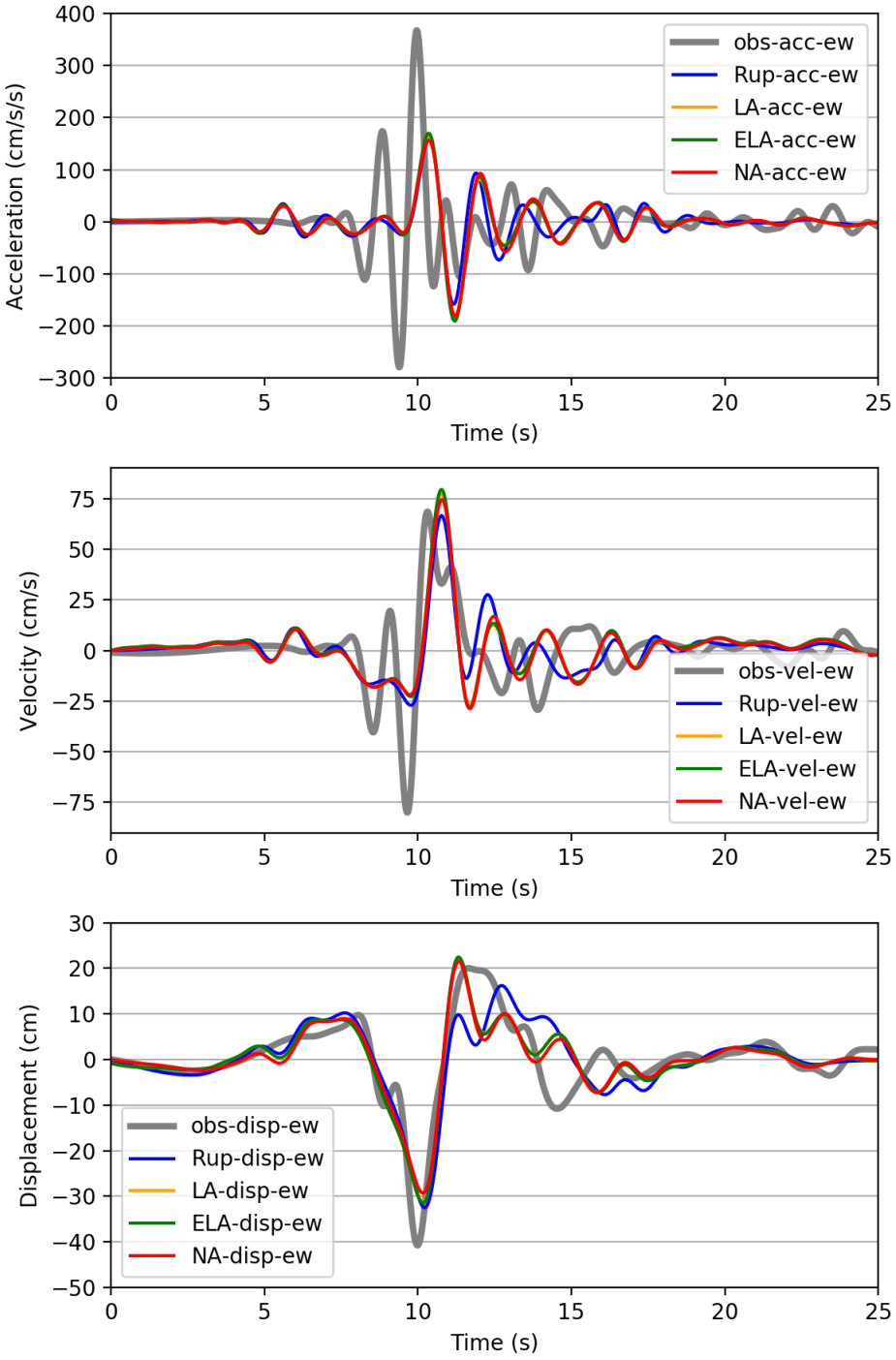

Fig. 9.36. Comparisons of LA, ELA, NA, rupture dynamics analyzed ground motions, and observed ground motions in EW direction at KMMH16. Top, middle, and bottom panels denote the comparisons of accelerations, velocities, and displacements. Blue, orange, green, and red color lines denote the estimated ground motions of rupture dynamics analysis, LA, ELA and NA in the EW direction at KMMH16, respectively; Heavy grey lines denote the observed ground motions in the EW direction at KMMH16.

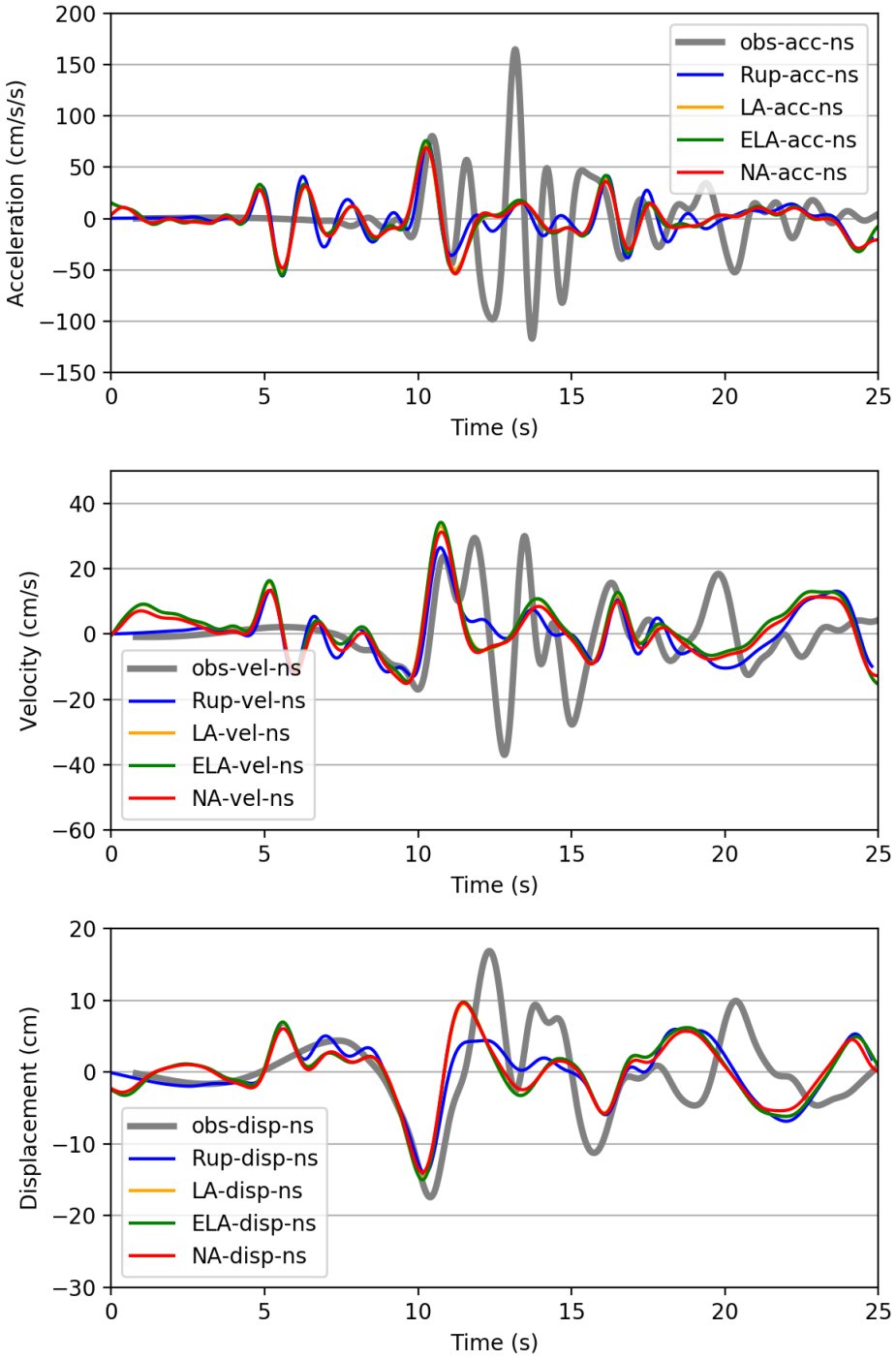

Fig. 9.37. Comparisons of LA, ELA, NA, rupture dynamics analyzed ground motions, and observed ground motions in NS direction at KMMH16. Each panel and each colored lines denote the similar meanings as in Fig. 9.36, but all are for the NS direction at KMMH16.

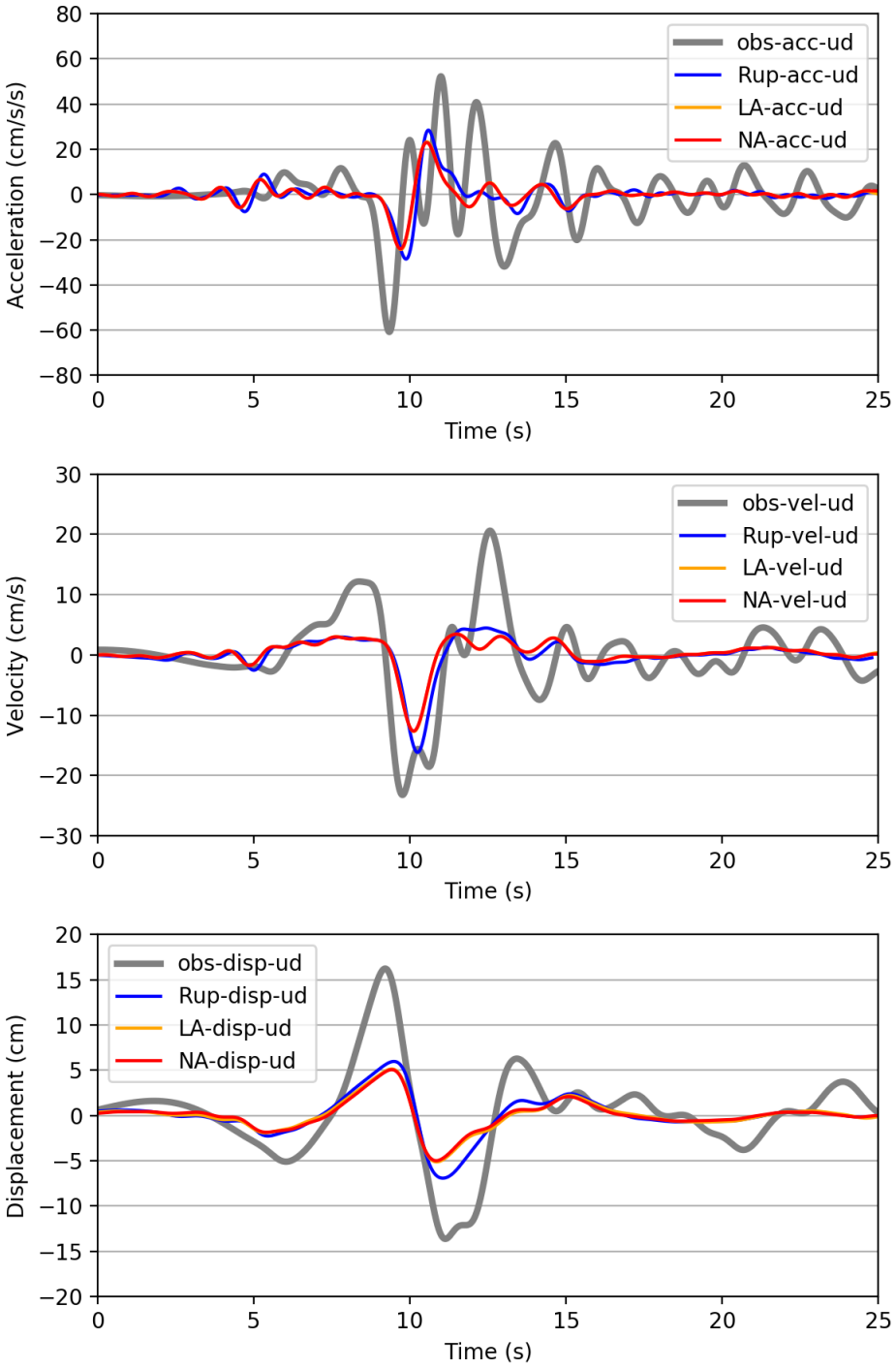

Fig. 9.38. Comparisons of LA, NA, rupture dynamics analyzed ground motions, and observed ground motions in UD direction at KMMH16. Each panel and each colored lines denote the similar meanings as in Fig. 9.36, but all are for the UD direction at KMMH16.

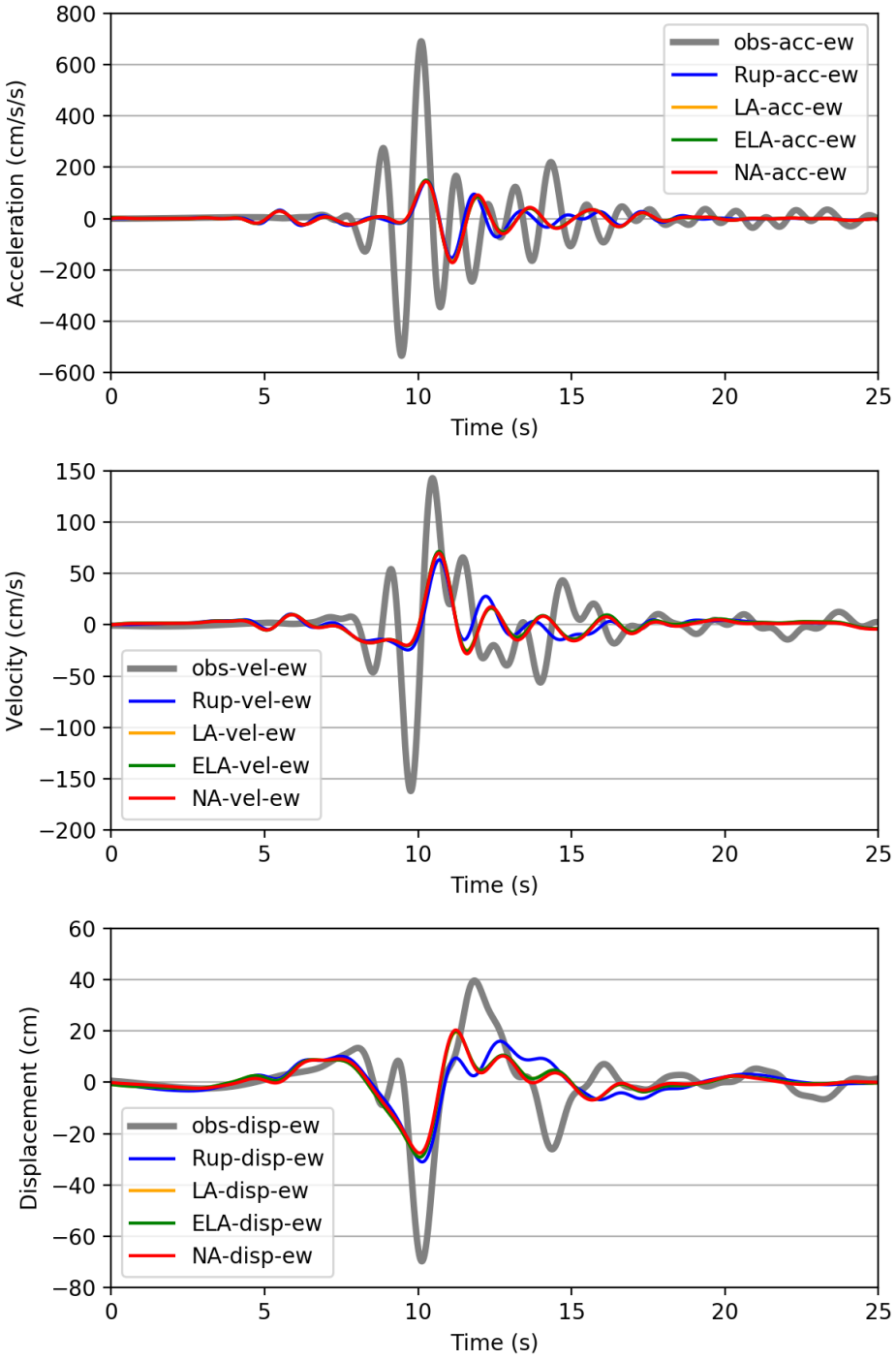

Fig. 9.39. Comparisons of LA, ELA, NA, rupture dynamics analyzed ground motions, and observed ground motions in EW direction at KMMP58. Each panel and each colored lines denote the similar meanings as in Fig. 9.36, but all are for the EW direction at KMMP58.

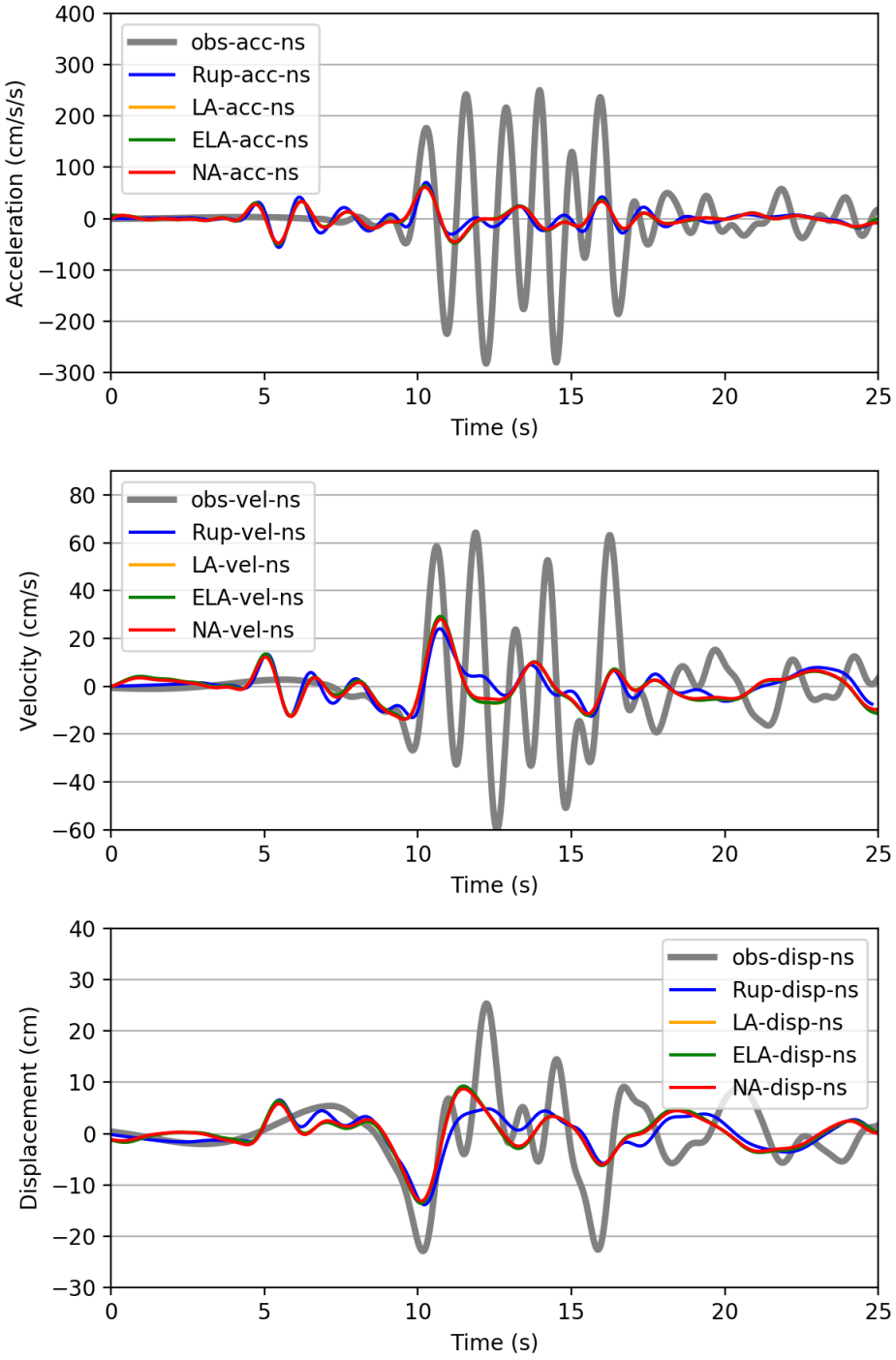

Fig. 9.40. Comparisons of LA, ELA, NA, rupture dynamics analyzed ground motions, and observed ground motions in NS direction at KMMP58. Each panel and each colored lines denote the similar meanings as in Fig. 9.36, but all are for the NS direction at KMMP58.

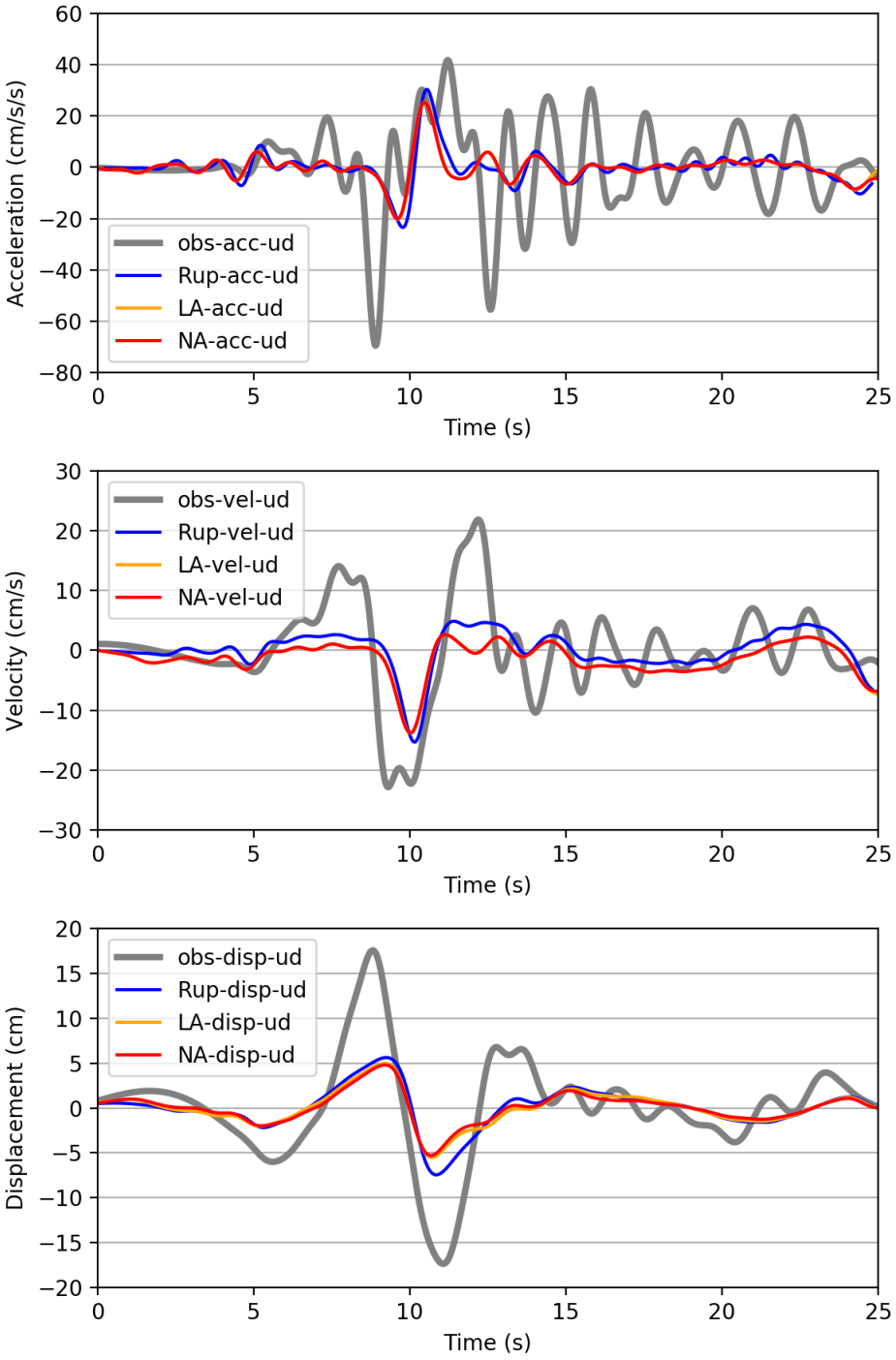

Fig. 9.41. Comparisons of LA, NA, rupture dynamics analyzed ground motions, and observed ground motions in UD direction at KMMP58. Each panel and each colored lines denote the similar meanings as in Fig. 9.36, but all are for the UD direction at KMMP58.

9.3.3. Distributions of PGV and PGD

224 observation stations were set on the ground surface along the fault direction surrounding Mashiki, as shown in Fig. 9.24. The PGV and PGD of every station were obtained after the rupture dynamics simulation. Figs. 9.42 – 9.44 display the PGV distributions of EW, NS, and UD components, respectively. Figs. 9.45 – 9.47 show the PGD distributions of EW, NS, and UD components, respectively.

According the PGV distribution of three components, PGVs were larger in the near fault zone areas, PGVs were larger surrounding the A3 area (25 − 38 km in fault parallel direction). Additionally, in the area near A_3, the farther away to the hypocenter, the greater the PGV. In the Mashiki area, from the southwestern corner point (SW point) to the northeast corner point (NE point), PGV EW showed slightly different between two points, while NS and vertical PGVs did not have a clearly visible difference. As for the PGD distributions, they were following the similar rule as for PGV. Thus, the source effects had slightly influence for the EW ground motions during the mainshock, while for the NS and vertical ground motions, source effects was not strong in Mashiki.

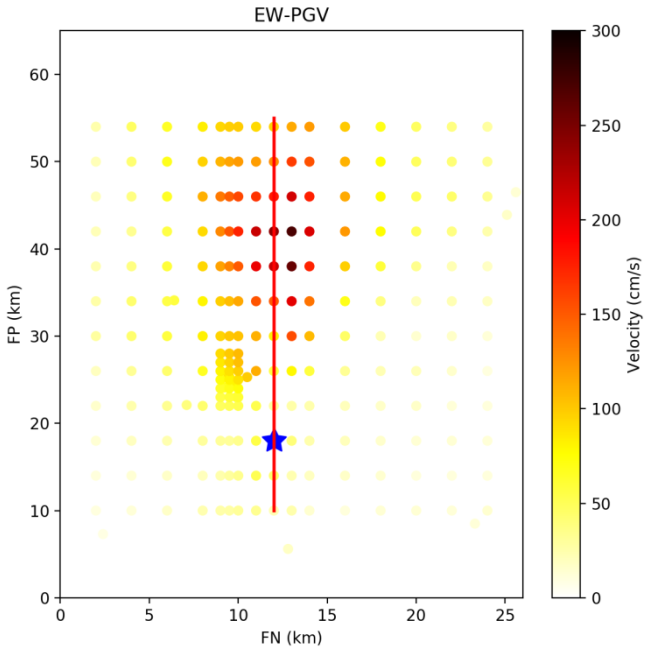

Fig. 9.42. PGV distribution of 224 sites in the EW direction. Red heavy solid line denotes the fault zone, big blue star denotes the epicenter location on the ground.

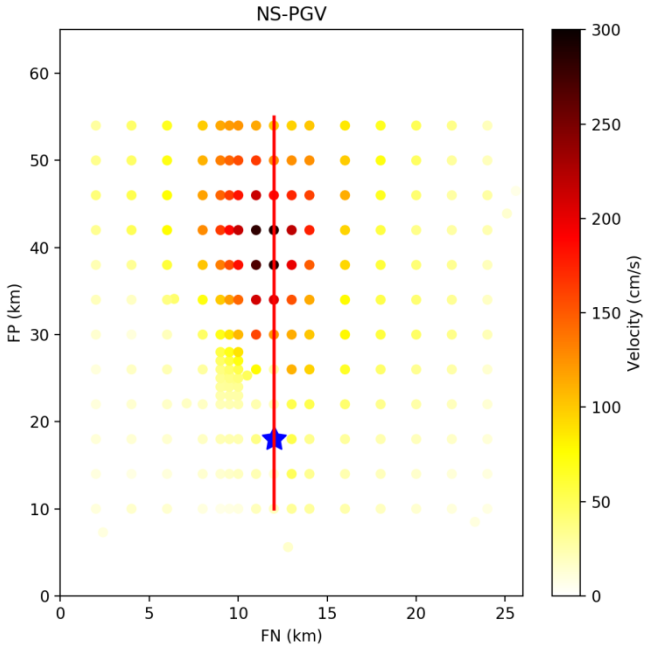

Fig. 9.43. PGV distribution of 224 sites in the NS direction. Red heavy solid line denotes the fault zone, big blue star denotes the epicenter location on the ground.

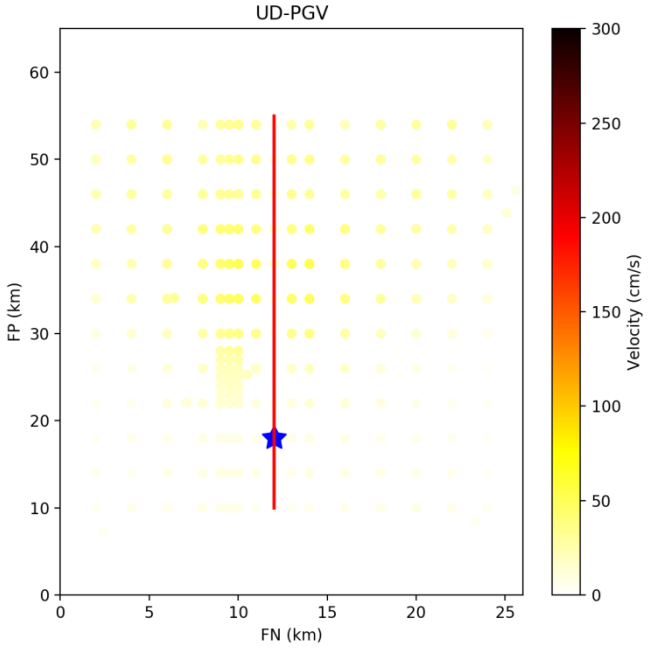

Fig. 9.44. PGV distribution of 224 sites in the vertical direction. Red heavy solid line denotes the fault zone, big blue star denotes the epicenter location on the ground.

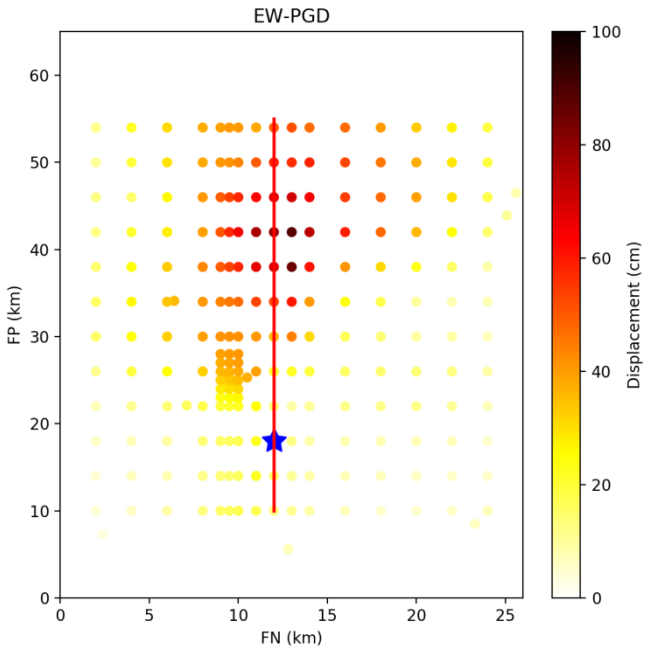

Fig. 9.45. PGD distribution of 224 sites in the EW direction. Red heavy solid line denotes the fault zone, big blue star denotes the epicenter location on the ground.

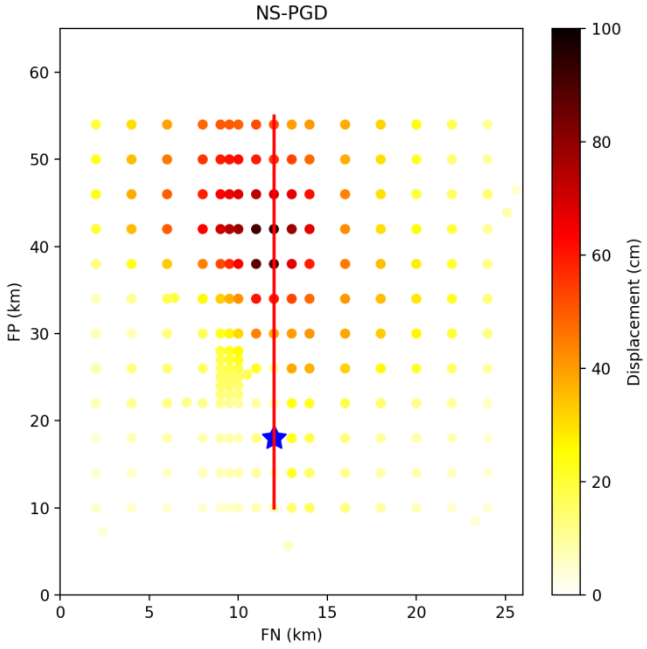

Fig. 9.46. PGD distribution of 224 sites in the NS direction. Red heavy solid line denotes the fault zone, big blue star denotes the epicenter location on the ground.

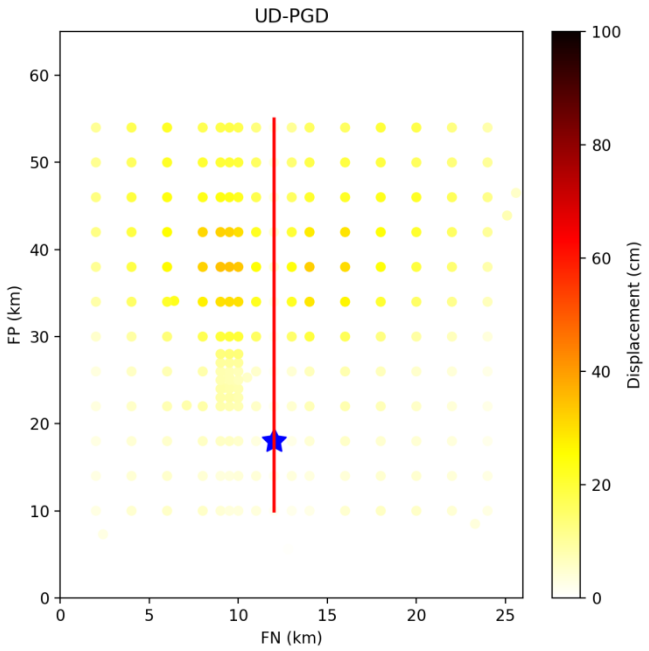

Fig. 9.47. PGD distribution of 224 sites in the vertical direction. Red heavy solid line denotes the fault zone, big blue star denotes the epicenter location on the ground.

9.4. Conclusion

Multiple cases of parameter studies were carried out to understand the rupture dynamic modeling. The significant influences of asperity locations and basin effects were discussed in detail. Rupture directivity were clearly captured in the testing models. Moreover, slip–rate functions were showed for both the background and asperity areas.

According to the estimated results of rupture dynamics simulation for the mainshock of 2016 Kumamoto earthquake, estimated ground velocities and displacements in time domain were close to the observed ones at KMMH16 in three directions. The estimated seismological bedrock motions of KMMH16 and KMMP58 were quite similar to each other in three directions. Associating with the ray–path study results in Chapter 5, the same seismological bedrock motions could be applied to the whole Mashiki area during the site response analysis. The estimated ground motions of LA, ELA, and NA were very close to the results of rupture dynamics simulations at both KMMH16 and KMMP58. In addition, the estimated velocities and displacements on the ground surface of LA, ELA, and NA were also close to the observed ground motions at KMMH16.

As shown in the PGV and PGD distributions in Mashiki, all the results in EW showed clearly rupture directivity effect. In the EW direction, PGVs and PGDs were appeared an obvious difference from southwestern to the northeastern areas, which signified the source effects had a little strong

effects on EW ground motions in Mashiki during the mainshock. However, the source effects were not strong in the NS and UD directions.

Reference (Chapter 9)

[1] Irikura K, Miyake H. Prediction of Strong Ground Motions for Scenario Earthquakes. Journal of Geography (Chigaku Zasshi) 2001;110:849–75. https://doi.org/10.5026/jgeography.110.6_849.

[2] Somerville P, Irikura K, Graves R, Sawada S, Wald D, Abrahamson N, et al. Characterizing Crustal Earthquake Slip Models for the Prediction of Strong Ground Motion. Seismological Research Letters 1999;70:59–80. https://doi.org/10.1785/gssrl.70.1.59.

[3] MIYAKOSHI K. Source characterization of inland earthquakes in Japan using source inversion results. 12WCEE 2000.

[4] Wells DL, Coppersmith KJ. New empirical relationships among magnitude, rupture length, rupture width, rupture area, and surface displacement. Bulletin of the Seismological Society of America 1994;84:974–1002.

[5] Irikura K, Miyakoshi K, Kamae K, Yoshida K, Somei K, Kurahashi S, et al. Applicability of source scaling relations for crustal earthquakes to estimation of the ground motions of the 2016 Kumamoto earthquake. Earth, Planets and Space 2017;69:10. https://doi.org/10.1186/s40623-016-0586-y.

[6] Asano K, Iwata T. Source rupture processes of the foreshock and mainshock in the 2016 Kumamoto earthquake sequence estimated from the kinematic waveform inversion of strong motion data. Earth, Planets and Space 2016;68:147. https://doi.org/10.1186/s40623-016-0519-9.

[7] Yoshida K, Miyakoshi K, Somei K, Irikura K. Source process of the 2016 Kumamoto earthquake (Mj7.3) inferred from kinematic inversion of strong-motion records. Earth, Planets and Space 2017;69. https://doi.org/10.1186/s40623-017-0649-8.

[8] Arben P, Sun J, Kawase H. Collaborative study on Earthquake Ground Motion Simulation Using Rupture Dynamics. Livermore, CA (United States): Lawrence Livermore National Lab. (LLNL); 2019.

[9] Pitarka A, Dalguer LA. Investigation of shallow crustal weak zone effects on rupture dynamics of surface and subsurface faulting. Proceedings and Abstracts Vol. XV, vol. 168, Palm Springs, California: 2005.

[10] Dalguer LA, Day SM. Staggered-grid split-node method for spontaneous rupture simulation. Journal of Geophysical Research: Solid Earth 2007;112. https://doi.org/10.1029/2006JB004467.

[11] Andrews DJ. A stochastic fault model: 1. Static case. Journal of Geophysical Research: Solid Earth 1980;85:3867–77. https://doi.org/10.1029/JB085iB07p03867.

[12] Andrews DJ. Rupture velocity of plane strain shear cracks. Journal of Geophysical Research 1976;81:5679–87.

[13] Day S. Three-dimensional simulation of spontaneous rupture: The effect of nonuniform prestress. Bulletin of the Seismological Society of America 1982;72:1881–902.

[14] Irikura K, Miyake H. Recipe for Predicting Strong Ground Motion from Crustal Earthquake Scenarios. Pure and Applied Geophysics 2011;168:85–104. https://doi.org/10.1007/s00024-010-0150-9.

[15] Matsuda T. Magnitude and Recurrence Interval of Earthquakes from a Fault. Zisin (Journal of the Seismological Society of Japan 2nd Ser) 1975;28:269–83. https://doi.org/10.4294/zisin1948.28.3_269.

[16] Si H, Midorikawa S. NEW ATTENUATION RELATIONSHIPS FOR PEAK GROUND ACCELERATION AND VELOCITY CONSIDERING EFFECTS OF FAULT TYPE AND SITE CONDITION. Journal of Structural and Construction Engineering (Transactions of AIJ) 1999;64:63–70. https://doi.org/10.3130/aijs.64.63_2.

[17] Kawase H, Sun J, Pitarka A, Nagashima F, Ito E. Rupture dynamic simulation considering spatial fluctuation of stress drop - case study of Mw6.5 class rupture, Hokuriku, Japan: Architectural Institute of Japan Assembly Synopsis; 2019.

[18] Kawase H, Sun J, Nagashima F, Ito E. Properties of spatial variation of slip amount and slip speed of dynamic fracture simulation results considering spatial inhomogeneity, Kanto, Japan: Architectural Institute of Japan Assembly Synopsis; 2020.

[19] Pitarka A, Graves R, Irikura K, Miyakoshi K, Rodgers A. Kinematic Rupture Modeling of Ground Motion from the M7 Kumamoto, Japan Earthquake. Pure and Applied Geophysics 2020;177:2199–221. https://doi.org/10.1007/s00024-019-02220-5.

[20] Geospatial Information of Japan. Information about 2016 Kumamoto earthquake 2016.

[21] Yoshida N. DYNEQ - A computer program for Dynamic response analysis of level ground by Equivalent Linear Method. 2014.

[22] Nagashima F, Kawase H. Estimation of the incident spectrum at the seismic bedrock by using the observed vertical motion at the ground surface based on diffuse field theory, Proceedings of the 15th Japan Earthquake Engineering Symposium; 2018.

Chapter 10

Conclusion

10.1. Conclusions

10.1. Conclusions

This thesis investigates the surface soil structures of Mashiki, Kumamoto from observed earthquake ground motions and microtremors, evaluates the contribution of nonlinear amplification characteristics in the strong ground motions, reproduces the building damage considering the construction periods, and evaluates possible contribution of the dynamic rupture propagation on the seismic fault to the observed high peak ground velocity at Mashiki during the mainshock of 2016 Kumamoto Earthquake. The contribution of local site effects, building construction period and source model of the earthquake to building damage in Mashiki during the mainshock were studied. The proposed approach can be used for investigating disaster for future earthquakes and the derived information can be used for more sophisticated earthquake risk evaluation.

In Chapter 2, based on the analysis MHVRs, the fundamental frequency in the northeastern part of Mashiki was found to be higher than those in the southwestern part. Especially, in the area adjacent to the Akitsu River in the southwestern part, the fundamental frequency is slightly lower than 1.0 Hz. This difference in the distribution of the fundamental peak frequency suggests that the thicknesses or the S-wave velocities of the underground layers vary drastically from one region of the town to the other.

The EMR method was introduced in Chapter 3, and showed the comparisons of the MHVR, pEHVR, and EHVR of three strong motion station sites. The EMR method was suitable in Mashiki, because the pEHVRs at the microtremor observation sites around the strong-motion stations were closer to the EHVRs than to the MHVRs at these sites, although the differences were not very large. Theoretically, the pEHVR is a suitable choice to identify the velocity structures in Mashiki based on the DFC for earthquakes. Practically, the pEHVR tends to have higher amplitude in the frequency range greater than the fundamental peak frequency. Therefore, the pEHVR will provide a velocity structure with a higher amplification in this frequency range.

In Chapter 4, some new findings were obtained. The stack of soft layers in the southwestern part are thicker than in the northeastern part, which is shown in the contour map of the lower boundary of the 8th subsurface layer (Vs equals approximately 830 m/s at the bottom of the 8th layer). The soft subsurface layers of the area between the Municipal Road No.28 and the Akitsu River are deeper than those of the northern part. The site effects of the soft subsurface layers may have been the major contribution to the dense concentration of building damage in Mashiki town. Also, the V_{s30} distribution showed close relationship to the depth of engineering bedrock in Mashiki.

According to results in Chapter 5, the estimated spatial PGV distribution of the EW component by ELA was similar to that of the building damage distribution by the AIJ survey. In addition, the estimated PGAs and PGVs of the EW component were considerably higher than those of the NS component. The analytical results for the 592 of 1D subsurface velocity structures have more detailed resolution (~50 m grid) than the previous studies. The 592 estimated ground motions

provides the conditions for analyzing the dynamic response of every building. Effects from the soil nonlinearity showed influence on the estimated ground motions in Mashiki by comparing LA and ELA results.

According to analysis results of Chapter 6, the estimated spatial PGV distribution of the EW by NA was close to the building damage distribution by the AIJ report than the results by ELA. Four categories was considered to classify the estimated velocity structures at 592 points according to the water table depth which corresponds to the location of four borehole drilling sites. The similarity of velocity structures fit the ground classification in Mashiki well. Sites with soil liquefaction were mainly concentrated in the southern area near the river which was the case in the MILT report and previous studies. The estimated ground motions at KMMH16 by NA were very close to the observation ones and were smaller than the ELA results. In addition, the estimated grounds at MS9-6 by NA were very close to the observed strong ground motions at KMMP58, which indicates soil liquefaction may have caused large velocity waveforms during the mainshock. Soil nonlinearity showed significant effects to the strong ground motions. This fact also indicated that the PGV is an important index for explaining the building damage distribution, as have been reported previously for the major earthquakes in Japan. Moreover, the estimated PGV distribution of NA was found to be smoother than the ELA, although the ELA–PGVs were stronger than the NA–PGVs in Mashiki. Additionally, the NA–PGA distribution did not show relationship with the AIJ building damage distribution result. Effects of soil liquefaction to strong ground motions at surface were clear from the comparison between the ELA and NA results. Thus, NA would be used to analyze site response when the soil liquefaction was found during a strong ground shaking.

With the research results in Chapter 7, the construction period for every building in the target area was investigated by the proposed research method in this study. The total percentage of the older buildings (constructed before 1950 and during 1951–1970) was slightly greater than that of another survey for all of Mashiki. Most of the buildings constructed before 1970 were located between the Road No.28 and Akitsu River in central Mashiki.

In Chapter 8, the estimated damage probabilities indicated heavy damage to older buildings (constructed before 1950 and during 1951–1970). The estimated damage probability distribution of each new cell generally matched the damage probability distribution of the AIJ survey. Moreover, in the northwestern part where the AIJ survey did not cover, it was found that non-negligible damage probabilities would have been caused by the mainshock. In several cells in the northwestern and southwestern parts of ELA results, the damage probabilities were clearly found to be greater than those of the AIJ survey. This may be because the buildings were not wooden, or newly built (after the building code was modified in 2000), which was not considered in details in this study. Referring to the NA results, the estimated damage probability of buildings were also similar to the AIJ report. Soil liquefaction also has decreased a smaller amount of damage to houses in the area near Akitsu River, because the NA–DPs of several sites were slightly smaller than the ELA–DPs, which were decreased

by the soil liquefaction. These results indicate that the presented building damage evaluation method can be used to estimate the damage probability distributions of other areas as long as the necessary building information is obtained in a similar manner. Thus, the detailed estimated ground motions can be served as a basis for dynamic analyses of structures for quantitative damage prediction. This method allows the building responses of a target area to be estimated precisely. It should be emphasized that the construction period of buildings and the soil conditions were necessary to be considered when evaluating the safety of a building.

According to the results of Chapter 9, dynamic rupture simulations using stochastic stress drop and asperity models constrained by Irikura Recipe produce fault slip and average peak ground motion velocity consistent with empirical relations. The asperities offset has no effect on fault maximum and average fault slip. However, larger asperity offsets reduce the peak ground motion velocity. Shallow asperities create a rather single shallow slip patch, whereas deep asperities create distinct slip concentrations in the asperity area. Shallow asperities also produce much larger shallow slip. In terms of rupture kinematics, deep asperities create a complex rupture time pattern, which is dominated by a very slow initial rupture and gradually faster rupture at depth. Both average peak velocity and fault slip increase when stress drop variations increase with depth. The shape of the sharp fault slip distribution in the asperity was different with the distribution area shape obtained by extracting the large displacement area by the kinematic inversion. The estimated fault slip distribution was smoother than the inversion results of the actual earthquake. The slip velocity function appeared a Kostrov shape within the asperity, while it showed a triangular shape in the shallow part and the region between the asperities. The peak slip velocity did not appear at the center of the asperity, it shifted to the direction of rupture propagation, due to the effect of rupture orientation on the shape of the slip velocity function. According to the results of rupture dynamics analysis of the mainshock, estimated velocity and displacement waveforms were close to the observed motions at KMMH16. The results of linear analysis, equivalent linear analysis, and nonlinear analysis were nearly the same to each other, and all of these waveforms were similar as that of the rupture dynamics analysis at KMMH16 and KMMP58. Moreover, the deconvoluted seismological bedrock waves at KMMH16 and KMMP58 from estimated ground surface motions were very close, and associating with the ray-path analysis of wave propagation, the same seismological bedrock waveforms could be used to conduct site response analysis in Mashiki. In addition, the effect of rupture directivity was strong and resulted in obvious difference on ground motions in EW component in Mashiki as shown by the PGV and PGD distributions in three directions.

Finally, it could be concluded that in order to reproduce ground motions with special features of the observed damage in Mashiki during the mainshock of the 2016 Kumamoto earthquake, it required to consider realistic nonlinear responses of both underground structures and buildings and the complicated dynamic rupture scenario on the surface of the seismic fault. This study will be the start

line for more sophisticated earthquake risk evaluations considering these effects for future damaging earthquakes that is expected to occurred in the near future.

Data and Resources

The K-NET & KiK-net catalog was searched using https://www.kyoshin.bosai.go.jp/ (last accessed December 2020). The NIED F-net Earthquake Mechanism information can be accessed at https://www.fnet.bosai.go.jp/top.php (last accessed December 2020). The borehole logging data at KMMH16 can be found at https://www.kyoshin.bosai.go.jp/kyoshin/db/ (last accessed December 2020). The J-SHIS velocity model was searched using http://www.j-shis.bosai.go.jp/en/ (last accessed December 2020). The website of MLIT could be found at https://www.mlit.go.jp/en/ (last accessed December 2020). The web site of JMA could be found at https://www.jma.go.jp/jma/indexe.html (last accessed December 2020). The "DYNEQ" software was downloaded at https://www.kiso.co.jp/yoshida/yoshida/computercodes/japanese/ (last accessed December 2020). The website of Geospatial Information Authority of Japan can be found at https://www.gsi.go.jp/ (last accessed December 2020). The Python3 could be downloaded from https://www.python.org/downloads/ (last accessed December 2020). The gfortran packages could be downloaded at https://gcc.gnu.org/wiki/GFortranBinaries (last accessed December 2020). Several figures used the GMT5 software which can be found at http://gmt.soest.hawaii.edu/projects/gmt/wiki/Installing (last accessed December 2020). Several figures were made with the QGIS3 software which can be found at https://qgis.org/en/site/ (last accessed December 2020). Several figures were used the GIMP, could be found at https://www.gimp.org/ (last accessed December 2020). Several figures used the packages of Matplotlib (https://matplotlib.org/3.3.3/users/installing.html , last accessed December 2020), seaborn (https://seaborn.pydata.org/, last accessed December 2020), Pillow (https://pillow.readthedocs.io/en/stable/index.html, last accessed December 2020). The scientific packages of numpy (https://numpy.org/doc/stable/index.html, last accessed December 2020), scipy (https://www.scipy.org/, last accessed December 2020), pandas (https://pandas.pydata.org/, last accessed December 2020), eqsig (https://eqsig.readthedocs.io/en/latest/, December 2020), and obspy (https://docs.obspy.org/, last accessed December 2020) were used in this study.

Acknowledgement

First, I want to thank two advisors of this study, Prof. Shinichi Matsushima, who is a professor of the Graduate School of Kyoto University and professor of the Disaster Prevention Research Institute of Kyoto University, and Prof. Hiroshi Kawase, who is a professor of the Disaster Prevention Research Institute of Kyoto University. They gave me a lot of professional guidance and encouragement during my PhD research and helped me overcome many difficulties. I pray for the future development of both Matsushima Laboratory and Kawase Laboratory.

Second, I want to say thanks to Dr. Fumiaki Nagashima, an Assistant Professor of the Disaster Prevention Research Institute of Kyoto University, who helped to solve a series of questions related to the site response analysis and seismological bedrock motion estimation. I also want to thank Dr. Arben Pitarka, a seismologist of Lawrence Livermore National Laboratory, CA, United States, who taught me a lot of important knowledges and theories of seismology and helped to build the rupture model of 2016 Kumamoto earthquake in Chapter 9. I also want to thank for the great help from Dr. Kiyoshi Fukutake, the senior researcher of Shimizu Corporation, who taught me the theories of nonlinear analysis of subsurface layers and helped to determine the nonlinear soil parameters in Chapter 6. I am very grateful for their kind help.

Third, I appreciate the help of Prof. Izuru Takewaki and Prof. Yasuhiro Hayashi, two Professors of the Graduate School of Kyoto University, who gave many valuable comments and suggestions for my PhD thesis.

Next, I want to express my gratitude for the help of the Kumamoto Prefecture, JMA, and NIED who shared with me the important observed strong ground motions at KMMP58, Bunkakaikan, and KMMH16. I also appreciate the help of the AIJ research teams and the BRI survey team, who shared with us the survey data of the building damages as well as the soil properties at Mashiki.

Then, I want to thank the team members of Matsushima Laboratory, Kawase Laboratory, and Nishino Laboratory, who helped to observe the microtremors in 2016 and 2018.

Some chapters of the research are funded by Sophisticated Earthquake Risk Evaluation (endowed by Hanshin Consultants of Japan) and the Grand-in-Aid by JSPS (Kakenhi) for Basic Research (B) No.19H02405. Moreover, the China Scholarship Council also supported me with a two-year scholarship during my doctoral period. I am very grateful for their help.

Finally, I would like to express my sincere appreciation to my parents and sisters. They gave me the great encouragement and support during these three years.

Thank you again for these great help.

Jikai Sun

February 13, 2021

Publication

[1] Sun J, Kawase H, Nagashima F. Estimation of The Strong Motions at Mashiki Town, Kumamoto, During The 2016 Kumamoto Earthquake, Based on Microtremor Horizontal-to-Vertical Spectral Ratios. Disaster Prevention Research Institude Annuals 2018;61:238–46.

[2] Sun J, Nagashima F, Kawase H, Matsushima S. Site effects analysis of shallow subsurface structures at Mashiki town, Kumamoto, based on microtremor horizontal-to-vertical spectral ratios. Bulletin of the Seismological Society of America 2020. https://doi.org/10.1785/0120190318.

[3] Sun J, Kawase H, Nagashima F, Matsushima S. Strong Motion Simulation in Downtown Mashiki during 2016 Kumamoto Earthquake to Reproduce The Damage Belt, Sendai, Japan: 17th World Conference on Earthquake Engineering; 2020.